

**Characterization of Myocardial Infarction and Its Repair in Pig Models Using MRI
and Optical Spectroscopy and Imaging**

by

Yanmin Yang

A Thesis submitted to the Faculty of Graduate Studies of
The University of Manitoba
in partial fulfillment of the requirement for the degree of

DOCTOR OF PHILOSOPHY

Department of Biochemistry & Medical Genetics

University of Manitoba

Winnipeg, Manitoba

Copyright © 2010 by Yanmin Yang

Abstract

The goals of the thesis were to, in pig models, (1) assess manganese-enhanced magnetic resonance imaging (MEMRI) in the characterization of acute and chronic ischemia-induced myocardial infarction (MI), (2) characterize cryoinjury-induced MI with contrast-enhanced MRI and optical methods, and (3) observe the effects of locally released angiogenic factors on the repair of cryoinjury-induced MI.

Firstly, after acute MI was established by occlusion of the coronary artery branches, the pig hearts were isolated and mounted onto an *ex vivo* perfusion system inside a 7T magnet. After administration of MnCl₂, T₁-weighted MR images showed gradual enhancement of signal intensity within the normal myocardium, whereas the ischemic counterpart remained hypointense. During chronic MI progression, the intensity increased slowly after exposure to MnCl₂ within the infarcted myocardium.

Secondly, a new MI model was tested via direct 2-min contact of left ventricular epicardium with a liquid nitrogen-cooled aluminum bar. Subsequent *in vivo* Gd-enhanced MRI showed a uniform hypointense area (~10 mm in depth) surrounded by a hyperintense rim. Histology showed erythrocytes embolism within the cryolesion with a thin necrotic rim neighboring the normal myocardium. Four weeks later, the cryoinjured myocardium was replaced by scar tissue.

Thirdly, *in vivo* MEMRI was tested on this cryoinjury model. After intravenous administration of MnCl₂ via intermittent bolus or continuous infusion, normal myocardium showed prolonged hyperintense, which led to significant signal contrast between it and cryoinjured myocardium. Continuous infusion scheme minimized hemodynamic fluctuation.

Finally, angiogenic therapy was assessed by anchoring of vascular growth factors-loaded alginate beads or adipose-derived stem cells (ADSCs)-loaded agarose patch on top of the cryoinjured myocardium. Gd-enhanced MRI revealed (1) growth of new tissue wrapping the growth factors-loaded alginate beads and (2) higher perfusion within the ADSCs-treated cryoinjured myocardium as compared with the growth factors-treated counterpart. Histological and fluorescent microsphere examination revealed that ADSCs induced more significant growth of mature microvasculature within the cryoinjured myocardium.

These results indicate that $MnCl_2$ could characterize MI *ex vivo* and *in vivo*. Epicardial implantation of ADSCs-loaded agarose hydrogel can induce angiogenesis within the cryoinjured myocardium, a form of MI with similar progression features as that induced by ischemia.

Acknowledgments and Contributions

The project presented in this thesis involved contributions from many other people besides myself. To establish cryoinjury-induced chronic myocardial infarction in pig hearts and assess the therapeutic efficiency using new angiogenic approaches, I first wrote an animal study protocol, based on which a grant was later proposed for application of CIHR funding (60%), though unsuccessful. During *in vivo* study for establishment of myocardial infarction induced by either coronary artery occlusion or cryothermia and image acquisition via either magnetic resonance or optical imaging, I was responsible for surgery (60%) and took part in postoperative care (40%). During *ex vivo* study on isolated pig hearts for magnetic resonance and optical imaging, I took part in perfusate preparation, heart isolation, setup and monitoring of the perfusion system (50%). During post-mortem study on isolated pig hearts, I prepared staining solution for macroscopic detection of jeopardized myocardium (80%) and took part in tissue preparation for microscopic assessment (50%). During assessment of angiogenic potential on cryoinjured pig hearts, I prepared the alginate beads containing vascular growth factors and labeled the beads with $GdCl_3$ trackable by magnetic resonance imaging (60%) and also took part in preparation of agarose patches loaded with adipose-derived stem cells (30%). During data analysis, I took part in image assessment, kinetic analysis of signal change after administration of the contrast agents and final comparison via statistical softwares (40%). With all the data, I participated in abstracts preparation for conference presentations (20 abstracts) and manuscripts preparation for publication in peer-reviewed journals (5 publications). Of course, I should also give my sincere gratitude for invaluable contributions from my supervisor and other people. Firstly, I would like to thank my

supervisor, Dr. Valery Kupriyanov, for his incessant guidance, constant encouragement and numerous help with protocol design, data analysis and review of the draft for this thesis. Secondly, more specific thanks were given to (1) Dr. Marco L.H. Gruwel for his continuous technical support in optimization of MR image acquisition on isolated pig heart within the 7T magnet and involvement in the measurement of contrast-labelled alginate hydrogel beads within the 11.7T magnet, (2) Patricia Gervai, Jiankang Sun and Dr. Hung-yu Lin for optimization of MR image in 3T and 7T, (3) Lori Gregorash, Allan Turner, Shelley Gernscheid, Rachelle Mariash, and Bo Xiang for their arrangement of and contribution in the animal surgery and postoperative care, (4) Dr. Eugene Gussakovsky and Dr. Olga Jilkina for acquisition and analysis of near infrared data, (5) Miriam Glogowski and Bozena Kuzio for their help in cell culture and biochemical measurement, and (6) Dr. Yijun Fan from Dr. Xi Yang's lab and Saro Bascaramurty for their help in tissue processing for histological study. Meanwhile, I also owe thanks to my committee members, Drs. Ganghong Tian, Xi Yang and Klaus Wrogemann for their helpful feedback and interest in this work.

Institute for Biodiagnostics at National Research Council of Canada is a great research environment to work. There are many people to thank for having helped me fulfill this project. I would like to be grateful to the University of Manitoba, the Manitoba Health Research Council, and the National Research Council for their financial support of this research project.

Finally, I would like to present my deepest gratitude to my wife, Dr. Jiming Cai, and son, Qilin Yang, as well as other family members in China for their constant support and encouragement when I was carrying out this study in Canada.

Table of Contents

Abstract	ii
Acknowledgments and Contributions	iv
Table of Contents	vi
List of Tables	ix
List of Figures	xi
List of Copyrighted Material for which Permission was Obtained	xv
Chapter 1: Introduction	1
Chapter 2: Review of literature	3
2.1. Myocardial Infarction	3
2.2. Evaluation of myocardial infarction with contrast-enhanced MRI	18
2.3. Evaluation of myocardial ischemia and infarction using optical techniques	44
2.4. Cryoinjury for establishment of experimental myocardial infarction in pig heart	48
2.5. Infarction repair by intrapericardial delivery of vascular growth factors and adipose-derived stem cells	52
2.6. Research goals of this project	60
Chapter 3: Material and Methods	62
3.1. Animal experiments and protocols	62
3.2. <i>Ex vivo</i> Mn-enhanced MRI on isolated hearts	65
3.3. <i>In vivo</i> Gd- and Mn-enhanced MRI	68
3.4. Visible/NIR point spectroscopy	69
3.5. NIR spectroscopic imaging of tissue perfusion after myocardial ischemia and Infarction	71

3.6. Hemodynamic and metabolic measurements -----	73
3.7. Postmortem analyses -----	74
3.8. Preparation of MRI-trackable alginate beads containing proteins -----	76
3.9. Preparation of agarose gel patch containing ADSCs -----	80
Chapter 4: Results -----	82
4.1. <i>Ex vivo</i> evaluation of MnCl ₂ as a MR contrast agent for acute cardiac ischemia --	82
4.2. <i>Ex vivo</i> evaluation of MnCl ₂ as a MR contrast agent for chronic myocardial infarction -----	91
4.3. Characterization of myocardial cryoinjury with contrast-enhanced MRI and Optical spectroscopy -----	101
4.4. <i>In vivo</i> evaluation of MnCl ₂ as a MR contrast agent to characterize myocardial cryoinjury -----	115
4.5. Design of MR trackable alginate hydrogel -----	124
4.6. Repair of cryoinjured myocardium with intrapericardially delivered alginate beads containing growth factors and agarose patch containing adipose- derived stem cells -----	129
Chapter 5: Discussion -----	145
5.1. Summary of major findings -----	145
5.2. Methodology and data interpretation -----	150
5.3. Mechanism of cryoinjury -----	162
5.4. Therapeutic angiogenesis for MI with alginate-entrapped vascular growth factors -----	164
5.5. Effects of adipose- derived stem cells immobilized in agarose gel patch on	

cryoinjured myocardium -----	168
Chapter 6: References -----	170
Abbreviations -----	195

List of Tables

Table 2.1. Severity of myocardial infarction	11
Table 2.2. Temporal classification of myocardial infarction	12
Table 2.3. Diagnosis of acute cardiac ischemia and prior myocardial infarction with ECG	13
Table 2.4. List of physiologically important nuclear species with their gyromagnetic ratio	19
Table 2.5. Classification of MR contrast agents	24
Table 3.1. Biochemical features of heme-proteins and growth factors	80
Table 4.1. Kinetics of signal enhancement by MnCl_2 after cardiac ischemia with or without reperfusion	84
Table 4.2. Effects of MnCl_2 on hemodynamic parameters of isolated pig hearts after acute ischemia with or without reperfusion	89
Table 4.3. Kinetics of signal enhancement by MnCl_2 in the normal and infarcted myocardium	95
Table 4.4. Kinetic parameters of signal enhancement by MnCl_2 with or without sarcolemmal depolarization	96
Table 4.5. Effects of MnCl_2 on hemodynamic parameters of isolated pig hearts after chronic myocardial infarction	100
Table 4.6. Kinetic parameters of manganese-induced signal enhancement in normal and damaged areas of hearts after acute cryoinjury	107
Table 4.7. Kinetic parameters of signal enhancement with <i>ex vivo</i> manganese-enhanced MRI in normal and damaged areas of hearts after cryoinjury	114

Table 4.8. Kinetic parameters of signal decay with <i>in vivo</i> Mn-enhanced MRI in blood, normal and damaged areas of hearts after cryoinjury	119
Table 4.9. Efflux constants of agents embedded in alginate beads	130
Table 4.10. The effects of intrapericardial treatment of cardiac cryoinjury on the first pass GdDTPA kinetics	132
Table 4.11. Fluorescence within the short-axis cryoinjured myocardium in pigs receiving agarose patches with or without adipose-derived stem cells	141

List of Figures

Figure 2.1. Inversion recovery sequence used to suppress signal from the normal myocardium.	31
Figure 3.1. Anchor of control and therapeutic agents on top of the cryoinjured left ventricular epicardium.	67
Figure 3.2. Optical spectra of the myocardial tissue.	72
Figure 4.1. Ischemic myocardium detected by perfusion staining with Evans blue and <i>ex vivo</i> Mn-enhanced MRI.	83
Figure 4.2. Enhancement kinetics of the MR signal intensity as a function of time after exposure to MnCl ₂ in an isolated ischemic pig heart.	85
Figure 4.3. Change of the MR signal intensity after intravenous injection of Gd-DTPA in a pig heart subjected to acute ischemia.	87
Figure 4.4. A representative short-axis slice of a pig heart stained by IR676 and TTC after 75-min ischemia followed by reperfusion.	90
Figure 4.5. Histological features of a chronically infarcted pig heart.	92
Figure 4.6. Manganese-enhanced MR images of an isolated pig heart after 7-day infarction.	94
Figure 4.7. Representative Gd-enhanced MR short-axis images of a pig heart after myocardial infarction.	97
Figure 4.8. Representative staining results with IR676 and TTC in a pig heart subjected to chronic myocardial infarction.	99

Figure 4.9. Epicardial appearance of an acutely cryoinjured pig heart and its image corresponding to <i>in vivo</i> perfusion map acquired by an NIR imaging system with indocyanine green as the intravascular flow tracer.	103
Figure 4.10. Kinetics of <i>in vivo</i> MR signal development in a short-axis pig heart slice following acute cryoinjury after intravenous infusion of Gd-DTPA.	104
Figure 4.11. A short-axis MR image enhanced by MnCl ₂ on an <i>ex vivo</i> perfused pig heart following acute cryoinjury.	106
Figure 4.12. Macroscopic and microscopic staining pictures of a pig heart subjected to acute cryoinjury.	108
Figure 4.13. Macroscopic and microscopic staining pictures of pig hearts subjected to chronic cryoinjury.	110
Figure 4.14. Change of the MR signal intensity in a cryoinjured pig hearts after intravenous injection of Gd-DTPA.	111
Figure 4.15. Changes of the MR signal intensity in a 4-week cryoinjured pig heart after addition of MnCl ₂ into the perfusate.	113
Figure 4.16. Representative MR images of short-axis pig heart slices after <i>in vivo</i> exposure to intravenously infused MnCl ₂ .	116
Figure 4.17. Representative Mn- and Gd-enhanced MR images as well as post-mortem staining pictures of short-axis pig heart slices	118
Figure 4.18. <i>In vivo</i> kinetics of MR signal change in the normal and cryoinjured myocardium and left ventricular blood pool after intravenous infusion of MnCl ₂ .	120

Figure 4.19. Changes of the heart rate during and after continuous or intermittent bolus intravenous infusion of MnCl ₂ .	121
Figure 4.20. Changes of the systolic blood pressure during and after continuous or intermittent bolus intravenous infusion of MnCl ₂ .	122
Figure 4.21. Changes of the diastolic blood pressure during and after continuous or intermittent bolus intravenous infusion of MnCl ₂ .	123
Figure 4.22. T ₁ - and T ₂ -weighted MR images acquired with a spin-echo sequence for the GdCl ₃ -labelled alginate hydrogel beads.	126
Figure 4.23. T ₁ - and T ₂ -weighted MR images acquired with a spin-echo sequence for the methemoglobin-labelled alginate beads.	127
Figure 4.24. Anchoring of alginate beads on top of the cryoinjured myocardium and corresponding short-axis MR images.	128
Figure 4.25. Release of methemoglobin from the alginate beads measured as a cumulative percentage.	131
Figure 4.26. Serial short-axis MR images of a cryoinjured pig heart receiving growth factors-loaded alginate beads.	134
Figure 4.27. Change of MR signal intensity within the chronically cryoinjured myocardium receiving growth factors-loaded alginate beads after administration of Gd-DTPA.	135
Figure 4.28. Short-axis contrast-enhanced MR images of a chronically cryoinjured pig heart receiving an agarose patch containing ADSCs.	136

- Figure 4.29.** Short-axis Mn-enhanced MR images of chronically cryoinjured pig hearts receiving growth factors-loaded alginate beads or anADSCs-loaded agarose patch. 138
- Figure 4.30.** A short-axis fluorescence image of a chronically cryoinjured pig heart receiving growth factors-loaded alginate beads after administration of fluorescent microspheres and its corresponding post-mortem pictures 139
- Figure 4.31.** Short-axis fluorescence images of a chronically cryoinjured pig heart receiving an ADSCs-loaded agarose patch and their corresponding post-mortem pictures. 140
- Figure 4.32.** A short-axis slice of a chronically cryoinjured pig heart receiving growth factors-loaded alginate beads (central). 143
- Figure. 4.33.** Hematoxylin & eosin staining results of chronically cryoinjured pig hearts receiving growth factors-loaded alginate beads or an ADSCs-loaded agarose patch. 144

List of Copyrighted Material for which Permission was Obtained

Title	Source	Page(s)
Manganese-enhanced MRI of acute cardiac ischemia and chronic infarction in pig hearts: kinetic analysis of enhancement development	<i>Wiley-Blackwell Inc.</i>	83, 85, 92, 94,
Characterization of cryoinjury-induced infarction with manganese- and gadolinium-enhanced MRI and optical spectroscopy in pig hearts	<i>Elsevier Inc.</i>	103, 104, 106, 108, 110, 111, 113
Magnetic resonance imaging tracking of alginate beads used for drug delivery of growth factors at sites of cardiac damage	<i>Elsevier Inc.</i>	126, 127, 131

1. INTRODUCTION

The central role of the heart in keeping the body alive and healthy has been well recognized. However, to maintain a good performance, its own function must be in a well controlled state, which relies mainly on incessant provision of oxygen (O₂), glucose and other nutrients as well as uninterrupted clearance of metabolic side products such as carbon dioxide (CO₂). To meet these requirements, continuous myocardial perfusion in the form of oxygenated blood through the coronary vascular network is required. A severe limitation of blood perfusion at various levels of the coronary artery system would lead to immediate loss of such homeostasis and resultant dysfunction of downstream cardiomyocytes. If such situation cannot be resolved quickly (4 ~ 6 hours), these endangered cardiomyocytes will die, a condition defined as acute myocardial infarction (MI). Subsequently, the host will start its healing process, *i.e.*, chronic MI, which is characterized by gradual replacement of injured myocardium with scar tissue. During this process, contrast-enhanced magnetic resonance imaging (MRI) is often employed to assess the progression status of injured myocardium. In this study, we planned to evaluate its progression with an intracellular contrast agent, *i.e.*, manganese chloride (MnCl₂), to characterize the signal features of acute and chronic ischemia-induced MI. Using contrast-enhanced MRI as well as optical spectroscopy and imaging, we would then characterize cryoinjury-induced MI in pig hearts, a model with similar progression feature as ischemia-induced MI, reduced occurrence of life-threatening arrhythmia, as well as such uniform pathological features as the size, location and transmural extent. Finally, we proposed a promising treatment that involved angiogenic approach with local delivery of either vascular growth factors (basic fibroblast growth factor, bFGF and

vascular endothelial growth factor, VEGF) entrapped in the alginate hydrogel beads) or adipose-derived stem cells (ADSCs) entrapped in an agarose hydrogel patch onto the cryoinjured epicardium.

2. REVIEW OF LITERATURE

2.1. Myocardial Infarction

The term MI mirrors cardiomyocytes death due mostly to ischemia, which results from the absence of oxygen-containing blood perfusion for myocardial tissue ¹. It is a major cause of death and disability in the developed world. Gradual atherosclerosis of coronary artery is the chief reason for the development of impaired myocardial perfusion. It has been indicated that the onset of MI often occurs during its progression from stable towards unstable stages ²⁻⁴, which usually involves simultaneous activation of inflammation within the atherosclerotic vessel wall ⁵.

2.1.1. Pathophysiology of MI progression

During normal myocardial perfusion, adenosine triphosphate (ATP) and phosphocreatine (PCr) are the two main energy intermediates in cardiomyocytes. Their production is coupled to the demand of the cells. Normally, their turnover rate is 20 – 50 mmol kg wet wt⁻¹ min⁻¹. As the storage is only ~ 15 mmol kg wet wt⁻¹, their exhaustion can occur within 30 s if production is shut off during certain serious situation such as ischemia ⁶. Most of their energy (85-90%) is used for the maintenance of periodic myocardial contraction, while the remaining portion is used to maintain other physiological activities such as ATP-dependent sarcolemmal and sarcoplasmic reticulum (SR) ion transport and protein synthesis ^{7,8}.

Immediately after total regional myocardial ischemia, the electrons produced by the mitochondrial electron transfer chain fail to be delivered to O₂, the result of which is interruption of oxidative phosphorylation and ATP synthesis. Meanwhile, the inhibition of electron transfer inhibits the pumping of protons across the inner membrane, which is

required to generate the electrochemical gradient across it. To maintain the gradient, the mitochondrion has to run the ATP synthase in reverse mode (*i.e.*, acting as an ATP hydrolase), contributing to the fast exhaustion of the intracellular ATP, which is hydrolyzed to adenosine diphosphate (ADP) and then adenosine monophosphate (AMP); it is broken down to adenosine. Consequently, concentration of ATP and PCr (via creatine kinase reaction) in the cardiomyocytes suffering ischemia drops quickly.

1) $\text{ATP} \rightarrow \text{ADP} + \text{P}_i$; ATPase reaction

2) $2\text{ADP} \rightarrow \text{ATP} + \text{AMP}$; adenylate kinase reaction

3) $\text{AMP} \rightarrow \text{Adenosine} + \text{P}_i$; 5'-nucleotidase reaction

Net: $\text{ATP} \rightarrow \text{Adenosine} + 3\text{P}_i$

During struggling for survival, the jeopardized cardiomyocytes make some important adjustments. Firstly, they immediately shut off their periodic contraction to maximally save energy expenditure⁹. Secondly, they quickly shift to the alternate energy-producing route, *i.e.*, anaerobic glycolysis, which relies mainly on intracellular conversion of glycogen. Unfortunately, this pathway is very inefficient in terms of energy production. Glycogenolysis produces only 3 ATP molecules per glycosyl unit, which is in contrast to ~ 36 ATP molecules produced by phosphorylation of ADP coupled to oxidation of the 10 nicotinamide adenine dinucleotide (NADH) and 2 succinate molecules made by converting one molecule of glucose to CO₂ and water (H₂O)¹⁰. Anaerobic glycolysis will produce excessive amounts of intermediate metabolites such as lactate and protons¹¹, which cannot be washed away and are all self-inhibiting substances limiting further glycolysis. Soon, intracellular stores of glycogen and ATP are depleted. For example, it was observed in isolated Langendorff-perfused rat hearts that 30-min total

normothermic ischemia led to significant loss of ATP (67% of normal control) and ADP (23.6% of normal control) with concomitant rise of AMP (278% of normal control). Meanwhile, total intracellular content of high energy phosphates (PCr + ATP) was reduced by 2/3 as compared with normal control, associated with further catabolism of AMP to adenosine, inosine, hypoxanthine or xanthine ¹². Several subsequent changes push these cardiomyocytes from a reversible stage of ischemic injury towards irreversible death. They include: (1) dysfunction of ion pumps on the sarcolemmal membrane leading to intracellular loss of ion homeostasis with vicious consequence, (2) loss of sarcolemmal integrity leading to gradual leakage of intracellular components, (3) massive formation of free radicals attacking various subcellular organelles, and (4) dysfunction of mitochondria leading to failure of cellular respiration.

As ATP is gradually depleted, several important sarcolemmal ATP-dependent ion pumps fail to pump such crucial ions as sodium (Na^+) and calcium (Ca^{2+}) out of the cells, leading to the loss of their homeostasis across the sarcolemmal membrane. Normally, intracellular $[\text{Na}^+]$ ($[\text{Na}^+]_i$) is between 5 and 10 mM, depending on the measuring techniques, the animal species and the site of cardiomyocytes across the ventricular wall ^{13, 14}. During decrement of ATP, there occurs a quick several-fold increase in $[\text{Na}^+]_i$ within 30 min due mainly to failed Na^+-K^+ ATPase and, to a lesser extent, to increased inward leak via Na^+-H^+ (hydrogen ion) exchanger resulting from anaerobic glycolysis-induced intracellular acidosis and impaired inactivation of other sarcolemmal channels ¹⁵⁻¹⁸. Subsequently, swelling of the cardiomyocytes is destined to occur due to elevated osmotic pressure ¹⁹. Increment of intracellular lactate and phosphate also leads to shift of H_2O from the extracellular to the intracellular space, the result of which is approximately

15% reduction of extracellular space after 10-min ischemia. Meanwhile, significant increase in $[\text{Na}]_i$ incurs secondary increment of $[\text{Ca}^{2+}]_i$ due to increased reverse transportation across the membrane by the sarcolemmal $\text{Na}^+-\text{Ca}^{2+}$ exchanger.

For cardiomyocytes with normal perfusion, $[\text{Ca}^{2+}]_i$ differs among the cytoplasm, the SR and the mitochondria. Normally, cytoplasmic free $[\text{Ca}^{2+}]$ is $\sim 0.1 \mu\text{M}$ during the diastolic phase, whereas it is close to $700 \mu\text{M}$ inside the SR. Thus, a huge gradient does exist between the two spaces. During systole, the majority of increased cytoplasmic Ca^{2+} is provided by SR. Normally, $[\text{Ca}^{2+}]$ inside the mitochondria is less than or close to it in the cytoplasm. Considering the fact that mitochondrial matrix is much more electronegative than the cytoplasm ($\Delta\Psi_m \sim -150 \text{ mV}$), inner mitochondrial membrane plays an active role in shielding its inward leak. During ischemia, $[\text{Ca}^{2+}]$ in the cytoplasm and mitochondria will gradually increase with concomitant decrease in the SR. Such increase is attributed to a reduced removal from the cell via the Na^+-Ca^+ exchanger, a less active uptake into the SR, an enhanced sarcolemmal inward leak, and massive displacement from its binding sites in the cytoplasm and in mitochondria by H^+ ²⁰⁻²².

Reperfusion after a prolonged period of ischemia may even worsen the situation. In such cases, elevation of $[\text{Ca}^{2+}]_i$ continues due to retarded recovery of Na^+ -pump activity. The catastrophic effects of Ca^{2+} overload include (1) impaired myocardial contraction and relaxation ²³ and (2) loss of electrical stability such as early after-depolarization and resulting ventricular arrhythmia ²⁴. In mitochondria, when O_2 supply is restored, an electrical gradient is reestablished during flow of the electrons through the respiratory chain, the result of which is a significant translocation of Ca^{2+} from the cytoplasm into the mitochondrion. Such a high $[\text{Ca}^{2+}]$ together with a low $[\text{ATP}]$ will further cause the

opening of mitochondrial permeability transition pore. To generate a proton gradient and limit the absorption of Ca^{2+} , the ATP, rather than being exported to the cytoplasm, may be *in situ* hydrolyzed. Ultimately, all mitochondrial gradients disappear with concomitant loss of cell viability²⁵. In general, cytoplasmic $[\text{Ca}^{2+}]$ higher than $1\ \mu\text{M}$ often indicates irreversible cardiomyocytes injury, which can occur as early as 20 min of ischemia.

The sarcolemma is composed of lipids, in which various proteins are embedded. The lipid consists mainly of phospholipids and cholesterol. The phospholipids are organized in a bilayer structure, in which the phosphate groups are extended outward and the hydrophobic fatty acid (FA) tails are directed to the interior side. Among phospholipids, phosphatidylcholine (~ 40%) and phosphatidylethanolamine (~ 30%) are the two major components, whereas phosphatidylserine, phosphatidylinositol and sphingomyelin are the minor components. It has been proved that distribution of these phospholipids across the bilayer membrane is not symmetric with most anionic phospholipids (*i.e.*, phosphatidylserine and phosphatidylinositol) present in the inner layer. In addition, the preferred location of phosphatidylethanolamine is also the inner leaflet. To maintain such an asymmetric distribution of the various sarcolemmal phospholipids across the bilayer membrane, sufficient ATP which can drive the aminophospholipid translocase within the sarcolemma to facilitate subsequent interaction of the aminophospholipid headgroups with the membrane skeleton is a precondition²⁶.

Upon the presence of ischemia, such sarcolemmal topology is gradually endangered. For example, 60-min ischemia leads to the shifted transbilayer distribution of phosphatidylethanolamine (~ 40% within the outer leaflet)²⁷. This change becomes a

potential cause of improper functioning of sarcolemmal proteins (*e.g.*, ion channels), as their activity is related to their immediate neighboring phospholipid components. However, such change is still reversible if reperfusion can be achieved soon ²⁶. If, however, no reperfusion is available or reperfusion is simply too late (depending on species), massively accumulated Ca^{2+} within the cytoplasm ²⁰⁻²² will lead to solidification of the negatively charged phosphatidylserine and phosphatidylinositol, a reason causing aggregation of intramembranous particles and lateral phase separation ²⁸. Quickly, solidified phospholipid patches are formed. As phosphatidylethanolamine itself “prefers” a non-bilayer topology ²⁷, the loss of stabilizing agent, *i.e.*, phosphatidylserine, will facilitate its fusion ²⁸, a result of which is ultimate sarcolemmal destruction and releasing of intracellular components ²⁹. As the phospholipids are in fluid semi-crystalline state, lateral diffusion of the phospholipids within the same monolayer can be very fast, whereas ‘flip-flop’ diffusion is very difficult. Meanwhile, other mechanisms also play an active role in the disruption of the sarcolemma. For example, during ischemia, the intracellular content of fatty acids and lysophospholipids rises significantly due to breakdown of the sarcolemmal phospholipids by phospholipase A_2 ^{30, 31}.

Oxidative stress during cardiac ischemia is due to (1) excessive generation of reactive oxygen species (ROS) such as radicals, peroxides, and singlet oxygen and (2) reduced ability of protection via enzymes, antioxidants and/or scavengers whose role is elimination of excessive amount of these molecules. Reactive oxygen species are characterized by high reactivity due to the presence of unpaired valence shell electrons. They are normal byproducts of the metabolic chains and some of them play a pivotal role in cell signaling (*e.g.*, nitric oxide). It has been indicated that, during aerobic metabolism,

~ 5% of the total O₂ is reduced to superoxide anion-radical during oxidation of NADPH to NADP⁺ ³². When intracellular metabolism becomes anomalous due to either ischemia or reperfusion, increased formation of ROS is a result of “leakage” of high-energy electrons out of the mitochondrial electron transport chain ³³⁻³⁵.

On the other hand, inadequate protection is the other key factor leading to the onset of oxidative stress. Among the enzymes capable of clearing ROS, superoxide dismutase (SOD), catalase and glutathione oxidase are the mostly studied representatives. For example, after SOD transforms the superoxide anion with protons to hydrogen peroxide (H₂O₂), catalase further catalyzes its transformation to H₂O and O₂. It has been proved that the catalytic potency of catalase is one of the highest among the enzymes as one molecule of catalase can convert millions of H₂O₂ molecules to H₂O molecules per second. As for lipid peroxidation, glutathione oxidase is responsible for converting them back to normal structure via oxidation of two molecules of glutathione to glutathione disulfide. In addition, deficiency of scavengers such as vitamin E, vitamin C, vitamin A, histidine and flavonoids during ischemia all contribute to the inadequate defense against oxidative stress. Excessive amount of the ROS will damage all components of the cell, including proteins, nuclear acids, and lipids via direct oxidation reactions. The peroxides of lipids, *esp.*, containing polyunsaturated FA, will further oxidize other FA, proteins and cholesterol, thus propagating the malicious reaction ³⁶. As such, intracellular homeostasis becomes completely disturbed. Electrophysiologically, upstroke and conduction velocity of the action potential are gradually reduced, and, eventually, the cardiomyocytes become inexcitable and develop contracture.

As mentioned above, a mitochondrion is an intracellular organelle responsible for ATP production from different substrates via oxidative phosphorylation. It contains outer and inner membranes which are composed of phospholipid bilayers and proteins. The integral proteins in the outer mitochondrial membrane are mainly porins, which form channels permeable to most molecules less than 5 kDa³⁷. As a result, this layer acts as a sieve allowing fast exchange of ATP, ADP, acetyl CoA, and other metabolites. Under normal physiological state, the permeability of the inner membrane is very low. In ischemic conditions, this membrane begins to leak abnormally due mainly to opening of the mitochondrial permeability transition pore (permeable to solutes < 1.5 kDa), the activation of which is triggered by low intramitochondrial [ATP] / [ADP] and high [Ca²⁺], [ROS] or [P_i]³⁸. The increment in permeability of the inner membrane is a big challenge for cell survival. It will dissipate $\Delta\Psi_m$ across the membrane due to massive entry of H⁺ and other cations; thus failed coupling between oxidation and phosphorylation will result. Meanwhile, accumulation of ions will further incur mitochondrial swelling, the result of which includes subsequent disorganization of the cristae and quick disruption of the outer membrane.

2.1.2. Morphological features of MI

After the onset of cardiac ischemia, cardiomyocytes at risk struggle for survival for several hours (up to ~ 6 h). As has been mentioned in the previous section, MI is indeed defined by its pathological feature which is characterized by coagulation necrosis and contraction band necrosis³⁹. *Coagulation necrosis* refers to pathological changes including: (1) formation of amorphous dense bodies inside the mitochondria so that production of energy is interrupted; (2) broken sarcolemmal membrane leading to leakage

of intracellular proteins; and (3) nuclear clumping leading to arrest of protein synthesis. Coagulation necrosis occurs mostly within the center of MI where provision of oxygen-containing blood stops completely⁴⁰. The other pathological feature of MI is *contraction band necrosis*, which is characterized by hypercontraction of the contractile elements. As this pathology is more often found at the border zone of MI, it is proposed that cells in jeopardy take up excessive amounts of Ca²⁺ due mainly to sparse reperfusion from neighboring collateral vessels. For a prolonged acute MI, even if complete reperfusion of the infarcted myocardium is achieved via medical intervention, all the tissue may still be mainly composed of contraction bands necrosis and, additionally, extravasated erythrocytes^{40, 41}. Later on, it is also found that apoptosis, a mode of cell death characterized by cytosolic proteolysis and enzyme-mediated DNA fragmentation without concomitant loss of sarcolemmal integrity⁴², also plays a role in cell death in reperfused or non-reperfused MI⁴³⁻⁴⁵, which occurs preferentially at the border zone^{46, 47}.

Table 2.1. Severity of myocardial infarction

Severity	Size (percentage of LV wall)
Microscopic	Focal necrosis
Small	< 10%
Moderate	10 – 30%
Large	> 30 %

LV = left ventricle

Classification regarding severity of MI is mainly based on the volume of the left ventricle (LV) wall involved (Table 2.1), as LV is the chief pump maintaining systemic circulation.

Myocardial infarction can also be further distinguished according to its progression stage as acute, healing, or healed MI. Presence of neutrophils is the key feature of acute MI, though it is difficult to find their massive accumulation during the initial several hours after MI due to lack of a direct transporting route after blockage of upstream coronary artery. Subsequently, the healing process, characterized by accumulation of mononuclear cells and fibroblasts, takes place for several weeks. Eventually, a scar tissue is formed which is termed as healed MI and contains only very limited amount of cells. The temporal profile constituting each stage is described in Table 2.2.

Table 2.2. Temporal classification of myocardial infarction

Stage	Time after onset of MI
Evolving	< 6 hours
Acute	6 hours ~ 7 days
Healing	1 ~ 3 weeks
Healed	> 3 weeks

MI = Myocardial Infarction

2.1.3 Choice of diagnostic tools for detection of MI

(1) Fast diagnosis for patient

In the emergency room, any methodologies that can provide simple and fast diagnosis of MI are always the most favorite choice. Recordings of electrocardiogram (ECG) and measurement of cardiac biomarkers' content in the serum are two most widely selected methods.

Electrocardiography has been deemed as an integral first-line option for diagnosing suspected patients since changes in the ST-T waveforms and the presence of Q-waves potentially enable the clinicians to know the approximate stage of MI, figure out the

Table 2.3. Diagnosis of acute cardiac ischemia and prior myocardial infarction with ECG

Stage	Representative ECG change
Acute cardiac ischemia	<p>ST elevation: new ST $\uparrow \geq 0.1$ mV (0.2 mV for men & 0.15 mV for women in leads V₂ & V₃) at the J-point in any 2 contiguous leads out of respective lead groups.</p> <p>ST depression: new ST $\downarrow \geq 0.05$ mV in 2 contiguous leads out of respective lead groups.</p> <p>T change: inverted T ≥ 0.1 mV in 2 contiguous leads out of respective lead groups with prominent R wave or R/S > 1.</p>
Prior MI	<p>QS or Q wave > 20 ms in V₂, V₃.</p> <p>QS or Q wave > 30 ms in any 2 contiguous leads out of respective lead groups (I/aVL/V₆, II/III/aVF, V₄-V₆)</p> <p>R/S > 1 + positive T wave or R > 40 ms without RBBB</p>

MI = myocardial infarction; ECG = electrocardiography; R/S=ratio of R wave amplitude to S wave amplitude; RBBB = right bundle branch block; ST = ST segment; T = T wave; QS = exclusive downward wave representing ventricular depolarization.

possibly involved coronary artery, and estimate the volume of endangered myocardium

^{39, 48}. The diagnostic criteria for acute cardiac ischemia that may cause MI and prior MI

(chronic) are detailed in table 2.3.

Briefly, the diagnosis of acute ischemia/infarction is based on the presence of elevation of ST segment in two or more contiguous leads, which is usually followed by a deeply inverted T wave for several days⁴⁹. However, ECG alone is often inconclusive for several reasons. Firstly, elevation of ST segment may be a result of acute pericarditis, LV hypertrophy, and early repolarization⁵⁰. It is also difficult to assess acute ischemia/infarction based on ST-T change alone when left bundle branch block is present and no previous ECG can be compared⁵¹. Secondly, it is not possible to determine whether the right or the left circumflex coronary artery is occluded when changes of inferior wall ischemia/infarction are accompanied by depression of the ST segment in leads V₁, V₂, and V₃. On the other hand, echocardiography or MRI often reveal lateral, rather than posterior (as indicated by ST depression in V₁, V₂ and V₃), wall experiencing acute ischemia/infarction. Thirdly, the inversion of T wave in leads V₂-V₄ can also be a result of recent intracranial hemorrhage, though there may exist some minor difference in the characteristics of inverted T and QT interval⁵². Additionally, quantification algorithms of infarction size based on altered ECG pattern alone are complicated and inaccurate⁵³.

As ST-T findings from ECG are sometimes not definitive, evaluation based on cardiac biomarkers is the other required fast approach for the diagnosis of suspected patients. This approach centers around the fact that necrosis in cardiomyocytes is accompanied by loss of sarcolemmal integrity, the result of which is the release of myocardium-specific proteins such as cardiac troponin T and I, myoglobin (Mb), creatine kinase isoenzymes and lactate dehydrogenase into the circulation⁵⁴. Among them, the preferred choice is troponin proteins as they have the feature of both high tissue

specificity and high clinical sensitivity⁵⁵. A rise above the 99th percentile of upper reference limit is currently the exclusive standard for the diagnosis of acute MI requiring immediate intervention or further investigation⁵⁶. However, current practical guide also recommends a repeat measurement 6 to 9 hours after the first one to exclude other diseases capable of increasing the baseline level of these biomarkers⁵⁷, which is especially important for patients with non-ST elevation acute MI.

Based on an abnormal rise of troponins combined with either clinical presentation and/or representative ECG change, acute MI can be diagnosed in the emergency room and therapy can be started¹. However, it should be further pointed out that the timing of an acute MI onset judged by these findings may not correspond exactly with the pathological counterpart. For example, ECG may still demonstrate evolving ST-T changes and cardiac troponin values may remain elevated for 7–14 days following the commencement of MI, when pathologically MI has progressed into the healing stage^{39, 58}.

(2) Accurate diagnostic imaging tools

Although ECG and cardiac biomarkers in the serum can provide results very quickly, they usually cannot provide more detailed information such as location, size, and function of the infarcted myocardium. To further improve the diagnostic accuracy of MI, it is highly desirable to apply new diagnostic tools which can reveal not only its pathological features such as size and the progression stage, but also other key characteristics such as (1) global function of the involved ventricle, (2) viability and regional function (if viable) of endangered cardiomyocytes, and (3) perfusion status of the myocardium at risk. Obviously, to satisfy all these requirements, careful selection from various imaging tools

currently used in clinic is the best way to achieve it. Unfortunately, it is difficult to find such an imaging modality that can provide all the desired information after one-stop examination, though considerable overlap does exist in the capabilities of such methods as echocardiography, radionuclide ventriculography, myocardial perfusion scintigraphy, and MRI.

Echocardiography is a very good real-time imaging tool with high temporal and moderate spatial resolution. Its robustness lies in the assessment of myocardial thickness, thickening, and motion at rest with the adjunct of Doppler ultrasonography. It can also detect severe complications including (1) infarcted tissue rupture leading to ventricular septal defect, pericardial tamponade, or mitral regurgitation as well as (2) acute heart failure. However, previous data indicated that it often underestimated the volumetric and functional status⁵⁹. It also can hardly assess tissue viability due to limited innate ultrasonic contrast between various tissues and lack of good contrast agents⁶⁰. Of course, it can exclude many non-ischemic causes of acute chest pain such as pericarditis, aortic dissection/aneurysm, valve problem, pulmonary embolism, or cardiomyopathy. More recently, myocardial contrast echocardiography was also introduced for noninvasive evaluation of myocardial perfusion due to development of new contrast agents and introduction of innovative ultrasound technologies^{61,62}. However, its specificity and over-all accuracy turned out to be relatively lower than that by contrast-enhanced MRI (detailed later), though high sensitivity could be achieved. Moreover, a main limitation of this method is a very limited amount of acquired segments suitable for analysis due to the short duration of contrast administration during gated image acquisition, often precluding the possibility to obtain more than a single view⁶³.

Consequently, imaging techniques based on the use of radionuclide tracers such as thallium-201 (^{201}Tl), technetium-99m methoxyisobutylisonitrile and tetrofosmin, as well as [^{18}F]2-fluorodeoxyglucose become important new options because these substances can be specifically taken up by viable cardiomyocytes if it can be delivered there with the blood. As a result, they can be used to detect perfusion deficit and infarcted myocardium. With the aid of ECG-gating, it can also provide general information regarding myocardial global and regional function ⁶⁴. However, concern on radiation exposure and relatively low spatial resolution limit their further wider use.

In case of inconclusive diagnosis based on results of ECG and cardiac biomarker in patients with acute chest pain, echocardiography or radionuclide examination may be an important alternative option as both have high negative-predictive value to exclude the occurrence of acute MI ^{65, 66}, which is important in the triage of suspected patients in emergency room. However, their positive-predictive value is still limited as they cannot exclude other conditions capable of inducing regional wall motion abnormality. As for the follow-up of chronic MI progression (healing or healed MI), their high cost effectiveness makes them remain in the first-line choice. They can provide information such as global shape and function of the involved ventricle as well as regional thickness and thickening of infarcted myocardium. However, it is still impossible to specifically present the healing/healed MI conforming to the pathological change.

Magnetic resonance imaging is a relatively new discipline in the realm of diagnostic sciences. Conventional MRI utilizes signals of H_2O protons, the intensity of which depends on their concentration and relaxation properties. With continuous improvement in hardware design and pulse sequence development, it can now readily

provide such important information as cardiac anatomy, ventricular function and other important physiological parameters relating to circulation. In addition, as the relaxivity of H₂O protons can be increased in the presence of paramagnetic contrast agents, it further opens a door towards non-invasive assessment of MI conforming to its pathophysiology and pathology status. Clinical studies have proved that combination of cine and contrast-enhanced MRI is the strongest predictor of acute cardiac ischemia or MI as either can be detected when patients lacking positive findings of either ECG or serum biomarkers are still in the triage.

2.2. Evaluation of myocardial infarction with contrast-enhanced MRI

2.2.1. Overview of MRI basic principles

(1). Nuclear spin, magnetic moment and macroscopic magnetization

It has been known for more than 50 years that atomic nuclei, which possess a spin angular momentum, will interact with magnetic fields. The discovery of this interaction has led to the development of MRI. Many atomic nuclei have a spin angular momentum. The most commonly studied nuclei in NMR experiments are those nuclei with a spin quantum number $I = \frac{1}{2}$, e.g., ¹H, ¹⁹F, ¹³C and ³¹P. The positively charged proton with spin angular momentum constitutes a ring current, which in turn gives rise to a dipolar magnetic moment μ .

When being placed in an external magnetic field, nuclei with a dipolar magnetic moment μ will thus try to align themselves along the external magnetic field. However, instead of “falling” exactly along the field direction, these spins tend to precess around

the direction of the external magnetic field. The angular frequency of such precession can be described by the following formula:

$$\omega = \gamma B_0 \quad (2.1)$$

where γ is a constant and called the ‘gyromagnetic ratio’, B_0 stands for the strength of external magnetic field, and ω is the angular frequency of spin precession, which is also termed as ‘Larmor frequency’. Each atom has its unique gyromagnetic ratio. Table 2.4 enlists several important atoms in human bodies. As hydrogen is naturally the most abundant nuclear spin within the body, it forms the basis of MRI. When a sample is put

Table 2.4. List of physiologically important nuclear species with their gyromagnetic ratio

Nuclears	γ (MHz/T)	Abundance in brain
^1H	42.58	88 M
^{23}Na	11.27	80 mM
^{31}P	17.25	75 mM
^{17}O	-5.77	16 mM

Certain important elements such as ^{12}C and ^{16}O are omitted due to their zero nuclear spin. The quoted abundances of respective nuclear in human body vary in different tissues.

inside a static magnetic field, precession of individual magnetic moments around the B_0 -field is not coherent. As a result, at any moment, their components within the transverse plane are distributed randomly (*i.e.*, lack of phase coherence) and, thus, will not produce any measurable net transverse magnetization. In contrast, their component in the longitudinal direction will not be zero as it equals the sum of the z-components of each individual spin, μ_z .

(2) Radio frequency excitation, signal generation and relaxation of excited spins

As macroscopic magnetization of the spins aligned with the main magnetic field B_0 (*i.e.*, longitudinal magnetization) is static, it cannot be directly detected. As mentioned before, provision of external energy in the form of radio frequency (RF) radiation with a specific frequency can flip the longitudinal magnetization into the transverse plane, which makes magnetization detectable. To achieve this goal, a coil capable of releasing an excitation radiofrequency field has to be placed close to the sample.

After the RF field is turned off, all the excited spins will have their transversal component rotating coherently. If a coil (usually the same coil for excitation) is placed nearby, this component will induce a current in the coil, the initial intensity of which is mainly determined by the percentage of excited protons (*i.e.*, “proton density”) and the flip angle of the pulse.

After the RF pulse is turned off, the spins still rotate around B_0 at the Larmor frequency, but the angle between the net magnetization vector and longitudinal axis (*i.e.*, flip angle) gradually reduces due to the process called ‘spin-lattice relaxation’ and the coherence of various excited protons also gradually disappears due to the process called ‘spin-spin relaxation’.

Spin-lattice relaxation is also called T_1 -relaxation because a time constant T_1 can be used to characterize it. The mechanism involves modulation of the local magnetic field by the random motions of the molecules in the surrounding medium. As a result, a gradual regrowth of longitudinal magnetization with time constant T_1 for a specific tissue can be achieved.

In the meantime, the magnetization present in the transverse plane will also undergo decay due to a process known as spin-spin relaxation characterized by a time constant of T_2 . Similar to the longitudinal relaxation, transverse relaxation is also catalyzed by fluctuating local magnetic fields due to random motion of the molecules. However, the actual decay rate of transverse magnetization is not only governed by the spin-spin interaction, but is also influenced by other factors such as a bulk inhomogeneity of the B_0 field by an amount of ΔB_0 . Under such circumstances, the spins within the same voxel will precess at different Larmor frequencies, as ΔB is position dependent. As a result, T_2^* reflects the actual transverse measured decay rate and its relationship with T_2 is as follows:

$$\frac{1}{T_2^*} = \frac{1}{T_2} + \gamma \cdot \int_{pos1}^{pos2} \Delta B(pos) \cdot d(pos) \cdot dt \quad (2.2)$$

Where 'pos' stands for x,y,z coordinates.

(3) Manipulation of the Larmor frequency and its translational application towards imaging

So far, all the discussion regarding the feature of proton spins within an external magnetic field is based on a presumption that all the hydrogens within an external magnetic field will experience the same field strength and, thus, will precess with the same Larmor frequency. In fact, there do exist minor differences in field strength experienced by different hydrogens in different molecules. Such difference mainly results from different extent of magnetic field shielding by electron clouds in different molecules. For example, the electron cloud of hydrogen deviates more towards oxygen in a water molecule than it does towards carbon in a fat molecule. Thus, protons in H_2O will precess faster than those in fat due to difference in local magnetic field they experience.

Such precessional difference provides a basis for chemical shift imaging for detection of fat tissue within a specific organ.

Differences in magnetic field can also be purposefully made for protons along any direction via superimposition of a magnetic field gradient on the main magnetic field (B_0) along that direction by gradient coils. As such, protons along that linear gradient will precess with predictable difference, which still follows the principle of Larmor precession, *i.e.*, $\Delta f = \gamma \Delta B$. The coil will thus receive a time-varying signal. With the help of Fourier transformation, the received integrated signals can thus be deciphered into a group of precessional frequencies corresponding to respective spatial locations. Signal intensity in respective locations, as reflected by respective pixel intensity in acquired images, is a function of proton density and their relaxation features in both the longitudinal (T_1) and transverse (T_2) directions within that corresponding voxel of tissue. The effect of both T_1 and T_2 can be purposefully manipulated by MR sequences to improve the contrast between different tissues.

(4) Choice of proper MRI sequences for specific imaging tasks

Currently, most MR images are acquired based on either 'Spin Echo' or 'Gradient Recalled Echo' sequences, which will be discussed in this section. Usually, following a 90° radio frequency (RF) excitation pulse, the transverse magnetization quickly decays due to T_2^* relaxation resulting from both intrinsic tissue-specific T_2 relaxation and, more importantly, external B_0 inhomogeneity. To remove influence from B_0 inhomogeneity, a second 180° pulse, named a *refocusing* pulse, is applied to flip the spins. Thus, the precessing rank of respective spins due to B_0 heterogeneity is reversed. However, due to continuance of local B_0 inhomogeneity, the originally faster precessing spins eventually

catch up with their slower counterparts, *i.e.*, become in phase again, and form an echo. Of course, original T_2 relaxation will still develop after the first 90° pulse. As a result, this sequence can eliminate the influence of B_0 inhomogeneity. With careful choice of different repetition times (TR) and echo times (TE), tissue contrast weighting either by proton density, T_1 or T_2 can be achieved.

In contrast, a gradient recalled echo sequence is characterized by application of controlled dephasing and subsequent rephrasing gradients along the x direction (by convention) within the transverse plane immediately after the excitation pulse. The rephrasing gradient can reverse the initial dephasing gradient and, thus, lead to maximum phase coherence to form an echo. As it doesn't eliminate B_0 inhomogeneity, tissue contrast will be T_2^* -weighted if TR is sufficiently long. Whereas, T_1 -weighting can be achieved via reduction of TR. To further manipulate tissue contrast and speed up acquisition time, flip angle can also be made smaller than 90° .

2.2.2 Contrast-enhanced MRI

As mentioned above, tissue contrast can be manipulated via choice of different imaging sequences. For example, T_2 -weighted imaging is capable of detecting area at risk based on extent of edema within the acutely injured myocardium⁶⁷. However, it only plays an additive role in the differentiation of acute or chronic MI as its exclusive presence within the myocardium is not a unique marker for acute MI^{68,69}. As a result, other practical methods have to be pursued. Myocardial injury following a heart attack can be either reversible or irreversible, which is mainly a function of ischemic duration and extent. Loss of membrane integrity is a key event reflecting the irreversible fate of jeopardized cardiomyocytes, the mechanism of which has been detailed previously. Similar to the

mechanism whereby intracellular components are detectable in the serum, extraneous chemicals in the blood can therefore also enter the irreversibly damaged cardiomyocytes via the broken sarcolemma, which serves as the basis for contrast agent-aided MRI in the assessment of the cardiomyocytes viability after ischemia. If the introduced extraneous chemicals can change the relaxation properties of H₂O protons (*i.e.*, either T₁ and/or T₂), the irreversibly injured myocardium can be detected with MRI. Such chemicals are called MR contrast agents. The use of contrast-enhancing agents has become an integral part of MRI for many applications.

(1) Categories of MR contrast agents

Currently, available MR contrast agents can be categorized according to their magnetic behavior or biodistribution (Table 2.5). All MR contrast agents work by reducing the T₁ and/or T₂ relaxation times, so they are commonly referred to as ‘T₁-agents’ or ‘T₂-agents’.

Table 2.5. Classification of MR contrast agents

Category	Type 1	Type 2	Type 3
Magnetic properties	Paramagnetic (predominant T ₁ - shortening)	Superparamagnetic (predominant T ₂ - shortening)	
Biodistribution	Extracellular	Intravascular (blood pool)	Tissue-specific (intracellular)

In fact, any contrast agent capable of reducing T₁ also reduces T₂. For example, metal ions (such as lanthanides) with one or more unpaired electrons are paramagnetic, and therefore have a permanent magnetic moment. In solution, there is a dipolar magnetic interaction between the electronic magnetic moments of the paramagnetic atom and the

much smaller magnetic moments of the nearby H₂O protons. Random fluctuations in this interaction, mainly a result of molecular motions, reduce both the longitudinal and transverse relaxation times of the protons. In contrast, some particulate agents that predominantly reduce T₂ may also exert influence on T₁ if their size can be made smaller. For example, iron oxide particles are made up of several thousand magnetic ions and are said to have superparamagnetic properties if the magnetic ions are mutually aligned. Their diameter is usually > 50 nm. As their magnetic moments do not cancel out, the particles have a permanent magnetic moment which is very large when exposed to a magnetic field, causing predominant changes in transverse relaxation of nearby H₂O protons. In contrast, when the size is modified to be < 50 nm, they are called ultra-small super paramagnetic particles with accompanied enhancement in T₁ shortening⁷⁰.

On the other hand, contrast agents also can be categorized based on their distribution in the biological tissue (Table 2.5). For example, contrast agents whose distribution is within the extracellular fluid (ECF) are referred to as ECF agents. Such agents, with various gadolinium(Gd)-based chelate complexes as representative agents, usually can quickly achieve uniform distribution within the ECF^{71,72}. Blood-pool agents, belonging to a new class of contrast media, are usually characterized by significantly larger size than ECF agents for the purpose of reduced leakage into the interstitial space. These agents have been primarily developed for use in MR angiography due to a longer imaging acquisition window, the result of which translates into improved image quality with corresponding higher image resolution and signal-to-noise ratio (SNR).

A tissue-specific agent can be defined as a contrast agent which is selectively taken up by a particular type of cells and thereby only enhances organs where these cells are

present. For example, the superparamagnetic iron oxides are mostly taken up by the reticuloendothelial system, so they can specifically enhance liver and spleen⁷⁰. For study in the cardiovascular field, it is extremely desirable to look for contrast agents capable of entering cardiomyocytes, the result of which serves as an important differential criterion in the evaluation of viability and status regarding diseased myocardium. Fortunately, manganese ion (Mn^{2+}) can be used for such purpose. Its detailed physicochemical and biochemical information will be described later. In addition, all contrast agents can be viewed as kidney and/or liver-specific agents as either organ is the main route for their excretion.

(2) Efficiency of MR contrast agents

The efficiency of a given contrast agent in stimulating either tissue H_2O hydrogens longitudinal or transverse relaxation can be defined in terms of relaxivity of the agent, r_1 and r_2 (in $mM^{-1} s^{-1}$), as follows:

$$\begin{aligned} R_1 &= r_1[CA] + R_{1_tissue}; \\ R_2 &= r_2[CA] + R_{2_tissue}; \end{aligned} \tag{2.3}$$

Where $[CA]$ is the concentration of the contrast agents in mM and R is the relaxation rate ($1/T$) of tissue H_2O protons. For many T_1 -shortening agents, their influence on longitudinal and transverse relaxation rate is comparable in magnitude (*i.e.*, $r_1 \approx r_2$). As the intrinsic T_1 (on the scale of seconds) is much longer than T_2 (on the scale of milliseconds) in most tissues including heart, a limited increase in the concentration will lead to a much more significant change initially in R_1 and, thence, in the signal intensity. However, due to increased influence on T_2 shortening with continuously increasing concentration, the extent of transverse dephasing will eventually overwhelm the effect of

enhanced longitudinal relaxation, the crossover point of which helps determine the optimal dosage range of different T_1 -contrast agents in various tissues. Of course, intensity enhancement is a linear function of [CA] at low concentrations only.

(3) MR contrast agents for the diagnosis of ischemic cardiac disease

To depict cardiac anatomy including complex congenital malformations, MRI alone is already an excellent approach for this task. As a result, a contrast agent is not required for the purpose of general morphological evaluation. On the contrary, they even tend to worsen the image quality of dark blood images (a spin echo sequence making flowing blood appear dark or black in the image) by shortening the T_1 relaxation time of blood. Similarly, in an attempt to assess ventricular global function, current sequences available for clinical MRI such as balanced steady-state free precession sequences (SSFP) can also meet the requirement of cine imaging (*i.e.*, continuous recording of respective cardiac phases within one cardiac cycle) requisition. As for the evaluation of ischemic cardiac disease, MRI pulse sequences alone cannot meet this requirement, though T_2 -weighted imaging allows detection of the area at risk size (edema) in the absence of contrast agents. It is contrast media that are undergoing continuous development aimed at providing more valuable information regarding (1) myocardium with perfusion deficit (ischemia); (2) myocardium with complete perfusion interruption (acute MI); (3) perfusion status and viability of the jeopardized myocardium after intervention (reperfusion) and (4) progression status of necrotic myocardium (chronic MI), all of which serve as the basis to anticipate a patient's prognoses.

Of course, there exist numerous technical challenges in the pursuit of suitable MR contrast agents which can provide good enhancement of targeted normal or diseased

myocardium, without concomitant degradation of image quality due to both respiratory and cardiac motion artifacts. To reduce breathing-induced artifact, breath hold is usually requested for patients during the process of MRI. In case the patients cannot hold their breath, non-breathhold navigator-imaging methods or an increment of acquisition numbers have to be applied. In animal studies breathhold is done by stopping the ventilator for 10-20 s. As for the heart, synchronizing acquisition with heart rhythm is usually the only choice for reducing the cardiac motion artifact. ECG signal is used to trigger image acquisition. Consequently, R-R interval-determined TR may be difficult to use to provide optimal T_1 -weighted cardiac image.

The status of myocardial perfusion is one of the key determinants for the fate of ischemic myocardium and prognosis of the subjects. All the measuring modalities currently used in clinic are based on the estimation of effects of contrast agents present within the myocardium during their first pass across the myocardial microvascular beds after bolus injection. Although computed tomography and/or percutaneous interventional angiography can depict the stenotic coronary arteries with high sensitivity and specificity⁷³, status of tissue perfusion within the downstream microvascular level remains a challenge for both X-ray-based imaging modalities. On the other hand, assessment of tissue perfusion with single photon emission computed tomography (SPECT), which involves the use of ^{201}Tl or $^{99\text{m}}\text{Tc}$ -labeled contrast agents, usually cannot provide images with high spatial resolution. Although positron emission tomography (PET) can provide images with a better spatial resolution^{74, 75}, the limiting factor for its broad use in the current stage is the requirement of short half-life radioactive tracers. As what was mentioned in the previous sections, the major technical obstacles for contrast-enhanced

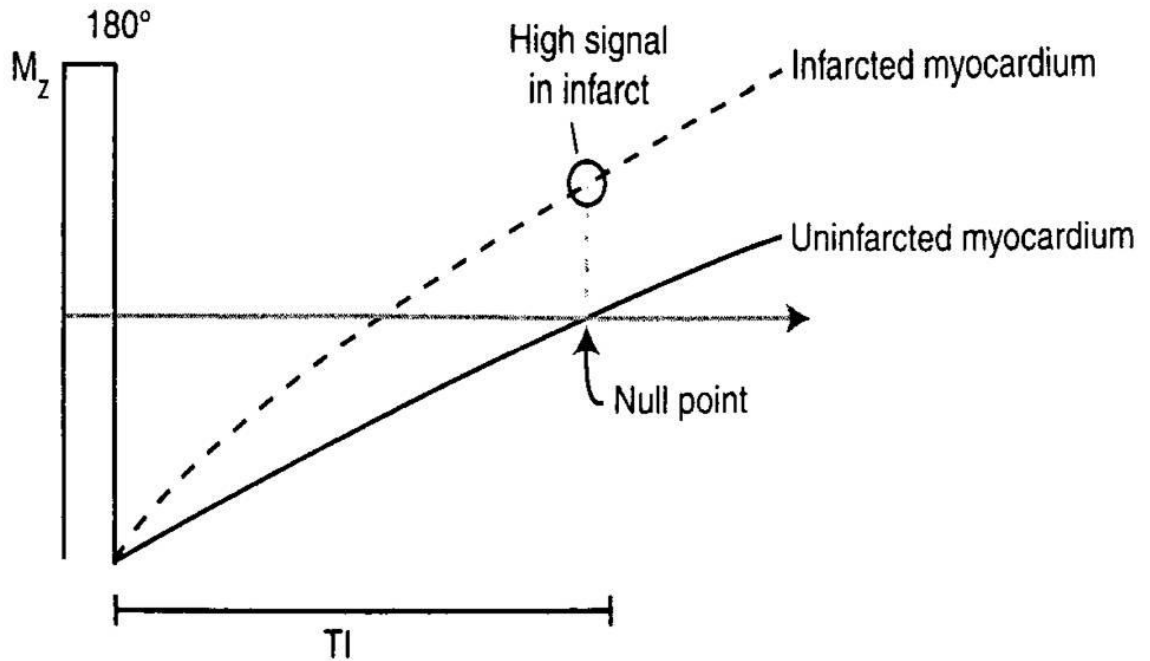
echocardiography include limited amount of acquired segments suitable for analysis and relatively lower specificity.

With the improvement in temporal resolution without concomitant significant compromise in spatial resolution due to development in pulse sequences and hardware such as coils and gradient systems, contrast-enhanced MRI can assess myocardial perfusion with better diagnostic accuracy⁷⁶. The choice of proper pulse sequence, which can provide a strong T_1 weighting, plays a central role in determining temporal and spatial resolution as well as final image contrast after administration of contrast agents. Sequences such as fast low angle shot (FLASH), echo-planar imaging, or balanced SSFP serve as a basis for variable ultra-fast imaging protocols. To achieve a good T_1 contrast between normal and injured myocardium, a preparation pulse such as saturation recovery or inversion recovery is delivered in advance to suppress tissue signal containing a significantly lower level of contrast agent. In the inversion recovery preparation sequence, a 180° pulse is delivered before the subsequent regular sampling RF pulse. Then, longitudinal relaxation will gradually recover. If we administer Gd-diethylenetriaminepentaacetate (Gd-DTPA) via intravenous routes, in those acute MI (broken sarcolemma) with reperfusion or chronic MI (inflammation and scar tissue formation), tissue will retain significantly higher amounts of Gd-DTPA. Thus, its signal recovery will be significantly faster (Fig. 2.1). However, the next preparation pulse cannot be applied until all the longitudinal magnetization has returned to its initial level. As a result, higher temporal resolution during a first-pass perfusion study is difficult to be achieved. In contrast, a saturation recovery preparation pulse can be applied independent of the myocardial magnetization history resulting from variable heart rate and acquisition

approaches. This preparation sequence is based on application of a 90° pulse, followed by a gradient (dephasing or crushing gradient) aimed at dephasing the spins to prevent their signal contribution during subsequent sampling pulse ^{77, 78}.

Usually, after a bolus injection of MRI contrast agents with Gd-DTPA as a representative, myocardial tissue with normal perfusion will appear hyperintense during its first pass across the myocardium. On the contrary, areas with reduced regional perfusion will appear hypointense. Quantification of relative perfusion deficit can thus be made using first-pass kinetics in both areas. As the downstream arterioles have already dilated during ischemia due to accumulation of metabolic products locally and, thus, cannot respond further to vasodilators, myocardial perfusion reserve can be further estimated when stress-inducing agents such as coronary vasodilators, adenosine or dipyridamole, are used with concomitant repeat acquisition of first-pass Gd-DTPA-enhanced MRI (Gd-MRI) ^{79, 80}. Adenosine can directly stimulate the A_{2A} receptor on the smooth muscle layer within the coronary microvasculature. Whereas, dipyridamole acts through inhibition of endothelial reuptake of interstitial adenosine, thus indirectly stimulating vessel dilation ⁸¹. To improve diagnostic accuracy and reduce influence from various artifacts with dark subendocardial rim artifacts as a representative, a protocol combining both delayed enhancement (detailed in next section) and first-pass perfusion Gd-MRI was proposed lately ⁸², which successfully diagnosed patients suffering cardiac ischemia only. However, due to limitation in spatial resolution associated with first-pass Gd-MRI, small ischemic lesions may not be easily detectable.

Figure 2.1. The inversion recovery sequence used to suppress signal from the normal myocardium



Acquisition was set around the null point of signal intensity. In contrast, longitudinal magnetization has recovered most in infarcted myocardium due to accumulation of contrast agents. Thus, T_1 -weighted image revealing myocardial infarction can be achieved. T_I , time after inversion = 'inversion time'.

Viability of myocardium after ischemic injury is the other major factor influencing the prognosis of cardiac function. In some settings, congestive heart failure is not only a result of nonviable myocardium, which is gradually replaced by scar tissue, but also is related to the extent of functional depression of the remaining injured, yet still viable, myocardium. This viable cardiac tissue is referred to as either stunned (*i.e.*, prolonged functional depression after reperfusion) or hibernating (a more persistent functional depression combined with reduced perfusion) myocardium⁸³. It is critical to differentiate viable from nonviable myocardium shortly after ischemic insult as the heart progresses rapidly towards congestive heart failure characterized by irreversible morphological change. Several non-invasive imaging approaches capable of indicating cellular viability and status have been proposed for its assessment. For example, SPECT with ²⁰¹Tl as a radioactive tracer can reflect the retaining ability of injured myocardium after it enters the cells. However, low spatial resolution often makes it a last choice. Metabolic activity of the viable cardiomyocytes can be assessed by PET scan with fluorodeoxyglucose, a glucose analogue, as a positron-emitting radiotracer. This method is deemed as the most reliable approach to validating myocardial viability⁷⁴. To further judge the functional status of viable myocardium suffering a period of ischemia, measurement of regional myocardial function with echocardiography or cine MRI under both rest and stress condition has become one routine examination in many medical centers. The stress condition can be induced by intravenous administration of dobutamine, a sympathomimetic agent capable of stimulating myocardial contraction via direct stimulation of β_1 receptors on cardiomyocytes. As for distinctive assessment matching

histological findings, delayed enhancement Gd-MRI is probably a universally accepted method.

Typically, after Gd-DTPA ($0.1\text{--}0.2\text{ mmol kg}^{-1}$) is injected into the vein, images are acquired 10 to 20 min later with the use of inversion recovery gradient recalled echo sequences^{84, 85}. Delayed enhancement after administration of Gd-DTPA is due to a significantly increased distribution volume and its delayed washout resulting from the loss of membrane integrity in the early stage and gradual replacement of nonviable myocardium by scar tissue in the late stage after MI. Consequently, T_1 -weighted MRI sequences can show set of cardiac 2D images with delayed hyperintense regions. Usually, the size and location of the hyperintense area analyzed with either manual contouring or computer-adjuncted estimation corresponds well with the histological results in animal models^{86, 87}. In patient studies, it was also found that the percentage of myocardium that was both dysfunctional and not hyperenhanced before surgery was strongly related to global wall motion improvement after revascularization⁸⁸. In comparison with the other imaging modalities mentioned previously, it is slightly more sensitive with similar specificity^{89, 90}. These results correlated closely with patients' prognosis as the extent of transmural involvement of injured myocardium predicts the likelihood of functional recovery after acute MI⁹¹. The unique advantage of MRI lies in its high spatial resolution capable of visualizing the transmural distribution of viable and infarcted myocardium and a "one-stop shop" capable of incorporating several imaging sequences for acquisition of anatomy, function, perfusion and viability within one imaging session. The high spatial resolution also translated to the ability to analyze more parameters such as diastolic wall thickness and contractile reserve in response to inotropic agents such as dobutamine.

These additional parameters play an additive role in predicting the potential of functional recovery after revascularization when the extent of transmural involvement of delayed enhancement is moderate (50 - 75%)⁹².

Although gadolinium chelates (*e.g.*, Gd-DTPA) are the most widely used contrast agents for diagnosing ischemic cardiac disease and other cardiovascular diseases, they usually cannot provide other useful information such as normal myocardial status due to exclusive nonspecific extracellular distribution. As a result, pursuit of new MR contrast agents capable of delineating the status of viable cardiomyocytes, which can enrich the menu of the “one-stop-shop” service with MRI, has been put on the agenda. Potential candidates are manganese-based contrast agents.

2.2.3. Manganese-enhanced cardiac MRI

Manganese (Mn) ion have been employed to monitor Ca^{2+} influx into excitable cells such as cardiomyocytes or neurons because its ionic radius is close to that of Ca^{2+} and thus can enter cells via plasmalemmal voltage-gated Ca^{2+} channels⁹³⁻⁹⁶. The other important feature of its ionic form is its paramagnetic property resulting in shortening of T_1 in water protons. Consequently, the ability of Mn to enter cells via the Ca^{2+} channels in conjunction with the T_1 -shortening property make it an attractive candidate as an MRI detectable *in vivo* contrast agent.

(1) Physicochemical properties and physiological role of manganese

Manganese has an atomic number of 25 and can exist in various oxidation states such as +2, +3, +4, +6, and +7 with +2 as the most stable state. Also, in life science, Mn^{2+} is the most important ionic form to execute its physiological function. The element Mn is also an essential trace element for our daily life with relatively high content in such foods as

nuts, cereals, fruits, vegetables, and grains. Our daily consumption is ~ 5 mg with an absorption rate < 5%. However, < 3% of the absorbed Mn^{2+} can enter the systemic circulation due to immediate clearance by the liver, which is followed by excretion into bile. In humans, the total amount of Mn is around 10 mg with liver and kidney as the main storing organs while normal serum level is very low (~ 0.10 $\mu g\ dl^{-1}$). The amount in the human heart has not been reported (to the best of our knowledge), but the normal amount in rat and guinea pig hearts is 0.04 - 0.07 $\mu mol\ g^{-1}$ dry wt ⁹⁷⁻⁹⁹ indicating that it is probably also a trace element in human heart. Within cells, Mn^{2+} plays an important cofactor role to facilitate the performance of many enzymes such as gluconeogenic enzymes, oxidoreductases, hydrolases, lyases, isomerases, and Mn-SOD, *etc.* Among them, Mn-SOD is probably the most widely known Mn-containing enzyme in life science. As it was mentioned in section 2.1., SOD plays a key role in clearing newly formed superoxide radicals during the process of mitochondrial respiration ¹⁰⁰.

Animal studies indicated that lack of nutritional Mn is linked to (1) the deficiency of glycosaminoglycans (*e.g.*, heparin, hyaluronan and chondroitin) synthesis, which may result in a retarded growth and development ¹⁰⁰, and (2) disturbed metabolism of lipids characterized by significant reduction of high density lipoproteins, cholesterol and apoprotein E ¹⁰¹. In human beings, occurrence of Mn deficiency is rare and short-term depletion is related to fleeting dermatitis and Miliaria crystalline ¹⁰², whereas, long-term deficiency has been found to cause Perthes' disease in children ¹⁰³. Recent studies even indicated that lack of Mn during pregnancy would endanger the fetus to develop intrauterine growth retardation ¹⁰⁴. On the contrary, long-term excessive exposure will lead to Mn poisoning, though short-term excessive exposure can be safely tolerated ¹⁰⁵.

Usually, chronic overexposure to Mn is related to such occupations as Mn mining and smelting as well as dry-cell battery production, the environment of which is usually enriched by air-borne Mn¹⁰⁵. As the brain is especially sensitive to high Mn¹⁰⁶, long-term overexposure will lead to neurological disturbances characterized by weak muscle strength, limb tremor, difficulty in speaking and swallowing, and other psychiatric disturbance. This disease is specifically termed as Manganism^{107, 108}. Of course, other organ systems may also suffer loss of functional homeostasis due to chronic Mn exposure^{109, 110}. For example, it has been indicated that workers with long-term exposure to Mn generally had lower fertility¹¹¹. In rats, it was observed that long-term dietary Mn overexposure could result in anemia¹¹², which was not observed in pigs. As a result, response to long-term Mn overexposure may also depend on animal species. One study in dogs found that intravenous continuous infusion of minimal amounts of MnCl₂ once a day could lead to severe liver injury¹¹³.

As for influence of chronic Mn exposure on the heart, the only available data are from animal studies. Theoretically, we could anticipate that long-term overexposure to Mn would impair cardiac function due to uptake by cardiomyocytes via the calcium channel, subsequent relocation into mitochondria and competitive binding to intracellular Ca²⁺ or magnesium ion (Mg²⁺)-sensing proteins. However, the results indicated that the effects of Mn on heart are related to the amount that animals were exposed. For example, in a middle-term study, the rats were exposed to Mn-containing food at low daily amount, *i.e.*, 0.25 mmol kg⁻¹, for 2 weeks. It was observed on isolated Langendorff-perfused rat hearts that 2-wk exposure to low level of Mn led to positive inotropic effects as evidenced by > 30% increment in peak LV developed pressure (LVDP) and maximal

pressure development rate, the mechanism of which may be related to increased $[Ca^{2+}]_i$ within the cytoplasm leading to improved accessibility by contractile proteins ¹¹⁴. Prolonged exposure for even 2 months at this level still had no significant influence on the myocardial respiratory activity. However, overexposure to a significantly higher amount (5 mmol kg^{-1}) for more than 2 months in rats lead to depression of intracellular O_2 consumption, which can be partially reversed by addition of extra Mg in the diet ¹¹². Similar result was also observed in pigs with 2-month overexposure to dietary high content of Mn. Conversely, Mg-deficient diets would enhance Mn absorption and tissue deposition ¹¹⁵. Moreover, these pigs easily developed life-threatening convulsions ¹¹⁶. The myocardial mitochondria showed more swelling than normal when provision of dietary Mg was also lower than normal. However, no obvious change in other subcellular structures was observed in these studies.

(2) Influence of temporary overexposure to manganese on cardiac function

As the risk of temporary overexposure to Mn is relatively low, researchers began to apply Mn in neurological and cardiac studies due to (1) its strong paramagnetic property comparable with Gd-based contrast agents and (2) specific uptake by excitable cells via the plasmalemmal Ca^{2+} channels. Initially, it was observed that Mn entered the cardiomyocytes via the mechanism involving slow inward currents ^{117, 118}. Later on, *in vitro* study proved that this current is mediated by the L-type voltage-dependent slow Ca^{2+} channels ¹⁰³, as its uptake could be blocked by verapamil or stimulated by reduction of $[Ca^{2+}]$ in the perfusate ^{93, 119}. The total amount entering cardiomyocytes appears to be linearly dependent on extracellular $[Mn^{2+}]$ when it is lower than 0.3 mM ¹²⁰. In reality, the initial entry via this route is a relatively fast process as it is followed by a much

slower influx phase around 30 min later ¹²¹. The total amount of Mn²⁺ entering cardiomyocytes is significantly higher during the 2nd stage ¹²², though the mechanism remains indefinite. As a further proof of intracellular distribution of Mn²⁺ as opposed to Gd-based chelators which stay mainly in the extracellular space, it was observed that MnCl₂ administered intravenously also led to significant T₁ shortening of phosphorus resonances (ATP and PCr) in ³¹P-NMR spectra of Langendorff-perfused rat hearts ¹²¹.

After entering the myocardium, Mn²⁺ can be retained by normal cardiomyocytes for hours, which is significantly longer than Gd retention during cardiac Gd-MRI. For example, with rat as an *in vivo* animal model and ⁵⁴Mn as an intravenous radioactive tracer, it was found that the myocardium-to-blood ratio of Mn could rise above 40 within 30 min, which was well above the other conventional tracer ²⁰¹Tl. Thereafter, its content inside the myocardium remained stable for at least 2 hours, though its blood level had already become almost undetectable ^{122, 123}. Inside the cardiomyocytes, a significant portion of Mn²⁺ further relocates into the mitochondria via their membranous Ca²⁺ uniporter ¹²⁴, and efflux from mitochondria seems to be very slow. However, it appears that it doesn't exert significant influence on high energy phosphate metabolism ^{98, 125}. For example, it was observed in isolated Langendorff-perfused rat heart that the relocated Mn, even after 20-25 fold overload inside the cardiomyocytes, had no immediate influence on oxidative phosphorylation as evidenced by negligible change in the production of ATP ¹²⁶. As mitochondria are also a main source of superoxide formation, a concern of *in situ* oxidization of Mn²⁺ to Mn³⁺ in them may be raised. However, available data suggest that there exists no such oxidization, which eliminates any further concern related to strong oxidant properties of Mn³⁺ ¹²⁷. Meanwhile, the remaining Mn²⁺ within the cytoplasm may

bind specific proteins and, consequently, influence some specific cellular physiology. For example, a small dose of Mn^{2+} could stimulate SR Ca^{2+} -ATPase with similar efficiency as intracellular Mg^{2+} ¹²⁶. Other Mn^{2+} within the cytosol may bind phosphate containing molecules such as ATP and PCr ¹²⁸.

If the level of extracellular Mn^{2+} begins to decrease, the intracellular Mn^{2+} will gradually leave the cardiomyocytes. Indeed, the measured efflux kinetics showed that it is a two-phase process with an initial faster exponential efflux (time constant = 2 min) of small Mn^{2+} pool, followed by a slower washout phase (time constant = 97 min) of larger pool. It is indicated that the initial faster washout component results mainly from Mn^{2+} located within the interstitial space ⁹³.

(3) Features of manganese as a MR contrast agent

Research on Mn^{2+} as a potential MR contrast agent can be traced back to as early as 1973, when the late Nobel Prize winner Paul Lauterbur published his seminal paper paving the way towards the establishment of modern MRI. In that study, he also proved that the T_1 of H_2O protons could be altered with a paramagnetic ions like Mn^{2+} ¹²⁹. Due to concern on its acute influence on hemodynamics and possible chronic influence on various organ functions, its subsequent translational studies in human beings were not performed. More attention was shifted to Gd-based chelators due to their presence in the market. In recent years, there has seen a renewed interest in the application of Mn-enhanced MRI (MEMRI) for studies related to brain and heart diseases. Such interest is initially stimulated by a strong desire of *in vivo* monitoring of various biological processes noninvasively in animals. For example, MEMRI has been successfully employed to sensitize brain activity in rats under different depth of anesthesia as entry of Ca^{2+} into neurons is a precondition

for the release of various neurotransmitters¹³⁰. In that study, mannitol was simultaneously used to facilitate the entry of intravenously injected MnCl_2 into the brain parenchyma as mannitol could temporarily break the blood-brain barrier¹³¹. Without induced disruption of this barrier, Mn^{2+} would firstly be present in those intracranial areas lacking this barrier such as the choroid plexus, pituitary gland, and pineal gland¹³². As a result, direct focal injection of Mn^{2+} into the area of interest within the central nervous system is an alternative option if the neural pathway originating from it is desired to be quickly pursued with MRI^{133, 134}.

In the heart, Mn^{2+} study as an MR contrast agent also could be traced back more than 20 years ago, which was followed by a period of scientific “silence” due to the presence of Gd-DTPA. For example, it had been proven in the early 1980s that MnCl_2 ($50 \mu\text{mol kg}^{-1}$) could delineate the area of risk in isolated canine hearts after 90-min¹³⁵ or 24-hour¹³⁶ occlusion of left circumflex coronary artery, the result of which correlated well with ^{201}Tl -based¹³⁵ or pathological^{135, 136} findings. To reduce its influence on hemodynamics (detailed in next section), its chelator forms were developed later. Manganese ethylenediaminetetraphosphonate (Mn-TP), a kind of phosphonate capable of tightly binding di- or tri-valent ions, was among the first tested chelators. It was found that intravenous use of Mn-TP in rats led to significant hyperenhancement of liver and heart shortly after its injection. The enhancement in both organs could last for at least 60 min, which was in contrast to much quicker clearance of it within the blood. Myocardial T_1 could remain significantly shortened by 50% even after 80-min exposure to Mn-TP¹³⁷. Due to difficulty in fine control of the stability of the chelator complex, its regular use as a contrast media for enhancing excitable cells such as neurons and cardiomyocytes needs

to be further studied. Another frequently tested Mn-based chelator is manganese dipyridoxyldiphosphate (MnDPDP) with prolonged plasma $t_{1/2}$ in the circulation¹³⁸⁻¹⁴⁰. Its T_1 and T_2 relaxivity in aqueous solution at 10 MHz and 37 °C is 2.4 $\text{mM}^{-1} \text{s}^{-1}$ and 3.7 $\text{mM}^{-1} \text{s}^{-1}$, respectively. However, biodistribution studies indicate that the contrast agent mostly enters liver, pancreas and kidney with much less distribution inside the cardiomyocytes after intravenous administration¹⁴⁰, though its plasma half life is around 15 min, which is longer than that of MnCl_2 . As a result, this chelator is now mainly used for imaging diseases within these organs¹⁴¹⁻¹⁴⁴. It is indicated from rat and guinea pig studies that the safe dosage of MnDPDP, in terms of acute inhibition of cardiac function, appears to be 10 times higher than MnCl_2 ⁹⁷. The Mn content inside the cardiomyocytes was related to the amount delivered, which further translated to a content-dependent change of myocardial proton relaxivity⁹⁹. Meanwhile, its influence on HR and intracellular energy metabolism is negligible⁹⁹. As a result, its bolus injection (5 – 40 $\mu\text{mol kg}^{-1}$) was tested *in vivo* to delineate the ischemic area in rat heart with a first-pass MR sequence. In comparison with Gd-based first-pass MRI, it could provide prolonged signal enhancement in the normally perfused area due to competitive uptake of Mn^{2+} by the cardiomyocytes from the chelating agent, DPDP¹⁴⁵. However, the rate of Mn^{2+} entry in the chelated form is very slow, though such formulation is designed to minimize hemodynamic fluctuations¹⁴⁶⁻¹⁴⁸. The reason for this is that only free Mn^{2+} dissociated from the chelate can be absorbed by cardiomyocytes. The ligand, DPDP, is metabolized by hydrolysis, which results in Mn^{2+} release.

(4) *Some practical considerations on Mn-enhanced cardiac MRI*

Electrophysiologically, it had been observed on isolated frog's atrial and ventricular fibers that the use of Mn^{2+} could lead to hyperpolarization of the membrane potential¹⁴⁹. This effect is not linear as a steep rise occurred at a certain level of $[Mn^{2+}]_o$. In the frog's heart, this concentration is around 2 mM, which was much higher than that required for reduction of T_1 in tissue. High $[Mn^{2+}]_o$ was also observed to reduce the excitability of frog's myocardial fiber as the strength and duration of the applied electrical stimuli had to be increased significantly¹⁴⁹. It was also observed that high $[Mn^{2+}]_o$ could lead to significant prolongation of action potential, though only persisted for several minutes¹⁵⁰. Such prolongation could lead to a prolonged Q-T interval in ECG¹⁵¹, which may induce life-threatening ventricular arrhythmia¹⁵². Based on the published data on *ex vivo* perfused heart, it seems that the half maximal inhibitory concentration (IC_{50}) of Mn^{2+} effect on HR is much higher than that on cardiac systolic function^{98, 146, 147}.

Theoretically, application of Mn^{2+} may also inhibit muscle contraction as (1) it enters the cardiomyocytes via the sarcolemmal L-type Ca^{2+} channels, which could inhibit the transmembrane conductivity of Ca^{2+} , (2) it consequently reduces the rate of Ca^{2+} -dependent Ca^{2+} release from the SR and (3) it, after entering cardiomyocytes, may competitively bind various intracellular Ca^{2+} - or other divalent ion-binding proteins including troponin C. The net result is, therefore, inhibition of contractile function. It has been proven that the contractile strength of either isolated myocardial fiber or isolated whole heart, stimulated by external electrodes, reduced significantly when a high concentration of Mn^{2+} was present in the perfusion medium⁹⁸. Further studies in isolated Langendorff rat heart indicated that the IC_{50} for inhibition of cardiac function including LVDP and maximal pressure development rate is around 0.25 mM^{98, 147}. However, in

some species, it was observed that such inhibition is temporary as spontaneous recovery occurred several minutes later¹⁵³. As a result, some researchers even proposed that Mn is also a positive inotropic agent. As the IC₅₀ effect of Mn²⁺ on cardiac function was derived from isolated rat heart perfused with protein-free Krebs-Henseleit buffer (KHB), this concentration may not be readily translatable to *in vivo* human study due to several reasons including (1) Mn-binding property of proteins within the plasma and (2) different response to the same amount of Mn²⁺ in various species. As a result, to facilitate successful bench-to-bedside translation, selection of a large animal model such as pig might be a better approach to observe the cardiac effects of MnCl₂ in blood-containing perfusate or *in vivo*.

In addition, due to significant absorption by the liver, oral administration of Mn-based contrast agents is mainly used for the detection of hepatobiliary diseases as the presence of Mn²⁺ in the systemic circulation is very limited^{154, 155}. When Mn²⁺ was administered into the circulation via direct intravenous infusion, its distribution was observed not only in the heart as liver and kidney also quickly uptake it^{156, 157}. As a result, its plasma clearance is very fast. In reality, 30 – 50% of totally applied Mn²⁺ was taken up by the liver in rats. The myocardium-to-liver ratio was ~ 0.5 at half an hour after intravenous administration with gradual reduction thereafter¹²². If applied orally, most of Mn²⁺ was absorbed by the liver before its arrival into the systemic circulation¹⁵⁸. As a result, the estimated dose-effects based only on studies from isolated heart may not be directly extrapolated to the *in vivo* situation. For successful *ex vivo*-to-*in vivo* translation, more comprehensive consideration should be practiced.

Clinical studies regarding the enhancing efficiency of Mn^{2+} for detection of cardiac disease by MRI remained sporadic. Due to concern on potential toxicity with the use of $MnCl_2$, MnDPDP was the only reported agent under investigation in clinic. In a study with healthy human volunteers, it was found that T_1 of LV myocardium increased $\sim 37\%$ one hour after its infusion at normal dose for liver enhancement ($5 \mu\text{mol kg}^{-1}$)¹⁵⁹. Double or triple doses failed to cause further enhancement. Another volunteer study from the same research group also indicated that either 5- or 30-min slow infusion of MnDPDP at this dose yielded the same effects on R_1 ¹⁶⁰. They further found, in patients with MI, that, after 60-min MnDPDP infusion, visually discernible infarcts were only observed in 4 out of 10 patients, though increment in R_1 began to be statistically significant in all the patients¹⁶¹. It seems that MnDPDP, at the dose recommended for liver enhancement, cannot provide satisfactory contrast between the normal and infarcted myocardium.

As a result, the exact role of Mn^{2+} for delineating the infarcted myocardium remains uncertain. It is necessary to carry out a comprehensive study which can answer such important questions: (1) what is the enhancement kinetics of Mn^{2+} within the normal myocardium, (2) which factors will influence it, and (3) what will be the kinetic change within the acutely and chronically infarcted myocardium?

2.3. Evaluation of myocardial ischemia and infarction using optical techniques

Considerable progress has been made towards a novel biomedical measuring modality using near infrared (NIR, 650-1200 nm) light to probe tissue¹⁶²⁻¹⁶⁵. It can detect concentration changes of various substances of interest in living tissue. This technology is based on delivering low-energy photons to the surface of the body/organ under

investigation and measuring the fraction of reflected photons. When photons impinge on tissue, their propagation depends on a combination of reflectance, scattering, and absorption effects. Reflectance is mainly related to the angle of the light beam impinging on the tissue surface, whereas scattering and absorption are wavelength-dependent properties. Scattering decreases with increasing wavelengths, thereby favoring the transmission of infrared light. Absorption occurs at specific wavelengths, determined by specific “chromophore” molecules. Variations occur in the effectiveness of transmission through animal tissues within the ultraviolet through the infrared ranges. Above 1300 nm, water absorbs most photons over a pathlength of a few millimeters in hydrated tissues. In the visible part of the spectrum (< 650 nm), by contrast, the intense absorption bands of hemoglobin (Hb), Mb and cytochromes as well as increasing light scattering again prevent transmission over longer pathlengths. Fortunately, in the NIR range a significant number of photons can effectively pass longer distances (~10 mm) in mammalian tissue.

It has been long well known that the visible absorption peaks for oxygenated hemoglobin (oxy-Hb) and myoglobin (oxy-Mb) are at 547 and 584 nm, whereas peak for their deoxygenated (deoxy-) counterparts are at 560 nm. However, it may not be well known that there also exist two much weaker transitional absorption peaks in the NIR range at 760 nm for the deoxygenated forms and at 920 nm for the oxygenated forms. These two absorption peaks are important as other molecules within a tissue have no significant absorption for the impinging photons within this wavelength window. As such, it paves a way for the measurement of oxygenation status in deep tissue.

Obviously, to measure tissue oxygenation *in vivo* during some specific physiological or pathophysiological process, the conventional instrumentation for

measuring absorption spectra of chemicals in the cuvette needs to be modified. As a result, new instrumentation suitable for this purpose was developed later, which allowed the following advances: (1) modification of brain protective strategies during cardiovascular surgery requiring temporary interruption of whole-body circulation¹⁶⁶⁻¹⁶⁸, (2) detection of myocardial metabolic changes during ischemia^{169, 170}, and (3) detection of cardiomyocytes damage with the aid of exogenous NIR chromophore¹⁶². Usually, the light was transferred to the tissue of interest via a fiberoptic guide. The most significant difference of the new *in vivo* instrumentation from the conventional *in vitro* instrumentation is measurement of photons scattering back to the tissue surface, which is collected by the optode of the other fiberoptic guide transferring the light back to the measuring instrument. In classical Lambert-Beer law, *i.e.*, $\log I_0/I = \varepsilon CL$, where I_0 , intensity of incident light; I , intensity of passed light; ε , molar absorptivity, $M^{-1} \text{ cm}^{-1}$; C , concentration (M) and L , pathlength (cm). In the reflectance spectroscopy, I is back-scattered light and L is unknown, therefore the measured value is the product of C and L . However ratiometric parameters such as oxygen saturation parameter (OSP) are independent of L assuming that L is wavelength independent in a narrow spectrum range (*i.e.*, $C_{\text{oxy(Hb+Mb)}} L / (C_{\text{oxy(Hb+Mb)}} + C_{\text{deoxy(Hb+Mb)}}) L$). The commercialized *in vivo* monitoring systems have been used to measure percutaneous blood oxygenation and has been extended to monitoring muscular and cerebral oxygenation. One disadvantage of commercialized systems used in clinic is that they usually have limited number of wavelengths, which are set in advance for monitoring tissue oxygenation (*e.g.*, Hb and cytochrome aa_3)^{171, 172}. Such limitation is usually inconvenient for experimental purposes.

As a result, continuous wavelength measurement within the NIR spectra window is preferred for laboratory research.

In addition, Institute for Biodiagnostics recently designed an NIR-based imaging system capable of mapping myocardial oxygenation¹⁶⁵. This modality combined the chemical sensitivity of spectroscopy (~10 nm spectral resolution) with the spatial sensitivity of imaging (< 1 mm² in one pixel area) to generate tissue oxygenation maps. An NIR-sensitive back-illuminated charge coupled device and an analog to digital converter are used in combination with a lens to create a 2D NIR camera. To sample different spectral bands in a row, a liquid crystal tunable filter is mounted onto the camera lens, providing an adjustable pass band between 650 and 1050 nm. By scanning different wavelengths of interest, a set of 2D images can be reconstructed providing both spatial and spectral information. Using the spectral data, images can decipher the relative concentrations of deoxy-, oxy- and total-(Hb+Mb) as well as the oxygen saturation parameter ($OSP = \text{oxy}-(\text{Hb}+\text{Mb})/\text{total}-(\text{Hb}+\text{Mb})$) at each pixel across the entire heart surface exposed to the camera. Previous studies from this group suggested that regional variations in cardiac oxygenation can readily be detected by the new imaging system^{164, 173}. For example, NIR images clearly show decreased OSP and total-(Hb+Mb) levels in the ischemic regions of both *ex vivo* perfused and *in vivo* open-chest beating pig hearts. Moreover, this system could also provide tissue perfusion information using indocyanine green (ICG) as an intravascular tracer with strong absorption peak at 805 nm¹⁷⁴.

As newly developed NIR imaging system has such a unique advantage, it would be worthwhile to employ this method to (1) track myocardial oxygenation and flow change

induced by either ischemia or cryoinjury (detailed later) and (2) assess the efficiency of angiogenic approach on injured myocardial tissue.

2.4. Cryoinjury for establishment of experimental myocardial infarction in pig heart

2.4.1. Large animal model of cardiac disease: a critical step in bench-to-bedside translation

Determining the experimental model of a human condition requires a number of decisions and compromises to reach an optimal balance, which is particularly true in studies of cardiac disease. In creating such a model, large animals (*e.g.*, pigs and dogs) offer unique advantages over small animal counterparts (*e.g.* rats and mice). Rat heart disease models, for instance, are relatively cheap and, due to short gestation periods, a large sample size can be produced in a short period. Therefore, it has been extensively used to study relatively “long-term” cardiac outcomes with various interventional strategies^{173, 174}. However, there remain several limitations related to its use, especially, in comparison with human heart, due to (1) much shorter action potential without a plateau phase^{175, 176}; (2) calcium removal out of the cytosol being mainly via the SR calcium pump with reduced relevance to Na⁺/Ca²⁺-exchanger activity^{177, 178} and (3) different intracellular myosin isoform dominance under normal status¹⁷⁹. As such, the results derived from small animal models may not be necessarily translatable to large animals and, ultimately, human beings. In addition, rats have much higher heart rate (300 bpm *vs.* 100 bpm in pigs and 75 bpm in humans) associated with proportionally higher rates of energy turnover and coronary flow per gram of cardiac tissue.

Obviously, use of large animal models such as dogs and pigs could reduce this innate difference across species. An added advantage is that large animals usually allow more accurate tracking of ventricular function/volume due to technical and practical limitations of currently available instrumentation. Despite cost and burden on housing and care, pigs remain a better option versus dogs due to (1) almost the same innate anatomical and physiological features of coronary circulation as human beings and (2) similar pathological and pathophysiological changes as human beings upon onset of ischemia and later infarction progression ¹⁸⁰.

2.4.2. Advantages of cryoinjury-induced experimental myocardial infarction

Currently, most reported studies on pig MI are based on occlusion of the left anterior descending coronary artery (LAD) or left circumflex coronary artery. However, occlusion of either artery also has its innate defects potentially influencing the correct interpretation of findings. For example, occlusion of LAD frequently led to ventricular fibrillation in as many as 50% pigs and mortality was > 20% ¹⁸¹. Therefore, any conclusions derived from it require intense prudence due to high missing data volume. An alternative option is occlusion of their diagonal branches, which could reduce the experimental morbidity and mortality ¹⁸². On the other hand, proposed methods for regenerating function in the damaged heart have included cell- and/or molecule-based approaches ¹⁸³. Validation of their efficacy, however, requires tissue injury with, ideally, uniform key features such as size, depth, and location of the lesion. Because of innate biological variability in coronary artery vasculature, these features in ischemia-induced lesions are difficult to control. For example, despite the presence of an area of risk occupying up to 41% of the LV, infarct size comprises only ~ 2/3 of the area of risk. Such diversity makes accurate assessment of

the damaged region, precise delivery of agents to the damaged area, and critical comparison of respective therapeutic strategies difficult.

Freezing kills cells, a response that has long been evident in frostbite injury. In the last 50 years the therapeutic uses of freezing, whether for preserving or destroying cells and tissues, have increased interest in cold injury. In these years substantial progress has been made in preserving cells and tissues by freezing, but organ preservation by cryogenic techniques remains a challenge. This progress has been paralleled by the development of techniques for cell destruction, commonly termed cryoinjury or cryotherapy. Cryoinjury techniques have developed over the years as technological advances were made ¹⁸⁴.

Because of the utility of cryosurgery, both in the cardiovascular realm and others, the mechanisms of cellular death associated with tissue freezing are well studied ¹⁸⁵. The characteristics of tissue injury from freezing have been known for many years. When tissue temperature is decreased below $-40\text{ }^{\circ}\text{C}$, especially if cooled rapidly, intracellular H_2O freezes and forms intracellular ice. This is considered lethal to cells, as it causes major and irreversible disruption of intracellular organelles and cellular membranes. In addition, as the minute ice crystals form, solutes are concentrated in the surrounding intracellular fluid, the result of which is formation of relative hyperosmolarity causing an osmotic shift between intracellular and interstitial H_2O . In the early rewarming phase, coalescence of ice crystals into larger ice crystals causes further disruption of intracellular organelles and cellular membranes. These are the direct injury to cells caused by ice crystal formation and microcirculatory failure which occurs in the thawing period ¹⁸⁶. Osmotic change leads to shifts in intracellular and extracellular H_2O . Besides, from the

molecular perspective, it has been indicated that apoptosis also plays a role in the development of cell death after cryoinjury¹⁸⁷. Apoptotic cells after freezing are found primarily in the peripheral zone of the cryogenic lesion, where the temperature was not sufficiently low to kill all the cells. In addition, freezing is known to have profound effects on the microvasculature. As tissue is cooled, vasoconstriction occurs and as the tissue freezes, circulation ceases altogether within the frozen tissue. Upon rewarming, there is a hyperemic vasodilation with increased vascular permeability and localized edema. Endothelial injury within the frozen tissue also easily incurs formation of microthrombi and, therefore, microcirculatory arrest within the lesion.

Available clinical findings of final pathological change have revealed that cryoinjured heart also progressed towards formation of scar tissue, a similar outcome as ischemia-induced injury. However, the scar tissue was much more uniform without mixture of normal myocardium, which is often seen in ischemia-induced MI. Watanabe *et al.*,¹⁸⁸ reported that, in a patient postmortem examination at 14 months after cryosurgery, histological examination revealed a homogeneous fibrous scar with surrounding sinusoid capillary proliferation. The border between the fibrosis and the normal myocardium was clear. In addition, cryoinjury (cryoablation) has been adopted for treating arrhythmias refractory to routine pharmacological medication in humans^{189, 190}. An added advantage is involvement of subepicardial layers, which is specifically suitable for assessing regenerative potential of intrapericardial therapy with optics-based methodologies. As mentioned above, the final size of chronic MI, even if established via complete coronary occlusion in pigs, often “shrinks” as compared with the initial area of risk. It usually does not involve a thin layer of subepicardium. Therefore in this case,

optical approaches (detailed before) cannot provide accurate information regarding the efficacy of tested agents. By contrast, cryoinjury will ensure involvement of subepicardium and make *in vivo* optical assessment of cardiac regeneration feasible.

Although this model has been successfully established in rodents and dogs^{191, 192}, there have been no reports on cryoinjury-induced infarctions in pigs. As a result, one major aim of this project is to determine whether cryoinjured pig LV myocardium can provide (1) pathological changes comparable with postischemic lesions but with more consistent sizes; and (2) a model in which infarction progression can be characterized *in vivo* in real time.

2.5. Infarction repair by intrapericardial delivery of vascular growth factors and adipose-derived stem cells

Both experimental and clinical studies have established that the best way to limit infarct size after ischemia is early reperfusion as the fate of cardiomyocytes is stringently dependent on the duration of coronary occlusion^{193, 194}. As such, drug-, catheter- or surgery-based¹⁹⁵⁻¹⁹⁷ reperfusion are the primary option for such patients. Due to practical (*e.g.* transfer delay) and/or technical (*e.g.*, diffuse blockages involving small coronary arterial branches) limitations, some patients may still develop MI because the adult heart lacks the ability to regenerate itself after acute massive loss of cardiomyocytes. Therefore approaches, aimed at restoration of cardiomyocytes population and/or vasculature within the infarcted myocardium, are pursued aggressively during the past 10 years.

As for therapeutic angiogenesis, it theoretically can be achieved by employing either growth factor proteins or by introducing genes encoding these proteins¹⁹⁸.

Although gene therapy may provide sustained local production and release of growth factors, this strategy also probably incur angio-proliferative lesions¹⁹⁹ or even leads to angioma formation²⁰⁰. The other drawback of gene therapy lies in the difficulty to accurately control the level of growth factors expressed within the delivered sites. In contrast, major advantages of protein-based therapy include (1) precise knowledge of the dose delivered, (2) the ability to combine several proteins into a single therapeutic formulation, and (3) a relatively well understood safety profile. Use of proteins, however, also has its innate limitations with short tissue half-life being a major concern. Several approaches have been tested to overcome this limitation. For example, heparin has been proved to be able to increase serum half-life of bFGF from hours to days. Moreover, slow release formulations, *e.g.*, alginate matrix hydrogel, can further prolong the exposure time of injured tissue to these angiogenic agents²⁰¹.

2.5.1. Choice of angiogenic factors

The fact that improvement in tissue perfusion and regional myocardial function was only observed in some reports after protein delivery pleads for more thorough investigations. Proper selection of angiogenic factors is one of the most important issues to be addressed. A variety of angiogenic factors have been tested, but VEGF and bFGF are the two most widely studied factors with high potential for bench-to-bedside translation.

(1) VEGF. Vascular endothelium growth factors are important signaling proteins involved in both vasculogenesis (the *de novo* formation of the embryonic circulatory system) and angiogenesis (the growth of blood vessels from pre-existing vasculature)²⁰². The broad term 'VEGF' covers a number of proteins from two families that result from alternate splicing of mRNA from a single, 8 exons of the VEGF gene. The two different

families are named based on their terminal exon (exon 8) splicing site, *i.e.*, the proximal site (denoted VEGF_{xxx}) or distal site (VEGF_{xxx}b). It has been determined that proteins spliced at the proximal site of exon 8 have pro-angiogenic effects. In addition, alternate splicing of exon 6 and 7 can change their amino acid number (in humans from 121 to 206) and binding affinity to heparin sulfate proteoglycans. VEGF activity has been widely studied in endothelial lineage cells, although it does have effects on a number of other cell types (*e.g.*, stimulation of monocyte/macrophage migration, neurons, cancer cells, and kidney epithelial cells).

The effect of VEGF on ischemic myocardium has been examined in many studies. For example, Hariawala *et al.*²⁰² treated ischemic pigs with an intracoronary bolus injection of VEGF. They found that high VEGF dosage (2 mg per pig) led to high mortality as compared with saline control due to severe hypotension and/or shock while lower dosage (0.5 mg per pig) could effectively promote the growth of collateral vasculature relative to the untreated control pigs. However, when being translated to clinic, this approach appeared unsuccessful²⁰³. In a phase 2 study, patients were randomly assigned to 1 of 3 treatment groups and received a 10-min intracoronary infusion of placebo or 17 or 50 ng kg⁻¹ min⁻¹ VEGF. This was followed by 3 sessions of 4 hours of intravenous infusions on days 3, 6, and 9. On day 60, the treated patients failed to meet the primary end point, *i.e.*, improved exercise tolerance. Such a failure might have been anticipated given the conflicting animal data relating to the brief intracoronary administration of VEGF.

(2) bFGF. Basic FGF belongs to the fibroblast growth factors family that is involved in wound healing and embryonic development. The fibroblast growth factors are a group of

heparin-binding proteins capable of interacting with cell-surface associated heparan sulfate proteoglycans, which are essential for its signal transduction. This family currently has 23 members. These proteins are distinguished by their pattern of expression and preference of different subclasses of FGF receptor (FGF-R) isoforms. As one of the most important functions of bFGF is the promotion of endothelial cell proliferation and the physical organization of endothelial cells into tube-like structures, it also becomes one of the most widely studied angiogenic factors. The ability of bFGF to induce angiogenesis in cardiac tissues was suggested by studies which found significantly higher vessel counts following intracoronary injections of bFGF in the setting of heart attack in animals^{204, 205}. These studies were followed by a more detailed functional assessment of therapeutic efficiency of bFGF in chronic myocardial ischemia animal models. For example, continuous administration of bFGF in a dog model can lead to augmentation of coronary flow²⁰⁶. Application of bFGF has also been indicated to be helpful in the repair of MI. For instance, in a pig model of coronary occlusion, direct intramyocardial bFGF administration can reduce scar size, preserve myocardial function, and increase the number of blood vessels²⁰⁷. When it comes to clinical applications, the fate of bFGF is similar to that of VEGF, which requires more detailed studies.

(3) Multifactor versus single factor administration. The molecular mechanisms responsible for angiogenesis are extremely complex: multiple genes must coordinately express their products in appropriate amounts and in appropriate time domains. For example, VEGF and angiopoietin (Ang)-1 have unique and specific interactions in the induction and maintenance of new blood vessel formation during embryogenesis. Studies indicated that VEGF is responsible for formation of early immature vasculature tube,

followed by Ang-1-mediated maturation step involving induction of vessel budding and branching, and recruitment of periendothelial support cells, including smooth muscle cells. This action helps maintain the integrity and stabilization of the newly formed blood vessels. It has been shown that pericardial fluid from patients suffering from severe ischemic heart disease contained more than two angiogenic factors, a process believed to be an intrinsic angiogenic attempt in response to hypoxia.

These observations raise an important issue: is it sufficient to administer only one angiogenic factor to induce angiogenesis? The answer to this question is not entirely clear and known factors may play a synergistic or complementary role (*e.g.*, VEGF + Ang-1) in the induction and/or maturation of blood vessels. An *in vitro* study using bFGF and VEGF has indicated that they could produce synergistic effects ²⁰⁸.

2.5.2. Pericardial compartment: a new route for cardiac angiogenic therapy

The conflicting data observed when either angiogenic factor was used in animal or clinical studies demands more thorough research. One important issue in angiogenic therapy is the optimal route for administration of angiogenic factors. The management of most cardiac diseases involves enteral or parenteral administration of therapeutic and diagnostic agents that reach specific tissues and organs through the bloodstream. These agents nearly always have widespread systemic effects, including toxicities and undergo dilution and dispersion before reaching the target tissue. Only 0.5% of bFGF delivered by intravenous or Swan Ganz catheter (a catheter placed in pulmonary artery) was recovered from cardiac tissue due to “first-pass” uptake by low affinity receptors in the lungs (consisting mainly of heparin sulfates, to which bFGF binds avidly) ²⁰⁷. Routes that are able to minimize shortcomings related to the systemic use and allow the agents to remain

near the targeting sites are urgently needed. The pericardial compartment is a site that potentially meets most, if not all, these requirements.

Cardiac tissue produces many physiologically active substances such as cytokines, growth factors and cardiac hormones, though the precise mechanisms of their synthesis, secretion, and metabolism are not fully understood. Most substances function locally in either an autocrine or paracrine manner in the heart and are difficult to be detected in the systemic circulation²⁰⁹. Although the major pathways of the substances released from the heart are not known, these substances, after their release into the extracellular space, may pass into the pericardial cavity via lymphatic channels. Fujita *et al.*²¹⁰ provided the first clinical evidence that cardiac tissue, during ischemia, could produce significant amounts of angiogenic growth factors such as bFGF, VEGF and acidic FGF, as they accumulated within the pericardial fluid. Thus, an attempt to stimulate angiogenesis by intrapericardial delivery of angiogenic factors was later carried out. Firstly, using ¹²⁵I-labeled FGF, Lazarous *et al.* demonstrated that intrapericardially delivered bFGF had a much longer half life than that delivered directly into coronary artery or systemic circulation via the left atrium²⁰⁷. Then, *in vivo* studies in pig cardiac ischemia model confirmed that intrapericardial delivery of bFGF not only improved myocardial blood flow in the ischemic myocardium, but also improved regional LV function²¹¹. To our knowledge, similar data are lacking for VEGF. However, like the FGF family of peptides, VEGF also binds heparin. The pilot observations regarding its functional role were first obtained from an *in vitro* study. In that research, the influence of pericardial fluids, collected from patients either with angina or with non-ischemic heart disease, on the growth of cultured human aortic vascular smooth muscle cells were studied. The results indicated that

angina-derived pericardial fluid could promote cell proliferation²¹². This again suggests that pericardial fluid has an angiogenic potential. As a result, it seems that inducing angiogenesis by intrapericardial delivery of angiogenic factors appears to be a promising therapeutic strategy.

2.5.3. Sustained delivery: alternative modes of administration

The duration of angiogenic factors delivery is an important issue. How long should exposure to angiogenic factors last? As most angiogenic factors also act as survival factors for endothelial cells, exposure to a single growth factor probably needs to be sustained to prevent early apoptosis of target cells²¹³. Several strategies have been proposed to prolong tissue exposure to these factors. Gene-based strategies are not so opportune at present. An alternative is sustained protein delivery via a matrix-based strategy. Using sepharose heparin beads for delivery of platelet derived growth factor, Post *et al.*²¹⁴ achieved excellent first-order release kinetics over 10 days, resulting in improvement of flow and function in ischemic myocardium. The design of more sophisticated carrier polymers has already evolved into effective dual release characteristics for two simultaneously delivered growth factors²¹⁵. Alginate has been used as a polymer carrier for slow drug release and has shown no toxicity and low immune response in humans²¹⁶.

Alginate is a natural polymeric polysaccharide and quite abundant as it is a structural component in marine brown algae. It gives algae both mechanical strength and flexibility, the effect of which is close to cellulose in terrestrial plant. Belonging to a family of linear binary block copolymer, alginate is composed of (1→4) linked β -D-mannuronic acid (M) and α -L-guluronic acid (G) residues. The composition and sequence

varies significantly in different algae. One of its most important properties is quick formation of hydrogel in the presence of certain ions. Further studies found that such a gelling process relies on two linked G building blocks, as they together form a diamond-like hole suitable for chemical binding with certain divalent ions such as Ca^{2+} , strontium, or barium²¹⁷. In addition, every alginate chain in H_2O solution can also form junctions with other chains in the presence of 'suitable' ions and, quickly, hydrogel is formed. However, monovalent ions and Mg^{2+} cannot quickly form gel with alginate solution²¹⁸. It has also been found that various proteins or peptides can be entrapped in alginate hydrogel cross-linked with Ca^{2+} ²¹⁹. Later on, the entrapped proteins/peptides can be gradually released out of the alginate hydrogel through diffusion. Such strategy was also successfully applied in entrapment of VEGF and bFGF, respectively^{201, 220-222}. However, its efficacy for MI remains unclear. As a result, in this project, we also plan to apply bFGF and VEGF immobilized in alginate gel as a therapeutic trial after MI.

2.5.4. Induction of angiogenesis by stem cells

One alternative to slow delivery of growth factors is their *in situ* generation by appropriate cells (*e.g.*, stem cells). Experimental studies aimed at evaluation of the role of various cells in therapeutic angiogenesis after MI have been carried out for approximately 10 years. Among them, stem cells from various organ sources are the most widely studied cell types for their angiogenic potential via paracrine function and *in situ* transdifferentiating potential into cardiomyogenic lines. For example, in 2001, Orlic *et al.* reported that direct intramyocardial injection of bone marrow-derived mononuclear cells containing endothelial progenitor cells, hematopoietic progenitor cells and mesenchymal stem cells into the infarcted myocardium can partially regenerate the injured tissue

including restoration of microvascular network ²²¹. Unfortunately, their claim that the newly formed vasculature was a result of local transdifferentiation of implanted mononuclear cells failed to be reproduced by many other groups. As a result, a paracrine effect, instead of transdifferentiation, in that study was proposed recently. In other words, the transplanted cells propagated host-mediated angiogenesis via secretion of synthesized angiogenic factors. However, it is difficult to exclusively attribute the observed angiogenesis to the secreted growth factors as the vasculature may contain transdifferentiated progenitor/stem cells. As a result, it is desirable to design an experiment capable of distinguishing such effect. However, an efficient and unlimited source of autologous cells is not easy to acquire. Adipose-derived stem cell is a good candidate for this purpose as (1) the fat tissue is abundant and easy to sample without much ethical concern and (2) a variety of angiogenic growth factors such as VEGF, bFGF and hepatocyte growth factors secreted by them have been identified ²²³⁻²²⁵.

The selected ADSCs can be placed within pericardial fluid in the form of suspension or “matrix-based” formulation. Pericardial fluid can support viability of the cells as it is well oxygenated and contains blood plasma levels of glucose and ions. Cells embedded into the matrix (*e.g.*, gel) are also partially protected from attack by the host immune system.

2.6. Research goals of this project

The general aim of this project was to characterize infarction progression and evaluate angiogenic effects in pig hearts with contrast-enhanced magnetic resonance imaging (MRI) as well as optical spectroscopy and imaging. More specific aims included (1)

characterization of properties of Mn^{2+} as an MRI contrast agent in the evaluation of infarction progression in pig heart induced by ischemia, a conventional method for establishing experimental myocardial infarction (MI); (2) characterization of pig myocardial cryoinjury, a new experimental MI model, with contrast-enhanced MRI as well as optical spectroscopy and imaging; and (3) assessment of angiogenic potential on cryoinjury-induced MI with either angiogenic factors entrapped in alginate hydrogel beads or ADSCs entrapped in agarose hydrogel patches.

3. MATERIAL AND METHODS

3.1. Animal experiments and protocols

All domestic pigs used in this series of studies received humane care in compliance with the guidelines of the Canadian Council on Animal Care (2nd edn., Ottawa, ON, 1993).

Following 12-hour fasting pigs were pre-medicated with ketamine (22 mg kg⁻¹, I.M.), midazolam (0.33 mg kg⁻¹, I.M.) and atropine (0.05 mg kg⁻¹, I.M.), Anesthesia was achieved with mask inhalation of isoflurane (4%), after which mechanical ventilation containing 40% oxygen and ~2% isoflurane was established via tracheal intubation.

3.1.1. Acute and chronic myocardial infarction established by coronary artery occlusion

(1) Acute cardiac ischemia with or without reperfusion. Pigs with body weight (BW) between 25 and 35 kg were used for the acute study. They were randomly divided into acute ischemia group (group 1, n = 5) and acute ischemia with reperfusion group (group 2, n = 6). Median sternotomy was performed to expose the hearts. After the pericardium was incised longitudinally, the 1st and 2nd diagonal branches originating from LAD were isolated and ligated. Typically lidocaine, an antiarrhythmic drug, was injected prior to the occlusion of LAD branches at 1 mg kg⁻¹ to minimize the occurrence of life-threatening arrhythmias. For pigs in group 1, heart was isolated 30 min later for subsequent *ex vivo* study. Whereas, for pigs in group 2, occlusion was released 75 min later and 45-min *in vivo* reperfusion of the jeopardized myocardium was allowed before isolation of the heart.

(2) Chronic myocardial infarction without reperfusion. Pigs weighing 18-28 kg were randomly assigned into 5 chronic MI groups: 3-day (group 3, n = 5, BW = 26-28 kg), 7-day (group 4, n = 6, BW = 24-27 kg), 14-day (group 5, n = 6, BW = 22-25 kg), 21-day (group 6, n = 5, BW = 20-23 kg) and 28-day (group 7, n = 5, BW = 18-20 kg) infarction.

In addition, 3 pigs (group 8, n = 3, BW = 18-20 kg) subjected to the same procedure as pigs in group 7 underwent repeated Gd-MRI (*i.e.*, 0-, 7-, 14- and 28-day MI) during the progression of chronic MI. Pigs selected with respective initial BW could gain BW at an averaged rate of ~ 3 kg per week. Therefore, upon the day of final surgery for study using isolated heart, their BW could be around 30 kg and their hearts (~ 200 g) would be within the optimal size for *ex vivo* MEMRI study in a 7T magnet (*vide infra*).

After stable anesthesia was established, a butterfly needle was inserted into the ear vein and connected to a saline infusion bag to allow delivery of medication whenever necessary. A three-lead ECG attached to the pig's chest and a pulse oximeter probe attached to the tail were used to monitor ECG signal and blood oxygenation. Sterile left thoracotomy through the left 4th and 5th intercostal space was chosen to expose the heart to minimize wound size. Lidocaine (1 mg kg⁻¹) was injected prior to the occlusion of LAD. Afterwards the same branches from the LAD as those for the establishment of acute ischemia were ligated. Prior to the closure of pericardium and chest, 4 mL of Na-hyaluronate (30 mg mL⁻¹, Lifecore Biomedical Inc., Chaska, MN) was applied into the pericardial cavity to reduce adhesion between the pericardium and epicardium. Then, the pigs were returned to the animal facility for recovery. Pain killer patches (buprenorphine released at 10 µg h⁻¹) and antibiotic (enrofloxacin, 5 mg kg⁻¹) injections were provided for 3-5 recovery days.

Following recovery for respective predetermined duration, pigs underwent repeat open chest surgery to remove the hearts for subsequent study. Similar to the previous procedure for pigs in the acute groups, median sternotomy and subsequent pericardiotomy was performed to expose the heart for *in vivo* measurement of NIR-

derived tissue parameters after a catheter was inserted into the right carotid artery for real-time measurement of aortic blood pressure (BP) and periodic check of blood oxygen, electrolytes, acid/base and glucose homeostasis.

3.1.2. Acute and chronic myocardial infarction produced by cryoinjury

Pigs weighing 18-30 kg were randomly assigned into 3 cryoinjury groups, *i.e.*, acute (group 9, n = 6, BW = 28 - 30kg), 7-day (group 10, n = 4, BW = 24-27 kg), and 28-day (group 11, n = 6, BW = 18-20 kg). To expose the LV, median sternotomy was performed for pigs in the acute group, whereas, sterile thoracotomy between the left 4th and 5th intercostal space was chosen for those in the chronic groups. After the pericardium was incised longitudinally, an LV epicardial area (anterior + lateral wall), free from large coronary vessels, was selected to undergo freezing. The tip of an aluminum rod ($\Phi = 2.5$ cm), which had been cooled with liquid nitrogen, was pressed firmly by the weight of the freezing device on the selected epicardial area for 2 min to produce cryoinjury. In chronic experiments, perioperative protocol was kept the same as for the other chronic MI study. In addition, evaluation of angiogenic effects with growth factors or stem cells was also based on this model (*vide infra*).

3.1.3. Angiogenic therapy after cryoinjury-induced MI with VEGF and bFGF entrapped

in alginate beads hydrogel or adipose-derived stem cells entrapped in agarose patch gel

After establishment of myocardial cryoinjury, 24 pigs were further used to test therapeutic efficiency of epicardial cardiomyoplasty with either angiogenic factors (VEGF + bFGF) or ADSCs (*vide infra*). These pigs were divided into 6 groups: (i) cryoinjury, empty beads (n = 5); (ii & iii) cryoinjury, beads loaded with FGF and VEGF implanted to the pericardium (ii, n = 3) or epicardium (iii, n = 5); (iv & v) cryoinjury,

agarose gel patch with (iv, n = 4) or without (v, n=2) ADSCs; (vi) sham-operated heart with/without control beads or patch (n=5). For pigs receiving epicardial implantation of agents after cryoinjury, alginate beads without (group i) or with (group iii) growth factors or agarose patch wrapped into 2×2 cm²-nylon patch with (group iv) or without (group v) ADSCs was anchored on top of the cryoinjured epicardium with 6-0 propylene suture (Johnson & Johnson, Somerville, NJ) (Fig. 3.1). For pigs in group ii, the beads were sutured onto the pericardium facing the cryoinjured myocardium. For pigs in group vi, empty alginate beads (n=2) or agarose patch (n=1) were sutured on top of the pseudo-cryoinjured myocardium. Then, the pericardium and chest wall was sequentially closed. Thereafter, these pigs were followed up with MRI once a week for 4 weeks.

3.2. *Ex vivo* Mn-enhanced MRI on isolated hearts

After establishment of occlusion- and cryoinjury-induced acute and chronic MI in pigs, their hearts were subsequently isolated to undergo *ex vivo* MEMRI in a 7T magnet.

3.2.1. Heart isolation and *ex vivo* perfusion

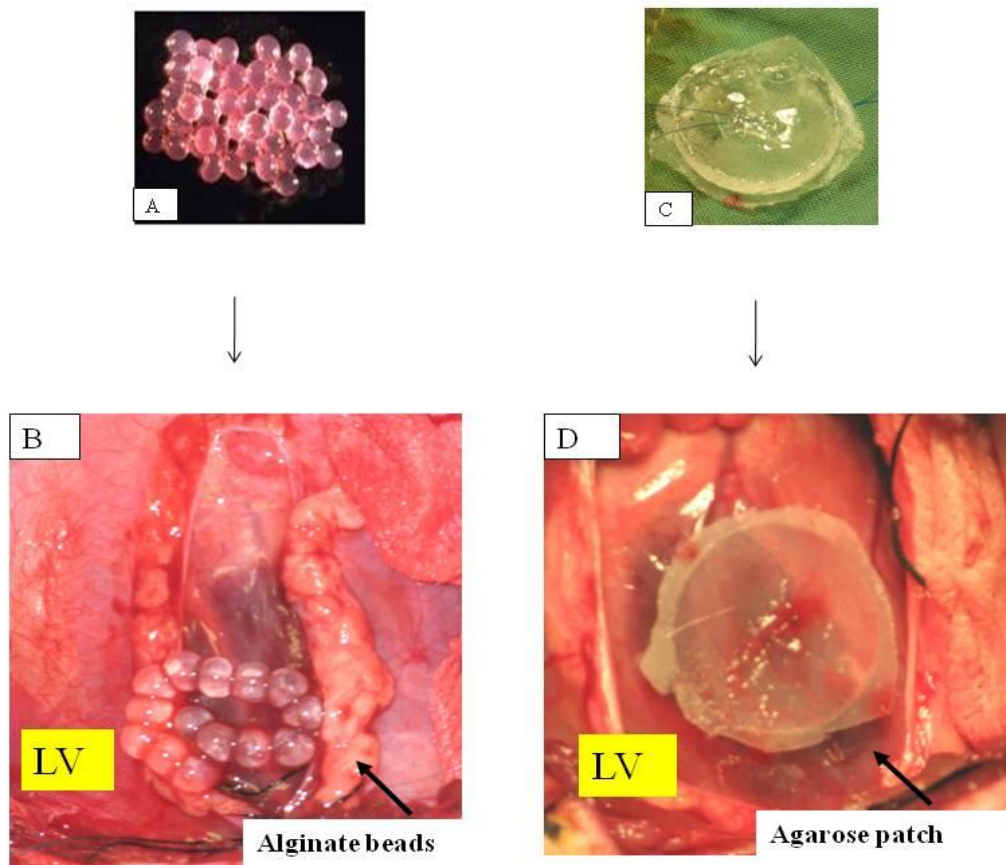
The pig hearts were arrested with ice-cold KHB cardioplegia ($[K^+] \sim 20$ mM) and excised. A cannula for directing perfusate to the heart was secured into the ascending aorta via the right brachiocephalic artery. Then, the hearts were perfused with a 1:1 mixture of low potassium KHB containing (in mM) NaHCO₃ (25), NaCl (118), KH₂PO₄ (1.2), CaCl₂ (1.75), MgSO₄ (1.2), glucose (11) and bovine serum albumin (6 g/L), and autologous blood containing cardioplegic solution administered to arrest the heart. The mixture contained 2.6 ± 0.4 mM Hb (12-15% hematocrit), 8.7 ± 0.8 mM glucose, 1.6 ± 0.3 mM lactate. Antiarrhythmic drugs (S-propranolol at 0.5 μ M and lidocaine at 15 μ M) and

antibiotic (Penicillin G, 100,000 U/L) were also added to the perfusate to maintain stable function. The perfusate was aerated in a membrane oxygenator (Cobe, Japan) with 95% O₂/5% CO₂ and the flow rate was adjusted to ~1.5 mL kg⁻¹ min⁻¹ with a roller pump (Sarns, Ann Arbor, MI). Typical baseline functional parameters of isolated pig heart were: left ventricular end-systolic pressure = 70-90 mmHg, left ventricular end-diastolic pressure = 0-5 mmHg, perfusion pressure (PP) = 55-65 mmHg and heart rate (HR) = 90-120 bpm. Homeostasis of gas, pH, electrolytes, Hb saturation in the perfusate and heart metabolic status was monitored by comparing arterial and venous samples of perfusate using an analyzer (Critical Care Xpress, Nova Biomedical Inc., Walham, MA).

3.2.2. Ex vivo Mn-enhanced MRI

The isolated heart and two fixed reference tubes containing H₂O (long T₁) and H₂O+10mM CuSO₄ (short T₁) were placed in the perfusion chamber within the Helmholtz coil. The chamber was moved to the center of a horizontal 7 T magnet (Magnex, Oxford Industrial Park, Yarnton, UK), interfaced to a Bruker Biospec console. Cardiac images were obtained using a conventional spin-echo sequence (FOV = 16x16 cm², TE = 8 ms, matrix size 128 × 128). Signal acquisition was gated by the first derivative of LV pressure which provided acquisition during every other heartbeat for T₁ weighting (TR of ~ 800 ms). The ratio of the intensities in the reference tubes (CuSO₄ to H₂O) served as an index of the degree of T₁ weighting and was about 5. Six 8 mm-thick slices separated by 2 mm gaps were obtained. After acquisition of the baseline image, 200 μM MnCl₂ was added to the perfusion reservoir, and serial images were taken every 5 min over a 30-45 min period. Signal intensities for each slice were normalized to those of the H₂O reference.

Figure 3.1. Anchor of control and therapeutic agents on top of the cryoinjured left ventricular epicardium.



A: alginate hydrogel beads with or without growth factors; B: epicardial fixation of the beads with suture; C: agarose hydrogel patch with or without adipose-derived stem cells; D: epicardial fixation of the patch with suture. LV = left ventricle.

3.3. *In vivo* Gd- and Mn-enhanced MRI

3.3.1. *In vivo* Gd-enhanced MRI

Among aforementioned groups, pigs subject to 4-week ischemia-induced MI (group 8) and 4-week cryoinjury-induced MI (group 11) underwent *in vivo* assessment of infarction progression via Gd-MRI immediately, 1 week, 2 weeks and 3 or 4 weeks after infarction initiation in a clinical 3T scanner (Trio, Siemens, Erlangen, Germany). Scout images in two- and four-chamber views were acquired to determine the LV short axis, based on which Gd-MRI was then carried out to assess infarction progression. After bolus injection of Gd-DTPA (0.2 mmol kg^{-1} , *i.v.*), we acquired cardiac images every 2 min over a 30-min period. The T_1 -weighted FLASH short-axis images (12 – 13 slices, 5 – 6 mm thick) were acquired using ECG gated to the diastolic phase before (baseline image) and after injection of the contrast agent. Respiratory hold during acquisition was not applied due to concern on life-threatening complications such as ventricular fibrillation when the time was longer than 18 - 20 sec. Typical acquisition parameters include: TR = 2 RR intervals, TE/flip angle = 1.7 ms/20°, pixel size = $1.2 \times 1.7 \text{ mm}$, matrix size = 256×256 .

In addition, pigs subjected to *in vivo* MEMRI (detailed in next section) and angiogenic therapy with either a growth factor-based or stem cell-based strategy were also arranged for serial follow-up with Gd-MRI.

3.3.2. *In vivo* Mn-enhanced MRI

In vivo MEMRI was carried out at the 4th week after cryoinjury or sham operation in pig hearts. Blood pressure was continuously monitored with the same setting as for *in vivo* studies before heart isolation (detailed in section 3.6). After acquisition of baseline T_1 -weighted short-axis images with the same sequence as Gd-MRI, MnCl_2 (0.1M) was

administered either as slow intermittent bolus IV injection (intermittent group, $n = 4$, $\sim 10 \mu\text{mol kg}^{-1}$ every 2 min $\times 7$ times, 14 min in total) or as continuous intravenous infusion with a syringe pump (continuous group, $n = 5$, $5 \mu\text{mol kg}^{-1} \text{ min}^{-1} \times 14$ min). Over the whole process of MnCl_2 infusion and subsequent 16 min clearance (*i.e.*, 30 min in total), we acquired cardiac images gated to diastolic phase by ECG signal every 2 min. Typical acquisition parameters remained unchanged, *i.e.*, TR = 2 RR intervals, TE/flip angle = 1.7 ms/20°; pixel size = 1.2 \times 1.7 mm, matrix size = 256 \times 256.

3.4. Visible/NIR point spectroscopy

Diffuse reflectance spectra of pig hearts in the range of 400-1100 nm with a 1 nm resolution were acquired using an integration time of 0.1 s, averaging 120 acquisitions. Broadband visible/NIR light from a fiber optic illuminator Oriel (model 77501, Stratford, CT) was transmitted to the epicardium of an open heart or a short-axis heart slice through one arm of a bifurcated fiber optic bundle. The common illumination/collection probe tip was placed in contact with the epicardium, or a slice, perpendicular to its surface, which allowed collection of diffusely reflected light through the other arm of the fiber bundle to the spectrometer (model PDA-512, Control Developments Inc., South Bend, IN). The light from the light source was delivered by a single fiber optic filament of 650- μm diameter. Collection of the reflected light was achieved by 36 fiber optic filaments of 15- μm diameter randomly surrounding the illuminating filament. The mean optode distance between the collecting and emission filaments was 850 μm .

After acquisition of the spectrum, some mathematical calculations were applied to figure out the concentration change of the substance of interest from the absorption

change at a particular wavelength. An absorption value (A_λ), analogous to that in conventional transmission spectroscopy, for any visible/NIR wavelength (λ) was calculated according to the formula:

$$A_\lambda = -\log_{10}(I_s/I_r) \quad (1)$$

where I_s is the intensity of the light diffusely reflected back by the sample and I_r is the intensity of the light reflected back by a reference standard (Spectralon[®]). A subsequent process aimed at the derivation of respective concentrations reflecting tissue oxygenation had been detailed in the previous studies from the same group^{164, 226}. Briefly, as (1) it is difficult to differentiate oxy- or deoxy-Hb (4 heme groups in each tetrameric molecule) from oxy- or deoxy-Mb (one heme group in each molecule) spectra due to nearly identical absorption features, (2) light can penetrate much deeper into the tissue within the NIR range, and (3) there lacks other intrinsic chromophores within the NIR range^{227, 228}, we applied the acquired data within the NIR range (650 – 1100 nm) into the final calculation formula to extract their relative tissue concentrations, *i.e.*, [deoxy-(Hb+Mb)] and [oxy-(Hb+Mb)], before and after occlusion of the LAD branches. Within this wavelength range, the highest extinction coefficient is at 760 nm for deoxy-(Hb+Mb) and at 920 nm for their oxygenated counterparts. Based on the Beer's Law, each absorbance value at each NIR wavelength can be deemed as a weighted (product of chromophore concentration and photon pathlength) sum of the extinction coefficient of oxy-(Hb+Mb) and deoxy-(Hb+Mb), respectively. Thereafter, we fitted the acquired spectra exclusively with the heme-protein extinction coefficient spectra (Fig. 3.2) with an assumption of invariant pathlength across the wavelength range of interest (650 – 890 nm). Due to

fluctuation of baseline spectra resulting from varied extent of tissue scattering, one more spectrum with “absorptivity” set at 1 was included in the final fitting algorithm:

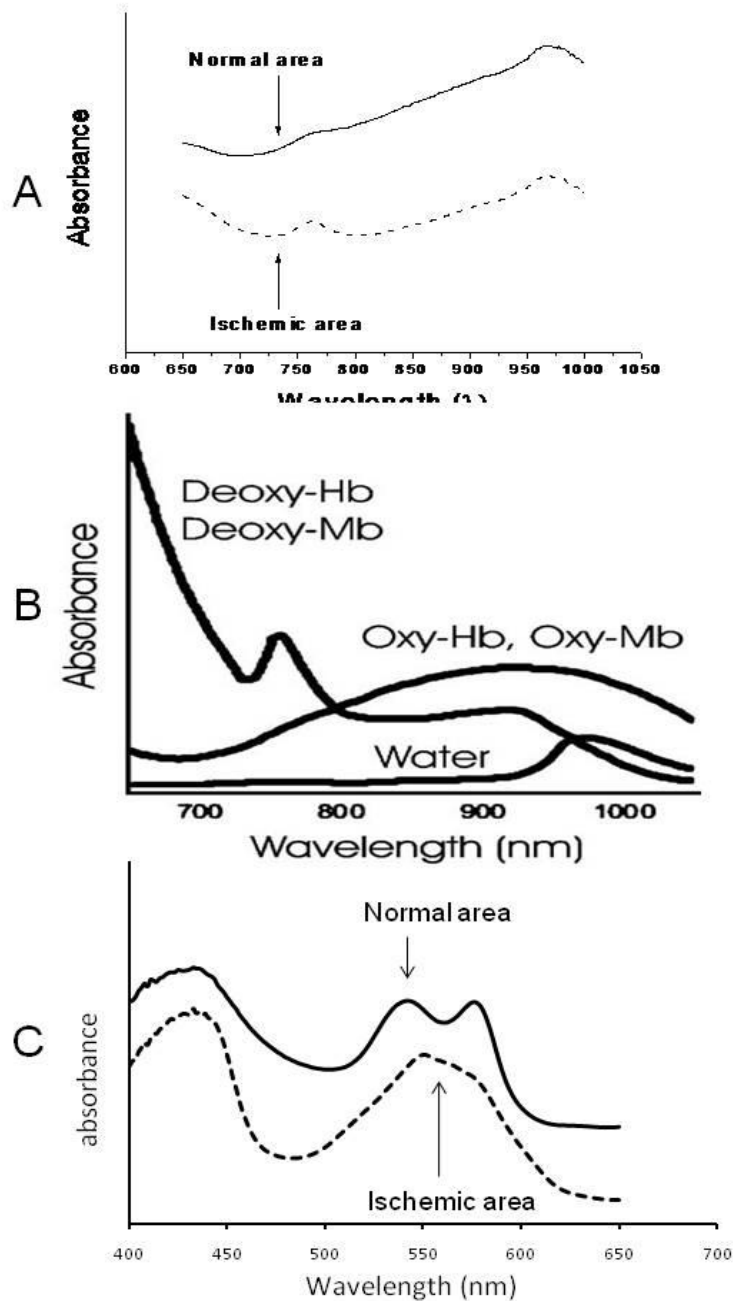
$$A = (C_{deoxy-(Hb+Mb)}L \times \varepsilon_{deoxy-(Hb+Mb)}) + (C_{oxy-(Hb+Mb)}L \times \varepsilon_{oxy-(Hb+Mb)}) + B_{baseline} \times [1] \quad (2)$$

Where C stands for tissue concentration of the chromophores of interest, L stands for pathlength of incident light within the tissue, and ε stands for extinction coefficient of the chromophores of interest. Thus, the relative concentration of deoxy- and oxy-(Hb+Mb) within the tissue can be derived. In addition, the acquired spectrum also included the visible portion (400 – 650 nm), which could be used for qualitative/semiquantitative evaluation of subepicardial tissue oxygenation due to much higher absorption coefficients for oxy-(Hb+Mb) at 560 & 580 nm and deoxy-(Hb+Mb) at ~570 nm (Fig. 3.2C).

3.5. NIR spectroscopic imaging of tissue perfusion after myocardial ischemia and infarction

The NIR imaging system was custom built at the Institute for Biodiagnostics, NRC, Winnipeg, Canada^{165, 226}. Following a bolus injection of 3-mL ICG solution (5 mg mL⁻¹), image acquisition (gated by the first derivative of the BP to diastole) of diffusely reflected light at 800 nm were performed with a charge-coupled device-array camera equipped with a liquid crystal tuneable filter (Cambridge Research and Instrumentation, Woburn, MA, USA). At the end of the experiments, a reflectance standard (Kodak Gray Card, Eastman Kodak, Rochester, NY) was placed in front of the heart to estimate I_r for each pixel of the 256 × 256 pixels. As a result, an absorption value at 800 nm (A_{800}) was

Figure 3.2. Optical spectra of the myocardial tissue.



A: Representative spectra acquired from ischemic (lower dashed line) and normal (upper straight line) LV epicardium. The two spectra were offset for illustrative purpose. B: Absorptivity spectra of deoxygenated and oxygenated hemoglobin/myoglobin as well as water^{229, 230}. C: visible spectra acquired from ischemic (lower dashed line) and normal (upper straight line) LV epicardium. The two spectra were offset for illustrative purpose. Deoxy- = deoxygenated, Hb = hemoglobin, LV = left ventricle, Mb = myoglobin.

calculated according to the equation (1). The wavelength of 800 nm corresponded to the maximal light absorption of ICG. The images for each time point represent “instantaneous” ICG distribution across the heart surface. Thus, a cine map reflecting coronary flow distribution over the subepicardium could be figured out.

The gating of image acquisition allowed us to capture each image at a diastolic phase, which prevented moving artefacts of the beating heart, and collect images with pre-determined time increment, which facilitated determination of the ICG first-pass kinetics within the subepicardium. After image collection in each kinetic experiment, normal and cryoinjured areas on the heart surface were visually determined and defined as two regions of interest using a Matlab program. The A_{800} values of all pixels inside each region were averaged and plotted versus time resulting in the ICG first-pass kinetics in normal and cryoinjured hearts.

3.6. Hemodynamic and metabolic measurements

During all the *in vivo* studies except Gd-MRI, BP was continuously monitored via a catheter placed inside the right carotid artery and connected to a pressure transducer (Cobe Labs, Lakewood, CO) interfaced with a recorder (Grass Polygraph, Grass Instrument, Quincy, MA). Its first derivative was used as a signal triggering the NIR camera acquisitions. The same catheter was also used for withdrawal of arterial blood samples, which were analyzed for PaO₂, Hb, PaCO₂, pH, glucose, lactate and ions using a blood-gas analyzer (Critical Care Xpress, Nova Biomedical Inc., Walham, MA). Level of PaO₂, pH and glucose values were maintained within the normal range (*i.e.*, pH: ~ 7.4, PaO₂: ~ 130 mm Hg, glucose: ~ 5.8 mM).

During *ex vivo* MEMRI, a latex balloon was placed and secured in the LV cavity and then filled with H₂O containing 1 mM MnCl₂. Continuous tracing of LV end-systolic pressure, LV end-diastolic pressure and HR was achieved via H₂O-filled tubing connecting LV balloon to the pressure transducer interfaced with the physiological recorder. To monitor perfusion pressure and sample perfusate during *ex vivo* perfusion, a catheter was placed into the left brachiocephalic artery. An additional catheter was placed into the coronary sinus to sample venous effluent during perfusion.

3.7. Postmortem analyses

3.7.1. Evaluation of transmural flow of jeopardized myocardium

At the end of experiment, perfusion was switched to blood-free KHB. For pigs in the acute ischemic group (group 1), the heart was stopped by a cold cardioplegic KHB ([K⁺] = 20 mM) containing 0.25% isotonic Evans blue to demarcate the area at risk. Then, the heart was sliced along the short axis and photographed. For pigs in the other groups, an intracellular NIR dye, IR-676 iodide (IR676, Aldrich-Sigma, St Louis, MO, USA), was infused over a 30-s period at 2 mL s⁻¹ to maintain its concentration in the range 7–9 μ M, which was followed by a 30-s washout of the extracellular dye, termination of perfusion and subsequent slicing along the short axis of each heart. The relative deposition of the dye among the normal and injured area on respective short-axis slices was estimated from the first derivative of its spectrum (680 nm), which could eliminate baseline fluctuation.

To evaluate myocardial blood flow *ex vivo* after angiogenic therapy with either alginate-entrapped VEGF and bFGF or agarose-entrapped ADSCs on cryoinjured pig hearts (*vide infra*), 15- μ m fluorescent microspheres (Molecular Probes, Eugene, Ore)

with excitation and emission wavelengths at 645/680 nm, respectively, were used. Before isolation of the heart for post-mortem examination, 5-ml microsphere solution ($1 \times 10^6 \text{ ml}^{-1}$) was injected into the LV cavity through apex immediately after the solution was agitated with an ultrasonic spray nozzle for ~ 30 sec to disperse well the sedimented microspheres. During manual injection, the aortic root was temporarily occluded to ensure maximal distribution of administered microspheres within the coronary circulation. Thereafter, the heart was arrested with the cold cardioplegic solution and sliced along the short axis. The respective slices were imaged with the same NIR spectroscopic imaging system as for *in vivo* evaluation of tissue perfusion with an exception of light source used. In this *ex vivo* study, each heart slice was sequentially illuminated with an NIR light at a wavelength of 635 nm provided by infrared laser diodes within a home-made black box. The fluorescence emission of the excited microspheres (680 nm) was detected using long-pass filter cutting excitation light off. Matlab was used for image processing using an algorithm specifically developed for current task.

3.7.2. Evaluation of tissue viability with triphenyltetrazolium chloride staining

At the end of each experiment, the heart slices except those in group 1 were immersed in phosphate buffered saline (pH=7.4) containing 2% 2,3,5-triphenyltetrazolium chloride (TTC) for 15 min at room temperature. This chemical is a redox indicator capable of differentiating metabolically active from inactive myocardium. Various dehydrogenases within the viable myocardium, in the presence of electron donor such as NADH, can reduce it to red 1,3,5-triphenylformazan, which is insoluble and will deposit *in situ* on the surface of viable myocardium. Thus, infarcted myocardium can be visually

distinguished based on significant difference in color on the transmural surface of each slice. Such unique appearance has been employed as a golden standard in the assessment of various imaging modalities and protective strategies after myocardial injury^{230, 231}.

3.7.3. Microscopic evaluation of MI progression

After macroscopic examination on respective heart slices, they were immersed in 10% phosphate-buffered formalin solution (40% formaldehyde), a standard fixative for biological tissues²³². Remote and injured tissue samples (~ 0.5 cm³) were further embedded in paraffin for subsequent slicing towards 5- μ m thick sections with a microtome. The sections were then mounted onto slides for subsequent staining with hematoxylin & eosin (H&E), which is the most widely used staining combination for histopathological diagnosis^{233, 234}. The staining method involves sequential use of the basic dye hematoxylin and acidic counterpart eosin. Hematoxylin tinges intracellular basophilic structures into blue-purple hue, which usually involves structures containing nucleic acids such as the ribosomes, the nucleus and the cytoplasmic regions rich in RNA. In contrast, eosin stains acidic structures bright pink, which generally consists of intracellular or extracellular proteins. As a result, most of the cytoplasm is pink. In addition, to validate the nature of the pink amorphous tissue after H&E staining, some chronically infarcted tissues were stained with the trichrome Masson's method²³³.

3.8. Preparation of MRI-trackable alginate beads containing proteins

3.8.1. Preparation of alginate beads labeled with gadolinium(III) chloride and methemoglobin

Sodium alginate (from brown algae, medium viscosity), porcine Hb (mainly methemoglobin, Met-Hb) and gadolinium(III) chloride hexahydrate ($\text{GdCl}_3 \cdot 6\text{H}_2\text{O}$) were purchased from Sigma-Aldrich Corp. (St. Louis, MO, USA). Calcium chloride dihydrate ($\text{CaCl}_2 \cdot 2\text{H}_2\text{O}$) was purchased from BDH Inc. (Toronto, ON, Canada). Syringes and needles for the extrusion of viscous alginate solution into the hardening solution (distilled water containing $\text{Ca}^{2+} \pm \text{Gd}^{3+}$) as well as centrifuge tubes (50 ml) used as containers for *ex vivo* MRI experiments were purchased from Becton, Dickinson and Company (Franklin Lakes, NJ, USA).

The alginate beads, labeled with Gd^{3+} or Met-Hb, were prepared using a needle extrusion/external gelation method. Briefly, sodium alginate was dissolved in deionized distilled water at a concentration of 2% (w/v) for 6 h at room temperature. For preparation of Gd^{3+} -labeled beads, the alginate solution (10 ml) was manually extruded dropwise through a syringe into a solution (100 ml) containing 30 mM CaCl_2 and 1 mM GdCl_3 , using an 18-G needle. This solution was left for 12 h to stabilize the alginate gel. The average bead diameter was ~ 3 mm. After washing ($\times 3$ times) with water to remove free ions, the gelled alginate beads were transferred to a 50-ml conical centrifugal tube containing 30 ml neutral KHB solution due to its close similarity to human extracellular fluid. A 1-ml syringe containing GdCl_3 (1 mM) as a reference fluid for the MRI experiments was placed at the center of the tube.

Preparation of Met-Hb-labeled beads followed a similar procedure. Briefly, sodium alginate was dissolved in distilled water at a concentration of 4% (w/v) for 24 h at room temperature. The alginate solution was then mixed with a Met-Hb (10%) solution in a 1:1 ratio, thus providing 5%, ~ 0.8 mM Met-Hb (tetramer). The alginate-Met-Hb solution (10

ml) was then extruded into a solution (100 ml) containing 30 mM CaCl₂. To reduce Met-Hb release during the subsequent stabilization period (12 h), the formed beads were immediately wrapped with a layer of cellulose dialysis membrane (molecular weight cut-off = 12,000–14,000 g/mol, VWR Inc., West Chester, PA, USA). After being washed (× 3) with water, the Met-Hb loaded alginate beads were transferred into a centrifugal tube with the same amount of KHB solution. A 1-ml syringe containing Met-Hb (1%) as a reference for the MRI experiments was placed at the center of the tube.

The average bead size was measured directly using strings of beads and a ruler. The average diameter of the beads was 3.2 ± 0.1 mm. These measurements were confirmed by random checks using MR images obtained on the 11.7T scanner.

3.8.2. *In vitro* and *in vivo* detection of alginate beads labeled with either Gd³⁺ or Met-Hb

In vitro MRI experiments were performed on an 11.7T (500 MHz) Magnex (Magnex Scientific Ltd. Yarnton, UK) vertical bore magnet equipped with a Magnex SGRAD 123/72/S 72-mm self-shielded, water-cooled, gradient set producing a maximum gradient strength of 600 mT/m. A Bruker (Milton, ON, Canada) Avance DRX console with a ParaVision 3.0.2 operating system was interfaced to the magnet. The probe and coil (Quadrature Birdcage configuration; 25 mm i.d.) were home built. All experiments were performed at room temperature (25.0 ± 0.5 °C). The effects of T₁ and T₂ weighting were measured with a standard spin-echo sequence, FOV = 3×3 cm², data matrix of 256×256 and six 1-mm-thick slices with a 6-mm interslice distance, changing TR (500–1500 ms range) or by measurement of the TE (12–48 ms range, fixed TR at 1500 ms) dependence, respectively.

An *in vivo* test of their MR trackability within the pericardial cavity was then carried out in pigs. After myocardial cryoinjury was established on pig hearts (detailed in section 3.1.), 10 alginate beads exclusively containing GdCl₃ (3 pigs) or Met-Hb (2 pigs) were anchored onto the pericardium facing the cryoinjury with sutures. After chest closing, each pig was followed up once a week within the 3T MRI system for 4 weeks. Again, T₁-weighted FLASH short-axis images were acquired using ECG gating to the diastolic phase before (baseline image) and after injection of Gd-DTPA (same dosage as before). Typical acquisition parameters were kept unchanged.

3.8.3. *In vitro* estimation of protein release kinetics from the alginate beads

As VEGF and bFGF are very expensive, their release profiles from alginate beads were simulated using other cheaper colored proteins with paramount chemical features including molecular weight (Mw) and isoelectric point (*pI*). To achieve this goal, 3 different proteins, *i.e.*, Met-Hb, Mb, and cytochrome C were selected for modeling purpose. One common feature is that they all contain heme group(s), which could simplify measurements with spectroscopic methods. Their chemical features are detailed in table 3.1.

3.8.4. Preparation of Gd-labeled alginate beads containing VEGF and bFGF

Preparation of alginate beads loaded with two growth factors, *i.e.*, VEGF and bFGF, followed a sterile procedure. Briefly, sodium alginate was dissolved in distilled water at a concentration of 4% (w/v) for 24 h at room temperature. After sterile filtration, the alginate solution containing 1% heparin (100 μ l) was then mixed with 0.1 mg (100 μ l) human recombinant VEGF (HumanZyme Inc., Chicago, IL) or 0.1 mg (100 μ l) human recombinant bFGF (HumanZyme Inc., Chicago, IL), respectively. These 2 solutions (200

Table 3.1. Biochemical features of heme-proteins and growth factors

Chemical properties	Met-Hb	Myoglobin	Cytochrome C	VEGF	bFGF
Molecular weight (kDa)	64.5	16.0	12.4	45	17
Isoelectric point	6.9	7.2	10.6	8.5	9.6

Met-Hb = Methemoglobin, VEGF = Vascular endothelial growth factor, bFGF = basic fibroblast growth factor.

μ l per solution) were then extruded into a sterile solution (20 ml) containing 30 mM CaCl_2 and 1 mM GdCl_3 to form bead-like hydrogel. After being wrapped with the cellulose dialysis membrane, these beads were further immersed within the hardening solution for 12 hours.

3.9. Preparation of agarose gel patch entrapping ADSCs

StemPro® Human ADSCs were purchased from Invitrogen Inc. (Carlsbad, CA) and grown according to the instructions. They were seeded at 4×10^4 cells ml^{-1} for culture at 37 °C, 5% CO_2 and 90% humidity. The culture medium was provided by the same company. Medium was changed after cells had attached to the growth surface. After reaching confluence (about 1 week), cells were detached using trypsin-EDTA, and washed with PBS. After centrifugation, the pellet was re-suspended in the complete medium with additional 10% serum (to compensate for the media without serum used to dissolve the agarose) to get a final concentration of 2×10^6 cells ml^{-1} .

Though alginate solution can readily form gel in the presence of Ca^{2+} , the requirement of a much higher Ca^{2+} concentration concerned us with respect to the fate of cells entrapped in it. As a result, we decided to use agarose solution, which can also form gel when the temperature is below a certain point. In this study, agarose type VII-A

(Sigma-Aldrich, St Louis, MO), which is characterized by the relatively low gelling temperature (26 ± 2.0 °C at 1.5%) to facilitate its mixing with the ADSCs, was used. After it was mixed with MesenPRO RS™ Medium (2% final concentration), the mixture was autoclaved for 15 min at 121 °C for sterilization and dissolution. Then, the solution was kept warm in a 40 °C water bath. A home-made circular molding device was used for establishment of the agarose gel-ADSCs patch. After equal volumes of 2×10^6 cells ml^{-1} and 2% agarose were mixed, 650 μl solution with 6.5×10^5 ADSCs and 1% of agarose was pipetted onto the molding device with a sheet of nylon on the bottom. Fifteen min later, the formed gel patch (~ 10 mm in diameter and ~ 2 mm in thickness) and nylon was transferred into a sterile Petri dish containing the ADSCs-specific culturing media. Thereafter, they were left within the incubator till the day (1-2 days later) scheduled for the *in vivo* study.

4. RESULTS

4.1. *Ex vivo* evaluation of MnCl₂ as a MR contrast agent for acute cardiac ischemia

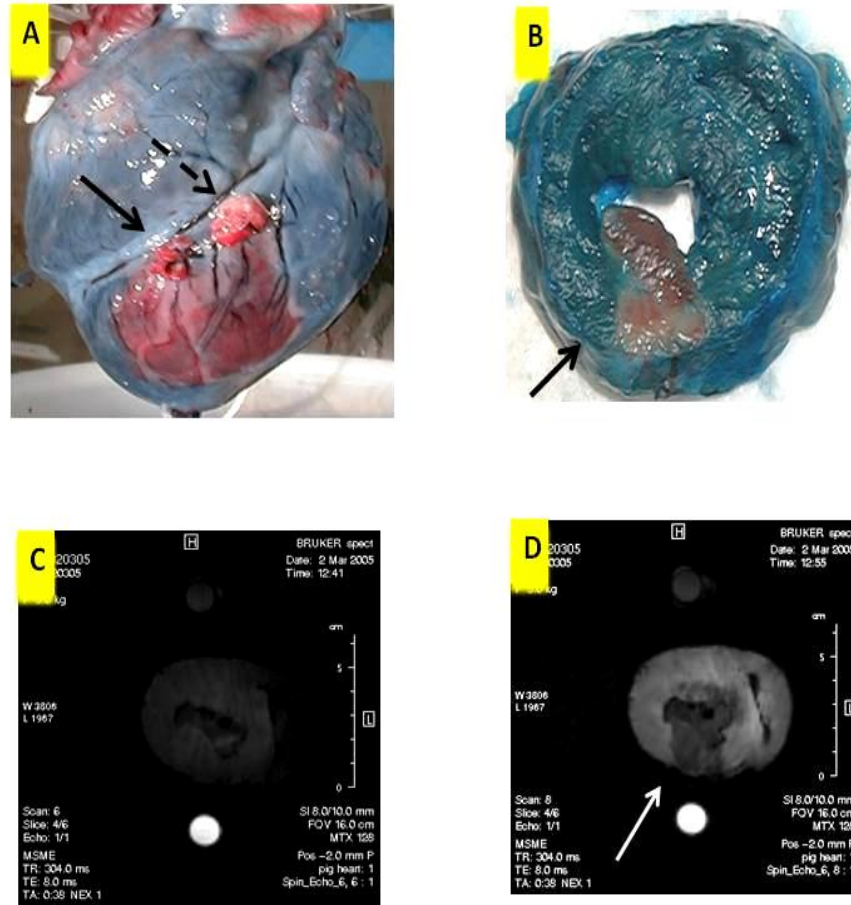
The aim of the experiments was to observe whether administration of MnCl₂ (0.2 mM) into the perfusate could differentially enhance the MR signal intensity in a Langendorff-perfused pig heart subjected to 30-min ischemia induced *in vivo*. Our hypothesis was that (1) Mn²⁺ could significantly increase the signal intensity (SI) within the normal myocardium on T₁-weighted MRI, (2) it could not increase SI within the acutely ischemic myocardium induced by ligation of upstream coronary artery, and (3) it might not be able to enhance SI within the reperfused myocardium subjected to 75-min ischemia at the same rate and extent as that in the normal myocardium.

4.1.1. Acute cardiac ischemia without reperfusion

Permanent occlusion of the 1st and 2nd LAD branches for 30 min almost completely blocked flow as evidenced by immediate cyanotic epicardial appearance, specific optical spectra changes (Fig. 3.2) and lack of Evans blue staining below the occlusion site (Fig. 4.1A, B). During the whole period of study, one pig died of congestive heart failure 3 days after establishment of cardiac ischemia and 2 pigs died of ventricular fibrillation refractory to defibrillation therapy.

Ex vivo MEMRI. In *ex vivo* perfused pig hearts, addition of MnCl₂ (0.2 mM) into the perfusate led to gradual enhancement of SI within the normal myocardium. Whereas, the myocardium supplied by the ligated LAD branches remained hypointense till the end of *ex vivo* perfusion, the area of which corresponded well to the macroscopic findings (Fig. 4.1C,D). The process of SI enhancement as a function of time was then fitted by a monoexponential function:

Figure 4.1. Ischemic myocardium detected by perfusion staining with Evans blue and *ex vivo* Mn-enhanced MRI.



A: Representative picture of perfusion staining using Evans Blue on isolated pig heart subjected to ligation of the 1st (dashed arrow) and 2nd (solid arrow) diagonal branches of the left anterior descending coronary artery. The picture showed absence of the dye on their downstream epicardium. B: Short-axis view of the same heart revealed transmural perfusion deficit (solid arrow). C & D: Corresponding *ex vivo* T₁-weighted MR images of the same short-axis slice before (C) and after (D) the addition of the MnCl₂ into the perfusate. The upper round hypointense filled circle is the water reference, whereas, the lower hyperintense circle is the reference composed of water+CuSO₄ (10 mM). It showed that signal intensity within the normal myocardium became much brighter after exposure to MnCl₂ than within the ischemic myocardium (white solid arrow). (Published in *NMR Biomed.* 2009; 22: 165–173, reprinted with permission on Jun. 10th, 2010 by Wiley-Blackwell Inc.)

$$SI = SI_0 + \Delta SI_{max} \cdot [1 - \exp(-t/t_1)] \quad (3)$$

where SI_0 was a baseline SI, ΔSI_{max} stood for maximal SI enhancement (at $t \rightarrow \infty$) and t_1 was a time constant of SI change (Fig. 4.2). The change of SI within the ischemic myocardium was almost negligible over the observation period, which resulted in a much lower ($\sim 15\%$) rate of SI enhancement ($\Delta SI_{max}/t_1$) as compared with the normal area (Table 4.1).

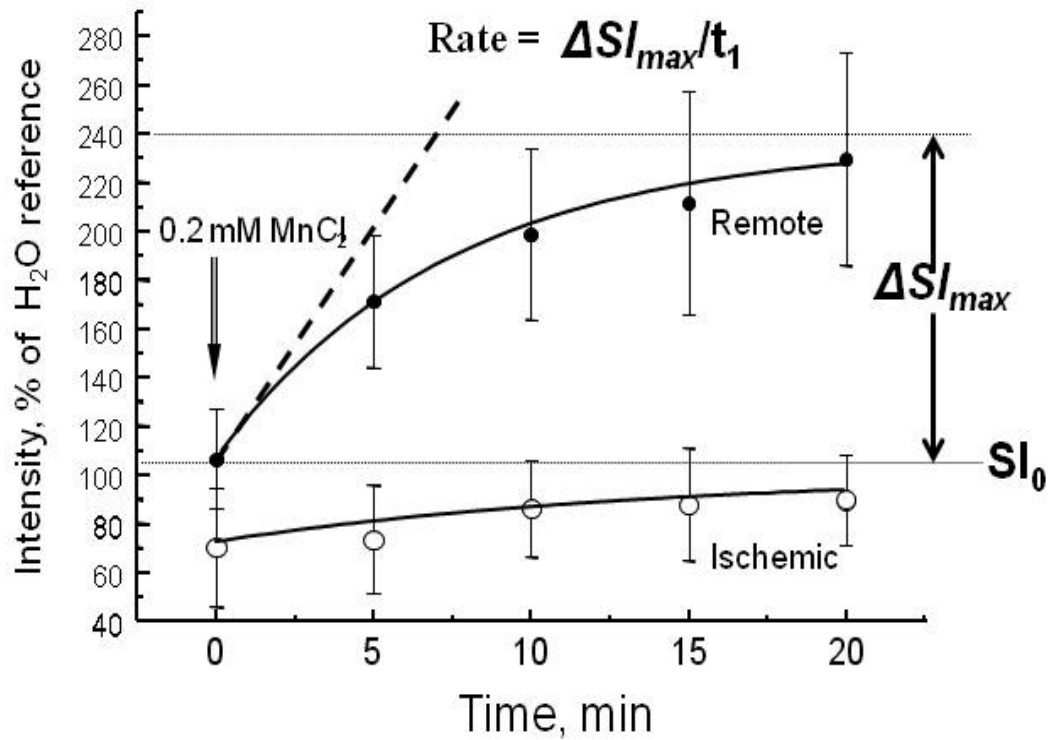
Table 4.1. Kinetics of signal enhancement by $MnCl_2$ after cardiac ischemia with or without reperfusion

Model	Myocardium	SI_0 (%)	ΔSI_{max} (%)	t_1 (min)	$\Delta SI/t_1$ (%/min)
Ischemia (30 min) (n = 5)	Normal	106 ± 12	144 ± 51	7.9 ± 2.8	19.0 ± 5.0
	Ischemia	73 ± 15	32 ± 12	14.4 ± 4.6	2.5 ± 1.2
	<i>P vs. Normal</i>	0.005	0.01	0.04	0.002
Ischemia (75 min) with reperfusion (n = 4)	Normal	108 ± 38	99 ± 46	8.9 ± 4.4	10.4 ± 4.1
	Ischemia	83 ± 23	32 ± 23	21.4 ± 13.1	1.8 ± 1.6
	<i>P vs. Normal</i>	0.02	0.01	0.06	0.02

Means ± SD are shown. SI_0 = baseline signal intensity, ΔSI_{max} = maximal enhancement in signal intensity (at $t \rightarrow \infty$), t_1 = the time constant of signal change, $\Delta SI/t_1$ = maximal rate of signal change.

In vivo Gd-MRI. Acute Gd-MRI data were obtained from chronic pig experiments. For technical reasons such as closure of chest wall, setup of MRI systems and acquisition of cine images, there existed a prolonged period of ischemia (*ca.* 2 h) before the beginning

Figure 4.2. Enhancement kinetics of the MR signal intensity as a function of time after exposure to MnCl_2 in an isolated ischemic pig heart.



Intensity change in the normal myocardium was fitted by a monoexponential function. In contrast, enhancement in the ischemic area was very limited and almost linear. ΔSI_{max} = maximal enhancement in signal intensity (at $t \rightarrow \infty$). t_1 = the time constant of signal change. (Published in *NMR Biomed.* 2009; 22: 165–173, reprinted with permission on Jun. 10th, 2010 by Wiley-Blackwell Inc.)

of T₁-weighted MRI. In *in vivo* Gd-MRI, myocardium suffering 2-h ischemia appeared as a hypointense transmural area, as compared with the surrounding normal myocardium (mildly hyperintense) and the LV blood cavity (heavily hyperintense), in the early (< 6~8 min) acquired images after infusion of the contrast agent (Gd-DTPA, 0.2 mmol kg⁻¹). Thereafter, the contrast between them quickly became indistinguishable with concomitant reduction of SI within the LV cavity (Fig 4.3A-D). Similarly, the process of SI reduction as a function of time was fitted by another monoexponential decay function (Fig. 4.3E):

$$SI = SI_{min} + \Delta SI_{max} \cdot \exp(-t/t_1) \quad (4)$$

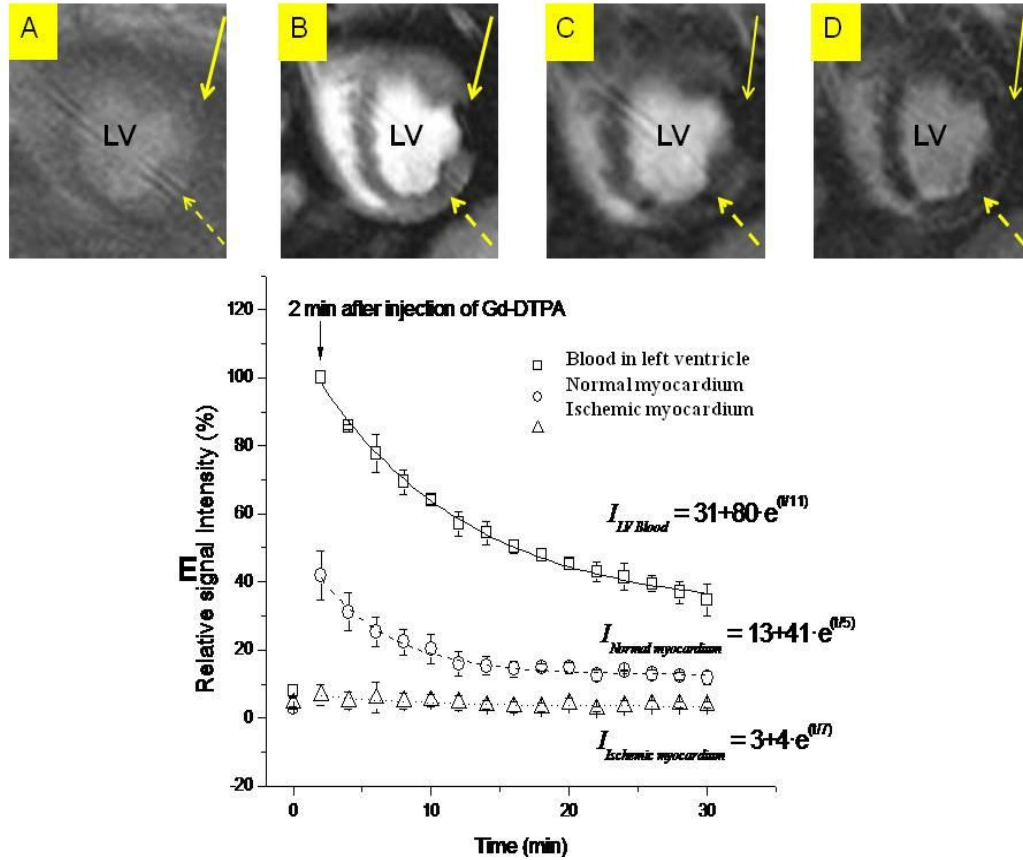
where SI_{min} is the lowest SI, ΔSI_{max} is maximal SI decrement ($t \rightarrow \infty$), and t_1 is a time constant.

Visible/NIR point spectroscopy Complete occlusion of the LAD branches led to severely reduced OSP within the areas at risk (OSP = 0.30 ± 0.06 vs. 0.84 ± 0.07 for normal myocardium, $p < 0.01$).

4.1.2. Acute cardiac ischemia with reperfusion

Pigs in group 2 underwent initial *in vivo* 75-min ischemia followed by reperfusion before isolation for *ex vivo* MEMRI. Perfusion staining with IR676 suggested that 4 out of 6 hearts lacked its presence within the jeopardized myocardium, as evidenced by direct visual inspection. Subsequent quantitative measurement with point NIR reflectance spectroscopy (Fig. 4.4.) revealed that only 17 ± 8 % of the dye deposited in the ischemic/reperfusion area as compared with it in the remote normal counterpart ($p = 0.009$). Further staining with TTC indicated that the various extent of myocardial necrosis

Figure 4.3. Change of the MR signal intensity after intravenous injection of Gd-DTPA in a pig heart subjected to acute ischemia.



A-D: Representative serial MR images of the same short-axis slice acquired from an acutely ischemic pig heart before and after intravenous injection of Gd-DTPA. A: baseline hypointense image which didn't show significant difference between the ischemic and normal myocardium; B: 2-min Gd-exposure image, which showed strong hyperintensity of the LV blood pool, medium hyperintensity of the LV normal myocardium and hypointensity of the LV ischemic myocardium; C: 10-min Gd-exposure image, which showed significant reduction of signal intensity in both LV blood pool and normal myocardium as well as remaining hypointense ischemic myocardium; D: 30-min Gd-exposure image, which showed further significant reduction of signal intensity in LV blood pool, almost complete loss of enhanced signal intensity within the normal myocardium and persistently hypointense ischemic myocardium. The solid arrow was pointed at the ischemic myocardium and the dashed arrow was pointed at the normal myocardium. E: Respective kinetics of signal intensity decay in LV cavity, normal and ischemic myocardium after intravenous injection of Gd-DTPA over a duration of 30 min. LV=Left ventricle, Gd=Gadolinium, Gd-DTPA= Gd-diethylenetriaminepentaacetate.

had occurred within this area (Fig 4.4A & B). A further proof of nonviable myocardium was the presence of oxy-Mb spectra within the jeopardized area (Fig. 4.4C). Complete deoxygenation of the surface Mb within the normal myocardial tissue indicated that cardiomyocytes were still metabolically active and capable of consuming all O₂ that diffused across the slice surface. In contrast, the area suffering 75-min ischemia followed by reperfusion contained significant amount of oxy-Mb, which implied failure of metabolic activity within this area. In the remaining 2 hearts, no significant infarctions were observed. Again, we fitted the time courses for those 4 infarcted hearts with the monoexponential function, the result of which indicated similar trend as in group 1 (Table 4.1.).

Hemodynamic changes The changes of major cardiac physiological parameters, after addition of MnCl₂ into the perfusate in either group, are detailed in Table 3.2. These parameters, including HR, LVDP and PP, provided a general measure of MnCl₂-induced influence on automaticity of sinoatrial pacemaker, contractility of LV myocardium and tonicity of coronary arterial vasculature, respectively. For example, change of perfusion pressure could serve as an index reflecting vascular conductance under constant flow perfusion. As there existed some baseline variations of these parameters across individual pig hearts, data acquired after the use of MnCl₂ were subsequently normalized to their respective baseline levels. From these two groups, it could be derived that MnCl₂ had no significant influence on HR. However, it did have negative influence on LV contractility as evidenced by 15 - 20% maximum reduction of LVDP, which appeared approximately after 20-min exposure to MnCl₂. Similarly, it also led to relaxation of coronary arterial smooth muscles as evidenced by ~ 25% maximal reduction of PP.

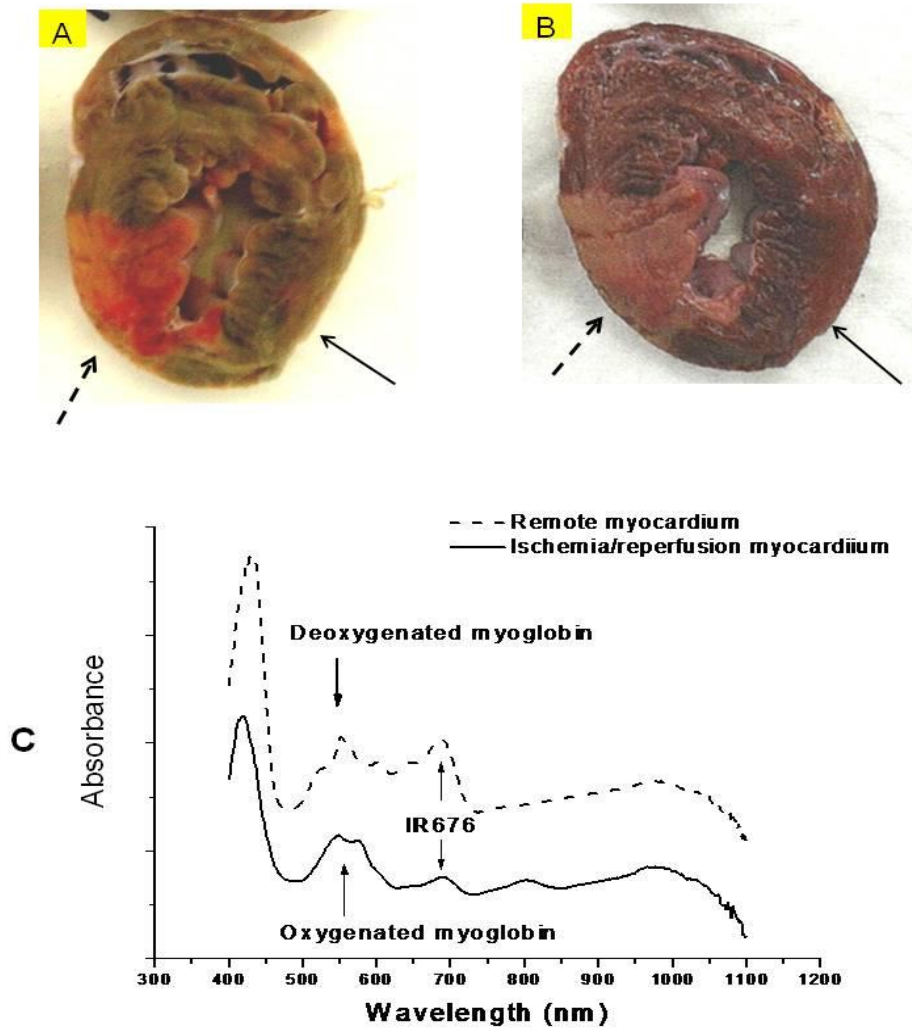
Table 4.2. Effects of MnCl₂ on hemodynamic parameters of isolated pig hearts after acute ischemia with or without reperfusion

		Baseline	MnCl ₂		
			3min	10 min	20 min
HR (bpm)	Ischemia	100%	99.6 ± 2.8%	101.7 ± 6.8%	101.6 ± 8.7%
	<i>P vs. baseline</i>		<i>NS</i>	<i>NS</i>	<i>NS</i>
	Ischemia with reperfusion	100%	101.3 ± 2.2%	104.3 ± 5.1%	104.6 ± 4.2%
	<i>P vs. baseline</i>		<i>NS</i>	<i>NS</i>	<i>NS</i>
LVDP (mmHg)	Ischemia	100%	91.0 ± 2.8%	83.3 ± 6.2%	80.0 ± 10.2%
	<i>P vs. baseline</i>		<i>0.04</i>	<i><0.01</i>	<i><0.01</i>
	Ischemia with reperfusion	100%	81.1 ± 4.4%	81.7 ± 3.4%	83.9 ± 3.9%
	<i>P vs. baseline</i>		<i><0.01</i>	<i><0.01</i>	<i><0.01</i>
PP (mmHg)	Ischemia	100%	90.5 ± 4.6%	81.3 ± 3.3%	78.4 ± 3.0 %
	<i>P vs. baseline</i>		<i><0.01</i>	<i><0.01</i>	<i><0.01</i>
	Ischemia with reperfusion	100%	84.8 ± 3.0%	76.2 ± 1.9%	72.8 ± 3.0 %
	<i>P vs. baseline</i>		<i><0.01</i>	<i><0.01</i>	<i><0.01</i>

Means ±SD are shown; HR = heart rate, LVDP = left ventricular developed pressure, PP = perfusion pressure.

Summary of major findings: Addition of MnCl₂ (0.2 mM) into the perfusate enhanced SI under T₁-weighted MRI within the normal myocardium in an *ex vivo*-perfused pig heart subjected to *in vivo* 30-min permanent ischemia or 75-min ischemia followed by reperfusion. However it did not increase SI within the permanently ischemic myocardium. Myocardium suffering *in vivo* 75-min ischemia had impaired tissue

Figure 4.4. A representative short-axis slice of a pig heart stained by IR676 and TTC after 75-min ischemia followed by reperfusion.



A: Perfusion staining with IR676 on an isolated heart. The dashed arrow pointed at the area of risk, indicating poor perfusion even after re-establishment of coronary perfusion. The solid arrow pointed at the remote myocardium with normal perfusion. B: Subsequent staining of the same slice with TTC, indicating necrosis of jeopardized myocardium (dashed arrow), as compared with remote normal myocardium (solid arrow). C: Representative optical spectra acquired from both jeopardized (lower solid line) and normal (upper dashed line) myocardium, the two spectra were offset for illustrative purpose.

perfusion and viability to various extents. As a result, increment of SI within the jeopardized myocardium was limited in some pig hearts. Exposure of myocardium to Mn^{2+} led to reduced contractility and coronary resistance, but the extent was relatively limited. It had no negative influence on sino-atrial automaticity and myocardial metabolism. The results within this section has been published ²³⁵.

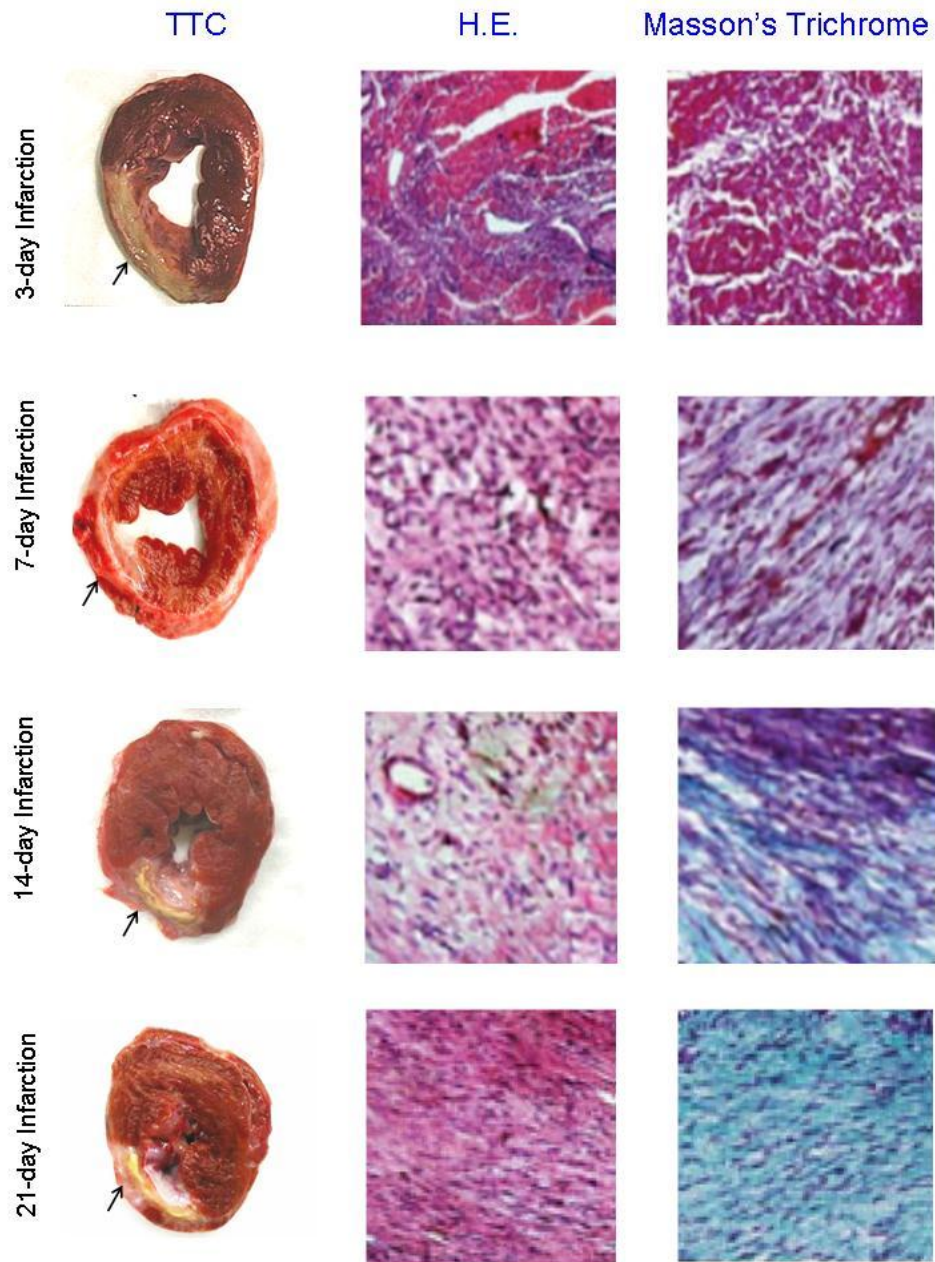
4.2. *Ex vivo* evaluation of $MnCl_2$ as a MR contrast agent for chronic myocardial infarction

The aim of the experiments was to observe whether $MnCl_2$ (0.2 mM) could differentially enhance SI using T_1 -weighted MRI in an *ex vivo*-perfused pig heart with various periods of chronic MI. The hypothesis was (1) Mn^{2+} could significantly increase SI within the normal myocardium on T_1 -weighted MRI; and (2) it also could enhance somewhat SI within the chronically infarcted myocardium under different healing stages.

Macroscopic and microscopic histology revealed that the necrotic myocardium after permanent occlusion of the corresponding artery underwent a classical healing process characterized by inflammatory degradation of injured myocardium and deposition of newly synthesized collagen tissue (Fig. 4.5).

Ex vivo MEMRI. In the normal myocardium, addition of $MnCl_2$ gradually enhanced SI in serial T_1 -weighted MR images with similar enhancement kinetics as it in the acute groups. In contrast, chronically infarcted myocardium of various durations, *i.e.*, 3 - 28 days, revealed itself as a relatively hypointense area after administration of Mn^{2+} into the perfusate in respective short-axis MR images. The location of the hypointense area corresponded well to the TTC-negative tissue (Fig. 4.6). The kinetics of SI enhancement

Figure 4.5. Histological features of a chronically infarcted pig heart.

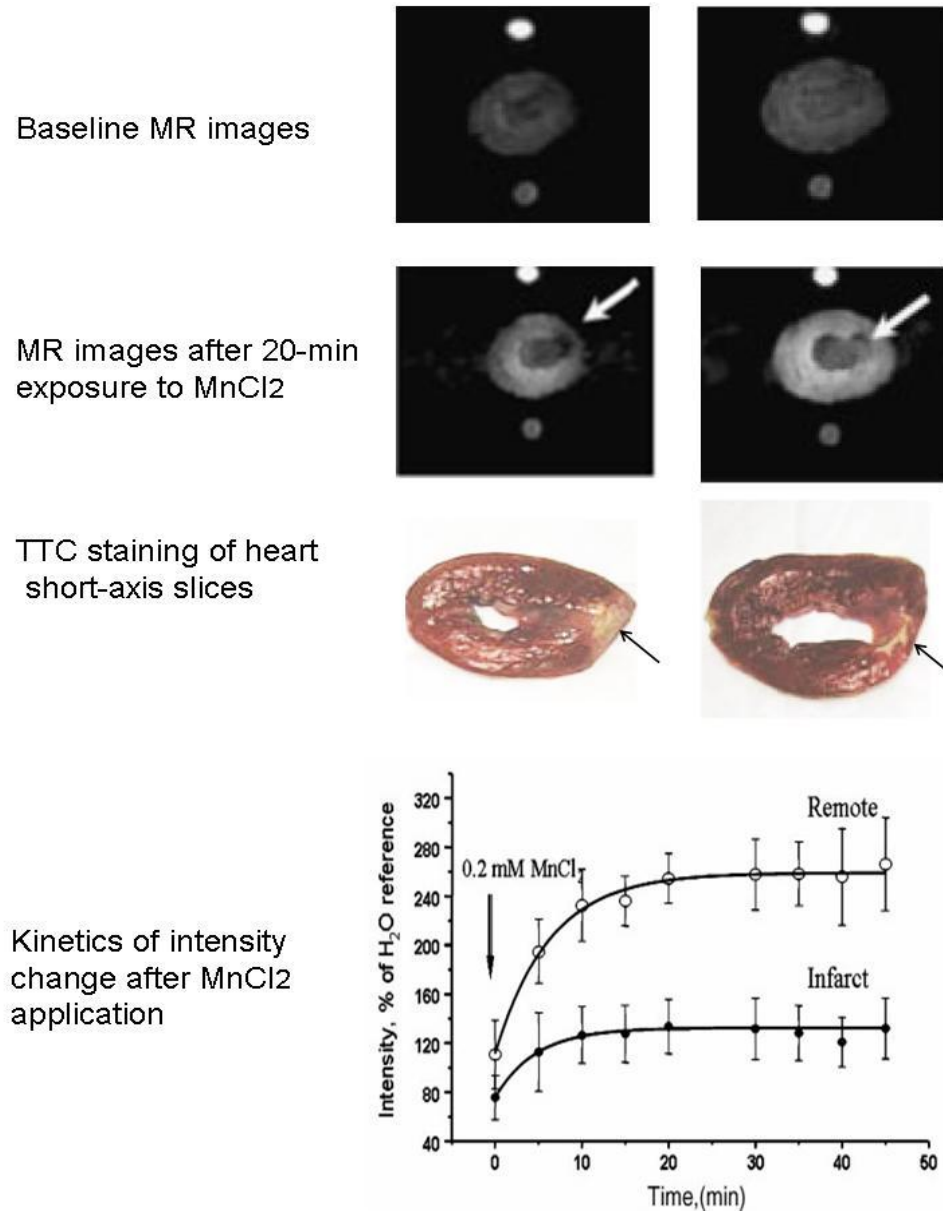


The first column included short-axis heart slices stained with TTC. The second column was infarcted tissues stained with hematoxylin & eosin. The third column was the infarcted tissue stained with Masson's Trichrome. (Published in *NMR Biomed.* 2009; 22: 165–173, reprinted with permission on Jun. 10th, 2010 by Wiley-Blackwell Inc.)

in respective groups could be fitted well with the monoexponential function (detailed parameters in Table 4.3). The maximal enhancements (ΔSI_{max}) and their rates ($\Delta SI_{max}/t_1$) were higher in all chronic MI groups than those in the acute group. There existed a common pattern of SI change in the infarct areas, *viz.*, (1) lower baseline intensities; (2) significantly lower maximal contrast enhancements (ΔSI_{max}) and (3) similar time constants (t_1) of SI enhancement in comparison to the normal myocardium. The second and third common features of SI enhancement within the healing myocardium translated to a slower rate of contrast development. However, this rate did show trends of gradual increment, though insignificant, during the evolving process from the subacute to the chronic healing stage.

To evaluate contribution of the extracellular Mn^{2+} in cardiac signal enhancement, two approaches were used. First, small molar excess (0.2 ~ 0.5 mM) of low Mw Mn^{2+} chelators such as nitrilo-triacetate, ethylenediaminetetraacetic acid and cyclohexyl-1,4-diamine tetraacetate were added 20 min after $MnCl_2$ addition. It was expected that the chelators would reduce the relaxivity of extracellular Mn^{2+} , disrupting its interactions with macromolecules in the interstitium. Addition of various chelators in some experiments didn't change relaxivity in either normal or infarcted myocardium, which had been exposed to Mn^{2+} for 20 min, as no significant changes were observed in SI in infarcted or normal areas. On the other hand, after switching from Mn^{2+} -containing blood/KHB perfusate to Mn^{2+} -free KHB perfusate, SI in both areas decreased significantly. However, decrement of SI was much more obvious within the infarcted myocardium than in the normal myocardium (85% \pm 14% decrement within the infarcted myocardium *vs.* 26% \pm 15% decrement within the normal myocardium, $p < 0.01$).

Figure 4.6. Manganese-enhanced MR images of an isolated pig heart after 7-day infarction.



T₁-weighted short-axis images gated to diastole were acquired before (row 1) and after (row 2) the addition of 0.2 mM MnCl₂ (20-min image is shown). Row 3 is the heart slices (~ 1 cm thick) stained with TTC to check the appearance of TTC-negative necrotic tissue (black arrow), which corresponded to hypointense area (white arrow) on row 2. The time courses of intensity enhancement in both normal and infarcted area were fitted with a monoexponential function. (Published in *NMR Biomed.* 2009; 22: 165–173, reprinted with permission on Jun. 10th, 2010 by Wiley-Blackwell Inc.)

Table 4.3. Kinetics of signal enhancement by MnCl₂ in the normal and infarcted myocardium

Group	SI_0 (%)		ΔSI_{max} (%)		t_1 , min		$\Delta SI/t_1$, %/min	
	Normal	MI	Normal	MI	Normal	MI	Normal	MI
3-day	107±37	68±18	110±30	48±28	6.8±4.1	10.7±11.0	23.0±15.9	8.2±6.3
<i>p vs. MI</i>	0.04		<0.01		NS		<0.01	
7-day	91±12	62±12	107±24	54±28	7.3±3.5	13.3±12.0	18.5±11.9	8.8±8.4
<i>p vs. MI</i>	<.01		0.01		NS		<0.01	
14-day	108±11	67±9	107±41	38±20	9.4±0.7	22±16	11.7±11.4	3.3±4.4
<i>p vs. MI</i>	0.05		0.04		NS		0.01	
21-day	108±21	78±15	130±43	57±6.3	5.7±2.7	4.7±1.4	26.0±12.6	13±4.4
<i>p vs. MI</i>	0.056		<0.01		NS		0.04	
28-day	88±37	64±21	127±35	59±14	8.0±2.8	8.1±3.2	17.7±9.4	8.5±5.0
<i>p vs. MI</i>	NS		0.04		NS		0.025	

Means ±SD are shown; the following monoexponential function was used to fit the experimental time courses: $SI = SI_0 + \Delta SI_{max} \cdot [1 - \exp(-t/t_1)]$ as table 4.1. MI = infarcted myocardium. N = 5 in the 3-day group, n = 6 in the 7-day group, n = 6 in the 14-day group, n = 5 in the 21-day group, n = 5 in the 28-day group.

To test the effect of sarcolemmal membrane potential, which is a driving force for Ca²⁺ and Mn²⁺ entry, we added more KCl into the perfusate. Sarcolemmal depolarization induced by increasing [K⁺] from 4.7 mM to 16 mM (*i.e.*, ~ 30 mV depolarization) in the perfusate led to arrest of cardiac periodical contractions. Compared with the beating hearts, this level of [K⁺] reduced SI increments within the normal myocardium after 15-20 min Mn²⁺ loading. The rate of ΔSI rise ($\Delta SI_{max}/t_1$) and maximal increment (ΔSI_{max})

were significantly lower whereas t_1 values did not differ (Table 4.4). In ischemic/infarct areas intensity increases were much smaller and not significantly affected by KCl arrest.

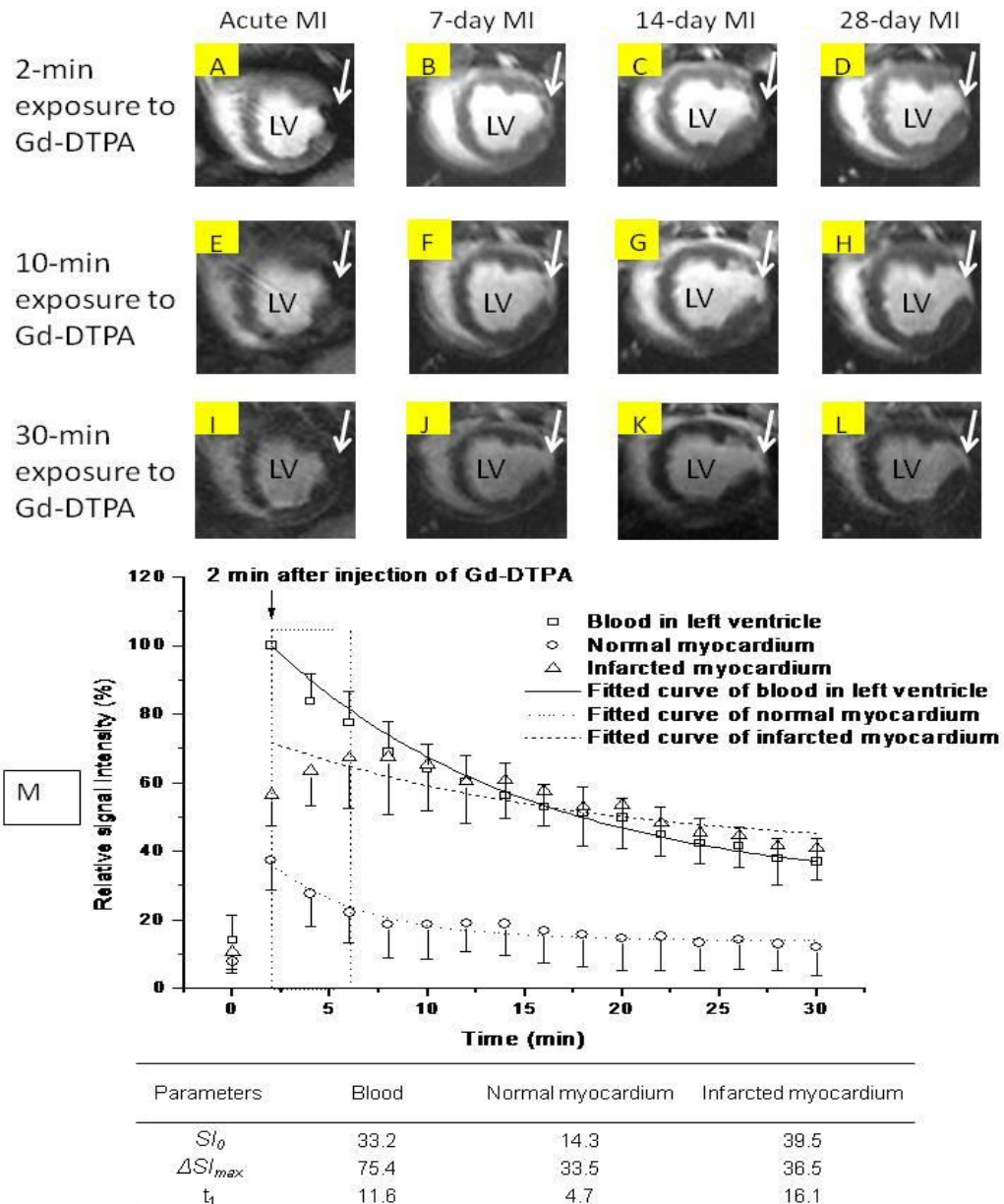
Table 4.4. Kinetic parameters of signal enhancement by $MnCl_2$ with or without sarcolemmal depolarization

Normal Myocardium (n)	ΔSI_{max} (%)	t_1 (min)	$\Delta SI/t_1$, %/min
Beating heart (17)	111 \pm 2.2	6.6 \pm 0.4	16.8 \pm 0.9
KCl-arrested heart (5)	67 \pm 6.9	5.2 \pm 1.4	12.5 \pm 3.5
<i>p</i>	< 0.01	NS	< 0.05

Means \pm SD are shown; the following monoexponential function was used to fit the experimental time courses: $SI = SI_0 + \Delta SI_{max} \cdot [1 - \exp(-t/t_1)]$ as in table 4.1.

In vivo Gd-enhanced MRI. Figure 4.7 shows that, in *in vivo* Gd-MRI from hearts after 7- to 28-day MI, the highest SI within the normal myocardium always appeared at the 1st set of MR images which were acquired 2 min after Gd-DTPA injection. This highest SI was still lower than that within the neighboring infarcted myocardium and decreased over 50% within 8-10 min, as reflected by representative SI kinetics curves of blood, normal and infarcted myocardium in 28-day MI (Fig. 4.7M). In contrast, SI change within the infarcted myocardium conformed to the classical pattern of delayed enhancement²³⁶, which was characterized by significantly enhanced SI within the infarcted myocardium at the earliest acquired image, *i.e.*, 2 min after intravenous Gd-DTPA injection. In addition, during the early stage of post-MI progression (usually < 14 days), there might still exist a hypointense subendocardial region within MI due to gradual invasion of inflammatory

Figure 4.7. Representative Gd-enhanced MR short-axis images of a pig heart after myocardial infarction.



Columns 1 to 4 represent images of acute, 7-day, 14-day and 28-day myocardial infarction. Rows 1 to 3 correspond to images acquired at 2, 10 and 30 min after intravenous injection of Gd-DTPA (0.2 mmol kg^{-1}). The white arrows indicate myocardial infarction areas induced by ischemia. LV = left ventricle. M: representative kinetics of SI decrease and its parameter of MRI signal intensity in LV blood, normal myocardium and infarcted myocardium after bolus intravenous injection of Gd-DTPA. The dotted box indicates the time window optimal for distinguishing these three areas.

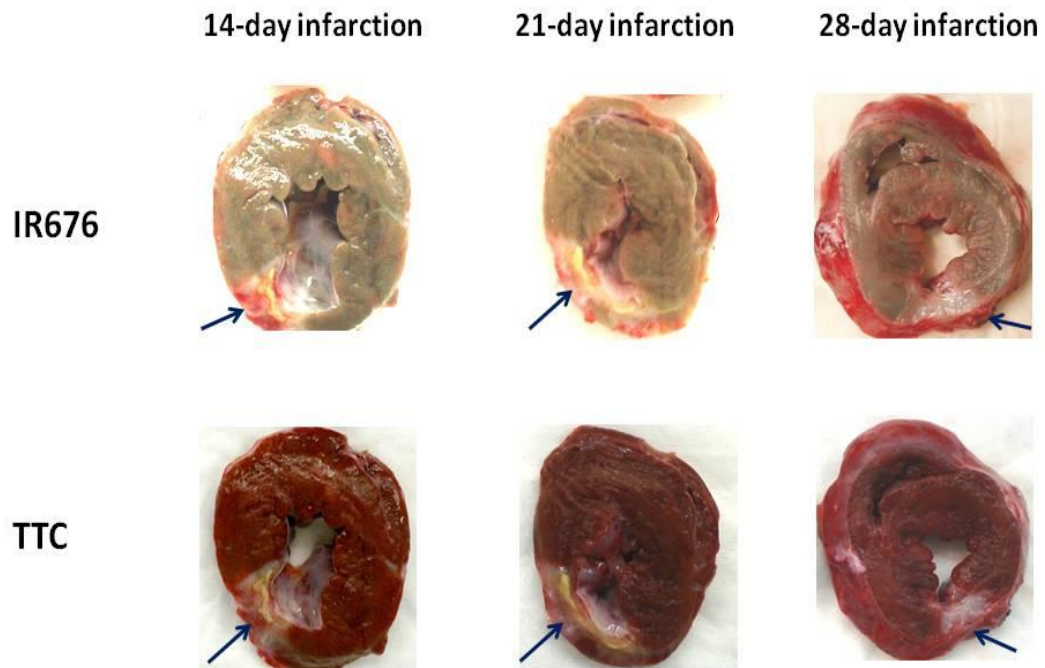
machinery from the border zone towards the core (Fig 4.7B&F). Reduction of SI in MI zone was much slower than it in the normal myocardium. As such, the maximal contrast between the two areas appeared at ~ 10 min after its administration.

Visible/NIR point spectroscopy Short perfusion (30 s) with the NIR deposit tracer IR676 followed by 30-s washout of the tracer revealed its reduced deposition within the infarcted zones under various healing stages (Fig. 4.8). With the infarction progression, signal from heme-containing proteins (mainly, Mb) reduced significantly within the infarction area, which corresponded to TTC-negative and Masson's trichrome-positive areas in histology study.

Hemodynamic parameters Table 4.5 summarized the effects of 0.2 mM MnCl₂ on HR, LVDP, and PP. Baseline parameters were similar in all groups. Administration of MnCl₂ did not affect HR, but it showed trend towards decrement of LVDP and PP. The differences became significant when all groups were combined such that, on average, LVDP decreased by 16% and PP by 20%, which conformed to our previous study for acute MI.

Summary of major findings: Addition of MnCl₂ (0.2 mM) into the perfusate enhanced SI within the normal myocardium in T₁-weighted MR images of an *ex vivo*-perfused pig heart experiencing various length (from 3 days to 28 days) of ischemia-induced MI. Signal intensity also increased gradually within the infarcted myocardium, the rate and extent of which was significantly reduced as compared with that in the normal counterpart. Reduction of transmembrane potential via addition of extra K⁺ into the perfusate led to decreased rate of SI enhancement within the normal area, whereas it had no obvious influence within the infarcted myocardium. Switching from Mn-containing

Figure 4.8. Representative staining results with IR676 and TTC in a pig heart subjected to chronic myocardial infarction.



Upper row: staining results with IR676 via perfusion. Lower row: staining results with TTC via surface reaction. Left column: 14-day MI; middle column: 21-day MI; right column: 28-day MI. The arrow pointed to the infarcted tissue. MI = myocardial infarction.

Table 4.5. Effects of MnCl₂ on hemodynamic parameters of isolated pig hearts after chronic MI

Infarction group	Heart rate (bpm)		LV developed pressure (mmHg)		Perfusion pressure (mmHg)	
	Baseline	MnCl ₂	Baseline	MnCl ₂	Baseline	MnCl ₂
3-day	124 ± 14	117 ± 13	72 ± 10	56 ± 8	47 ± 14	42 ± 14
<i>p vs. bsln</i>		<i>NS</i>		<i>0.05</i>		<i>NS</i>
7-day	133 ± 9	126 ± 10	81 ± 9	72 ± 7	44 ± 8	37 ± 4
<i>p vs. bsln</i>		<i>NS</i>		<i>NS</i>		<i>NS</i>
14-day	135 ± 15	131 ± 15	72 ± 11	62 ± 9	48 ± 20	40 ± 15
<i>p vs. bsln</i>		<i>NS</i>		<i>NS</i>		<i>NS</i>
21-day	120 ± 16	116 ± 17	81 ± 8	71 ± 12	56 ± 12	42 ± 8
<i>p vs. bsln</i>		<i>NS</i>		<i>NS</i>		<i><0.01</i>
28-day	131 ± 9	130 ± 6	68 ± 4	55 ± 5	62 ± 13	41 ± 3
<i>p vs. bsln</i>		<i>NS</i>		<i>0.03</i>		<i><0.01</i>
Total (% of baseline)	125 ± 15	123 ± 14 (98 ± 6)	75 ± 12	63 ± 12 (84 ± 8)	55 ± 17	42 ± 12 (80 ± 14)
<i>p vs. bsln</i>		<i>NS</i>		<i><0.01</i>		<i><0.01</i>

Means ±SD are shown; LV = left ventricle; Baseline parameters were measured prior to MnCl₂ addition, while MnCl₂ effect was measured 20 min thereafter.

perfusate composed of blood/KHB mixture to Mn-free KHB perfusate enhanced the signal contrast between the normal and infarcted myocardium, the location and size of which corresponded well to those revealed by Gd-MRI and final post-mortem

examination. Similar to the findings from the previous study, exposure of myocardium to Mn^{2+} led to reduction in LVDP and PP. It had no negative influence on sino-atrial automaticity and myocardial metabolism. The results within this section has been published ²³⁵.

4.3. Characterization of myocardial cryoinjury with contrast-enhanced MRI and optical spectroscopy

The aim of the experiment was to test whether cryothermia in pig hearts could (1) induce sub-epicardial MI with similar healing features as in ischemia-induced MI, and (2), if so, be characterized by contrast-enhanced MRI and optical methods. Our hypothesis was that cryothermia could induce acute myocardial necrosis with similar progression features as in ischemia-induced MI but with more uniform pathological features.

Post-mortem results revealed that reaction of the myocardium to cryothermal injury followed a standard pattern of host-mediated repair of necrotic tissue through the stages of healing with collagen deposition and scar formation, which conformed the reported studies from other groups ^{188, 191, 237, 238}. No pigs developed acute congestive heart failure and/or life-threatening arrhythmia after cryoinjury.

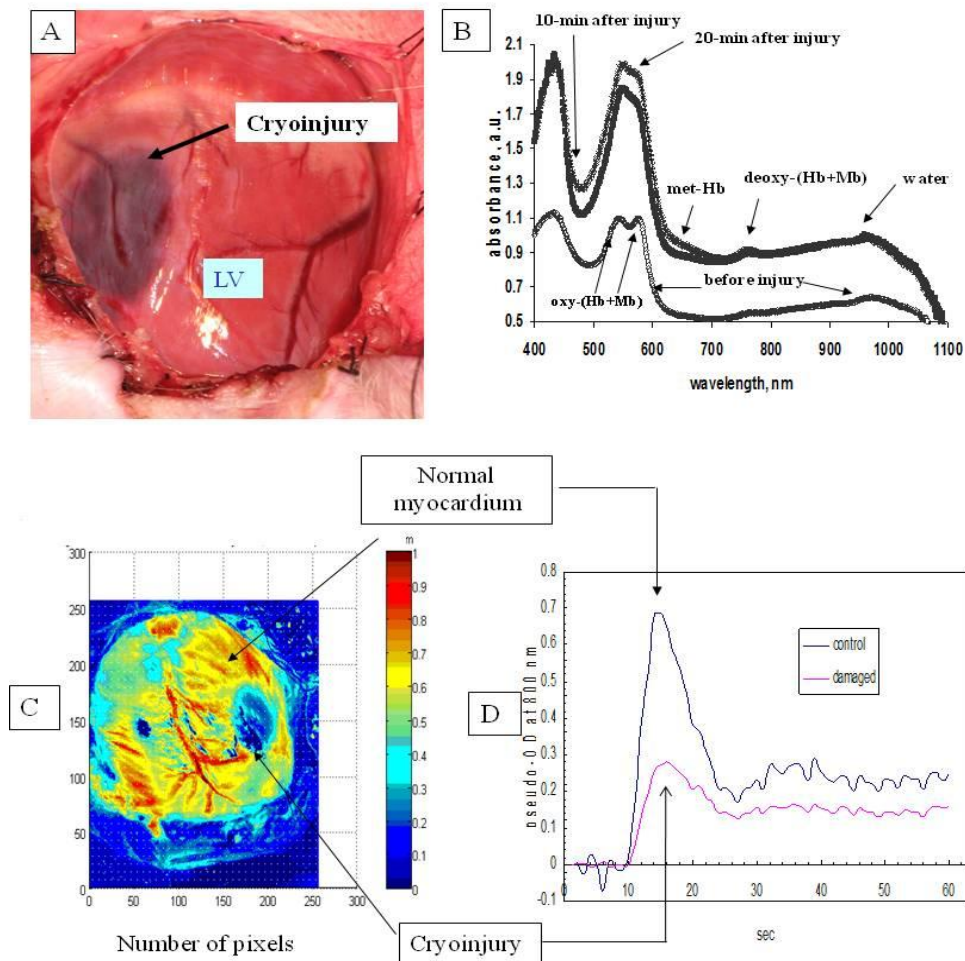
4.3.1. Acute myocardial cryoinjury

The LV myocardium subjected to 2-min cryoinjury and thawed over a period of ~ 5 min, assumed a cyanotic epicardial appearance (Fig. 4.9A) with an accompanying visually discernible absence of contraction. The shape of the cryolesion was semicircular in the short-axis slice with an averaged diameter of 29.7 ± 1.3 mm and an averaged depth of 9.2 ± 0.9 mm. In all groups, optical point spectroscopy showed a significant increase in

absorption peaks at 550 and 580 nm corresponding to oxy-(Hb+Mb) and a change in their relative intensities characteristic of deoxy-(Hb+Mb) (Fig. 4.9B). The latter was also confirmed by the appearance of a deoxy-(Hb+Mb) peak in the NIR range at 760 nm. Interestingly, there emerged a met-Hb peak at 660 nm, characteristic of blood coagulation and formation of thrombi. Near infrared imaging of first-pass kinetics of ICG revealed a circular sub-epicardial area of reduced absorbance at 800 nm (Fig. 4.9C). Normally, its peak appeared 5-6 s after dye appearance in the LV wall blood (15 s post-injection, Fig. 4.9D).

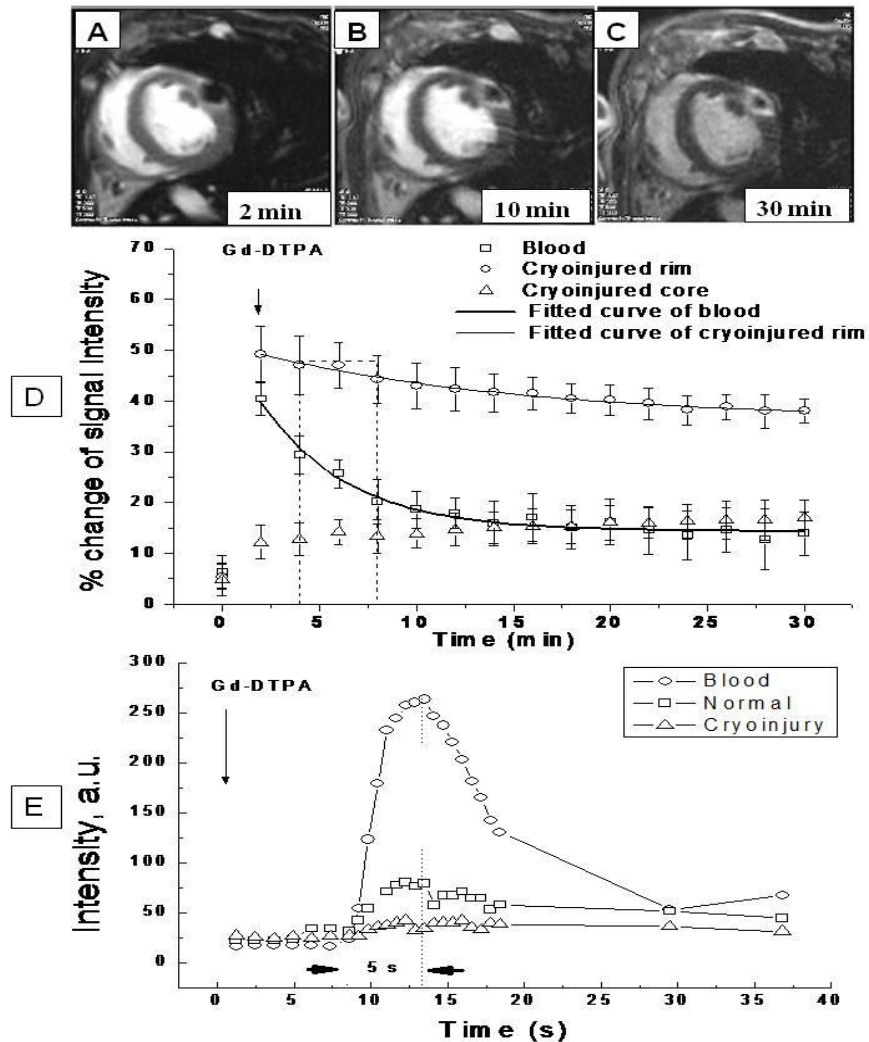
In the acute cryoinjury phase (~ 2.5 h, group 9) serial acquisitions of short-axis MR images after injection of Gd-DTPA revealed a thin hyperintense rim surrounding the hypointense core. The highest SI appeared in the first set of acquired images, *i.e.*, 2 min after administration of the contrast agent (Fig. 4.10A). Meanwhile, SI of the remote myocardium was also higher than that in the hypointense area, but such a difference was much less than that between the hyperintense rim and the hypointense core. Thereafter, SI in both remote and hyperintense myocardium began to decrease. As the rate of SI decrement was much faster within the remote area, the difference in SI between it and the cryoinjured core gradually disappeared in the later images (~ 10 min post-Gd, Fig. 4.10B). The respective time courses of SI decrement within both the normal myocardium and the hyperintense rim were then approximated by the monoexponential decay function (Eq. 4, Fig. 4.10D). As the kinetics of SI decrement was much faster in the remote myocardium ($t_1 = 5$ min *vs.* 14 min in the hyperintense rim), the optimal time window capable of distinguishing the remote myocardium, hyperintense rim and hypointense core

Figure 4.9. Epicardial appearance of an acutely cryoinjured pig heart and its image corresponding to *in vivo* perfusion map acquired by an NIR imaging system with indocyanine green as the intravascular flow tracer.



A: Photograph of anterior-lateral epicardium of acutely cryoinjured pig heart *in vivo* (10 min after cryoinjury); B: Optical reflectance spectra of cryoinjured and normal myocardium; C: A near infrared image showing subepicardial indocyanine green (ICG) distribution in cryoinjured heart. Red and dark-blue pseudo-colors correspond to the highest and lowest ICG absorption, respectively; D: Corresponding first-pass kinetics of ICG passage through normal and cryoinjured sub-epicardium. LV = Left ventricle. (Published in *Magn Reson Imaging*. 2010;28:753-66, reprinted with permission on May 10th, 2010 by Elsevier Inc.)

Figure 4.10. Kinetics of *in vivo* MR signal development in a short-axis pig heart slice following acute cryoinjury after intravenous infusion of Gd-DTPA.



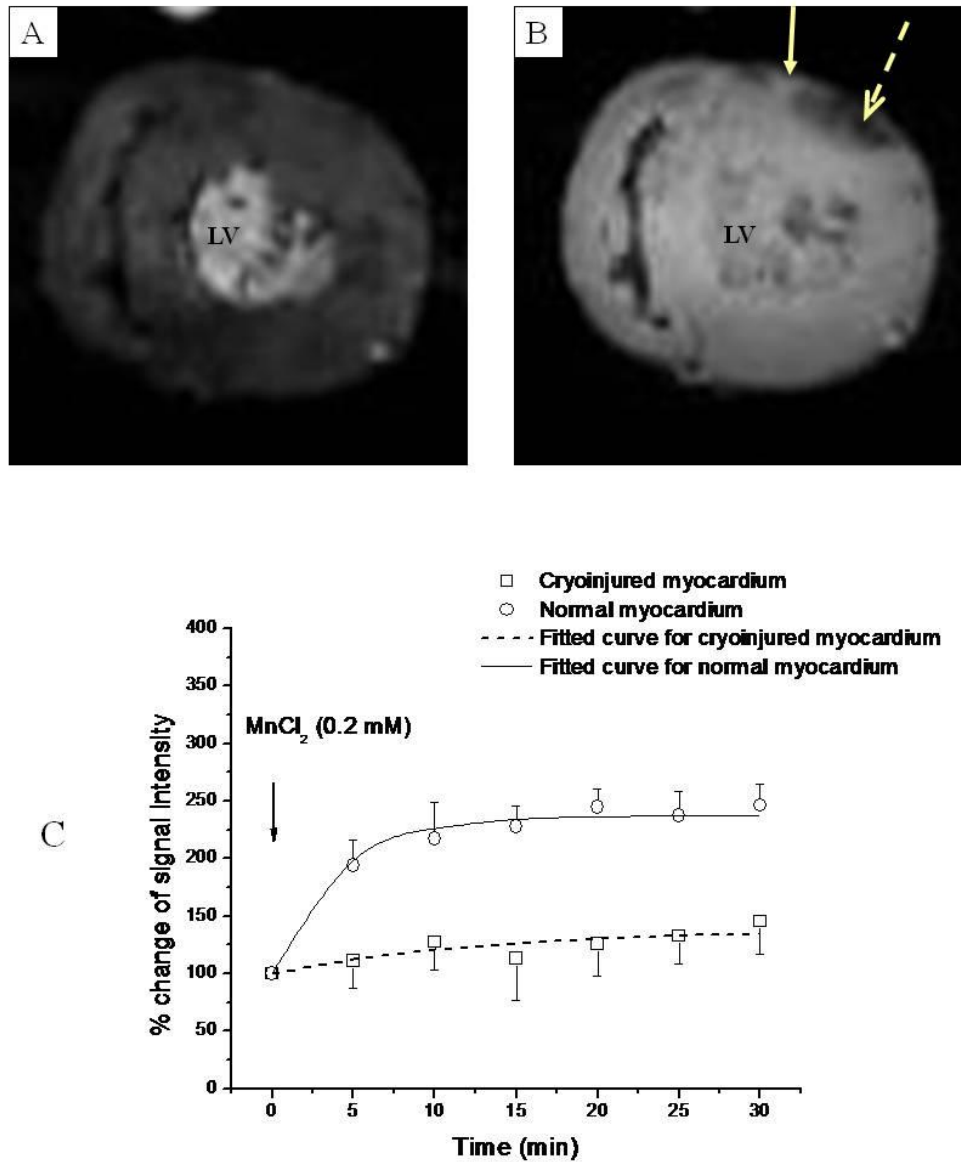
A: Early (2-min) MR image after Gd-DTPA administration, B: late (10-min) MR image after Gd-DTPA administration, and C: Final (30-min) MR image after Gd-DTPA administration. D: Time courses of SI in normal, hyperintense and hypointense cryoinjured areas. The lines are the least square mono-exponential fits of SI decay according to Eq. (2). The optimal time window to distinguish normal, hyperintense and hypointense myocardium is between 4 and 8 min after Gd-DTPA administration (indicated by dotted rectangle). E: First-pass Gd-enhancement kinetics. In this case low dose of Gd-DTPA ($0.05 \text{ mmol kg}^{-1}$) was injected followed one min thereafter by high dose ($0.15 \text{ mmol kg}^{-1}$) injection to assess late Gd-enhancement kinetics. In this case fast T_1 -weighted images were acquired from 2 slices that contained cryoinjured areas. Gd = gadolinium, LV=left ventricle, MR = magnetic resonance. SI = signal intensity. (Published in *Magn Reson Imaging*. 2010;28:753-66, reprinted with permission on May 10th, 2010 by Elsevier Inc.)

was therefore very short and was best observed between 4 and 6 min after injection of Gd-DTPA (the dotted rectangle in Fig 4.10D). In addition, during 30-min Gd-MRI, the hyperintense rim expanded gradually towards the hypointense core (Fig. 4.10A-C), which indicated slow diffusion of contrast agent into the cryolesion. In some experiments first-pass Gd-enhancement kinetics was investigated (Fig. 4.10E) using low dose Gd-DTPA ($0.05 \text{ mmol} \cdot \text{kg}^{-1}$) injection. Intensity of LV blood and normal LV tissue reached maximum approx. 5 s after the contrast agent entered the LV ventricle. Cryoinjured tissue (black spot in Fig. 4.10A) did not show any significant intensity increase. This pattern resembles first-pass kinetics of optical contrast agent passage in the sub-epicardium (Fig. 4.9D).

Following optical measurements *in vivo*, pigs in the acute group underwent heart isolation and an *ex vivo* MEMRI study ~ 1.5 h after cryoinjury. Serial images acquired every 5 min after MnCl_2 administration revealed gradual increase in SI in the remote myocardium and much slower increase in SI within the cryoinjured myocardium (Figs. 4.11A & B). The time courses of SI enhancement in both areas were fitted by the monoexponential function (Eq. 3). Maximal enhancement (ΔSI_{max}) and rates of intensity enhancement ($\Delta SI_{\text{max}}/t_1$) in the cryoinjured myocardium were significantly lower ($p < 0.001$) than that in the remote myocardium (Fig. 4.11C and Table 4.6).

Finally, the isolated heart perfused with blood-free KHB underwent an *ex vivo* perfusion study to determine perfusion deficit, if any, with IR676. The short-axis slice across the acute cryolesion revealed cyanotic contusion-like cryoinjured submyocardium, which contained increased amounts of oxy/deoxy-(Hb+Mb) and very little IR676 (spectra in Fig. 4.12C), in contrast to the normal myocardium containing deoxy-Mb and a

Figure 4.11. Short-axis Mn-enhanced MR images on an *ex vivo* perfused pig heart following acute cryoinjury.



A: Baseline, B: 20-min exposure to MnCl₂ (0.2 mM). A solid arrow pointed to the normal myocardium and a dashed arrow pointed to the cryoinjured myocardium. C: Kinetics of SI enhancement following MnCl₂ addition. The lines represented best monoexponential fit by using Eq. (3). LV = left ventricle, SI = signal intensity. (Published in *Magn Reson Imaging*. 2010;28:753-66, reprinted with permission on May 10th, 2010 by Elsevier Inc.)

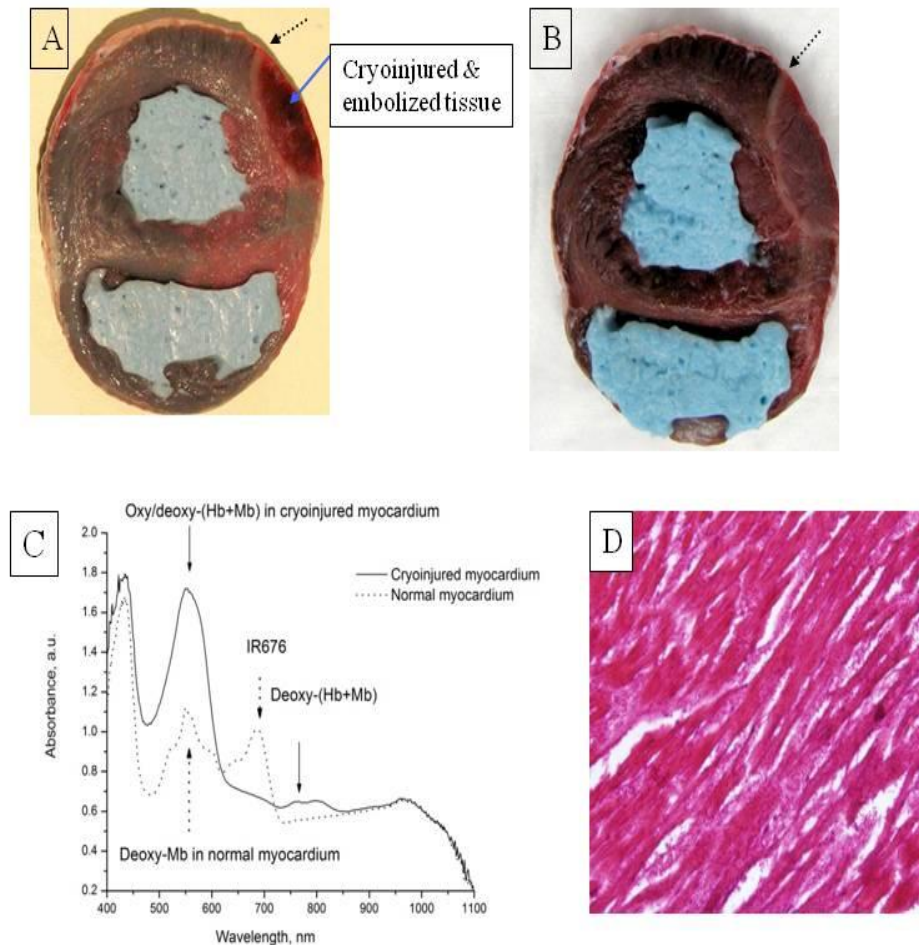
Table 4.6. Kinetic parameters of manganese-induced signal enhancement within the normal and cryoinjured myocardium after acute cryoinjury

Group/area	ΔSI_{max} , %	t_1 , min	$\Delta SI_{max}/t_1$, %/min	R^2
Control area	102 ± 5.2	4.4 ± 0.57	23.2	0.98
Cryoinjured	27 ± 2.5	12.3 ± 3.1	2.2	0.96
<i>p vs. control</i>	<0.01	<0.01	<0.01	

Mean ±SD values were shown for ΔSI_{max} and t_1 . The parameters were derived from the monoexponential fit using Eq. (3). ΔSI_{max} = maximal amplitude of signal increase normalized to the reference water signal amplitude; t_1 = time constant; $\Delta SI_{max}/t_1$ = the initial (maximal) rate of intensity increase.

significant amount of IR676. Presence of Hb and absence of IR676 in the cryoinjured area reflected inability of blood-free perfusate to reach this area and remove RBC. This observation corroborated our *in vivo* data (Figs. 4.9 & 4.10) showing greatly reduced perfusion of the cryoinjured area due to microvascular embolization by the erythrocytes. A rim of optically lighter myocardium without contusion-like appearance (Fig. 4.12A) closely correlated with the hyperintense rim seen on early Gd-enhanced MR images (Fig. 4.10). Subsequent viability staining with TTC further proved that the myocardium in the rim was necrotic (Fig. 4.12B). However, results of TTC staining of the contusion-like cryoinjured portion were not conclusive as this area was already intensely red thereby masking any possible red TTC staining. Optical point spectra of the slices shown in Fig. 4.12C helped to solve this problem. Complete deoxygenation of the surface Mb in normal areas indicated that cardiomyocytes were still metabolically active and capable of consuming all O₂ that diffused across the slice surface. In contrast, the area of embolized cryoinjury contained significant amount of oxy-(Hb+Mb), presence of which implied the

Figure 4.12. Macroscopic and microscopic staining pictures of a pig heart subjected to acute cryoinjury.



A & B: The short-axis slice of a cryoinjured heart prior to (A) and after TTC staining (B). Prior to slicing, the heart was perfused with blood-free KHB buffer containing 7-9 μM deposit flow tracer, IR676, which was taken up by cardiomyocytes in perfused areas. The red septal region was possibly due to perfusion deficit during *ex vivo* IR676 perfusion. C: The optical spectra of the cryoinjured and normal myocardium. It shows very limited content of the dye within the cryoinjured core (dotted arrow) and higher than normal content of hemoglobin. D: H&E staining revealed massive microvascular entrapment of erythrocytes within the cryolesion and coagulative cardiomyocytes necrosis. Magnification = 40x. (Published in *Magn Reson Imaging*. 2010;28:753-66, reprinted with permission on May 10th, 2010 by Elsevier Inc.)

inability of this tissue to metabolize O₂ diffusing across the slice surface. Indeed, a microscopy study revealed coagulating cardiomyocytes necrosis and massive entrapment of erythrocytes within this cardiac tissue (red staining in Fig. 4.12D).

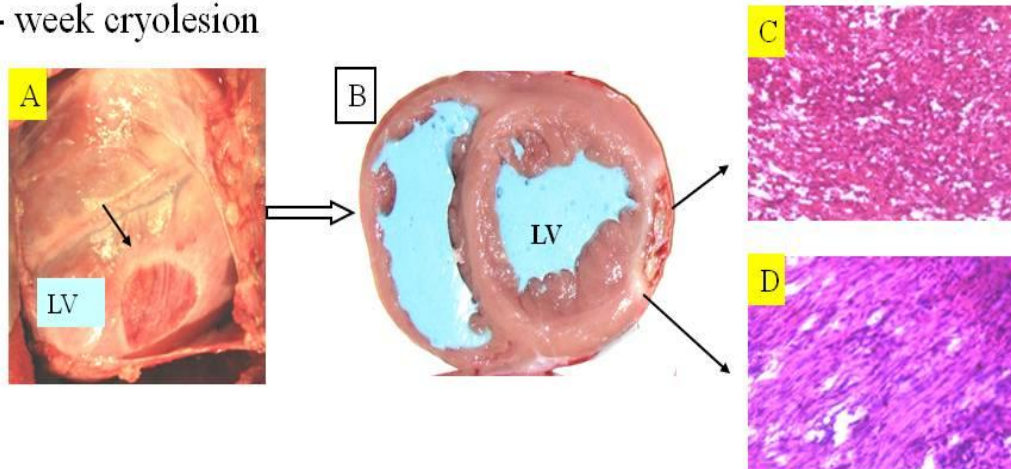
4.3.2. Chronic myocardial cryoinjury

The cryoinjured myocardium subsequently experienced the same host-mediated healing process as ischemia-induced MI. Upon one week, the edge of the lesion began to be sharply demarcated by a rim of granulation tissue containing inflammatory cells (macrophages, lymphocytes, fibroblasts), deposited collagen and newly formed capillaries, whereas the lesion close to the epicardium remained 'intact', as evidenced by remaining necrotic myocardium and entrapped erythrocytes (Fig. 4.13 A-D). Four weeks later, the lesion was completely replaced by scar tissue (Fig 4.13E-G). As a result, Gd-MRI carried out at week 1, 2 and 4 revealed gradual vanishing of the hypointense core (Fig 4.14A-C). Kinetic analysis of SI change within the remote and the scar tissue in images acquired 4 weeks after cryoinjury showed that (1) SI maximized in both areas after 2-min exposure to Gd-DTPA, (2) SI in the cryolesion doubled relative to that in the remote myocardium, (3) the decay time constant (t_1) was much shorter for the remote myocardium than that for the scar tissue ($t_1 \sim 5$ min *vs.* ~ 27 min, respectively), which translated to a maximized contrast enhancement in a time frame ranging from 4 to 14 min (Fig. 4.14D). In addition, the cryolesion size measured from late enhancement MR images decreased significantly to 41% \pm 4.5% of the initial size during 4-week chronic infarction progression (Fig. 4.14E).

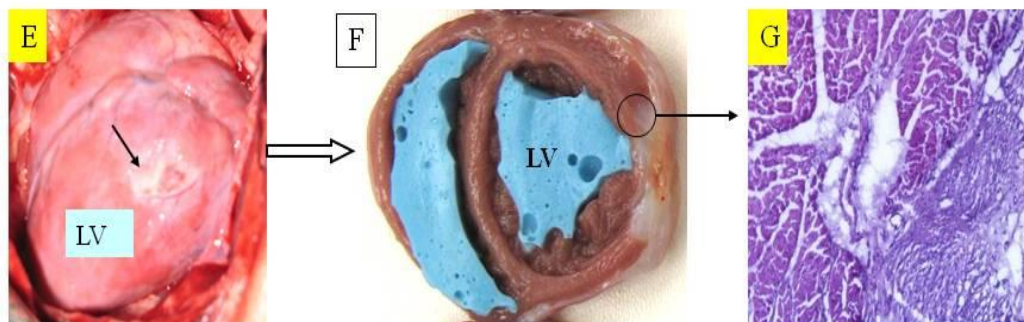
After isolation of the hearts following 4-week cryoinjury, MEMRI showed a relatively reduced intensity of scar tissue perhaps due to the absence of viable

Figure 4.13. Macroscopic and microscopic staining pictures of pig hearts subjected to chronic cryoinjury.

1- week cryolesion

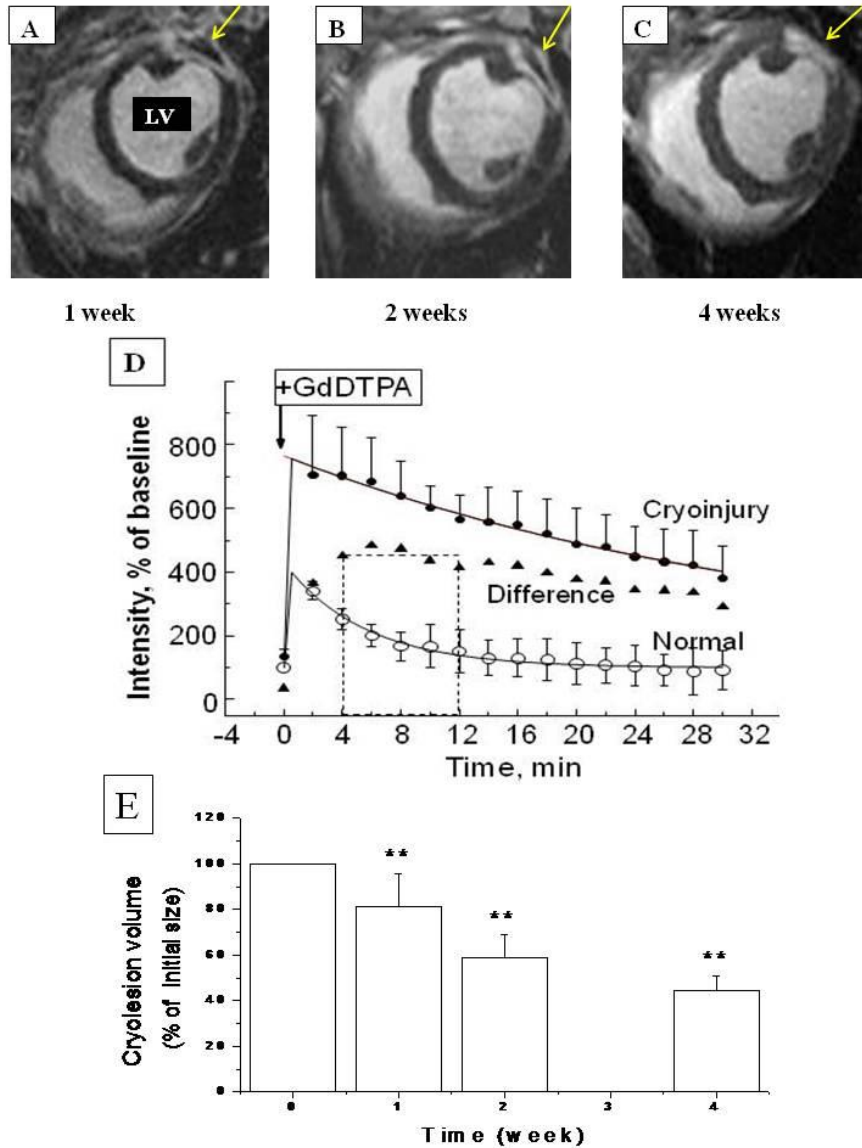


4- week cryolesion



A-D: macroscopic & microscopic features of 1-week cryolesion in a pig heart. The central bright red spot seen in both epicardium (A) and subepicardium of short-axis slice (B) contained embolic erythrocytes (C). The white border zone was newly formed collagen tissue from host-mediated inflammatory repair (D). E-G: macroscopic & microscopic features of 4-week cryolesion in a pig heart. The cryolesion was almost completely replaced by scar tissue. The microscopic picture (G) shows both normal myocardium (upper left) and neighboring scar (lower right). Magnification is 40x. (Published in *Magn Reson Imaging*. 2010;28:753-66, reprinted with permission on May 10th, 2010 by Elsevier Inc.)

Figure 4.14. Change of the MR signal intensity in a cryoinjured pig hearts after intravenous injection of Gd-DTPA.



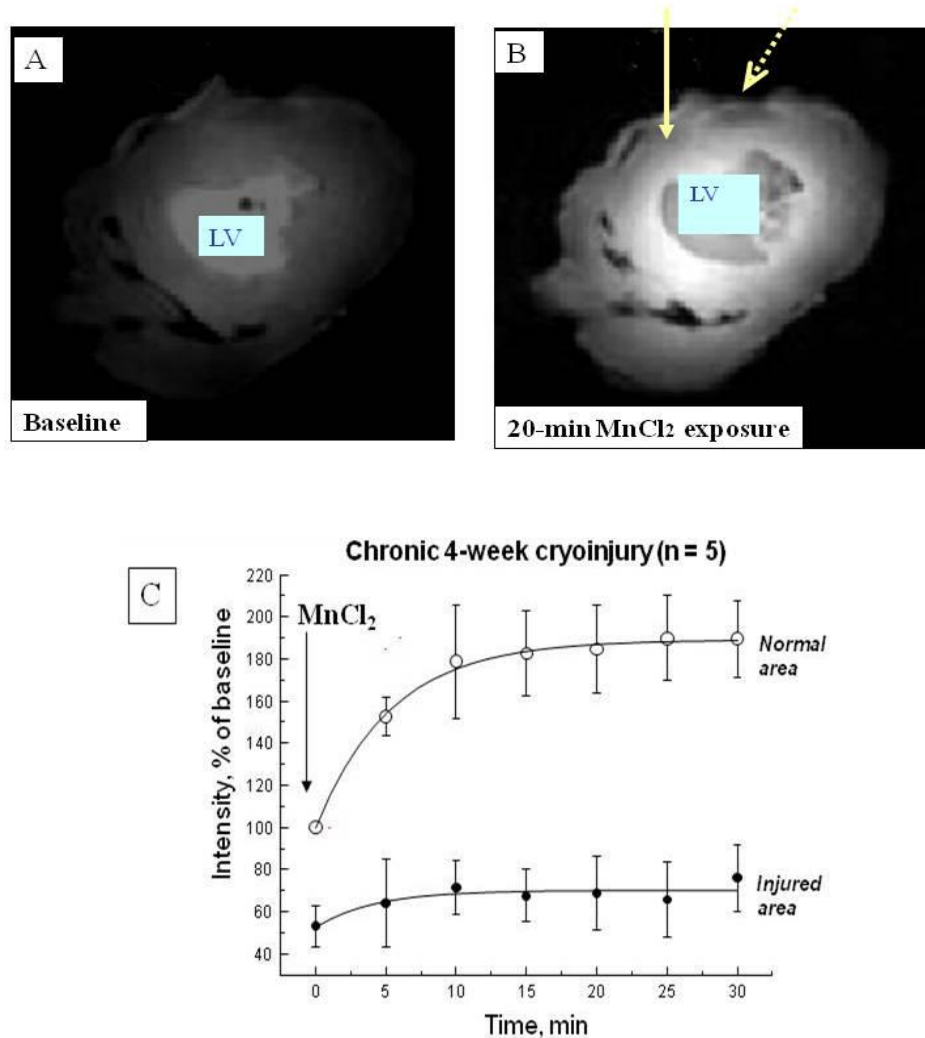
A-C: Late enhancement short-axis MR images of a chronically cryoinjured pig heart after 10-min exposure to Gd-DTPA. The images correspond to week 1 (A), 2 (B) and 4 (C) post-injury; the solid arrow indicates the cryolesion. D: Kinetics of signal intensity decay in normal and scar tissue after exposure to Gd-DTPA (0.2 mmol kg^{-1}) 4 weeks post-cryoinjury. The lines represent least-square monoexponential fit. The optimal time window for the largest difference in the SI (contrast) occurred between 4 and 14 min. E: Gradual decrease in the relative cryolesion volume measured from Gd-enhanced MR images. Gd=gadolinium, LV=left ventricle, SI=signal intensity; **indicates $p < 0.01$. (Published in *Magn Reson Imaging*. 2010;28:753-66, reprinted with permission on May 10th, 2010 by Elsevier, Inc.)

cardiomyocytes, which actively accumulated and retained Mn^{2+} in normal areas (Fig. 4.15A, B). Kinetic analysis showed considerable decrease in the maximal enhancement (ΔSI_{max}) and the rates of intensity enhancement ($\Delta SI_{max}/t_1$) in the cryoinjured myocardium relative to the remote myocardium (Fig. 4.15C and Table 4.7). The changes in ΔSI_{max} were similar to those observed in the acute cryoinjury. However the time constant was shorter and, thus, the rate of enhancement was faster due to better perfusion of the scar tissue as compared with acutely embolized tissue. Chronic 1-week cryoinjury showed similar pattern of Mn distribution kinetics (not shown).

Summary of major findings: 1) Acute cryoinjury (10-150 min): Freezing LV cardiac tissue for 2 min and subsequent thawing (5-10 min) resulted in formation of red-brown round-shaped spot on the epicardium, which appeared as a semicircular zone surrounded by a thin rim of whitish tissue on the short-axis slices. The area showed signs of vascular embolization with erythrocytes resulting in formation of a no/low-reflow region.

Indicators included: (i) an increased Hb content detected by optical point spectroscopy both *in vivo* and post-mortem; (ii) a slow first-pass *in vivo* kinetics of the optical and MR flow tracers (ICG and Gd-DTPA) and a reduced content of optical deposit flow tracer, IR676 in *ex vivo* experiments; (iii) a considerable hypointense core zone on Gd-enhanced MR images surrounded by a thin hyperintense rim; (iv) a hypointense area on Mn-enhanced *ex vivo* MR images; (v) a high content of erythrocytes in H&E-stained samples of injured tissue. 2) Chronic cryoinjury (1 – 4 weeks): Gd-MRI revealed that the no-reflow core zone gradually reduced whereas the hyperintense zone increased upon injury progression over 1 and 2 weeks. After 4 weeks, the hypointense area was completely replaced by a hyperintense one, which was characterized by slower intensity decay upon

Figure 4.15. Changes of the MR signal intensity in a 4-week cryoinjured pig heart after addition of MnCl_2 into the perfusate.



A-C: *Ex vivo* Mn-enhanced MR images and SI kinetics in pig hearts 4 weeks post cryoinjury. A: The baseline short-axis image; B: The image acquired after 20-min exposure to MnCl_2 (0.2mM); solid arrow indicated normal myocardium, dotted arrow indicated chronic cryolesion; C: Time courses of signal intensity enhancement in both normal and injured areas after exposure to MnCl_2 . The lines represent mono-exponential least-square fits (Eq. (2), see text for detail). LV = left ventricle. (Published in *Magn Reson Imaging*. 2010;28:753-66, reprinted with permission on May 10th, 2010 by Elsevier Inc.)

Table 4.7. Kinetic parameters of signal enhancement with *ex vivo* manganese-enhanced MRI within the normal and the cryoinjured myocardium.

Group/area	ΔSI_{\max} , %	t_1 , min	$\Delta SI_{\max}/t_1$, %/min	R^2
1-week (n = 4)				
Control area	114.0 \pm 2.5	7.1 \pm 0.4	16.1	0.99
Cryoinjured area	50*	22.6 \pm 4.7	2.19	0.95
<i>p</i> vs. control area		<.01	<.01	
4-week (n = 5)				
Control area	89.0 \pm 2.7	5.3 \pm 0.4	16.8	0.99
Cryoinjured	17.0 \pm 4.5	4.2 \pm 2.9	4.1	0.78
<i>p</i> vs. control area	<.001	NS	<.05	

Mean \pm SD values are shown for ΔSI_{\max} and t_1 . The parameters were derived from the monoexponential fit mentioned before. ΔSI_{\max} , maximal amplitude of signal increase normalized to the reference water signal amplitude; t_1 , time constant; $\Delta SI_{\max}/t_1$, the initial (maximal) rate of intensity increase. * ΔSI_{\max} value was set at 50 during fitting procedure to minimize χ^2 value.

Gd-DTPA washout relative to the normal myocardium. Total size of the cryoinjured area (hypointense + hyperintense) gradually decreased to approximately 40% of initial level over a 4-week period. Manganese-enhanced MRI showed a hypointense area 1 and 4 weeks post cryoinjury; the latter corresponded to the necrotic region revealed by TTC staining. H&E staining revealed gradual deposition of collagen by the end of the 4-week period. The results within this section has been published²³⁹.

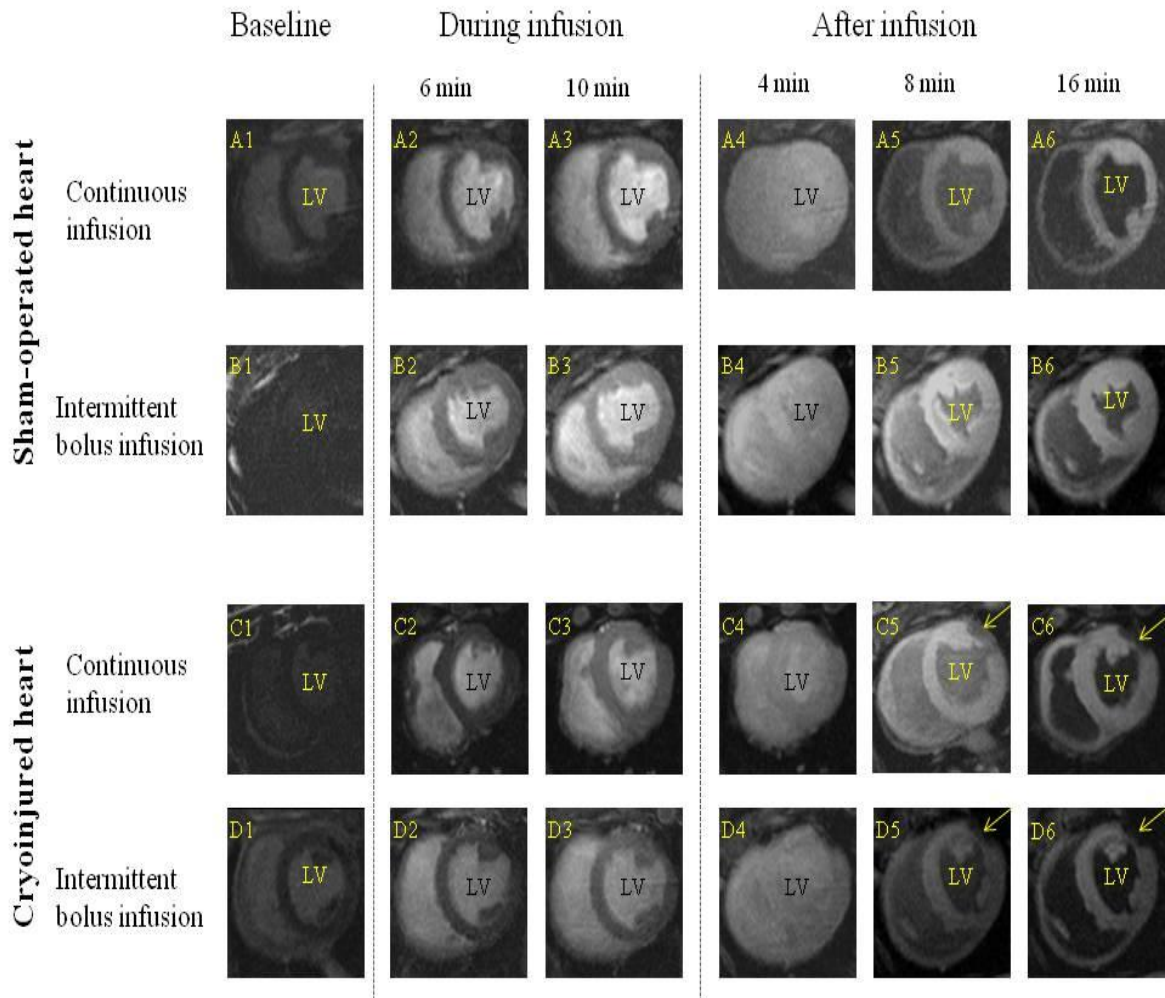
4.4. *In vivo* evaluation of MnCl₂ as a MR contrast agent to characterize myocardial cryoinjury

The aim of the experiments was to test whether MnCl₂ could differentially enhance SI measured by T₁-weighted MRI in *in vivo* chronically cryoinjured pig heart and, if so, what kind of administration was optimal for this purpose. Our hypothesis was that (1) administration of MnCl₂ could provide greater enhancement within the normal myocardium relative to the cryoinjured tissue on T₁-weighted MR images, and (2), in comparison with intermittent bolus injection, continuous slow infusion could minimize the influence on hemodynamics while maintain good contrast between the normal and cryoinjured myocardium on T₁-weighted MR images.

All the pigs survived this study during or after the contrast infusion, though more significant hemodynamic variations were observed in the intermittent group. All pigs with or without cryoinjury had a definite diagnosis based on the final image results.

***In vivo* MEMRI.** In *in vivo* pig heart, intravenous use of MnCl₂ as intermittent slow bolus injection (*i.e.*, 10 $\mu\text{mol kg}^{-1}$ within 10 sec per 2 min \times 7 times) or continuous pump infusion (5 $\mu\text{mol kg}^{-1} \text{ min}^{-1} \times$ 14 min) into the ear vein all led to gradual SI enhancement within the normal myocardium (Fig. 4.16A1-3 and B1-3). Such enhancement in SI can be maintained for a prolonged period, which only reduced by \sim 15% 15 min after infusion cessation (Fig. 4.16A4-6 and B4-6). In comparison, both infusion schemes also led to significant SI enhancement within the chronically cryoinjured myocardium (Fig. 4.16C1-3 and D1-3). The peak of SI enhancement had no visually discernible difference as compared with neighboring normal myocardium, but its duration was very short as it stringently followed SI change within the LV blood pool, which decreased to

Figure 4.16. Representative MR images of short-axis pig heart slices after *in vivo* exposure to intravenously infused $MnCl_2$.



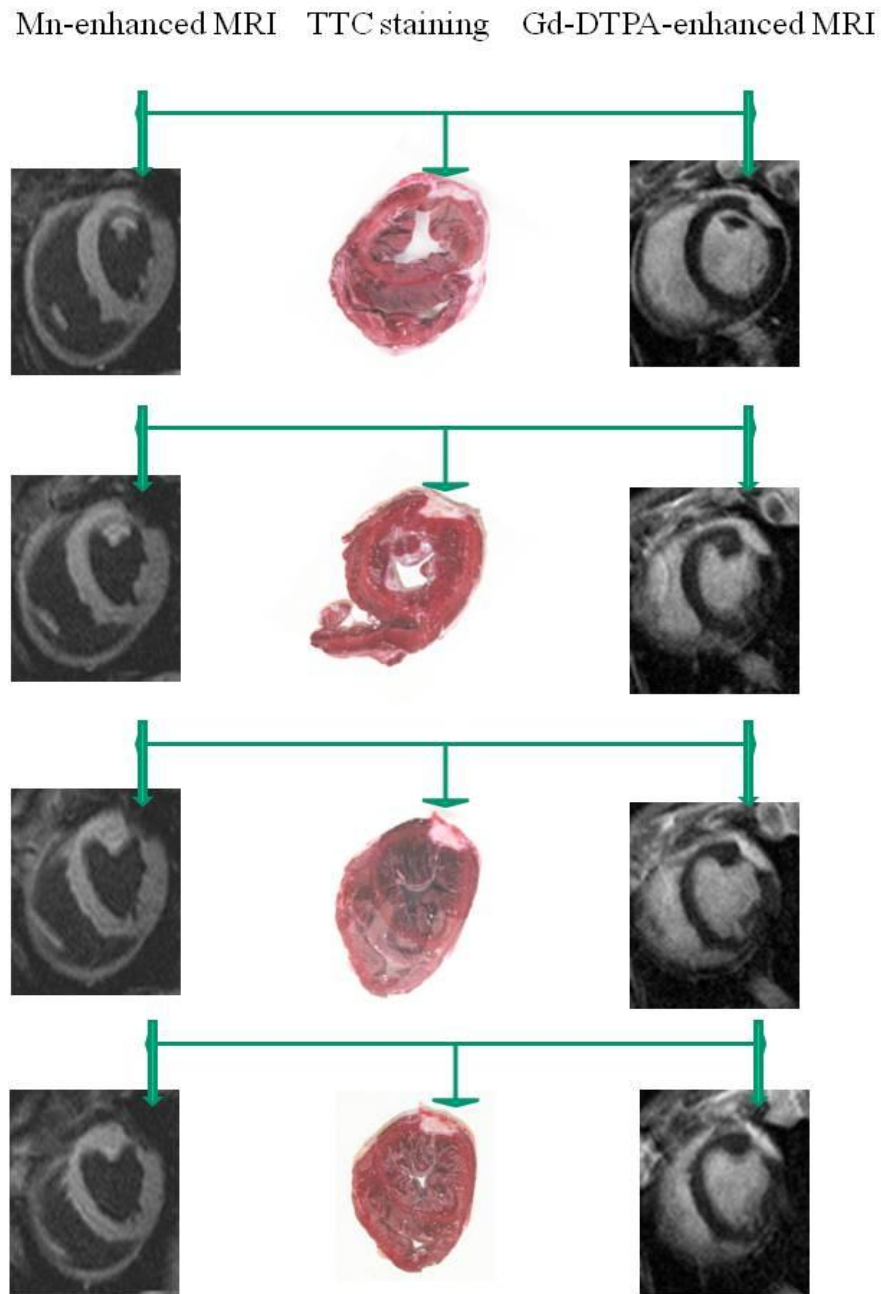
Column 1: baseline image, Column 2: 6 min after the beginning of contrast infusion; Column 3: 10 min after the beginning of contrast infusion; Column 4: 4 min after the completion of contrast infusion (14-min infusion); Column 5: 8 min after infusion completion; Column 6: 16 min after its completion. Row 1(A1-A6): continuous infusion on sham-operated heart; Row 2(B1-B6): intermittent bolus infusion on sham-operated heart; Row 3(C1-C6): continuous infusion on cryoinjured heart; Row 4 (D1-D6): intermittent bolus infusion on cryoinjured heart. Solid arrow is pointed at myocardial cryoinjury. LV = left ventricle.

baseline level within 15 min following infusion termination (Fig. 4.16 C4-6 and D4-6). As a result, beginning from ~ 8 min after completion of contrast infusion, there appeared a significant SI difference between the normal myocardium and the chronically cryoinjured myocardium. The time window for acquisition of such a unique SI difference lasted at least 8 – 10 min, as we finished acquisition 16 – 18 min after completion of the MnCl₂ infusion. The detected MI conformed to the results revealed by both Gd-MRI, which was performed at the 3rd week after cryoinjury, and final TTC-staining findings (Fig. 4.17).

Compared with continuous pump infusion, intermittent bolus infusion resulted in a more significant SI fluctuations during the course of SI enhancement within the LV blood pool, normal myocardium and cryoinjured myocardium (Fig. 4.18). The kinetics of SI decrement after completion of the contrast infusion as a function of time in both LV myocardium and blood was then fitted by the same monoexponential function as for estimation of SI decrement in these anatomic areas of interest after Gd-DTPA infusion (see detail in the previous related sections). The SI decrease within the normal myocardium was very small over the observation period, which resulted in a much lower (~ 15%) rate of SI decrement ($\Delta SI_{max}/t_1$) as compared with it in both the LV blood pool and the cryoinjured myocardium (Fig. 4.18 and Table 4.8).

Hemodynamic changes Infusion of MnCl₂ led to fluctuation of HR (Fig. 4.19), systolic arterial BP (Fig. 4.20) and diastolic arterial BP (Fig. 4.21) in both groups, but the extent was much more substantial in pigs receiving intermittent bolus injection. For pigs in the continuous infusion group, administration of MnCl₂ led to a short duration (~ 2 min) of respective BP decrements, the lowest levels of which were > 90% of their respective

Figure 4.17. Representative Mn- and Gd-enhanced MR images as well as the post-mortem staining pictures of short-axis pig heart slices.



Representative 4-week myocardial cryoinjury revealed by manganese-enhanced MRI (left column). The corresponding post-mortem histology revealed by TTC staining is in the middle column. Its corresponding images revealed by Gd-enhanced MRI acquired at the 3rd week after cryoinjury is on the right column. The arrow heads indicate the cryoinjury in respective short-axis slices from the base (upper) to the apex (lower).

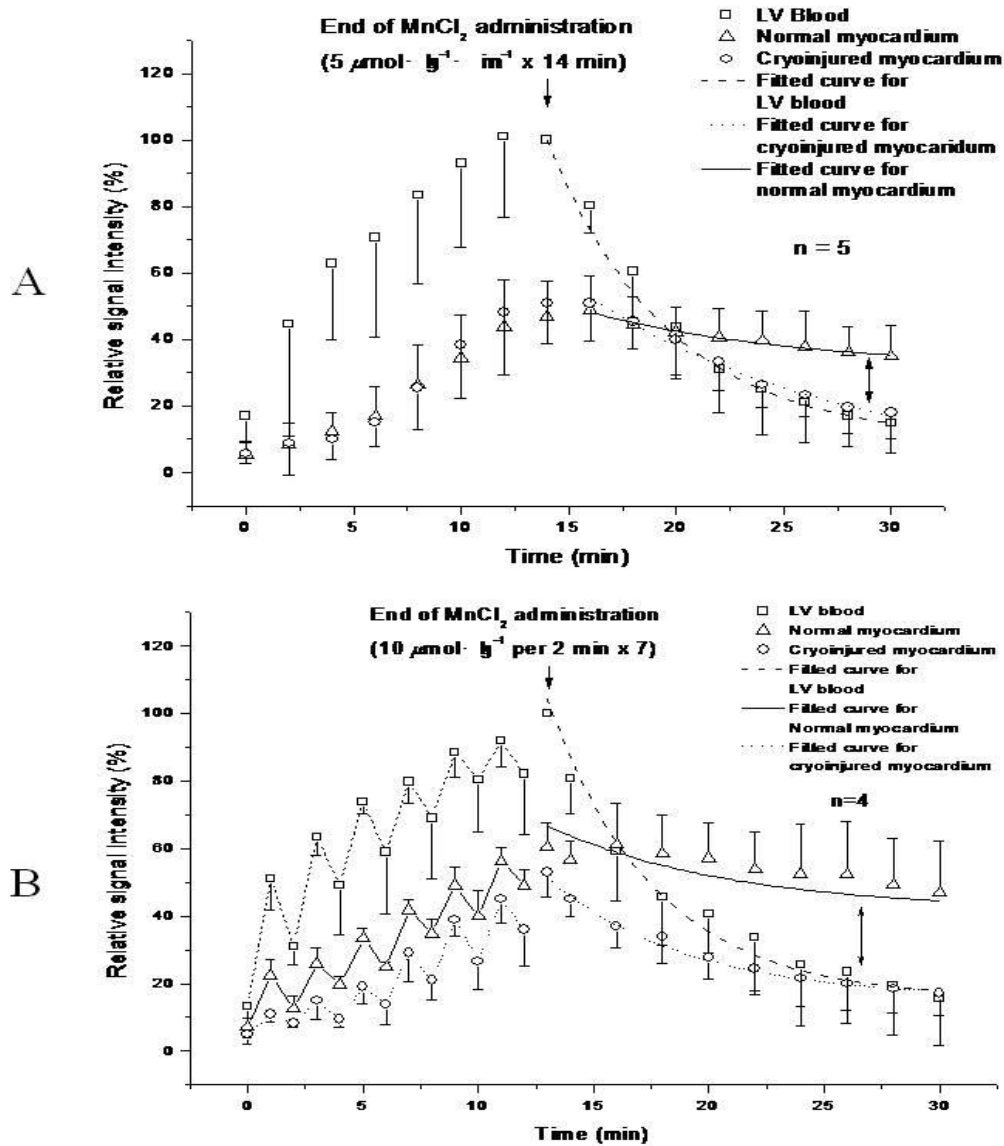
Table 4.8. Kinetic parameters of signal decay with *in vivo* Mn-enhanced MRI in blood, normal and damaged areas of hearts after cryoinjury

Group/area	ΔSI_{max} , %	t_1 , min	$\Delta SI_{max}/t_1$, %/min
Intermittent infusion (n = 4)			
LV blood	86.6 ± 5.6	5.2 ± 0.9	16.5
Cryoinjured myocardium	42.0 ± 4.8	5.7 ± 1.9	7.4
Normal myocardium	15.6 ± 3.2**##	7.2 ± 1.6**##	2.2
Continuous infusion (n = 5)			
LV blood	90.6 ± 7.8	4.9 ± 1.2	18.5
Cryoinjured myocardium	37.8 ± 6.2	5.4 ± 1.2	6.9
Normal myocardium	17.2 ± 2.4**##	8.4 ± 1.8**##	2.0

Mean ± SD values are shown for ΔSI_{max} and t_1 . The parameters were derived from the monoexponential fitting mentioned before. ΔSI_{max} = maximal amplitude of signal decrement normalized to the highest SI in the LV blood; t_1 = time constant; $\Delta SI_{max}/t_1$, the initial (maximal) rate of intensity decrease. **, $p < .01$ vs. LV blood; ##, $p < .01$ vs. cryoinjured myocardium.

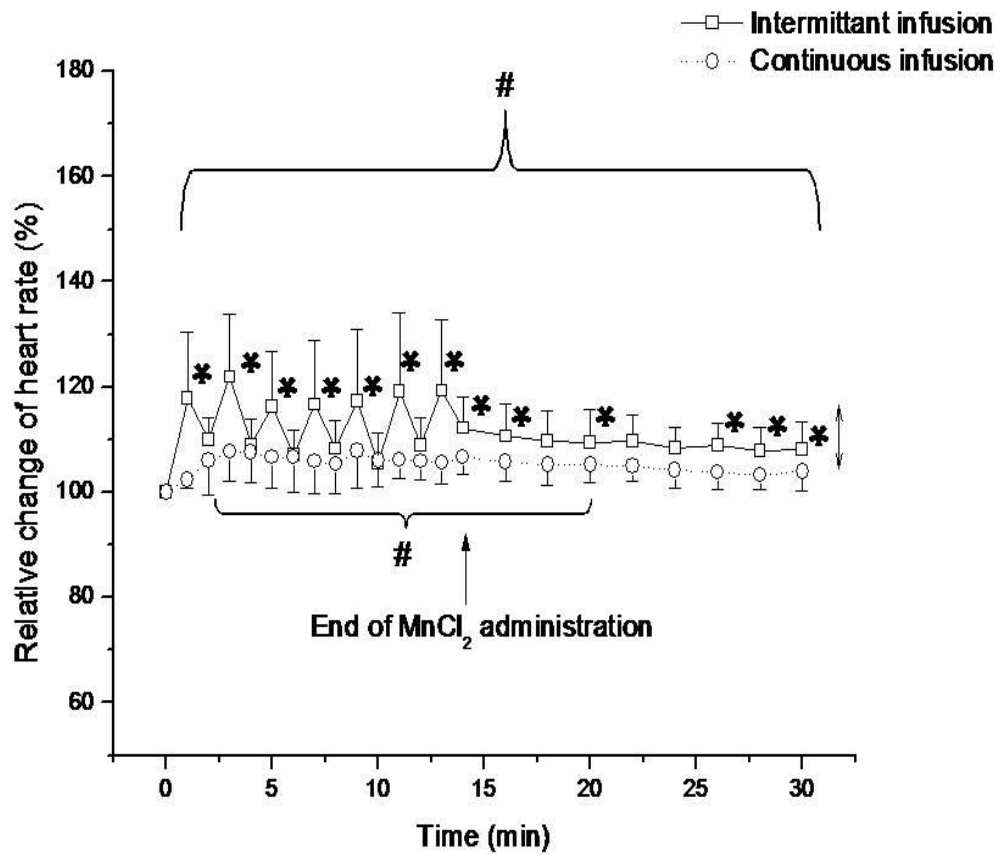
baseline levels. Thereafter, both parameters began to increase gradually with peak < 115% of respective baseline levels. A second decrement followed thereafter, which usually began from 6 – 8 min during infusion. Its rate and extent were much less considerable as compared with them of the first one. After completion of the contrast infusion, systolic and diastolic arterial BP continued to decrease slowly, the lowest level of which remained > 95% of baseline level at the end of experiment (*i.e.*, ~ 16 min after

Figure 4.18. *In vivo* kinetics of MR signal change in the normal and cryoinjured myocardium and left ventricular blood pool after intravenous infusion of MnCl₂.



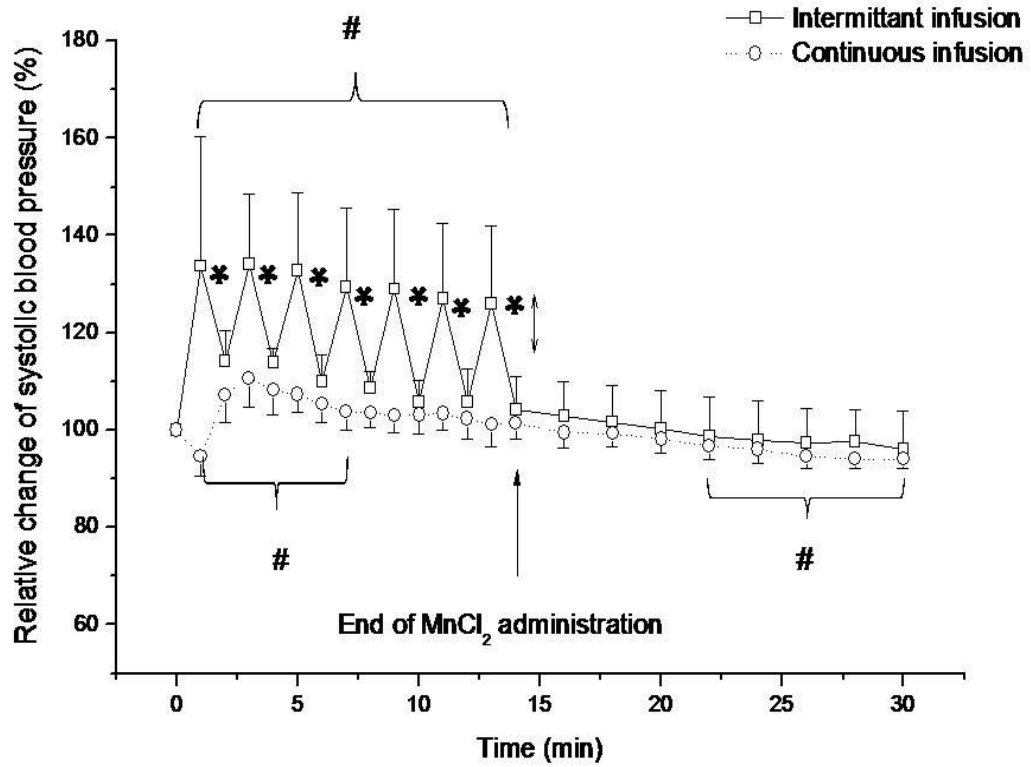
The data include intensity changes during and after continuous (A) or intermittent bolus (B) infusion. Acquired data were normalized to the intensity of the LV blood at the end of MnCl₂ infusion. The ascending time courses of signal intensity during infusion of the contrast agent varied more significantly with intermittent bolus protocol. After completion of MnCl₂ infusion, decreasing time courses of signal intensity in LV blood, normal and cryoinjured myocardium were similar in either protocol.

Figure 4.19. Changes of the heart rate during and after continuous or intermittent bolus intravenous infusion of $MnCl_2$.



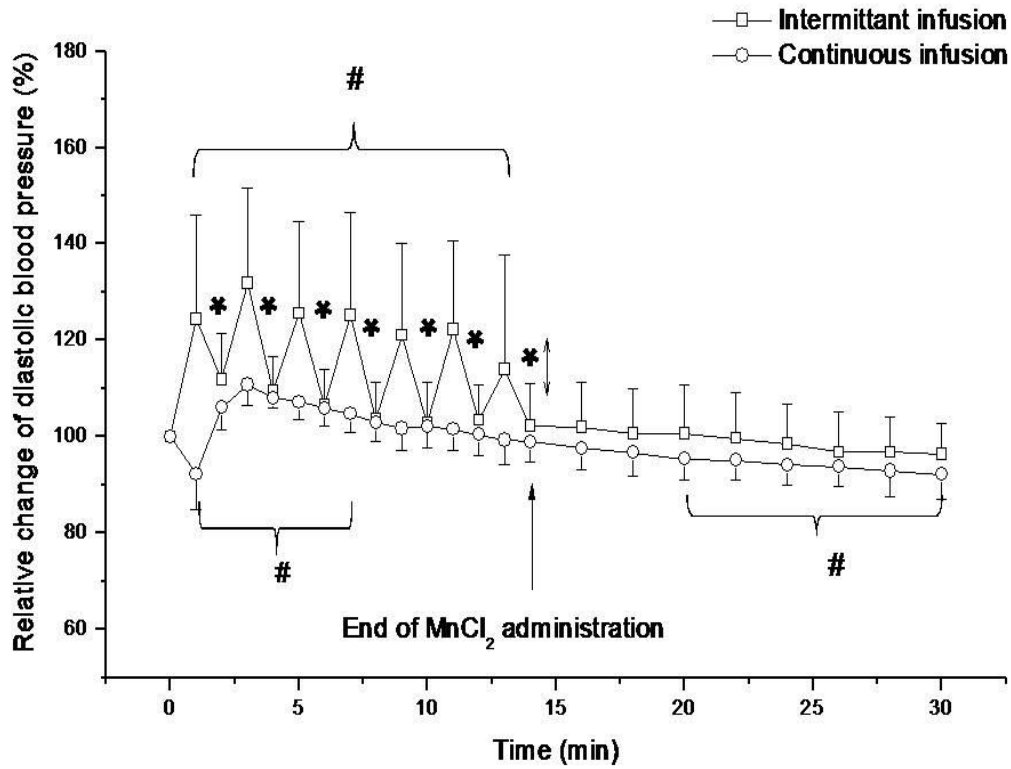
indicates significant change as compared with baseline level in each group; * indicates significant difference as compared with the other group.

Figure 4.20. Changes of the systolic blood pressure during and after continuous or intermittent bolus intravenous infusion of $MnCl_2$.



indicates significant change as compared with baseline level in each group; * indicates significant difference as compared with the other group.

Figure 4.21. Changes of the diastolic blood pressure during and after continuous or intermittent bolus intravenous infusion of $MnCl_2$.



indicates significant change as compared with baseline level in each group; * indicates significant difference as compared with the other group.

completion of infusion). During and shortly after continuous infusion, HR increased slightly as reflected by < 10% increment as compared with baseline level. In comparison, intermittent bolus injection led to more significant fluctuations immediately after each bolus in both BP and HR. The maximal extent was higher than 40% in BP and 30% in HR.

Summary of major findings: *In vivo* intravenous administration of MnCl₂ via either intermittent bolus infusion (10 $\mu\text{mol kg}^{-1}$ within 10 seconds per 2 min \times 7 times) or continuous pump infusion (5 $\mu\text{mol kg}^{-1} \text{ min}^{-1} \times$ 14 min) provided prolonged SI enhancement within the normal myocardium on T₁-weighted MR images after termination of its infusion. However, it decreased very quickly after termination of its infusion within the chronically cryoinjured myocardium, which followed stringently the SI decrement within the LV blood pool. Thus, a significant contrast between the two areas began to appear \sim 8 min after infusion termination. Compared with intermittent bolus infusion, continuous slow infusion minimized fluctuation in HR and BP. This advantage translated to a more stable process for subject care and image acquisition during MRI.

4.5. Design of MR trackable alginate hydrogel

The aim of the experiments was to test whether GdCl₃ and Met-Hb could be used to label alginate hydrogel for MR detection and, if so, how long it could maintain its visually discernible SI on T₁-weighted MR images in the pig pericardial cavity. Our hypothesis was that labeling of alginate hydrogel beads with either GdCl₃ or Met-Hb could enhance its SI on T₁-/T₂-weighted MR images.

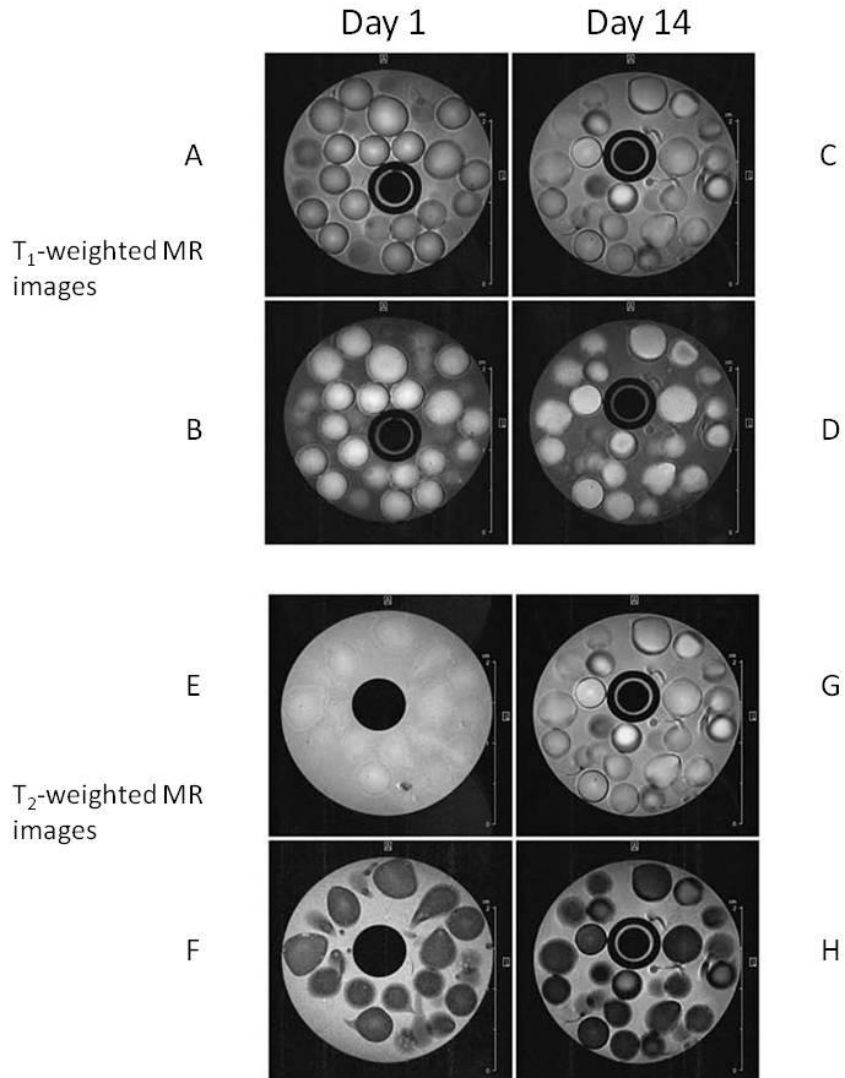
In vivo experiments at 3T with alginate beads without any contrast agents did not allow the beads to be distinguishable from the background due to lack of contrast. As a result, alginate formulations containing contrast agent were tested. Figure 4.21 showed the results of the *in vitro* tests at a 11.7T MRI. At this field strength, the beads containing $GdCl_3$ clearly showed a T_1 -weighting effect that remained present over the 14-day incubation of the beads in buffer (Fig. 4.22 A-D). Similarly, the beads could also be observed in T_2 -weighted images (Fig. 4.22 E-H).

For beads containing Met-Hb, lack of T_1 effect, in the range of $500 \leq TR \leq 1500$ ms, could be observed (Fig. 4.23 A-D). However, Met-Hb-labeled beads could easily be tracked using a T_2 -weighted MR sequence as indicated by Fig. 4.23E-H, using an echo time of 48 ms. This is likely due to a strong susceptibility (T_2^* -like) effect resulting from the restricted mobility of Met-Hb inside the beads.

Lower field (3T) *in vivo* experiments using a pig model confirmed the high-field (11.7T MRI) *in vitro* observation regarding MR visibility of the beads loaded with $GdCl_3$. Figure 4.24 showed that the T_1 -weighted baseline cardiac images, obtained over a 4-week period, clearly displayed the location of the $GdCl_3$ -labeled alginate beads relative to the heart, though their SI gradually decreased. Meanwhile, no detectable toxic effects were observed during this period. On the other hand, alginate beads loaded with Met-Hb could also be tracked on MR image immediately after surgery. However, its SI decreased very fast. No distinguishable contrast between the heart and the beads could be observed one week later.

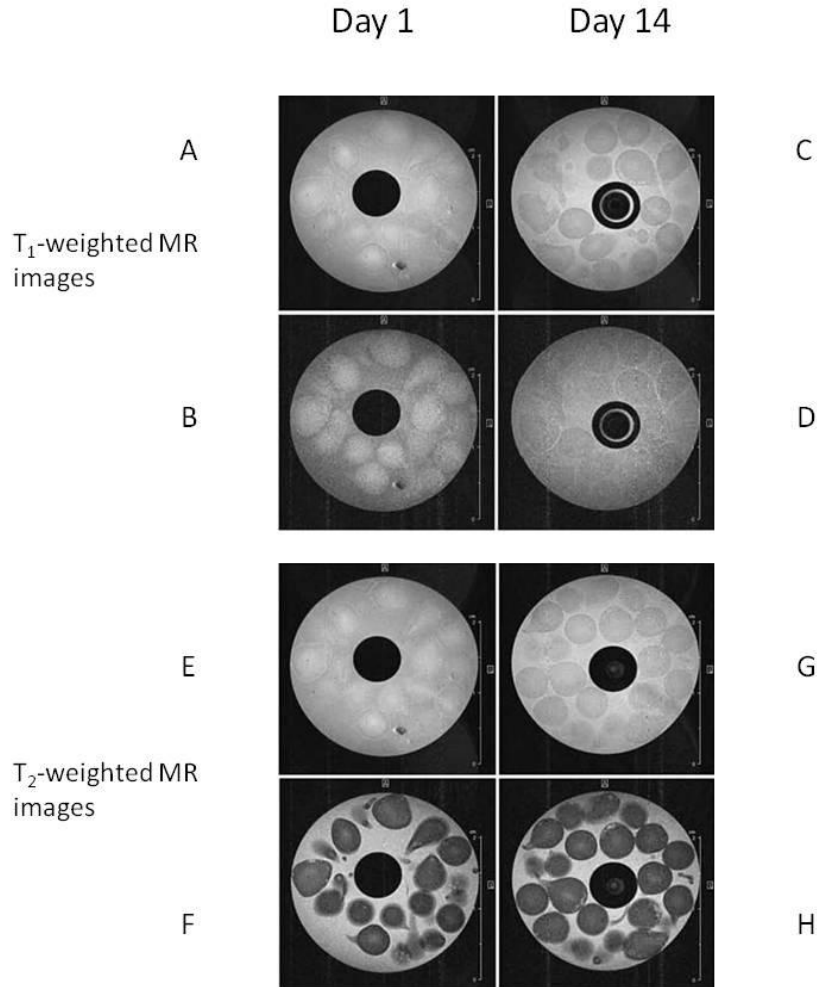
Summary of major findings: Labeling of alginate hydrogel beads with $GdCl_3$ enhanced their *in vitro* SI on T_1 -/ T_2 -weighted MR images over a period of 2 weeks. Whereas, their

Figure 4.22. T₁- and T₂-weighted MR images acquired with a spin-echo sequence for the GdCl₃-labelled alginate hydrogel beads.



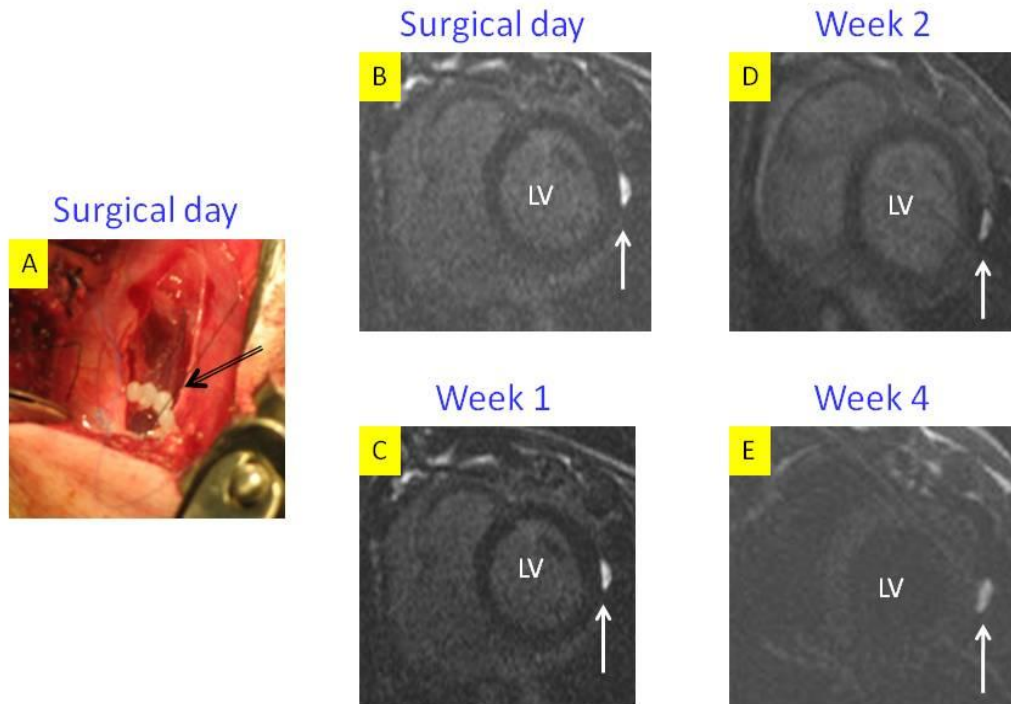
Images (A), (B), (E) and (F) were obtained 1 day after the preparation of the beads, while images (C), (D), (G) and (H) represented images of the beads on Day 14. In T₁-weighted data (A-D), images A & C were acquired with a TR of 1500 ms, while images B & D were acquired with a TR of 500 ms. The T₁-weighting effect was clearly observed for the GdCl₃-labelled beads. In T₂-weighted data (E-H), images E & G were acquired with a TE of 12 ms (TR=1500 ms), while image F & H were acquired with a TE of 48 ms (TR=1500 ms). The beads-to-buffer ratio in the tube was 1:1. The central black spot in each image was GdCl₃ (1mmol L⁻¹) solution as a reference. (Published in *Magn Reson Imaging*. 2009;27:970-5, reprinted with permission on May 10th, 2010 by Elsevier Inc.)

Figure 4.23. T₁- and T₂-weighted MR images acquired with a spin-echo sequence for the methemoglobin-labelled alginate beads.



Images (A), (B), (E) and (F) were obtained 1 day after the preparation of the beads, while images (C), (D), (G) and (H) represented images of the beads on Day 14. In T₁-weighted data (A-D), images A & C were acquired with a TR of 1500 ms, while image B & D were acquired with a TR of 500 ms. The T₁-weighting effect was not obvious for any data set. In T₂-weighted data (E-H), images E & G were acquired with a TE of 12 ms (TR=1500 ms), while images F & H were acquired with a TE of 48 ms (TR=1500 ms). The contrast was obvious for beads imaged with TE of 48 ms. The beads-to-buffer ratio in the tube was 1:1. The central black spot in each image was GdCl₃ (1mmol L⁻¹) solution as a reference. (Published in *Magn Reson Imaging*. 2009;27:970-5, reprinted with permission on May 10th, 2010 by Elsevier Inc.)

Figure 4.24. Anchoring of alginate beads on top of the cryoinjured myocardium and corresponding short-axis MR images.



A: Surgical anchoring of the alginate beads (black arrow) labeled with $GdCl_3$ onto the pig epicardium. B-E: baseline T_1 -weighted MR images (prior to Gd-DTPA injection) of pig heart (short axis) after epicardial anchoring of these beads from the surgical day to 4 weeks later. The white arrow is pointed at the beads. LV = left ventricle.

labeling with Met-Hb could only provide significant *in vitro* SI enhancement in T₂-weighted MR image. In comparison with Met-Hb, GdCl₃ provided a much stronger and longer enhancement in *in vivo* pig pericardial cavity without obvious side effects. The results within this section has been published²⁴⁰.

4.6. Repair of the cryoinjured myocardium with intrapericardially delivered alginate beads containing growth factors or an agarose patch containing ADSCs

The aim of the experiments was to test whether VEGF and bFGF entrapped in alginate hydrogel beds or ADSCs entrapped in an agarose patch could stimulate angiogenesis in the cryoinjured myocardium when they are anchored on top of the cryoinjured myocardium. Our hypothesis was that (1) slow release of proteins could be achieved when they are entrapped in alginate beads; (2) improvement in perfusion within the cryoinjured tissue could be achieved with either alginate beads loaded with VEGF and bFGF or an agarose patch loaded with ADSCs, which served as growth factors generators, anchored on top of the cryoinjured myocardium.

All the pigs survived during the period of 4-week observation. No pigs developed significant life-threatening arrhythmia or congestive heart failure. Alginate beads remained at the original anchoring site inside the pericardial cavity in all the pigs receiving them. In contrast, the agarose patch combined with its nylon buttress disappeared after a 4-week epicardial implantation.

Release profile of proteins from the alginate hydrogel beads Release of growth factors from the alginate beads was simulated using proteins with similar Mw and *pI*. The release profile of Met-Hb from Met-Hb-labeled alginate beads was shown in Fig. 4.25. Release

of Met-Hb was monitored over a period of 30 days. It showed an initial fast releasing phase of ~ 20% in total in the first 3 days. Subsequently, a slow sustained release pattern of Met-Hb was observed throughout the study with up to 35% of Met-Hb released over 4 weeks (see Table 4.9). The data could be fitted to a single exponential function with a release rate of $15 \pm 2\%$ per day (n=3) (Fig. 4.25). The release rate was defined as the plateau value divided by the half-time for the release, both parameters obtained from the fit (Table 4.10).

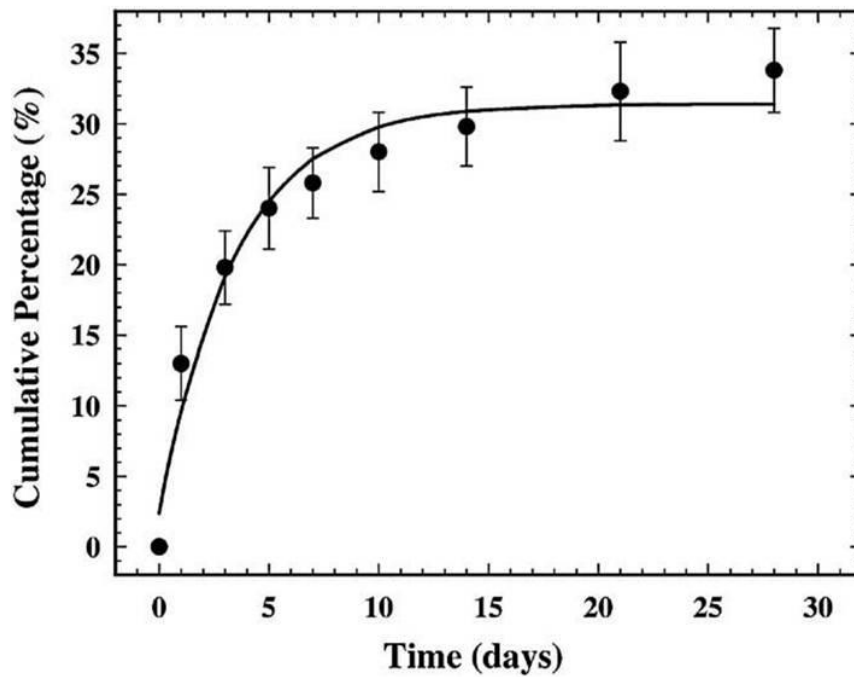
As for Mb-loaded beads, the release rate was $1456 \pm 164\%$ per day for beads gelled by Ca^{2+} only and $1212 \pm 119\%$ per day for beads gelled by Ca^{2+} plus Gd^{3+} , respectively (n=3). Cytochrome C was released from the beads with rates of $882 \pm 64\%$ per day and $652 \pm 60\%$ per day for Ca^{2+} only and $\text{Gd}^{3+} + \text{Ca}^{2+}$ gelled beads, respectively (n=3). Results from all efflux measurements were summarized in Table 4.9.

Table 4.9. Efflux constants of agents embedded in alginate beads

	Met-Hb	Myoglobin (Ca^{2+})	Myoglobin ($\text{Ca}^{2+} + \text{Gd}^{3+}$)	Cytochrome C (Ca^{2+})	Cytochrome C ($\text{Ca}^{2+} + \text{Gd}^{3+}$)
Half-life(d)	2.1 ± 0.3	0.06 ± 0.01	0.08 ± 0.01	0.09 ± 0.01	0.13 ± 0.01
Release rate (%/d)	15 ± 2	1456 ± 164	1212 ± 119	882 ± 64	652 ± 60
Plateau (%)	31 ± 1	90 ± 3	92 ± 3	82 ± 2	84 ± 2

(Ca) and (Ca+Gd) indicated the ions present during the preparation of the beads (see text). Efflux (n=3) was fitted to a mono-exponential function: $C\%(t) = C\%_{\infty} [1 - \exp(-k \cdot t)]$. $C\%$ represents the cumulative percentage, the plateau is given by $C\%_{\infty}$, the half-life by $\ln 2/k$ and the release rate by $C\%_{\infty} \cdot k / \ln 2$. The medium was not refreshed during these measurements (see text).

Figure 4.25. Release of methemoglobin from the alginate beads measured as a cumulative percentage.



The ratio of total bead volume to buffer volume was 1:10. The release rate of Met-Hb in these beads (30 mM CaCl₂) was 15 ± 2% per day. (Published in *Magn Reson Imaging*. 2009;27:970-5, reprinted with permission on May 10th, 2010 by Elsevier Inc.)

In vivo Gd-MRI. After injection of Gd-DTPA for first-pass and late enhancement sessions, contrast development features in both normal and cryoinjured myocardium for pigs receiving either growth factor-loaded alginate beads or ADSCs- loaded agarose patch followed the same pattern as in the previous cryoinjury studies (detailed in the previous section). However, compared with control, angiogenic approach achieved improvement in tissue perfusion as reflected by first-pass kinetics of Gd-DTPA across the cryoinjured myocardium with more significant effects in pigs receiving ADSCs-loaded agarose patch (Table 4.10).

Table 4.10. The effects of intrapericardial treatment of cardiac cryoinjury on the first pass GdDTPA kinetics

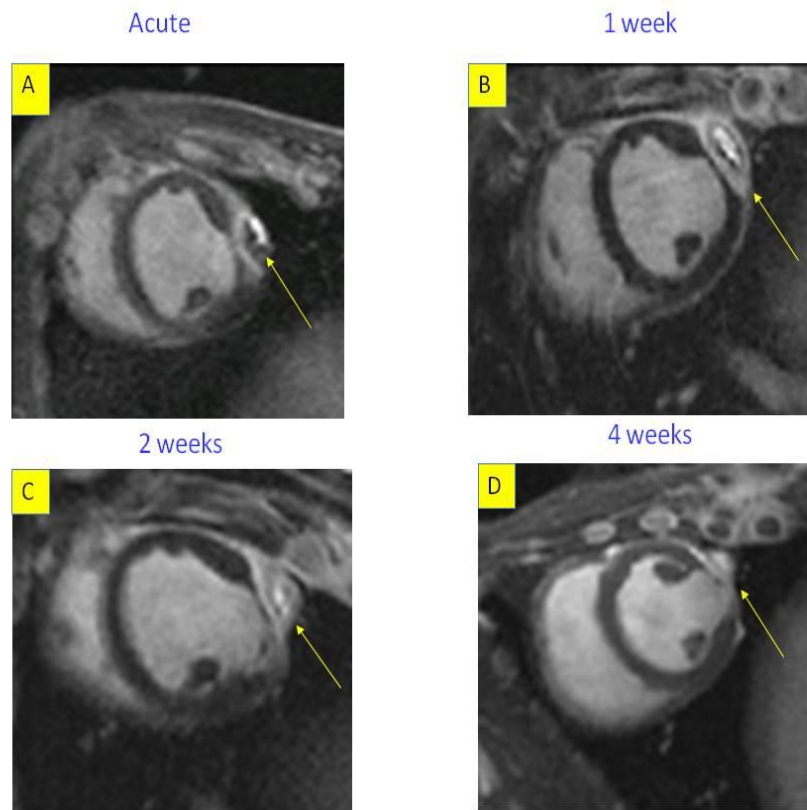
Group (n)	LV tissue		LV blood	
	Initial rate (Infarct/Normal, %)	Tail intensity	Time-to peak (sec)	Peak intensity (a.u.)
Control (5)	54±5.3	77±28	15.3±4.1	211±31
GF-beads (3)	67±4.6	55±39	17.7±5.6	208±59
<i>P vs. control</i>	<i>0.02</i>	<i>NS</i>	<i>NS</i>	<i>NS</i>
ADSC patches (6)	152±89	132±44	12.8±0.42	180±35
<i>P vs. control</i>	<i>0.03</i>	<i>0.04</i>	<i>NS</i>	<i>NS</i>

The initial rates of intensity enhancement were calculated using least-square fit of linear part of kinetic curves. Tail intensities were calculated from the last 3 data points of kinetic curves and normalized to LV blood intensity. This parameter reflects percentage of LV wall tissue accessible to GdDTPA over 35-60 s period: normal LV, 37±14%; control infarct, 31±15%; GF-treated infarct, 27±18%. These values are not significantly different from normal LV. Time-to-peak and peak intensity were obtained from enhancement course for the LV blood.

In pigs receiving alginate beads containing VEGF+bFGF, one unique finding was that there formed a layer of new tissue, with feature of late enhancement as neighboring healing infarct, encapsulating the implanted alginate beads containing growth factors in 5 out of 6 pigs (Fig. 4.26). Such newly grown tissue was not observed in pigs receiving the control beads. Specifically, in one pig subjected to 2-week cryoinjury and receiving growth factor-loaded alginate beads, there appeared an early enhancement (2-min exposure to Gd-DTPA) within the cryoinjured myocardium, which continued till the end of 30-min image acquisition. However, this pattern of SI enhancement was not observed 2 weeks later in the same pig. Instead, a hypointense subepicardial area (hypointense island) appeared at the earliest acquired image, the size of which gradually shrank thereafter (Fig. 4.27). Such pattern of SI enhancement was not observed for cryoinjured pig hearts receiving control beads or growth factor-loaded beads attached to the pericardium. In pigs receiving agarose patch incorporating ADSCs, only 1 out of 4 pigs had a thin layer of newly grown tissue in place of the implanted patch (Fig. 4.28A) ($p < 0.05$). There was no detectable new layer of tissue within the cryoinjured myocardium in pigs receiving alginate or agarose patch without therapeutic agents.

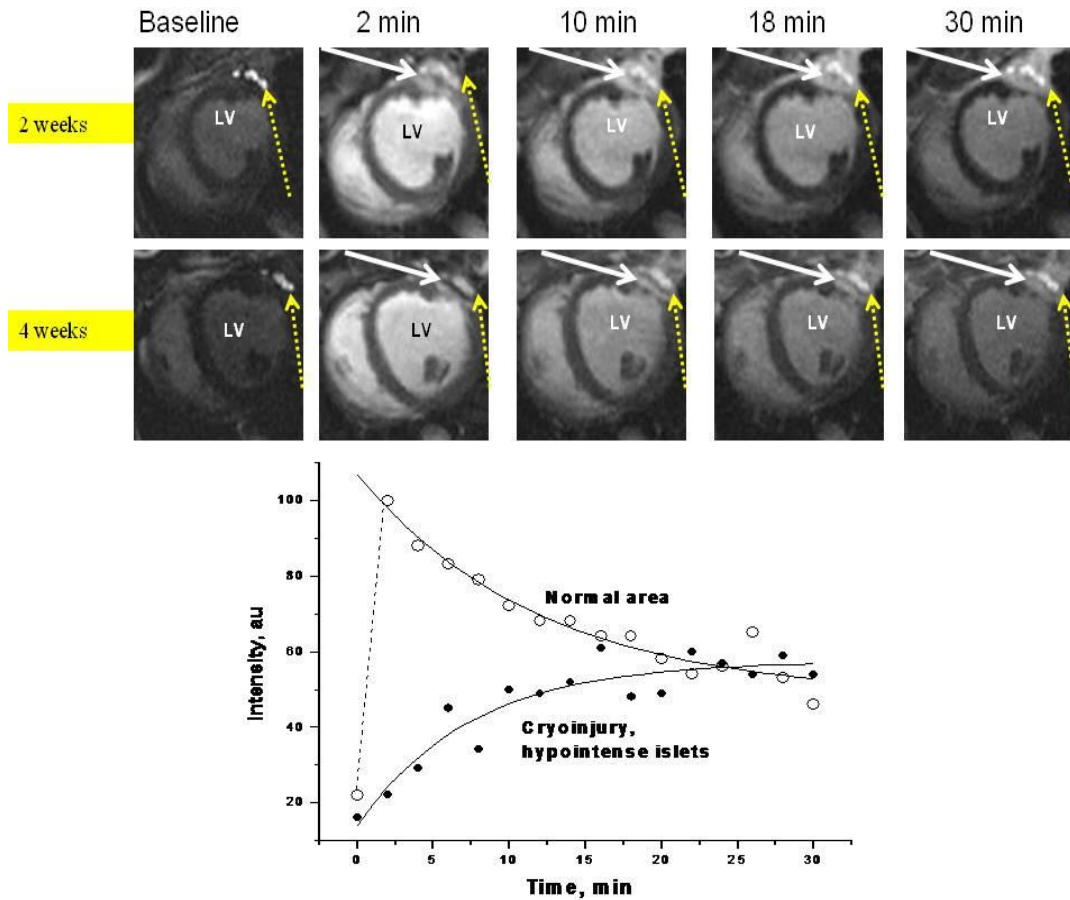
In vivo MEMRI Contrast development pattern within the normal and cryoinjured myocardium for pigs among these groups was similar to the previous study (detailed in the previous sections). Within the infarction area, wash-in and wash-out of $MnCl_2$ didn't show prolonged SI enhancement within the cryoinjured myocardium in pigs receiving either therapeutic agents or within the new tissue in pigs receiving alginate beads incorporating growth factors (Fig. 4.29). There was no prolonged SI enhancement within

Figure 4.26. Serial short-axis MR images of a cryoinjured pig heart receiving growth factors-loaded alginate beads.



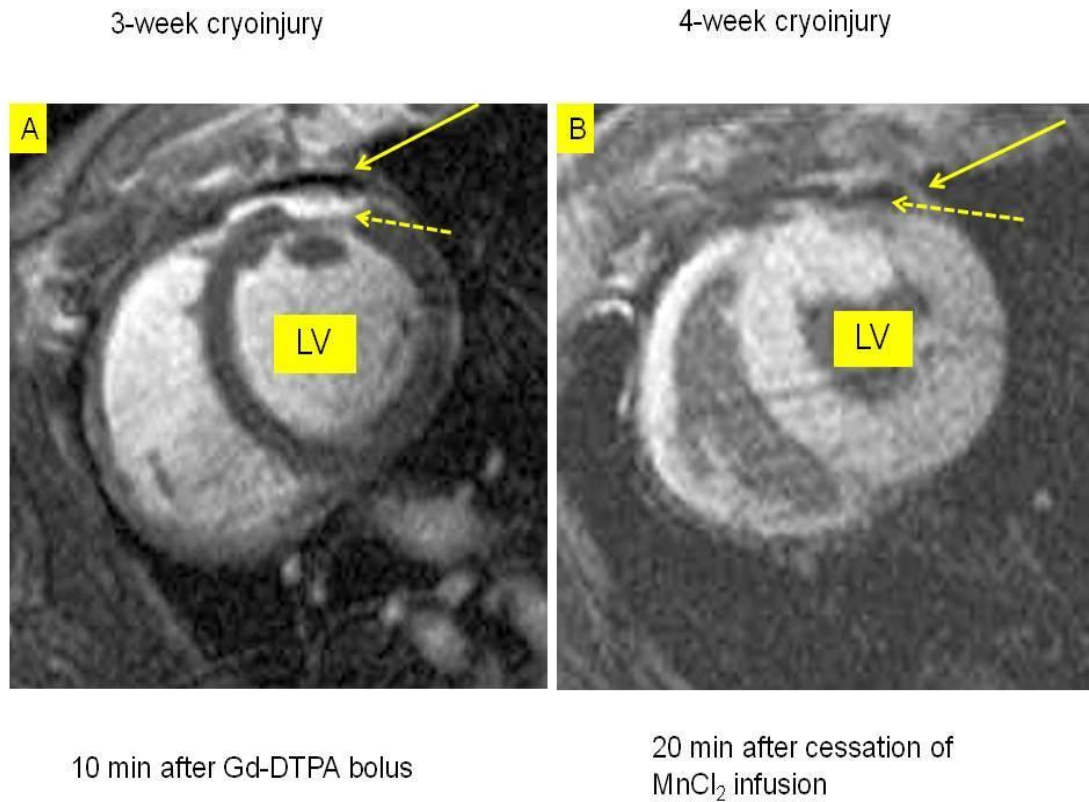
Alginate beads loaded with VEGF and bFGF were anchored onto the top of cryoinjured epicardium with suture. The solid arrow pointed at the implanted beads, labeled with $GdCl_3$, on top of the cryoinjury-induced infarct. A new layer of tissue wrapping the implant beads could be detected 7 days after cryoinjury.

Figure 4.27. Change of MR signal intensity within the chronically cryoinjured myocardium receiving growth factors-loaded alginate beads after administration of Gd-DTPA.



The first row include images acquired after 2-week exposure to the beads, which indicates early SI enhancement within the subepicardium (solid arrow). The second row included images acquired after 4-week exposure from the same pig, which indicates loss of early SI enhancement within the same area. The dashed arrow is pointed towards the Gd³⁺-labeled alginate beads, which were anchored on top of the cryoinjured myocardium. The kinetics of SI enhancement within that hypointense area is shown in the bottom figure. LV = left ventricle, SI = signal intensity.

Figure 4.28. Short-axis contrast-enhanced MR images of a chronically cryoinjured pig heart receiving an agarose patch containing ADSCs.

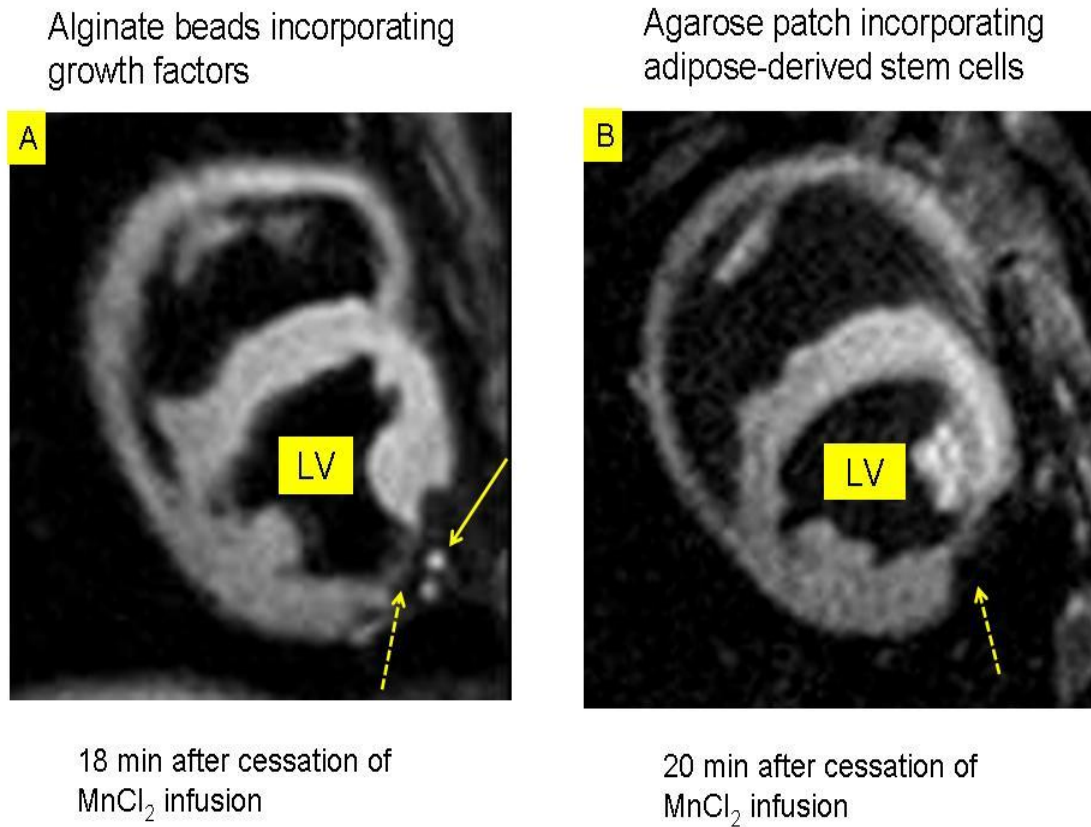


A layer of new tissue could be observed on top of the infarction as shown by both Gd-enhanced (A) and Mn-enhanced (B) MRI. The solid arrow is pointed at the new tissue. The dashed arrow was pointed at the cryoinjury. LV = left ventricle.

the cryoinjured myocardium in pigs receiving alginate or agarose patch without therapeutic agents.

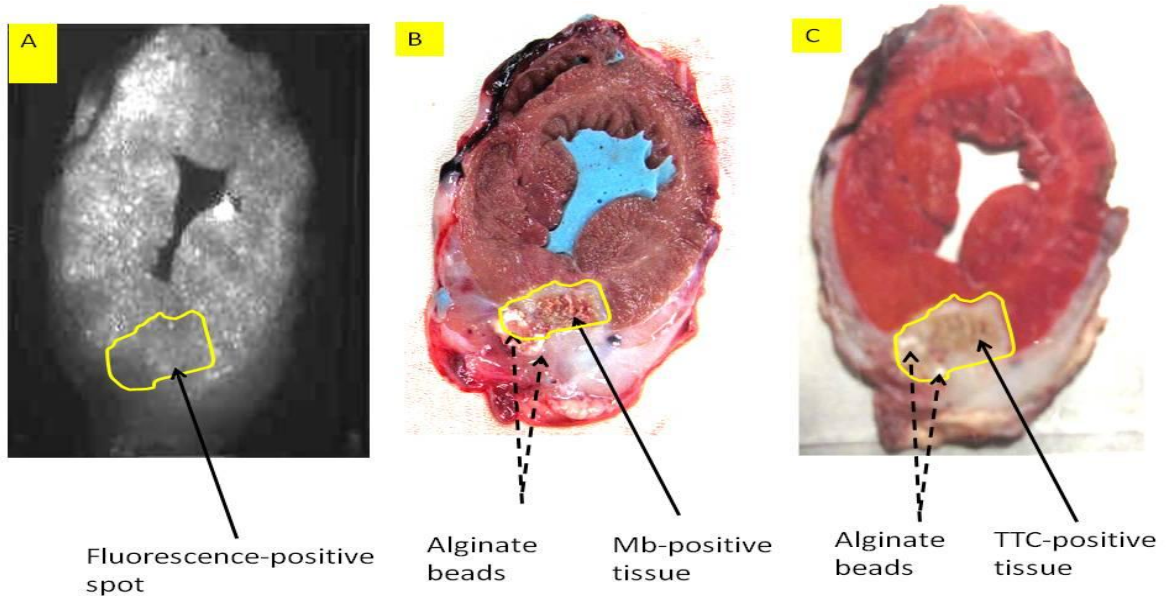
Fluorescence imaging study. Within the cryoinjured scar tissue in pig hearts receiving growth factor-loaded alginate beads, there appeared some spots with relatively higher NIR fluorescence than that in the immediate necrotic tissue surrounding beads (Fig. 4.30A), implying better perfusion via a better developed capillary network. This heterogeneity in fluorescence was not observed in the experiments with control beads, in which the necrotic area showed little microspheres' fluorescence. To take into account non-uniform distribution of fluorescence in the infarcted area, it was divided into two sub-regions, *i.e.*, subepicardial and mid-mural, and average intensities were normalized to that of normal areas. Relative intensities for mid-mural and subepicardial regions of growth factor-treated hearts were 0.64 ± 0.14 and 0.31 ± 0.14 ($p < 0.0001$) and for controls 0.37 ± 0.09 ($p < 0.05$ vs. mid-mural). However, short-axis slices revealed significantly increased fluorescence within the cryoinjured myocardium receiving agarose patches incorporating ADSCs (Fig. 4.31., Table 4.10), though the extent of the fluorescence increment as compared with neighboring normal myocardium was different among different pigs and its distribution was not uniform across the cryoinjured area. There existed limited fluorescence within the cryoinjured myocardium in pigs receiving alginate or agarose patch without the therapeutic agents.

Figure 4.29. Short-axis Mn-enhanced MR images of chronically cryoinjured pig hearts receiving growth factors-loaded alginate beads or an ADSCs-loaded agarose patch.



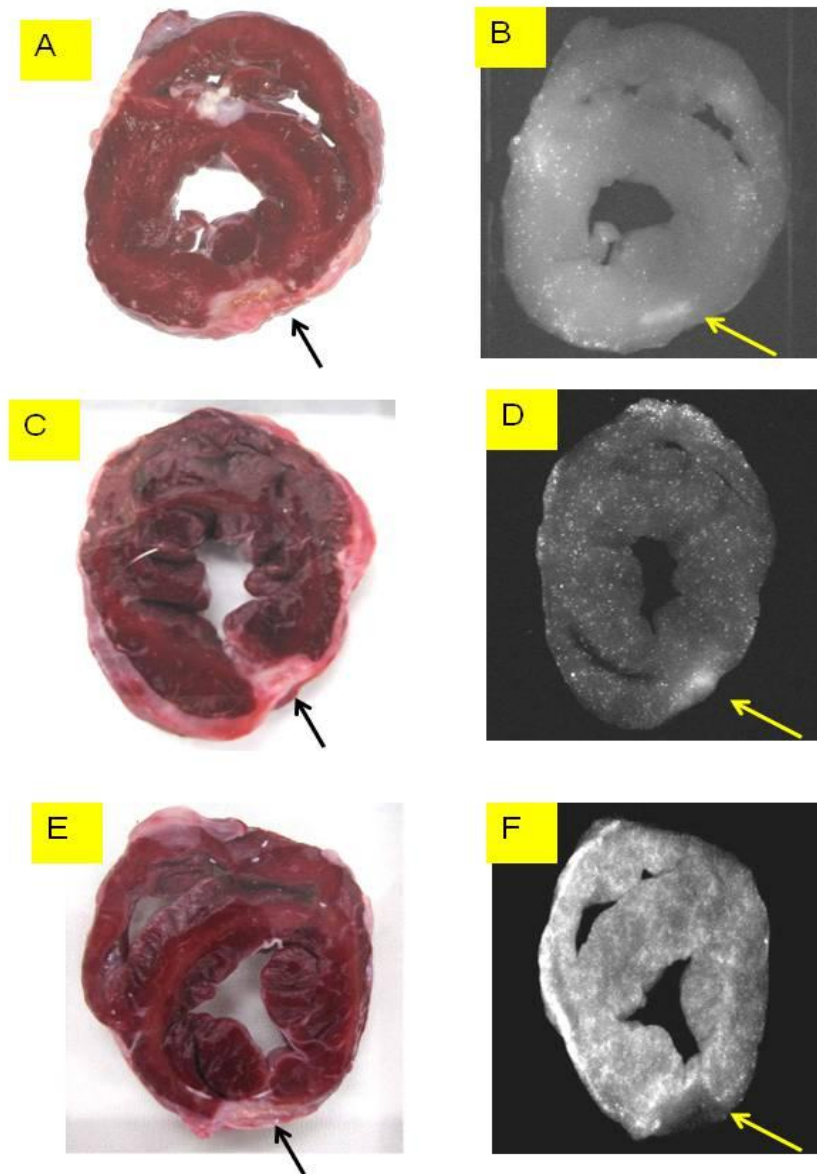
There was no prolonged enhancement in signal intensity within the cryoinjured area (dash arrow) in both images. The solid arrow was pointed towards the alginate beads labeled with $GdCl_3$. LV = left ventricle.

Figure 4.30. A short-axis fluorescence image of a chronically cryoinjured pig heart receiving growth factors-loaded alginate beads after administration of fluorescent microspheres (A) and corresponding post-mortem pictures (B,C).



A: A short-axis fluorescence image of a cryoinjured pig heart receiving growth factor-loaded alginate beads. There appeared heterogeneous fluorescent spots within the cryoinjured myocardium (encircled). B: the original heart slice. There existed Mb+Hb absorption, detected by point spectroscopy, within the cryoinjured myocardium (solid arrow). C: the same slice after TTC-staining. There appeared TTC-positive spots within the cryoinjured myocardium (solid arrow).

Figure 4.31. Short-axis fluorescence images of a chronically cryoinjured pig heart receiving an ADSCs-loaded (A-D) or empty (E,F) agarose patch and corresponding post-mortem pictures.



The left column is post-mortem short-axis slices stained with TTC. The right column is their corresponding fluorescence images after *in vivo* injection of 15- μ m fluorescent microspheres into the coronary circulation through the apex. A-D: a pig heart receiving an ADSCs-loaded agarose patch. E&F: a pig heart receiving an ADSCs-free agarose patch.

Table 4.11. Fluorescence within the short-axis cryoinjured myocardium in pigs receiving agarose patches with or without adipose-derived stem cells

	ADSCs	Control group
Fluorescence (cryoinjured/Normal myocardium) (n = 10)	1.44 ±0.59	0.58 ±0.13
<i>p</i>	0.0002	

Mean ±SD values were shown for fluorescence in the cryoinjured myocardium normalized to the neighboring normal myocardium. ADSCs = adipose-derived stem cells.

Post-mortem analyses

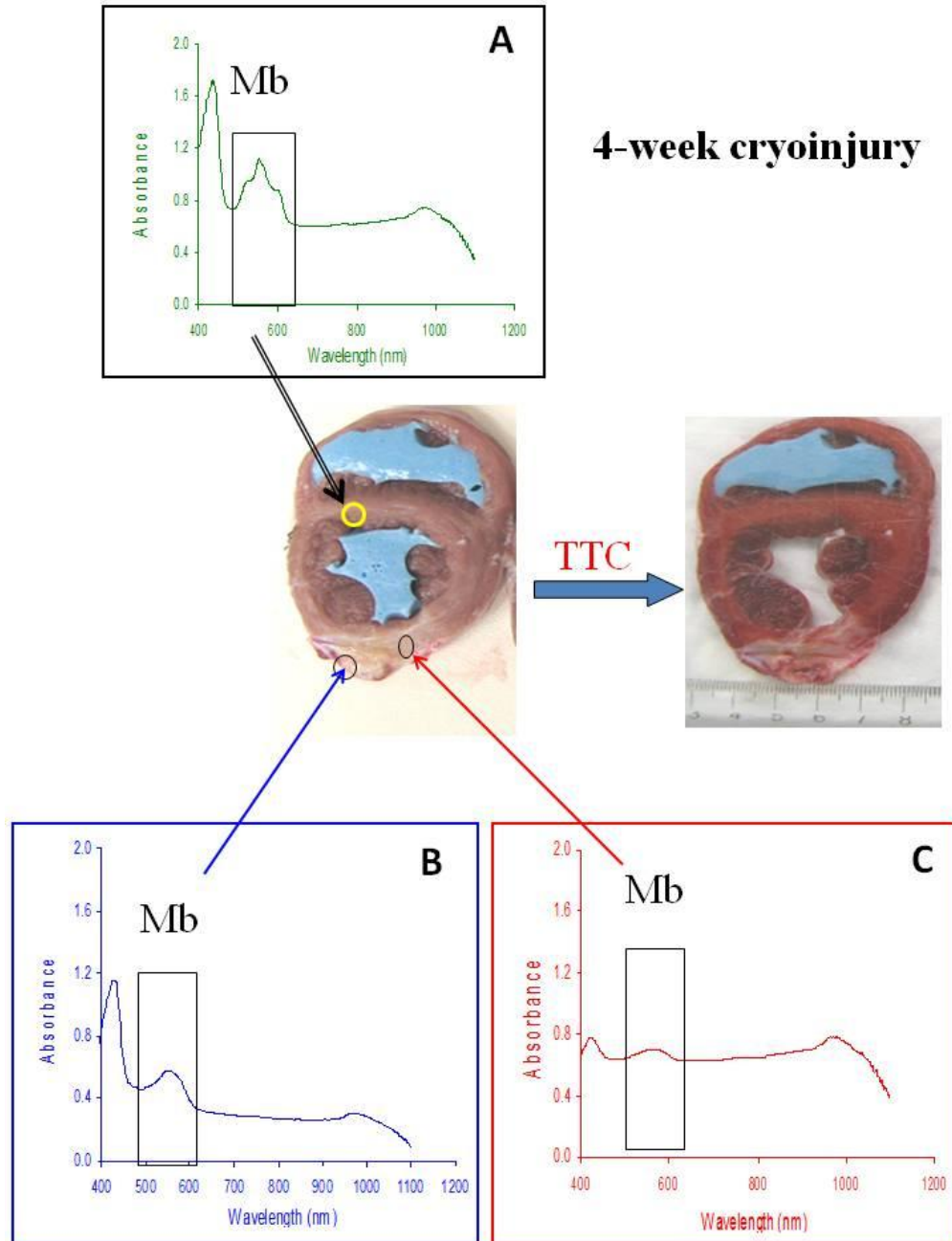
In pigs receiving VEGF/bFGF-loaded beads, the short-axis slices with enhanced fluorescence also showed heterogeneous injured areas where the white scar tissue coexisted with a considerable portion of TTC positive material (Fig. 4.30C). Furthermore, epicardial growth of the connective tissue was clearly visible in all the hearts. Optical point spectroscopy detected visible and NIR absorption bands (Fig. 4.32) characteristic of Hb/Mb in the TTC-positive tissue while in the necrotic scar areas these bands were weak. There lacked significant Hb/Mb absorption detectable with point spectroscopy in the cryoinjured myocardium for pigs receiving the ADSCs-loaded agarose patches. In addition, there were no TTC-positive spots within the scar.

H&E staining revealed that the capillary density in the infarct area was highest in pigs treated with the agarose patches containing ADSCs, followed by the alginate beads containing VEGF/bFGF and controls ($36 \pm 17.5/\text{mm}^2$ vs. $26 \pm 11.5/\text{mm}^2$ vs. $10.5 \pm 7/\text{mm}^2$ in the control pig hearts, $p < 0.01$). However, satisfactory growth of the mature arterioles was absent within the cryoinjured myocardium receiving growth factors. Furthermore,

erythrocytes retained within the cryoinjured tissue close to the alginate beads were observed. In addition, there still existed massive invasion of inflammatory cells within the infarction sites in both therapeutic groups even after 4 weeks of cryoinjury, while fibroblasts and deposited collagen were the main components in pig hearts receiving the control alginate beads or agarose patches (Fig. 4.33).

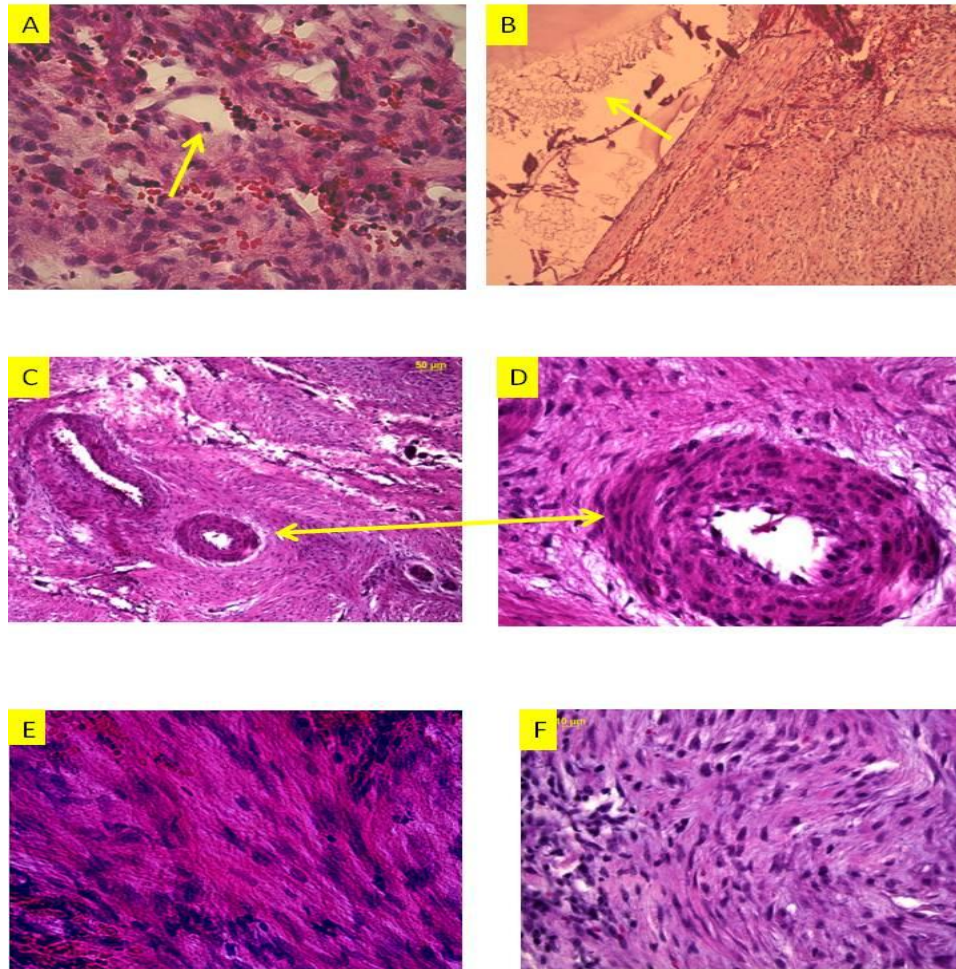
Summary of major findings: Slow release of proteins, as evidenced by the test on heme-proteins simulating VEGF and bFGF release, could possibly be achieved when they were entrapped in alginate beads. Improvement in tissue perfusion, as evidenced by the increased fluorescence after *in vivo* perfusion with the fluorescent microspheres, within the cryoinjured tissue could be observed in pig hearts receiving either the growth factors-loaded alginate beads or, much more significantly, the ADSCs-loaded agarose patches. Microscopic studies revealed that angiogenesis occurred in the cryoinjured tissue receiving either growth factors or ADSCs. However, there lacked formation of mature arterioles in pigs receiving only growth factors. In addition, there appeared erythrocytes within its cryoinjured tissue.

Figure 4.32. Spectroscopic features of A short-axis slice of a chronically cryoinjured pig heart receiving growth factors-loaded alginate beads (central).



Its respective visible/NIR spectrum in normal tissue (A), TTC-positive cryoinjured myocardium (B) and TTC-negative cryoinjured myocardium (C) were included. The right picture was the final TTC staining result.

Figure 4.33. Hematoxylin & eosin staining of chronically cryoinjured pig hearts receiving growth factors-loaded alginate beads or an ADSCs-loaded agarose patch.



A: A pig heart receiving alginate beads containing both VEGF and bFGF. The tissue was still full of inflammatory cells and had high capillary density (solid arrow). Erythrocytes also appeared within the tissue (bright red) (400x). B: The same slide imaged with lower amplification (50 x) to indicate that the extent of entrapped erythrocytes was more significant when the tissue was close to the alginate beads (arrow). C: The cryoinjured area of a pig heart receiving an agarose patch incorporating ADSCs. There appeared higher density of capillary vessels and mature arterioles (arrow) (100x). D: The same slide with higher amplification to indicate the growth of mature arterioles (~ 50 μm in internal diameter) (400x). E: The cryoinjured myocardium receiving alginate beads without VEGF or bFGF. F: The cryoinjured myocardium receiving a cell-free agarose patch. Both tissue slides indicated that the tissue had progressed to the stage of scar formation characterized by fibroblast accumulation and collagen deposition (400x).

5. DISCUSSION

5.1. Summary of major findings

5.1.1 *Ex vivo* MEMRI in analysis of acute cardiac ischemia and chronic myocardial infarction

(1) Acute cardiac ischemia: For pig hearts subjected to *in vivo* 30-min ischemia, addition of MnCl_2 into the perfusate at 0.2 mM could significantly enhanced the SI within the normal myocardium in T_1 -weighted MRI within a 7T magnet. In contrast, it remained unchanged within the ischemic area. Such a difference led to a visually discernible contrast between the two areas within 10-min exposure to the contrast agent. The area of risk revealed by MEMRI correlated to the morphological results revealed by Evans blue perfusion staining.

(2) Acute cardiac ischemia with reperfusion: the same pattern of SI enhancement was observed within the normal myocardium for the *ex vivo* perfused pig hearts after exposure to MnCl_2 . However, the SI change within the reperfused myocardium subjected to *in vivo* 75-min ischemia followed by 45-min reperfusion was very limited in some pigs and, thus, there appeared an obvious contrast between the two areas within 10-min exposure to the contrast agent. Post-mortem examination of the short-axis slices ~ 4 hours later revealed impaired perfusion within the reperfused tissue as evidenced by reduced IR676 deposition and necrosis of the jeopardized myocardium as evidenced by the presence of the oxy-Mb and the absence of TTC staining within this area.

(3) Chronic MI: in the *ex vivo* perfused pig hearts subjected 3-, 7-, 14-, 21- or 28-day MI, addition of MnCl_2 (0.2 mM) led to SI enhancement within the normal myocardium, the kinetics of which was similar to those derived from the other two acute studies. However,

20-min exposure to MnCl_2 also led to significant SI enhancement within the infarcted myocardium, though its rate was relatively slow and the extent was lower than that within the neighboring normal area. The difference in SI between the two areas became more obvious when Mn-free perfusate was later reinstated to wash out the contrast agent residing within the interstitial space. The location and size of the infarcted myocardium were in good accordance with the results revealed by post-mortem TTC staining findings. Perfusion staining with intracellular type of perfusion tracer, IR676, revealed its reduced deposition within the infarcted area.

(4) Acute hemodynamic and metabolic changes: it was found in all the *ex vivo* studies that 20-min exposure to 0.2-mM MnCl_2 led to reduced contractile function and coronary artery resistance as evidenced by reduced LVDP and PP. However, MnCl_2 had no significant influence on sino-atrial automaticity and didn't lead to arrhythmias such as premature atrial or ventricular contraction. In addition, myocardial short-term exposure to MnCl_2 did not affect gas exchange, electrolytes and acid-base homeostasis, as well as energy metabolism (O_2 consumption).

5.1.2. Myocardial infarction induced by cryoinjury

(1) Acute cryoinjury (10-150 min): Freezing LV cardiac tissue for 2 min and subsequent thawing (5-10 min) resulted in formation of red-brown round-shaped spot on the epicardium, which appeared as a semicircular zone surrounded by a thin rim of whitish tissue on the short-axis slices. The area showed signs of vascular embolization with entrapped erythrocytes forming a no/low-reflow region. Indicators were: (i) an increased Hb content detected by optical point spectroscopy both *in vivo* and post-mortem; (ii) slow first-pass *in vivo* kinetics of the optical and MR flow tracers (ICG and Gd-DTPA) and a

reduced content of optical deposit flow tracer, IR676, in *ex vivo* experiments; (iii) a considerable hypointense core zone on Gd-MR images surrounded by a thin hyperintense rim; (iv) a hypointense area on Mn-enhanced *ex vivo images*; (v) a high erythrocytes content in H&E stained samples of injured tissue.

(2) Chronic cryoinjury (1 – 4 weeks): Gd-MRI revealed that the no-reflow core zone gradually reduced whereas the hyperintense zone increased upon injury progression over 1 and 2 weeks. Four weeks later, the hypointense area was completely replaced by a hyperintense one, which was characterized by slower intensity decay upon Gd-DTPA washout relative to the normal myocardium. Total size of the injured area (*i.e.*, hypointense + hyperintense zone) gradually decreased to ~ 40% of the initial volume over a 4-week period. *Ex vivo* MEMRI showed a hypointense area 1 and 4 weeks post cryoinjury; the latter corresponded to a necrotic region determined by lack of TTC staining. Microscopic examination revealed gradual replacement of the cellular material with collagen by the end of a 4-week observation period.

5.1.3. *In vivo* MEMRI for characterization of chronic cryoinjury-induced MI

In vivo administration of MnCl₂ via either intermittent bolus infusion (10 $\mu\text{mol kg}^{-1}$ within 8-10 sec per 2 min \times 7 times) or continuous pump infusion (5 $\mu\text{mol kg}^{-1} \text{ min}^{-1} \times$ 14 min) enhanced the SI in the LV blood pool, which was followed by gradual enhancement of the SI within the normal myocardium and the 4-week cryoinjured myocardium. Enhancement of the SI in both the LV blood pool and the cryoinjured myocardium oscillated more significantly when intermittent scheme was applied. At the end of infusion, the SI peaked within the LV blood pool followed by similar change within both the normal and the cryoinjured myocardium, which was not visually

discernible. Immediately after termination of contrast agent infusion, the SI began to quickly decrease within both the LV blood pool and the cryoinjured myocardium, whereas its reduction was much slower within the normal myocardium. Consequently, beginning from ~ 8 min after termination of the contrast infusion, there appeared a late time window when cryoinjured myocardium could be easily distinguished from neighboring normal myocardium. In addition, compared with intermittent bolus infusion, continuous pump infusion minimized fluctuation in HR and arterial BP. Consequently, it provided a more stable course beneficial for image acquisition and subject care.

5.1.4. Design of MR trackable alginate hydrogel beads

It was feasible to label alginate hydrogel beads with both $GdCl_3$ and Met-Hb. Gd-labeled beads could be detected *in vitro* over an observation period of 2 weeks with T_1 - and T_2 -weighted MRI and *in vivo* over a 4-week observation period with T_1 -weighted MRI.

Whereas, beads labeled with Met-Hb could only provide significant *in vitro* SI enhancement with T_2 -weighted MRI over a 2-week observation period. Implantation of alginate beads labeled with either tracer didn't incur significant complications.

5.1.5. Repair of the cryoinjured myocardium with intrapericardially delivered alginate beads containing growth factors or agarose patch containing ADSCs

Alginate beads could incorporate VEGF and bFGF. Simulation study with cheaper heme-proteins, some of which had similar biochemical properties as both factors, indicated that their controlled release could be achieved with this strategy. The rate of release was mainly determined by M_w and pI . After VEGF/bFGF-loaded beads were transplanted on top of the cryoinjured myocardium, a new layer of tissue encapsulating the beads was observed at the earliest follow-up MR imaging session (*i.e.*, 7-day cryoinjury). This layer

of tissue had similar MR enhancement as the cryoinjured myocardium after Gd-DTPA injection. However, within the cryoinjured tissue, tissue blood flow estimated by either *in vivo* first-pass Gd-MRI or post-mortem count of the entrapped fluorescent microspheres on short-axis slices had no significant difference as compared with the control cryoinjured myocardium receiving alginate beads alone or without any intervention. In contrast, deeper layers of the cryoinjured tissue had increased fluorescence intensity reaching $64\% \pm 13\%$ of that within the normal tissue. This correlated with 25% faster first-pass Gd-DTPA kinetics in the entire area relative to control. Histological study with TTC staining didn't show obvious viable tissue within this area. Microscopic study revealed that new capillaries formed within the cryoinjured tissue, but arterioles were seldom observed. Meanwhile, there also appeared many erythrocytes within the cryoinjured tissue, which was more obvious near the alginate beads. New growth of cardiomyogenic tissue was absent as MEMRI, TTC staining and H&E staining failed to provide convincing proof.

In contrast, epicardial transplantation of the agarose hydrogel patch incorporating ADSCs incurred efficient angiogenesis as evidenced by significantly enhanced microsphere fluorescence from the cryoinjured myocardium as well as appearance of the mature arterioles and venules within the cryoinjured myocardium. In most pigs, there lacked new growth of tissue around the gel patch was not observed. In addition, there also lacked new growth of the cardiomyocytes as evidenced by (i) lack of prolonged enhancement of the SI using MEMRI, (ii) absence of the reddish spots after TTC staining, and (iii) absence of the cardiomyogenic cells as revealed by H&E staining within the cryoinjured tissue.

5.2. Methodology and data interpretation

5.2.1. Ex vivo MEMRI for characterization of acute cardiac ischemia and chronic myocardial infarction

Detection of cardiac ischemia with the intracellular MR contrast agent, MnCl_2 , relied mainly on specific uptake of the contrast agent by normal cardiomyocytes and its reduced accumulation within the ischemic area, the result of which was a lower SI within this area as compared with normal myocardium on T_1 -weighted MR images²⁴¹⁻²⁴³.

Meanwhile, it had also been suggested that relaxivity change by anionic biopolymers (*e.g.*, proteins, polysaccharides and nucleic acids) resulting from interactions with the accumulated Mn^{2+} might also play a role in contrast development²⁴⁴. As such, it could be anticipated that the rate of SI enhancement within a specific region in the heart was determined by (i) its delivery rate into the tissue interstitium and (ii) its subsequent extraction rate by surrounding cells. The first factor depended mainly on tissue blood perfusion and $[\text{Mn}^{2+}]$ in blood plasma. Normally, this process was incessant due to continuous tissue perfusion. As such, interruption of tissue perfusion could lead to failure of the contrast delivery. In this study, a baseline perfusion rate of $\sim 1.5 \text{ mL min}^{-1} \text{ g}^{-1}$ wet weight and 0.2 mM MnCl_2 in the perfusate could provide Mn^{2+} supply of $\sim 0.3 \mu\text{mol min}^{-1} \text{ g}^{-1}$ wet weight. A previous study indicated that the maximal rate of Mn^{2+} uptake by rat cardiomyocytes was $\sim 4 \text{ nmol min}^{-1} \text{ g}^{-1}$ wet weight when 0.1 mM of Mn^{2+} was in the perfusate¹²⁵. If we assumed that cellular uptake of Mn^{2+} was proportional to its interstitial concentration and that the plasmalemmal calcium channel activity in pig cardiomyocytes was similar to that in the rat counterparts, the maximal uptake rate of Mn^{2+} was expected to be at $\sim 8 \text{ nmol min}^{-1} \text{ g}^{-1}$ wet weight. This rate translated to $< 3\%$

extraction of the supplied Mn^{2+} , which would not limit Mn^{2+} uptake due to excessive provision. In contrast, when a pig coronary artery or its branch was acutely occluded like it occurred in this study, supply of Mn^{2+} would become a major rate-limiting factor for its fast accumulation inside the cardiomyocytes as there possibly existed very limited collateral flow characteristic of pig heart ($< 1\%$)^{245, 246}.

The other important factor controlling the rate of Mn^{2+} accumulation was its extraction by the myocytes, which were further determined by (i) the amount of the viable cells taking up Mn^{2+} via the sarcolemmal Ca^{2+} channels (*i.e.*, cardiomyocytes within the myocardial tissue), (ii) the density of these channels per unit of cytoplasmic volume and (iii) their functional activity. For example, previous study had suggested that channel activity can be regulated by various factors such as interstitial concentration of catecholamines²⁴⁷, intracellular ATP and other nucleotides²⁴⁸, as well as intracellular pH²⁴⁹ through different pathways^{250, 251}. In addition, the amount of nearby competitive ions such as Ca^{2+} and Mg^{2+} also influenced its extraction rate²⁵².

Of course, eventual equilibrium distribution of the contrast agent between the perfusate and the heart was determined by their relative volume ratio ($\sim 3,000$ ml : 150 - 200 ml, respectively) and its active retention by cardiac tissue. Such active retention was prompted by several factors such as (i) the sarcolemmal and mitochondrial membrane potentials²⁴¹, (ii) competitive binding to the intracellular Ca^{2+} or Mg^{2+} binding sites on various proteins²⁵³, as well as (iii) the intracellular (0.5 ml g^{-1}) and extracellular (0.3 ml g^{-1}) water volumes²⁵⁴⁻²⁵⁶.

Another potential factor which might also influence its equilibrium distribution was its active retention by blood cells with the erythrocyte as a representative candidate due to

its natural abundance as compared with the leukocytes and platelets. As the perfusate in the current study contained 50% pig blood, the volume of erythrocytes would be expected to be ~ 150 ml per 1000 ml perfusate. Thus, the total volume of erythrocytes in our perfusion system would be ~ 450 ml, which was 4.5 times of that in cardiomyocytes (~ 100 ml = 200 g \times 0.5 mL g⁻¹). However, entry of Mn²⁺ into the erythrocytes was mainly via a passive diffusion mechanism characterized by a very low coefficient at ~ 3 \times 10⁻¹¹ m s⁻¹ ^{257, 258}. As a result, short-time exposure (< 30 - 45 min) of the erythrocytes to Mn²⁺ in this study precluded its significant retention by these cells. On the other hand, the volume ratio of microvasculature to cardiomyocytes within the myocardium was ~ 1:6 ²⁵⁹, which translated to 1.2% erythrocytes within a unit volume of myocardial tissue as the hematocrit in this perfusate was 15%. Thus, potential contribution of SI enhancement from Mn²⁺-loaded erythrocytes should be negligible.

After ligation of the 1st and 2nd LAD diagonal branches, *in vivo* Gd-MRI revealed that the jeopardized myocardium devoided of the contrast agent (Fig. 4.3B), which corroborates the previous NIR spectroscopic imaging study from the same group with ICG as an intravascular NIR contrast agent ¹⁶⁴. This suggested that almost complete interruption of blood perfusion occurred within the jeopardized myocardium, which was consistent with limited collateral coronary vasculature (< 1%) in pig heart ^{245, 246}. A further suggestion of insufficient perfusion after coronary occlusion was immediate shift from the oxygenated heme-proteins, *i.e.*, oxy-(Hb+Mb), to the deoxygenated counterparts, *i.e.*, deoxy-(Hb+Mb) within this area as evidenced by *in vivo* visible/NIR point reflectance spectroscopy (Fig. 3.2). Of course, absence of Evans blue within this area after perfusion staining on the isolated heart (Fig. 4.1A, B) serves as a final proof of

perfusion deficit after occlusion of the LAD branches. As a result, the observed hypointense area on Mn-enhanced MR images could be attributed mainly to the reduced perfusion (Fig. 4.1D).

It had been repeatedly observed that myocardial blood flow remained much lower than normal even after establishment of reperfusion, which was termed as “no-reflow” phenomenon²⁶⁰. It seemed that its occurrence was a time-dependent phenomenon as early reperfusion (< 30 min in pig hearts) could prevent its development. Upon ischemia continuing for 60 min or more, it would lead to > 50% reduction of the myocardial blood flow after tissue reperfusion²⁶¹. It seemed that its development was related to the injury of microvasculature and development of microvascular plugging due to neutrophil accumulation²⁶². As such, the hypointense area found in Mn-enhanced MR images and reduced deposition of IR676 within the jeopardized myocardium resulted from both reduced perfusion due to “no-reflow” phenomenon and failure of active retention due to cardiomyocytes necrosis.

Infarction progression was characterized by destruction of the injured cardiomyocytes and subsequent deposition of the collagen secreted by the invading myofibroblasts. Inflammatory cells invaded the infarcted tissue and, sometime later, myofibroblasts appeared in the wound. Degradation of the interstitial proteins can be significant ~ 48 h after coronary artery occlusion in the rat²⁶³. This process was mediated by increased activities of the collagenases and other neutral proteinases secreted by the infiltrating inflammatory cells. Myofibroblasts were responsible for the reconstruction of a new collagen network and final solid scar tissue formation 4-8 weeks later, when myofibroblasts themselves became sparse within the tissue. As a result, this host-

mediated healing process required accurate orchestration of the sequential invasion, action and apoptosis of various cell types²⁶⁴.

Our data fitted well to this scenario. Indeed, the rates of contrast enhancement ($\Delta SI_{max}/t_1$) and maximal enhancements (ΔSI_{max}) were significantly higher in all pigs subjected to various periods of MI than in pigs subjected to acute ischemia. Faster SI enhancement implied partial restoration of tissue perfusion during inflammation progression, which was confirmed by delayed enhancement in *in vivo* Gd- MRI experiments (Fig. 4.7.). Greater Mn-induced equilibrium enhancement indicated more significant Mn^{2+} retention in the infarct areas as compared with the ischemic regions. Three factors could contribute to this: (i) larger extracellular space, (ii) active binding to the extracellular structures (*e.g.*, collagen) and (iii) uptake by the cells that populated the infarcted area. At the early infarct stages it could be inflammatory cells, neutrophils and macrophages, while at the later stages fibroblasts and vascular cells (smooth muscle and endothelial) were the most plausible candidates. Mn^{2+} washout experiments proved that ~ 15% of the observed enhancement in the 4-week infarct could be attributed to some “non-washable” Mn^{2+} pool, most probably entrapped inside the cells. In contrast, in normal regions intracellular contributions reached 75%.

The kinetics of the SI enhancement from this *ex vivo* MEMRI study was not complicated by the fast clearance provided by the liver and kidney *in vivo*. As such, in the closed *ex vivo* perfusion system, the plasma [Mn^{2+}] becomes gradually constant after equilibrium distribution between the extracellular and intracellular (mainly a function of total uptake amount by cardiomyocytes) spaces reached. In addition, kinetic properties of the infarcted and ischemic tissues, as assessed by the contrast development, became

available with this closed perfusion system, though possible presence of the extracellular Mn^{2+} in the bound form could reduce the contrast between the normal and infarcted areas due to the significantly larger interstitial volume within the injured tissue.

5.2.2. Myocardial infarction induced by cryoinjury

Although the cryoinjury-induced MI had been previously described in other animals²³⁷,²³⁸, this was the first report to outline the morphological, optical and contrast-enhanced MRI features of cryoinjury-induced MI in pigs. Morphological variations of cryolesions in the present study significantly reduced as this feature depended mainly on exposure time and the cryoprobe tip-shape. Possible concern with the use of cryoinjury on the myocardium was its potential negative influence on medium and small coronary vessels (artery and vein) and the intravascular blood as it was difficult to find a “clean” LV epicardial area free from their passage. The potential danger was development of freezing-thawing-induced thrombosis/embolism within such vessels leading to MI of the downstream myocardium. However, such complications did not develop as Gd-MRI and NIR imaging didn't show perfusion deficits outside the cryolesion, which was in agreement with previous publications²³⁷. In addition, NIR imaging revealed patent vessels (both artery and vein) within the cryolesions using ICG as an intravascular flow tracer.

We used *in vivo* and *post-mortem* imaging and spectroscopic methods to characterize perfusion and viability of the cryoinjured myocardium. Gd-MRI provided kinetics of contrast development (Figs. 4.10D and 4.14D), from which early and late enhancement data were extracted. The former revealed no-reflow phenomenon, which was most obvious in acute cryoinjury (Fig. 4.10), less obvious after 1-2 weeks and was

not observed following 4-week cryoinjury (Fig. 4.14A-C). Severe flow restrictions were revealed in both the first-pass kinetics (Fig. 4.10E, <1s time resolution) and slow kinetics with low time resolution (2 min, Fig. 4.10D). Partial flow limitations in the hyperintense zone could be inferred from slower washout kinetics (Fig. 4.10D, upper curve). Late enhancement data showed hyperintense infarction areas, which could also contain edematous tissue with higher distribution volume for Gd-DTPA during acute cryoinjury (Fig. 4.10A-C). Mature 4-week infarctions (Fig. 4.14C) were composed of predominantly scar tissue with high collagen and low cellular contents (Fig. 4.13G). Furthermore, changes in fast Gd-MRI (<2 min) and slower kinetics of SI decay in the 4-week infarction area (Fig. 4.14D) implied substantial perfusion of this tissue. Note that the time courses and derived time constants were only semi-quantitative perfusion measures as they were not directly related to local Gd contents due to its high initial blood concentration, which resulted in non-linear relations between concentration, relaxivity and signal enhancement.

Kinetics of Mn enhancement revealed abnormal areas as hypointense zones in acutely (Fig. 4.11C) and chronically (Fig. 4.15C) cryoinjured hearts. The nature of abnormality (hypoperfusion or necrosis) could not be identified without help of Gd-MRI (see above). However, Gd-MRI might potentially overestimate the necrotic zone due to the similarity between edema and necrosis in terms of increased extracellular space. Necrotic regions determined by MEMRI hardly could involve viable edematous tissues. In mature 4-week cryoinjured myocardium, perfused scar tissue was dominant and should not significantly differ in size on Gd- and Mn-enhanced MR images.

It was not easy to compare cryoinjury sizes determined by different contrast agents because of (i) thicker slice thickness in MEMRI (8 mm vs. 5 mm in Gd-enhanced MR images) and (ii) the systolic phase of acquired images in MEMRI (vs. the diastolic phase in Gd-MRI). Theoretically thicker slices increased the error in determination of infarction size towards overestimation due to the round shape of the injury, which did not occupy the entire thickness of border slices. On the other hand, the necrotic zone might somewhat shrink during systole, which was a usual configuration of isovolumic Langendorff-perfused heart used in the MEMRI study.

Optical spectroscopy provided information on chemical changes related to cryoinjury in the sub-epicardial layer (~ 5 mm in thickness) *in vivo* (Fig. 4.9B) and in cardiac slices *post-mortem* (Fig. 4.12C). Dramatic increase in 560 and 580 nm absorbance (Fig. 4.9B) *in vivo* and *ex vivo* (Fig. 4.12C) resulted from deposition of the erythrocytes rich in Hb in the LV capillaries as the content of Mb, an intracellular hemeprotein with nearly identical optical properties, could not change in a few minutes. This explained dark-red color of acutely cryoinjured tissue seen in short-axis slices (Fig. 4.12A) and was confirmed by histological H&E analysis showing red staining due to presence of erythrocytes (Fig. 4.12D). In the short-axis slices, changes in cryoinjured area coexisted with complete deoxygenation of Hb+Mb in normal areas (Fig. 4.12C). The latter indicated that normal tissue was still metabolically active 15 - 30 min after cardiac arrest as cell respiration consumes all O₂ that diffused through the tissue-air interface.

Near infrared spectroscopic imaging of first-pass kinetics of ICG, an intravascular NIR flow tracer, revealed its slower passage through the subepicardium of cryoinjured region (Fig. 4.9D) confirming substantial flow deficit observed with Gd-MRI. The data

were semi-quantitative in nature and allowed evaluation of perfusion values relative to the normal area using, *e.g.*, upslope velocities¹⁶⁴. Furthermore, “equilibrium” levels of ICG absorbance (30-60 s) permitted estimation of relative circulating blood volume in the LV wall sub-epicardium. Measurements of “equilibrium” ICG concentration in blood samples enabled conversion of tissue absorbance to absolute concentration due to its linear relation to absorbance if the light pathlength was known. A disadvantage of this method in comparison with MRI was an “interrogation” volume limited to the sub-epicardium (~ 5 mm thick) of the anterior side of the left and right ventricles.

5.2.3. *In vivo* MEMRI for chronic myocardial infarction induced by cryoinjury

When Mn^{2+} was administered into the circulation via direct intravenous infusion, it would not be only taken up by the cardiomyocytes. Liver and kidney also actively absorbed it when Mn^{2+} passed these organs¹⁵⁶. As a result, its clearance within the plasma was very fast. In reality, after an intravenous bolus injection of MnCl_2 in rats ($33 \mu\text{mol kg}^{-1}$), the concentration-time profile of Mn^{2+} in plasma appeared to fit into a two-compartment model with first-order elimination from the central compartment²⁶⁵, a hypothetical volume into which a drug initially distributed upon administration. The estimated volume (~ 140 ml kg^{-1}) from that study for initial drug distribution was well above the total blood volume within the rat body (~ 58 ml kg^{-1}) due to fast absorption by organs which could actively uptake it. From that study, the first-order initial $t_{1/2}$ was estimated to be ~ 12 min. However, another study also in rats indicated that the first-order initial $t_{1/2}$ was around ~ 4.7 min after completion of 7-min continuous intravenous infusion at ~ $11 \mu\text{mol kg}^{-1}$ ¹⁵⁷. The difference indicated that repeated intermittent bolus injections might be better than continuous infusion with the same total dosage as the integrated blood concentration

every 2 min would be higher with this protocol, which translated to a more significant entry of Mn^{2+} into the cardiomyocytes. Our results show that myocardium in the intermittent injection group had higher peak SI (~ 55% relative to the blood peak SI) than that in the continuous infusion group (~ 46% relative to the blood peak SI, Fig. 4.18) might be partially explained by that. Of course, higher amount of catecholamines released from chromaffin cells within the adrenal medulla in the intermittent group, which could be deduced from more significant fluctuation in hemodynamics after each bolus injection (Fig. 4.19-21), could also enhance L-type Ca^{2+} channel activity²⁶⁶. As a result, it might be also related to higher amount of Mn^{2+} present inside the myocardium. The higher SI peak within the normal myocardium translated to an earlier presence and a longer effective acquisition window revealing significant contrast between it, LV blood pool and infarcted myocardium, assuming similar kinetics within the three spaces between the two groups (Fig. 4.18).

On the other hand, more significant hemodynamic fluctuation incurred by a bolus injection of MnCl_2 could jeopardize animal/subject safety and image acquisition, though we separated the dose into $10 \mu\text{mol kg}^{-1}$ per injection by 110 s intervals. In clinic, it might lead to life-threatening complications such as stroke, ventricular fibrillation and congestive heart failure. Also, it would change TR significantly during T_1 -weighted MR image acquisition. As a result, it is highly desirable to apply slow intravenous continuous infusion as it can minimize hemodynamic fluctuation.

Compared with *ex vivo* MEMRI, the difference between the cryoinjured and normal myocardium during their respective peak SI was not obvious for pigs receiving either continuous infusion or intermittent bolus injection of MnCl_2 . The reason for this

discrepancy was related to significantly lower averaged tissue concentration (relative to blood) achieved by use of either infusion scheme than that during *ex vivo* infusion. However, after removal by liver of nearly all Mn^{2+} from blood over 16-20 min ($t_{1/2} \sim 5\text{min}$), difference between infarct and normal areas became evident ($\sim 35\%$ of SI in normal area, see Figs. 4.17-18 and table 4.8).

5.2.4. Design of MR trackable alginate beads capable of releasing incorporated proteins

Alginates are polysaccharides abundant in brown algae. The building blocks are copolymers of β -D-mannuronic (M) and α -L-guluronic (G) residues. They have been widely applied for entrapment of various therapeutic macromolecules aimed at controlling their release²⁶⁷⁻²⁶⁹, as they can form heat-stable hydrogels via cross-linking of M residues in the presence of divalent cations such as Ca^{2+} . On the other hand, their *in vivo* tracking after entering the body remains to be addressed as it can help predict therapeutic efficiency based on their biodistribution. The fast development of various imaging techniques, *esp.*, MRI, computed tomography and radioisotope nuclear imaging, provides new chances for visualizing their biodistribution *in vivo*. Compared with computed tomography and nuclear imaging, MRI has no potential biosafety concern resulting from repeated exposure to X- or γ -rays. To achieve this goal, appropriate imaging agents have to be incorporated into the alginate matrix.

Gadolinium ion is a trivalent paramagnetic ion and known to shorten both the longitudinal (T_1) and the transverse (T_2) relaxation times of water protons²⁷⁰. As cross-linked alginate could also be formed in the presence of trivalent atoms in addition to conventional bivalent agents^{271, 272}, we decided to test whether alginate solution could form stable hydrogel when GdCl_3 was added into the cross-linking solution. Due to

concern on potential negative influence of high concentration of GdCl_3 when the beads will be implanted into the body^{273, 274}, lower concentration of GdCl_3 within the cross-linking solution with concomitant use of CaCl_2 was applied. The present results indicated that 30 mM CaCl_2 solution containing 1mM GdCl_3 , which is a relatively safe dosage²⁷³, was sufficient to form MRI-detectable alginate hydrogel using T_1 -weighted MR sequence. Binding of Gd^{3+} within the alginate beads was rather strong as it was still trackable with the same sequence even after 4-wk *in vivo* residence within the pericardial cavity. As a result, we believe that its release from the alginate hydrogel was rather slow, reducing the potential side effects on organ function.

In contrast, MR trackability of alginate hydrogel loaded with Met-Hb was not satisfactory. *In vivo* experiments showed that the beads loaded with Met-Hb could only be tracked for a limited period (*ca.* 1 week) using the T_1 -weighting sequence (FLASH) as the beads could not be found during the MR session 2 weeks after surgery. Although this tracer would alleviate problems with possible toxicity of Gd^{3+} tracer, it would be insufficient when longer tracking period was desired.

All compounds studied displayed a plateau in their efflux kinetics due to establishment of equilibrium between intra-bead and buffer concentrations. Myoglobin displayed the fastest release from the beads, likely due to its low Mw (16.7 kDa) and near-neutral *pI* compared with the larger Met-Hb (tetramers, Mw: 64 kDa) and cationic cytochrome c (Mw: 12.4 kDa). Cytochrome c has a lower Mw than Mb, but has a significantly higher isoelectric point of 10.6 which facilitates its binding at neutral pH with carboxylic groups within the alginate beads. As observed for Met-Hb, both cytochrome c and Mb displayed an initial fast release followed by a much slower release

from the beads in the second stage. It should be noted that the molecules used in these studies have Mw's comparable to those of the recombinant human growth factors bFGF (Mw ~ 16 kDa) and VEGF (Mw ~ 38.2 kDa). It was expected for reasons indicated above that these growth factors could show release kinetics comparable with Mb and Met-Hb. However, due to the more alkaline nature of these proteins ($pI = 9.6$ and 8.5 , respectively) their release kinetics could be expected to be slower. Indeed, our experiment using enzyme-linked immunosorbent assay showed that the initial release rate from the beads was ~ 3.0% and ~ 1.0% per day for VEGF and bFGF, respectively. Geometric factors might also play a role in the release rate. For instance, VEGF is known to have a more elongated, cylindrical shape, while cytochrome c and myoglobin are nearly spherical. These observations were in line with the report of slow and continuous release of VEGF, measured over 30 days, from an alginate formulation that used a slightly different, low-molecular-weight alginate, providing a network with a likely different permeability²⁰⁰.

5.3. Mechanism of cryoinjury

Acute cryoinjury was mainly induced by microembolization of the core area with erythrocytes (Figs 4.9 & 4.12), due most probably to swelling of the vascular endothelial cells and cardiomyocytes resulting in narrowing of capillary lumen and “plugging” by erythrocytes. The thin rim of cryoinjured area, which appeared light on photographs of slices both prior to and after TTC staining and hyperintense on Gd-enhanced MR images, perhaps corresponded to perfused tissue where the permeability of the cardiomyocytes membrane was compromised and extracellular (vasogenic) edema occurred. Although the

mechanism of the rim formation is unknown, possibly it is related to the temperature gradient between the epicardium and deeper LV layers. For instance, the rim could correspond to the border layer with a near freezing temperature where ice crystals coexist with liquid water. Qualitatively, these features resembled the development of ischemia-reperfusion damage, with the formation of a core of poorly perfused tissue (“no-reflow” phenomenon)²⁷⁵⁻²⁷⁷. This implied that cell death in the no-reflow core of cryoinjury was at least partially due to ischemia in addition to possible direct injury induced by ice crystals and osmotic destruction of cardiomyocytes²⁵⁹. Upon cryoinjury progression, the no-reflow zone was gradually replaced by scar tissue (Fig. 4.13), which virtually did not differ from that formed after occlusion infarction. Interestingly an MRI study of the progression of injury evoked by radiofrequency ablation²⁷⁸ showed patterns similar to that observed for cryoinjury.

Shrinkage of infarction size determined as a sum of hyper- + hypo-intense areas can be partially explained by reduction of edema at least during the first 2 weeks after cryoinjury (by ~ 40%, Fig. 4.14E). However we could not exclude recovery of reversibly damaged tissue in the infarction periphery. Interestingly, the time courses of the reduction of infarctions induced by the occlusion of the LAD branches and by cryoinjury were virtually identical, so that after 4 weeks they reached 45% ± 5.8% and 41% ± 4.5% of the initial size, respectively. This implied that the mechanisms governing this process were likely similar.

Of course, some limitations do exist when cryoinjury model was employed for assessment of therapeutical angiogenic potential on infarcted myocardium. As it has been described above, freezing led to immediate cell death within frozen tissue, the size of

which conformed to the temperature and duration of contact. However, cardiomyocytes upon acute complete ischemia usually still can be resuscitated, depending on the location of the jeopardized myocardium, if perfusion can be restored within several hours. Even without reperfusion, there may also exist a layer of viable subepicardial tissue due to slow diffusion of oxygen and other nutrients from the pericardial fluid. In some patients with chronic ischemia, ultimate infarction volume upon acute complete occlusion of the upstream coronary artery may even be much smaller than initial anticipation due to previously formed collateral vessels from the neighbouring arteries. As a result, it might be anticipated that epicardial continuous delivery of angiogenic factors released from growth factors-loaded alginate beads or secreted from ADSCs entrapped in agarose hydrogel patch would lead to enhanced formation of collateral vessels within the jeopardized subepicardium, the result of which would possibly be improved salvation of viable myocardium within this area.

5.4. Therapeutic angiogenesis for MI with alginate-entrapped vascular growth factors

Relatively large alginate beads were chosen as growth factors' carriers for the following reasons: (i) low surface to volume ratio prolonging diffusion for at least several days; (ii) protection from proteolytic enzymes generated during inflammation phase of infarct development and (iii) ability to be sutured to cardiac surfaces (epicardium or pericardium).

After acute MI, new blood vessels formed primarily from the ischemic border zone towards the infarcted tissue, which could help restore local delivery of nutrients including

O₂ and remove metabolic products. However, this process was very slow by the host healing system. Recent experimental studies on ischemia-induced MI indicated that angiogenic therapy might be a promising strategy to improve myocardial perfusion and preserve its function, but there existed conflicting results in clinical trials. Therefore, its efficiency was being tested by various groups around the world. Various agents and formulation have been tried. One approach was using genes encoding vascular growth factors. Depending on implantation routes and vectors chosen, varied extents of angiogenesis within the infarcted myocardium were observed. For example, Furlani *et al.* found that local multi-spot injection of VEGF plasmid into a 7-day infarct in dog heart could improve vessel density including arterioles and capillaries with concomitant improvement of global ventricular function²⁷⁹. Due to concern on uncontrollable growth of new vessels, we tested the efficiency of protein products instead of their encoding genes.

Several growth factors had been found to be able to stimulate angiogenesis. Among them, VEGF and bFGF were the two most extensively studied stimulants^{280, 281}. For VEGF, two plasmalemmal receptor proteins (VEGF receptor-1 and -2) on endothelial precursor cells can be stimulated to promote angiogenesis. Plasmalemmal tyrosine kinase on endothelial precursor cells is the receptor for bFGF to bind with. It can stimulate endothelial cell proliferation, which then form tube-like structures through their physical organization. Recent studies further indicated that development and final maturation of neovasculature do need various growth factors as they play different roles during the whole process²⁸². For example, VEGF can improve microvascular permeability, stimulate endothelial proliferation and enhance local endothelial transmigration. It is

deemed as a key moderator during angiogenesis²⁸³. Meanwhile, it also has been observed that exclusive use of VEGF for angiogenic therapy may not be sufficient. It may lead to formation of immature neovasculature with abnormally high permeability (leaky vessels)²⁸⁴. Basic FGF has various effects on numerous types of cells, including endothelial cells. Their combined use within several polymer carriers showed great potential in various animal models^{285, 286}. Our results also indicated that combined delivery of VEGF and bFGF entrapped in alginate hydrogel beads could induce greater angiogenesis. Such results were only observed for those beads that were anchored on top of the cryoinjured epicardium. In contrast, delivery of beads directly into the pericardial cavity or anchoring to the neighboring pericardium didn't show such effect (data not shown). They were unable to induce growth of new tissue surrounding the beads. As a result, it seemed that success of angiogenic therapy was also related to the spatial location.

Additional vessel formation induced by delivery of the VEGF/bFGF would be expected to translate to improved blood flow. However, we did not observe such phenomenon in the vicinity of beads (*i.e.*, subepicardium). A potential explanation was that they were still in their early stage of angiogenesis as a multitude of erythrocytes leaked into the interstitium (Fig. 4.33A, B). However, at the same time mid-mural areas showed increase in perfusion as evidence by microsphere data (Fig. 4.30A). This implied improved formation of capillaries capable of passing blood. Such heterogeneity was not observed by Gd-MRI due to methodological limitation in these measurements. For example, first-pass Gd-MRI is an imaging method with relatively low spatial resolution due to requirement of high temporal resolution. As a result, it was difficult to observe the perfusion difference among different areas within the cryoinjured infarction. On the other

hand, to achieve higher spatial resolution and limit motion artifact for T₁-weighted MRI, acquisition of full data for each slice has to be separated by ~ 10 heart beats at the same phase during a contraction cycle. Consequently, each imaging session would take almost 2 min, during which heterogeneous perfusion, if any, across infarcted myocardium cannot be easily detected.

In addition, the newly formed vasculature within the cryoinjured myocardium after exposure to slowly released exogenous VEGF/bFGF seemed to be immature as evidenced by lack of arterioles and leakage of erythrocytes into the interstitium. Potential explanation might include (i) lack of other important vascular growth factors and cytokines which altogether play complementary roles for inducing stable and functional vascular networks^{287, 288} and (ii) lack of proper regional VEGF-to-bFGF ratio at different stages of vascular formation due to their different diffusing rates out of the alginate matrix.

Obvious concern related to the use of xenogeneic proteins (human VEGF and bFGF) and cells (human ADSCs) is their potential induction of host-mediated immune reaction, which might reduce the angiogenic potential of tested agents. However, it seems that the immune response, if it existed, did not play a significant role as judged by several previous studies from other groups employing donor and recipient mismatches in species²⁸⁹⁻²⁹¹. In fact, alginate-based or agarose-based hydrogel matrix possibly protected immobilized proteins or cells from attack by host immune system.

5.5. Effects of ADSCs immobilized in agarose gel patch on cryoinjured myocardium

Adipose-derived stem cells have the potential of transdifferentiation into multi-lineage cell lines including both cardiomyocytes and smooth muscle cells ²⁹². It may not be suitable to directly inject the ADSCs into the border zone of infarcted myocardium as it is difficult to distinguish the source of newly formed vessels, though genetic analysis may help. In addition, regionally implanted ADSCs can only provide limited, if any, angiogenic paracrine effects. As a result, we decided to encapsulate the ADSCs into a gel patch, which could prevent/reduce their migration into the host tissue. As for the gelling material, alginate was a potential candidate as pig pancreatic islet had been successfully encapsulated into it ^{293, 294}. However, a concern related to potential negative effects of non-physiological gelling ions (high $[Ca^{2+}]$ and presence of Gd^{3+}) on ADSCs was raised when we prepared the alginate-cells patch. Consequently, we decided to use agarose as its solution would only form hydrogel upon temperature drop. As the melting point was much higher than the gelling point, we had chosen the agarose gel with gelling temperature below 37 °C for its easy mix with ADSCs. Our *in vitro* assessment regarding the viability of ADSCs after being entrapped in the agarose matrix indicated that more than 50% of entrapped ADSCs could survive for 2 weeks. In addition, a significant amount of VEGF was detected within the cultured medium.

Choice of cryoinjury-induced MI model also made the results more convincing than conventional ischemia-induced MI as, in most times, there remains a thin subepicardial layer of viable myocardium in ischemia-induced MI. The reason might be related to close proximity to the pericardial cavity, where from oxygen and nutrients could still diffuse into the subepicardium. It would have made estimation of angiogenic and regenerative

potential with epicardial anchoring of interventional agents inaccurate. Cryoinjury helped solve this problem. The observed new vessel network within the cryoinjury-induced MI could be reliably attributed to the effects of external agents. Our microscopic results did indicate growth of new vessels including capillaries, arterioles and venules within the scar tissue. Unlike growth factor-induced angiogenesis in the other group, the newly formed vasculature was functionally competitive as erythrocytes appear inside, instead of outside, the vessel lumen (not shown here). A further proof of mature angiogenesis was the appearance of fluorescent microspheres within the scar tissue, indicating the successful bridging of the vessel network with host coronary vasculature (Fig. 4.31). Our results indicate that mature angiogenesis could be achieved within 4-week after MI which might be correlated with the interplay of all related angiogenic growth factors. Based on our control results and previous reports by other groups^{223, 225, 295}, these growth factors were most probably produced by ADSCs entrapped in agarose gel patch through the epicardial interface. Of course, we still can not exclude the possibility that the newly formed vessel structure emerged due to transdifferentiation of ADSCs migrated from the agarose gel. However, if ADSCs did transdifferentiate into smooth muscle cells, they might also be able to transdifferentiate into cardiomyocytes as both *in vitro* and *in vivo* study all found this potential within the infarcted myocardium²⁹⁶⁻²⁹⁸. However, in histological and MEMRI data, we did not find such evidence. Of course, genetic-based *in situ* hybridization should be employed in the future to further ensure the cell source within the vasculature.

6. REFERENCES

- (1) Thygesen K, Alpert JS, White HD et al. Universal definition of myocardial infarction. *Circulation* 2007 November 27;116(22):2634-53.
- (2) Naghavi M, Libby P, Falk E et al. From vulnerable plaque to vulnerable patient: a call for new definitions and risk assessment strategies: Part I. *Circulation* 2003 October 7;108(14):1664-72.
- (3) Naghavi M, Libby P, Falk E et al. From vulnerable plaque to vulnerable patient: a call for new definitions and risk assessment strategies: Part II. *Circulation* 2003 October 14;108(15):1772-8.
- (4) Naghavi M, Falk E, Hecht HS et al. From vulnerable plaque to vulnerable patient--Part III: Executive summary of the Screening for Heart Attack Prevention and Education (SHAPE) Task Force report. *Am J Cardiol* 2006 July 17;98(2A):2H-15H.
- (5) Shiomi M, Fan J. Unstable coronary plaques and cardiac events in myocardial infarction-prone Watanabe heritable hyperlipidemic rabbits: questions and quandaries. *Curr Opin Lipidol* 2008 December;19(6):631-6.
- (6) Griese M, Perlitz V, Jungling E, Kammermeier H. Myocardial performance and free energy of ATP-hydrolysis in isolated rat hearts during graded hypoxia, reoxygenation and high K^+ -perfusion. *J Mol Cell Cardiol* 1988 December;20(12):1189-201.
- (7) Opie LH. Myocardial infarct size. Part I. Basic considerations. *Am Heart J* 1980 September;100(3):355-72.
- (8) Stanley WC, Recchia FA, Lopaschuk GD. Myocardial substrate metabolism in the normal and failing heart. *Physiol Rev* 2005 July;85(3):1093-129.
- (9) Allen DG, Orchard CH. Myocardial contractile function during ischemia and hypoxia. *Circ Res* 1987 February;60(2):153-68.
- (10) Rich PR. The molecular machinery of Keilin's respiratory chain. *Biochem Soc Trans* 2003 December;31(Pt 6):1095-105.
- (11) Opie LH. Effects of regional ischemia on metabolism of glucose and fatty acids. Relative rates of aerobic and anaerobic energy production during myocardial infarction and comparison with effects of anoxia. *Circ Res* 1976 May;38(5 Suppl 1):I52-I74.
- (12) Barandier CE, Boucher FR, de Leiris JP. Manganese reduces myocardial reperfusion injury on isolated rat heart. *J Mol Cell Cardiol* 1998 April;30(4):837-47.

- (13) Yao A, Su Z, Nonaka A et al. Effects of overexpression of the Na⁺-Ca²⁺ exchanger on [Ca²⁺]_i transients in murine ventricular myocytes. *Circ Res* 1998 April 6;82(6):657-65.
- (14) Cook SJ, Chamunorwa JP, Lancaster MK, O'Neill SC. Regional differences in the regulation of intracellular sodium and in action potential configuration in rabbit left ventricle. *Pflugers Arch* 1997 February;433(4):515-22.
- (15) Belardinelli L, Shryock JC, Fraser H. Inhibition of the late sodium current as a potential cardioprotective principle: effects of the late sodium current inhibitor ranolazine. *Heart* 2006 July;92 Suppl 4:iv6-iv14.
- (16) Bollensdorff C, Knopp A, Biskup C, Zimmer T, Benndorf K. Na⁽⁺⁾ current through KATP channels: consequences for Na⁽⁺⁾ and K⁽⁺⁾ fluxes during early myocardial ischemia. *Am J Physiol Heart Circ Physiol* 2004 January;286(1):H283-H295.
- (17) Eng S, Maddaford TG, Kardami E, Pierce GN. Protection against myocardial ischemic/reperfusion injury by inhibitors of two separate pathways of Na⁺ entry. *J Mol Cell Cardiol* 1998 April;30(4):829-35.
- (18) Saint DA. The role of the persistent Na⁽⁺⁾ current during cardiac ischemia and hypoxia. *J Cardiovasc Electrophysiol* 2006 May;17 Suppl 1:S96-S103.
- (19) Steenbergen C, Hill ML, Jennings RB. Volume regulation and plasma membrane injury in aerobic, anaerobic, and ischemic myocardium in vitro. Effects of osmotic cell swelling on plasma membrane integrity. *Circ Res* 1985 December;57(6):864-75.
- (20) Kaplan P, Hendrikx M, Mattheussen M, Mubagwa K, Flameng W. Effect of ischemia and reperfusion on sarcoplasmic reticulum calcium uptake. *Circ Res* 1992 November;71(5):1123-30.
- (21) Gambassi G, Hansford RG, Sollott SJ, Hogue BA, Lakatta EG, Capogrossi MC. Effects of acidosis on resting cytosolic and mitochondrial Ca²⁺ in mammalian myocardium. *J Gen Physiol* 1993 September;102(3):575-97.
- (22) Bersohn MM, Morey AK, Weiss RS. Sarcolemmal calcium transporters in myocardial ischemia. *J Mol Cell Cardiol* 1997 September;29(9):2525-32.
- (23) Pieske B, Maier LS, Bers DM, Hasenfuss G. Ca²⁺ handling and sarcoplasmic reticulum Ca²⁺ content in isolated failing and nonfailing human myocardium. *Circ Res* 1999 July 9;85(1):38-46.
- (24) Muller CA, Opie LH, Pineda CA, McCarthy J, Kraljevic V. Combination of a calcium antagonist, verapamil, with an angiotensin converting enzyme inhibitor, trandolapril, in experimental myocardial ischemia and reperfusion: antiarrhythmic

and hemodynamic effects of chronic oral pretreatment. *Cardiovasc Drugs Ther* 1998 October;12(5):449-55.

- (25) Griffiths EJ, Halestrap AP. Mitochondrial non-specific pores remain closed during cardiac ischaemia, but open upon reperfusion. *Biochem J* 1995 April 1;307 (Pt 1):93-8.
- (26) Musters RJ, Probstl-Biegelmann E, van Veen TA et al. Sarcolemmal phosphatidylethanolamine reorganization during simulated ischaemia and reperfusion: reversibility and ATP dependency. *Mol Membr Biol* 1996 July;13(3):159-64.
- (27) Musters RJ, Otten E, Biegelmann E et al. Loss of asymmetric distribution of sarcolemmal phosphatidylethanolamine during simulated ischemia in the isolated neonatal rat cardiomyocyte. *Circ Res* 1993 September;73(3):514-23.
- (28) Verkleij AJ, Post JA. Physico-chemical properties and organization of lipids in membranes: their possible role in myocardial injury. *Basic Res Cardiol* 1987;82 Suppl 1:85-91.
- (29) Van Nieuwenhoven FA, Musters RJ, Post JA, Verkleij AJ, van d, V, Glatz JF. Release of proteins from isolated neonatal rat cardiomyocytes subjected to simulated ischemia or metabolic inhibition is independent of molecular mass. *J Mol Cell Cardiol* 1996 July;28(7):1429-34.
- (30) van d, V, van BM, Reneman RS. Ischemia and reperfusion induced alterations in membrane phospholipids: an overview. *Ann N Y Acad Sci* 1994 June 17;723:1-14.
- (31) Post JA, Verkleij AJ, Langer GA. Organization and function of sarcolemmal phospholipids in control and ischemic/reperfused cardiomyocytes. *J Mol Cell Cardiol* 1995 February;27(2):749-60.
- (32) Beckman JS, Koppenol WH. Nitric oxide, superoxide, and peroxynitrite: the good, the bad, and ugly. *Am J Physiol* 1996 November;271(5 Pt 1):C1424-C1437.
- (33) O'Neill CA, Fu LW, Halliwell B, Longhurst JC. Hydroxyl radical production during myocardial ischemia and reperfusion in cats. *Am J Physiol* 1996 August;271(2 Pt 2):H660-H667.
- (34) Chen Q, Moghaddas S, Hoppel CL, Lesnefsky EJ. Ischemic defects in the electron transport chain increase the production of reactive oxygen species from isolated rat heart mitochondria. *Am J Physiol Cell Physiol* 2008 February;294(2):C460-C466.
- (35) Kukreja RC, Hess ML. The oxygen free radical system: from equations through membrane-protein interactions to cardiovascular injury and protection. *Cardiovasc Res* 1992 July;26(7):641-55.

- (36) Kramer JH, Misik V, Weglicki WB. Lipid peroxidation-derived free radical production and postischemic myocardial reperfusion injury. *Ann N Y Acad Sci* 1994 June 17;723:180-96.
- (37) Bay DC, Court DA. Origami in the outer membrane: the transmembrane arrangement of mitochondrial porins. *Biochem Cell Biol* 2002;80(5):551-62.
- (38) Lemasters JJ, Qian T, He L et al. Role of mitochondrial inner membrane permeabilization in necrotic cell death, apoptosis, and autophagy. *Antioxid Redox Signal* 2002 October;4(5):769-81.
- (39) Alpert JS, Thygesen K, Antman E, Bassand JP. Myocardial infarction redefined--a consensus document of The Joint European Society of Cardiology/American College of Cardiology Committee for the redefinition of myocardial infarction. *J Am Coll Cardiol* 2000 September;36(3):959-69.
- (40) Matsuda M, Fujiwara H, Onodera T et al. Quantitative analysis of infarct size, contraction band necrosis, and coagulation necrosis in human autopsied hearts with acute myocardial infarction after treatment with selective intracoronary thrombolysis. *Circulation* 1987 November;76(5):981-9.
- (41) Mattfeldt T, Schwarz F, Schuler G, Hofmann M, Kubler W. Necropsy evaluation in seven patients with evolving acute myocardial infarction treated with thrombolytic therapy. *Am J Cardiol* 1984 September 1;54(6):530-4.
- (42) Diamantis A, Magiorkinis E, Sakorafas GH, Androutsos G. A brief history of apoptosis: from ancient to modern times. *Onkologie* 2008 December;31(12):702-6.
- (43) Fliss H, Gattinger D. Apoptosis in ischemic and reperfused rat myocardium. *Circ Res* 1996 November;79(5):949-56.
- (44) Haunstetter A, Izumo S. Apoptosis: basic mechanisms and implications for cardiovascular disease. *Circ Res* 1998 June 15;82(11):1111-29.
- (45) Cheng W, Kajstura J, Nitahara JA et al. Programmed myocyte cell death affects the viable myocardium after infarction in rats. *Exp Cell Res* 1996 August 1;226(2):316-27.
- (46) Yaoita H, Ogawa K, Maehara K, Maruyama Y. Attenuation of ischemia/reperfusion injury in rats by a caspase inhibitor. *Circulation* 1998 January 27;97(3):276-81.
- (47) Okamura T, Miura T, Takemura G et al. Effect of caspase inhibitors on myocardial infarct size and myocyte DNA fragmentation in the ischemia-reperfused rat heart. *Cardiovasc Res* 2000 February;45(3):642-50.
- (48) Antman EM, Anbe DT, Armstrong PW et al. ACC/AHA guidelines for the management of patients with ST-elevation myocardial infarction: a report of the

American College of Cardiology/American Heart Association Task Force on Practice Guidelines (Committee to Revise the 1999 Guidelines for the Management of Patients with Acute Myocardial Infarction). *Circulation* 2004 August 31;110(9):e82-292.

- (49) Wagner GS, Macfarlane P, Wellens H et al. AHA/ACCF/HRS recommendations for the standardization and interpretation of the electrocardiogram: part VI: acute ischemia/infarction: a scientific statement from the American Heart Association Electrocardiography and Arrhythmias Committee, Council on Clinical Cardiology; the American College of Cardiology Foundation; and the Heart Rhythm Society. Endorsed by the International Society for Computerized Electrocardiology. *J Am Coll Cardiol* 2009 March 17;53(11):1003-11.
- (50) Wang K, Asinger RW, Marriott HJ. ST-segment elevation in conditions other than acute myocardial infarction. *N Engl J Med* 2003 November 27;349(22):2128-35.
- (51) Wong CK, French JK, Aylward PE et al. Patients with prolonged ischemic chest pain and presumed-new left bundle branch block have heterogeneous outcomes depending on the presence of ST-segment changes. *J Am Coll Cardiol* 2005 July 5;46(1):29-38.
- (52) Catanzaro JN, Meraj PM, Zheng S, Bloom G, Roethel M, Makaryus AN. Electrocardiographic T-wave changes underlying acute cardiac and cerebral events. *Am J Emerg Med* 2008 July;26(6):716-20.
- (53) Pahlm US, Chaitman BR, Rautaharju PM, Selvester RH, Wagner GS. Comparison of the various electrocardiographic scoring codes for estimating anatomically documented sizes of single and multiple infarcts of the left ventricle. *Am J Cardiol* 1998 April 1;81(7):809-15.
- (54) Jaffe AS, Ravkilde J, Roberts R et al. It's time for a change to a troponin standard. *Circulation* 2000 September 12;102(11):1216-20.
- (55) Wu AH. Cardiac troponin: friend of the cardiac physician, foe to the cardiac patient? *Circulation* 2006 October 17;114(16):1673-5.
- (56) Jaffe AS. Chasing troponin: how low can you go if you can see the rise? *J Am Coll Cardiol* 2006 November 7;48(9):1763-4.
- (57) Luepker RV, Apple FS, Christenson RH et al. Case definitions for acute coronary heart disease in epidemiology and clinical research studies: a statement from the AHA Council on Epidemiology and Prevention; AHA Statistics Committee; World Heart Federation Council on Epidemiology and Prevention; the European Society of Cardiology Working Group on Epidemiology and Prevention; Centers for Disease Control and Prevention; and the National Heart, Lung, and Blood Institute. *Circulation* 2003 November 18;108(20):2543-9.

- (58) Jaffe AS, Babuin L, Apple FS. Biomarkers in acute cardiac disease: the present and the future. *J Am Coll Cardiol* 2006 July 4;48(1):1-11.
- (59) Gardner BI, Bingham SE, Allen MR, Blatter DD, Anderson JL. Cardiac magnetic resonance versus transthoracic echocardiography for the assessment of cardiac volumes and regional function after myocardial infarction: an intrasubject comparison using simultaneous intrasubject recordings. *Cardiovasc Ultrasound* 2009;7:38.
- (60) Colonna P, D'Agostino C, Del SB, Sorino M. New echocardiographic technologies in the study of acute myocardial infarction. *Ital Heart J* 2004 June;5 Suppl 6:25S-40S.
- (61) Marwick TH, Brunken R, Meland N et al. Accuracy and feasibility of contrast echocardiography for detection of perfusion defects in routine practice: comparison with wall motion and technetium-99m sestamibi single-photon emission computed tomography. The Nycomed NC100100 Investigators. *J Am Coll Cardiol* 1998 November;32(5):1260-9.
- (62) Abe Y, Muro T, Sakanoue Y et al. Intravenous myocardial contrast echocardiography predicts regional and global left ventricular remodelling after acute myocardial infarction: comparison with low dose dobutamine stress echocardiography. *Heart* 2005 December;91(12):1578-83.
- (63) Lombardo A, Rizzello V, Galiuto L et al. Assessment of resting perfusion defects in patients with acute myocardial infarction: comparison of myocardial contrast echocardiography, combined first-pass/delayed contrast-enhanced magnetic resonance imaging and 99mTC-sestamibi SPECT. *Int J Cardiovasc Imaging* 2006 June;22(3-4):417-28.
- (64) Mahmarian JJ, Dwivedi G, Lahiri T. Role of nuclear cardiac imaging in myocardial infarction: postinfarction risk stratification. *J Nucl Cardiol* 2004 March;11(2):186-209.
- (65) Udelson JE, Beshansky JR, Ballin DS et al. Myocardial perfusion imaging for evaluation and triage of patients with suspected acute cardiac ischemia: a randomized controlled trial. *JAMA* 2002 December 4;288(21):2693-700.
- (66) Mollema SA, Nucifora G, Bax JJ. Prognostic value of echocardiography after acute myocardial infarction. *Heart* 2009 March 9.
- (67) bdel-Aty H, Simonetti O, Friedrich MG. T2-weighted cardiovascular magnetic resonance imaging. *J Magn Reson Imaging* 2007 September;26(3):452-9.
- (68) bdel-Aty H, Zagrosek A, Schulz-Menger J et al. Delayed enhancement and T2-weighted cardiovascular magnetic resonance imaging differentiate acute from chronic myocardial infarction. *Circulation* 2004 May 25;109(20):2411-6.

- (69) Stork A, Muellerleile K, Bansmann PM et al. Value of T2-weighted, first-pass and delayed enhancement, and cine CMR to differentiate between acute and chronic myocardial infarction. *Eur Radiol* 2007 March;17(3):610-7.
- (70) Wang YX, Hussain SM, Krestin GP. Superparamagnetic iron oxide contrast agents: physicochemical characteristics and applications in MR imaging. *Eur Radiol* 2001;11(11):2319-31.
- (71) Bellin MF, Vasile M, Morel-Precetti S. Currently used non-specific extracellular MR contrast media. *Eur Radiol* 2003 December;13(12):2688-98.
- (72) Bellin MF, Van Der Molen AJ. Extracellular gadolinium-based contrast media: an overview. *Eur J Radiol* 2008 May;66(2):160-7.
- (73) Mahnken AH, Muhlenbruch G, Gunther RW, Wildberger JE. Cardiac CT: coronary arteries and beyond. *Eur Radiol* 2007 April;17(4):994-1008.
- (74) Machac J. Cardiac positron emission tomography imaging. *Semin Nucl Med* 2005 January;35(1):17-36.
- (75) Knesaurek K, Machac J. Comparison of 18F SPECT with PET in myocardial imaging: a realistic thorax-cardiac phantom study. *BMC Nucl Med* 2006;6:5.
- (76) Kitagawa K, Sakuma H, Nagata M et al. Diagnostic accuracy of stress myocardial perfusion MRI and late gadolinium-enhanced MRI for detecting flow-limiting coronary artery disease: a multicenter study. *Eur Radiol* 2008 December;18(12):2808-16.
- (77) Schreiber WG, Schmitt M, Kalden P, Mohrs OK, Kreitner KF, Thelen M. Dynamic contrast-enhanced myocardial perfusion imaging using saturation-prepared TrueFISP. *J Magn Reson Imaging* 2002 December;16(6):641-52.
- (78) Fenchel M, Helber U, Simonetti OP et al. Multislice first-pass myocardial perfusion imaging: Comparison of saturation recovery (SR)-TrueFISP-two-dimensional (2D) and SR-TurboFLASH-2D pulse sequences. *J Magn Reson Imaging* 2004 May;19(5):555-63.
- (79) Barmeyer AA, Stork A, Muellerleile K et al. Contrast-enhanced cardiac MR imaging in the detection of reduced coronary flow velocity reserve. *Radiology* 2007 May;243(2):377-85.
- (80) Utz W, Greiser A, Niendorf T, Dietz R, Schulz-Menger J. Single- or dual-bolus approach for the assessment of myocardial perfusion reserve in quantitative MR perfusion imaging. *Magn Reson Med* 2008 June;59(6):1373-7.
- (81) Kim HH, Liao JK. Translational therapeutics of dipyridamole. *Arterioscler Thromb Vasc Biol* 2008 March;28(3):s39-s42.

- (82) Klem I, Heitner JF, Shah DJ et al. Improved detection of coronary artery disease by stress perfusion cardiovascular magnetic resonance with the use of delayed enhancement infarction imaging. *J Am Coll Cardiol* 2006 April 18;47(8):1630-8.
- (83) Camici PG, Prasad SK, Rimoldi OE. Stunning, hibernation, and assessment of myocardial viability. *Circulation* 2008 January 1;117(1):103-14.
- (84) Cochet A, Lalande A, Walker PM et al. Comparison of the extent of delayed-enhancement cardiac magnetic resonance imaging with and without phase-sensitive reconstruction at 3.0 T. *Invest Radiol* 2007 June;42(6):372-6.
- (85) Breuckmann F, Mohlenkamp S, Nassenstein K et al. Myocardial late gadolinium enhancement: prevalence, pattern, and prognostic relevance in marathon runners. *Radiology* 2009 April;251(1):50-7.
- (86) Amado LC, Gerber BL, Gupta SN et al. Accurate and objective infarct sizing by contrast-enhanced magnetic resonance imaging in a canine myocardial infarction model. *J Am Coll Cardiol* 2004 December 21;44(12):2383-9.
- (87) Wang Y, Sun W, Cao G, Meng L, Song L, Du X. Delayed hyperenhancement patterns in occlusive and reperfused myocardial infarcts during different healing stages. *J Magn Reson Imaging* 2006 October;24(4):851-7.
- (88) Kim RJ, Wu E, Rafael A et al. The use of contrast-enhanced magnetic resonance imaging to identify reversible myocardial dysfunction. *N Engl J Med* 2000 November 16;343(20):1445-53.
- (89) Wang YN, Jin ZY, Zhang ZH et al. Assessment of myocardial viability with contrast-enhanced magnetic resonance imaging and comparison with single-photon emission computed tomography. *Chin Med Sci J* 2006 December;21(4):239-44.
- (90) Kuhl HP, Beek AM, van der Weerd AP et al. Myocardial viability in chronic ischemic heart disease: comparison of contrast-enhanced magnetic resonance imaging with (18)F-fluorodeoxyglucose positron emission tomography. *J Am Coll Cardiol* 2003 April 16;41(8):1341-8.
- (91) O'Regan DP, Ahmed R, Neuwirth C et al. Cardiac MRI of myocardial salvage at the peri-infarct border zones after primary coronary intervention. *Am J Physiol Heart Circ Physiol* 2009 July;297(1):H340-H346.
- (92) Krittayaphong R, Laksanabunsong P, Maneesai A, Saiviroonporn P, Udompunturak S, Chaithiraphan V. Comparison of cardiovascular magnetic resonance of late gadolinium enhancement and diastolic wall thickness to predict recovery of left ventricular function after coronary artery bypass surgery. *J Cardiovasc Magn Reson* 2008;10(1):41.

- (93) Hunter DR, Haworth RA, Berkoff HA. Cellular manganese uptake by the isolated perfused rat heart: a probe for the sarcolemma calcium channel. *J Mol Cell Cardiol* 1981 September;13(9):823-32.
- (94) Payet MD, Schanne OF, Ruiz-Ceretti E. Competition for slow channel of Ca²⁺, Mn²⁺, Verapamil, and D-600 in rat ventricular muscle? *J Mol Cell Cardiol* 1980 June;12(6):635-8.
- (95) Khodorov BI, Fayuk DA, Koshelev SG et al. Effect of a prolonged glutamate challenge on plasmalemmal calcium permeability in mammalian central neurones. Mn²⁺ as a tool to study calcium influx pathways. *Int J Neurosci* 1996 December;88(3-4):215-41.
- (96) Narita K, Kawasaki F, Kita H. Mn and Mg influxes through Ca channels of motor nerve terminals are prevented by verapamil in frogs. *Brain Res* 1990 March 5;510(2):289-95.
- (97) Brurok H, Schjott J, Berg K, Karlsson JO, Jynge P. Effects of MnDPDP, DPDP--, and MnCl₂ on cardiac energy metabolism and manganese accumulation. An experimental study in the isolated perfused rat heart. *Invest Radiol* 1997 April;32(4):205-11.
- (98) Brurok H, Schjott J, Berg K, Karlsson JO, Jynge P. Manganese and the heart: acute cardiodepression and myocardial accumulation of manganese. *Acta Physiol Scand* 1997 January;159(1):33-40.
- (99) Brurok H, Skoglund T, Berg K, Skarra S, Karlsson JO, Jynge P. Myocardial manganese elevation and proton relaxivity enhancement with manganese dipyridoxyl diphosphate. Ex vivo assessments in normally perfused and ischemic guinea pig hearts. *NMR Biomed* 1999 October;12(6):364-72.
- (100) Horsburgh MJ, Wharton SJ, Karavolos M, Foster SJ. Manganese: elemental defence for a life with oxygen. *Trends Microbiol* 2002 November;10(11):496-501.
- (101) Kawano J, Ney DM, Keen CL, Schneeman BO. Altered high density lipoprotein composition in manganese-deficient Sprague-Dawley and Wistar rats. *J Nutr* 1987 May;117(5):902-6.
- (102) Friedman BJ, Freeland-Graves JH, Bales CW et al. Manganese balance and clinical observations in young men fed a manganese-deficient diet. *J Nutr* 1987 January;117(1):133-43.
- (103) Hall AJ, Margetts BM, Barker DJ et al. Low blood manganese levels in Liverpool children with Perthes' disease. *Paediatr Perinat Epidemiol* 1989 April;3(2):131-5.
- (104) Wood RJ. Manganese and birth outcome. *Nutr Rev* 2009 July;67(7):416-20.

- (105) Finley JW, Penland JG, Pettit RE, Davis CD. Dietary manganese intake and type of lipid do not affect clinical or neuropsychological measures in healthy young women. *J Nutr* 2003 September;133(9):2849-56.
- (106) Lucchini R, Albini E, Placidi D et al. Brain magnetic resonance imaging and manganese exposure. *Neurotoxicology* 2000 October;21(5):769-75.
- (107) Bleich S, Degner D, Sprung R, Riegel A, Poser W, Ruther E. Chronic manganese: fourteen years of follow-up. *J Neuropsychiatry Clin Neurosci* 1999;11(1):117.
- (108) Huang CC, Chu NS, Lu CS, Chen RS, Schulzer M, Calne DB. The natural history of neurological manganese over 18 years. *Parkinsonism Relat Disord* 2007 April;13(3):143-5.
- (109) Bowler RM, Roels HA, Nakagawa S et al. Dose-effect relationships between manganese exposure and neurological, neuropsychological and pulmonary function in confined space bridge welders. *Occup Environ Med* 2007 March;64(3):167-77.
- (110) Huang YL, Tseng WC, Lin TH. In vitro effects of metal ions (Fe²⁺, Mn²⁺, Pb²⁺) on sperm motility and lipid peroxidation in human semen. *J Toxicol Environ Health A* 2001 February 23;62(4):259-67.
- (111) Lauwerys R, Roels H, Genet P, Toussaint G, Bouckaert A, De CS. Fertility of male workers exposed to mercury vapor or to manganese dust: a questionnaire study. *Am J Ind Med* 1985;7(2):171-6.
- (112) Miller KB, Caton JS, Finley JW. Manganese depresses rat heart muscle respiration. *Biofactors* 2006;28(1):33-46.
- (113) Khan KN, Andress JM, Smith PF. Toxicity of subacute intravenous manganese chloride administration in beagle dogs. *Toxicol Pathol* 1997 July;25(4):344-50.
- (114) Dudek H, Pytkowski B. Effects of in vivo manganese administration on calcium exchange and contractile force of rat ventricular myocardium. *Basic Res Cardiol* 1991 November;86(6):515-22.
- (115) Sanchez-Morito N, Planells E, Aranda P, Llopis J. Magnesium-manganese interactions caused by magnesium deficiency in rats. *J Am Coll Nutr* 1999 October;18(5):475-80.
- (116) Miller KB, Caton JS, Schafer DM, Smith DJ, Finley JW. High dietary manganese lowers heart magnesium in pigs fed a low-magnesium diet. *J Nutr* 2000 August;130(8):2032-5.
- (117) Vitek M, Trautwein W. Slow inward current and action potential in cardiac Purkinje fibres. The effect of Mn plus,plus-ions. *Pflugers Arch* 1971;323(3):204-18.

- (118) Ochi R. The slow inward current and the action of manganese ions in guinea-pig's myocardium. *Pflugers Arch* 1970;316(1):81-94.
- (119) Kohlhardt M, Bauer B, Krause H, Fleckenstein A. Selective inhibition of the transmembrane Ca conductivity of mammalian myocardial fibres by Ni, Co and Mn ions. *Pflugers Arch* 1973 January 22;338(2):115-23.
- (120) Chapman RA, Ellis D. Uptake and loss of manganese from perfused frog ventricles. *J Physiol* 1977 November;272(2):355-66.
- (121) Scholz TD. Reduction in myocardial high energy phosphate spin lattice relaxation times using manganese. *NMR Biomed* 1994 May;7(3):137-40.
- (122) Chauncey DM, Jr., Schelbert HR, Halpern SE et al. Tissue distribution studies with radioactive manganese: a potential agent for myocardial imaging. *J Nucl Med* 1977 September;18(9):933-6.
- (123) Atcher RW, Friedman AM, Huizenga JR, Rayudu GV, Silverstein EA, Turner DA. Manganese-52m, a new short-lived, generator-produced radionuclide: a potential tracer for positron tomography. *J Nucl Med* 1980 June;21(6):565-9.
- (124) Hunter DR, Komai H, Haworth RA, Jackson MD, Berkoff HA. Comparison of Ca²⁺, Sr²⁺, and Mn²⁺ fluxes in mitochondria of the perfused rat heart. *Circ Res* 1980 November;47(5):721-7.
- (125) Brurok H, Berg K, Sneen L, Grant D, Karlsson JO, Jynge P. Cardiac metal contents after infusions of manganese. An experimental evaluation in the isolated rat heart. *Invest Radiol* 1999 July;34(7):470-6.
- (126) Ogurusu T, Wakabayashi S, Shigekawa M. Activation of sarcoplasmic reticulum Ca(2+)-ATPase by Mn²⁺: a Mn²⁺ binding study. *J Biochem* 1991 March;109(3):472-6.
- (127) Gunter TE, Miller LM, Gavin CE et al. Determination of the oxidation states of manganese in brain, liver, and heart mitochondria. *J Neurochem* 2004 January;88(2):266-80.
- (128) Vander EL, Colet JM, Muller RN. Spectroscopic and metabolic effects of MnCl₂ and MnDPDP on the isolated and perfused rat heart. *Invest Radiol* 1997 October;32(10):581-8.
- (129) Lauterbur PC. Image formation by induced local interactions. Examples employing nuclear magnetic resonance. 1973. *Clin Orthop Relat Res* 1989 July;(244):3-6.
- (130) Lin YJ, Koretsky AP. Manganese ion enhances T1-weighted MRI during brain activation: an approach to direct imaging of brain function. *Magn Reson Med* 1997 September;38(3):378-88.

- (131) Sage MR, Wilcox J, Evill CA, Benness GT. Comparison and evaluation of osmotic blood-brain barrier disruption following intracarotid mannitol and methylglucamine iohalamate. *Invest Radiol* 1982 May;17(3):276-81.
- (132) Watanabe T, Natt O, Boretius S, Frahm J, Michaelis T. In vivo 3D MRI staining of mouse brain after subcutaneous application of MnCl₂. *Magn Reson Med* 2002 November;48(5):852-9.
- (133) Leergaard TB, Bjaalie JG, Devor A, Wald LL, Dale AM. In vivo tracing of major rat brain pathways using manganese-enhanced magnetic resonance imaging and three-dimensional digital atlas. *Neuroimage* 2003 November;20(3):1591-600.
- (134) Pautler RG, Mongeau R, Jacobs RE. In vivo trans-synaptic tract tracing from the murine striatum and amygdala utilizing manganese enhanced MRI (MEMRI). *Magn Reson Med* 2003 July;50(1):33-9.
- (135) Brady TJ, Goldman MR, Pykett IL et al. Proton nuclear magnetic resonance imaging of regionally ischemic canine hearts: effect of paramagnetic proton signal enhancement. *Radiology* 1982 July;144(2):343-7.
- (136) Goldman MR, Brady TJ, Pykett IL et al. Quantification of experimental myocardial infarction using nuclear magnetic resonance imaging and paramagnetic ion contrast enhancement in excised canine hearts. *Circulation* 1982 November;66(5):1012-6.
- (137) Pflugfelder PW, Wendland MF, Holt WW et al. Acute myocardial ischemia: MR imaging with Mn-TP. *Radiology* 1988 April;167(1):129-33.
- (138) Pomeroy OH, Wendland M, Wagner S et al. Magnetic resonance imaging of acute myocardial ischemia using a manganese chelate, Mn-DPDP. *Invest Radiol* 1989 July;24(7):531-6.
- (139) Saeed M, Wagner S, Wendland MF, Derugin N, Finkbeiner WE, Higgins CB. Occlusive and reperfused myocardial infarcts: differentiation with Mn-DPDP--enhanced MR imaging. *Radiology* 1989 July;172(1):59-64.
- (140) Hustvedt SO, Grant D, Southon TE, Zech K. Plasma pharmacokinetics, tissue distribution and excretion of MnDPDP in the rat and dog after intravenous administration. *Acta Radiol* 1997 July;38(4 Pt 2):690-9.
- (141) De FM, Bocchi C, Quartieri L, Corradi D, Zompatori M. Mangafodipir-DPDP enhanced MRI visualization of a pancreatic adenocarcinoma previously undetected by extracellular contrast enhanced CT and MRI. *Acta Biomed* 2007 December;78(3):225-8.
- (142) Eser G, Karabacakoglu A, Karakose S, Eser C, Kayacetin E. Mangafodipir trisodium-enhanced magnetic resonance imaging for evaluation of pancreatic mass and mass-like lesions. *World J Gastroenterol* 2006 March 14;12(10):1603-6.

- (143) Chung JJ, Kim MJ, Kim KW. Mangafodipir trisodium-enhanced MRI for the detection and characterization of focal hepatic lesions: is delayed imaging useful? *J Magn Reson Imaging* 2006 May;23(5):706-11.
- (144) Kim JH, Kim MJ, Park YN et al. Mangafodipir trisodium-enhanced MRI of hepatocellular carcinoma: correlation with histological characteristics. *Clin Radiol* 2008 November;63(11):1195-204.
- (145) Wyttenbach R, Saeed M, Wendland MF et al. Detection of acute myocardial ischemia using first-pass dynamics of MnDPDP on inversion recovery echoplanar imaging. *J Magn Reson Imaging* 1999 February;9(2):209-14.
- (146) Jynge P, Brurok H, Asplund A, Towart R, Refsum H, Karlsson JO. Cardiovascular safety of MnDPDP and MnCl₂. *Acta Radiol* 1997 July;38(4 Pt 2):740-9.
- (147) Brurok H, Schjott J, Berg K, Karlsson JO, Jynge P. Effects of manganese dipyridoxyl diphosphate, dipyridoxyl diphosphate--, and manganese chloride on cardiac function. An experimental study in the Langendorff perfused rat heart. *Invest Radiol* 1995 March;30(3):159-67.
- (148) Southon TE, Grant D, Bjornerud A et al. NMR relaxation studies with MnDPDP. *Acta Radiol* 1997 July;38(4 Pt 2):708-16.
- (149) Chapman RA, Ellis D. The effects of manganese ions on the contraction of the frog's heart. *J Physiol* 1977 November;272(2):331-54.
- (150) Vierling W, Reiter M. An intracellularly induced positive inotropic effect of manganese in guinea-pig ventricular myocardium. *Naunyn Schmiedebergs Arch Pharmacol* 1979 April 30;306(3):249-53.
- (151) Charash B, Placek E, Sos TA, Kligfield P. Dose-related effects of manganese on the canine electrocardiogram. *J Electrocardiol* 1982 April;15(2):149-52.
- (152) Meyer JS, Mehdirad A, Salem BI, Kulikowska A, Kulikowski P. Sudden arrhythmia death syndrome: importance of the long QT syndrome. *Am Fam Physician* 2003 August 1;68(3):483-8.
- (153) Conrad LL, Trendley RL, Baxter DJ. Positive inotropic effect of manganese on dog myocardium. *Am J Physiol* 1966 February;210(2):357-9.
- (154) Kreft BP, Baba Y, Tanimoto A, Finn JP, Stark DD. Orally administered manganese chloride: enhanced detection of hepatic tumors in rats. *Radiology* 1993 February;186(2):543-8.
- (155) Burnett KR, Goldstein EJ, Wolf GL, Sen S, Mamourian AC. The oral administration of MnCl₂: a potential alternative to IV injection for tissue contrast

- enhancement in magnetic resonance imaging. *Magn Reson Imaging* 1984;2(4):307-14.
- (156) Wolf GL, Baum L. Cardiovascular toxicity and tissue proton T1 response to manganese injection in the dog and rabbit. *AJR Am J Roentgenol* 1983 July;141(1):193-7.
- (157) Gerdin B, McCann E, Lundberg C, Arfors KE. Selective tissue accumulation of manganese and its effect on regional blood flow and haemodynamics after intravenous infusion of its chloride salt in the rat. *Int J Tissue React* 1985;7(5):373-80.
- (158) Mamourian AC, Burnett KR, Goldstein EJ, Wolf GL, Kressel HY, Baum S. Proton relaxation enhancement in tissue due to ingested manganese chloride: time course and dose response in the rat. *Physiol Chem Phys Med NMR* 1984;16(2):123-8.
- (159) Skjold A, Vangberg TR, Kristoffersen A, Haraldseth O, Jynge P, Larsson HB. Relaxation enhancing properties of MnDPDP in human myocardium. *J Magn Reson Imaging* 2004 December;20(6):948-52.
- (160) Skjold A, Kristoffersen A, Vangberg TR, Haraldseth O, Jynge P, Larsson HB. An apparent unidirectional influx constant for manganese as a measure of myocardial calcium channel activity. *J Magn Reson Imaging* 2006 November;24(5):1047-55.
- (161) Skjold A, Amundsen BH, Wiseth R et al. Manganese dipyridoxyl-diphosphate (MnDPDP) as a viability marker in patients with myocardial infarction. *J Magn Reson Imaging* 2007 September;26(3):720-7.
- (162) Nighswander-Rempel SP, Shaw RA, Kuzio B, Kupriyanov VV. Detection of myocardial cell damage in isolated rat hearts with near-infrared spectroscopy. *J Biomed Opt* 2004 July;9(4):779-87.
- (163) Yang L, Li Z, Yang Y et al. Increased pressure during retrograde cerebral perfusion provides better preservation of the Na⁺, K⁺-ATPase activity. *Perfusion* 2006 November;21(6):319-24.
- (164) Kupriyanov VV, Nighswander-Rempel S, Xiang B. Mapping regional oxygenation and flow in pig hearts in vivo using near-infrared spectroscopic imaging. *J Mol Cell Cardiol* 2004 November;37(5):947-57.
- (165) Nighswander-Rempel SP, Anthony SR, Mansfield JR, Hewko M, Kupriyanov VV, Mantsch HH. Regional variations in myocardial tissue oxygenation mapped by near-infrared spectroscopic imaging. *J Mol Cell Cardiol* 2002 September;34(9):1195-203.

- (166) Li Z, Yang L, Jackson M et al. Increased pressure during retrograde cerebral perfusion in an acute porcine model improves brain tissue perfusion without increase in tissue edema. *Ann Thorac Surg* 2002 May;73(5):1514-21.
- (167) Li Z, Yang L, Summers R, Jackson M, Deslauriers R, Ye J. Is maintenance of cerebral hypothermia the principal mechanism by which retrograde cerebral perfusion provides better brain protection than hypothermic circulatory arrest? A study in a porcine model. *J Card Surg* 2004 January;19(1):28-35.
- (168) Ye J, Li Z, Yang Y et al. Use of a pH-stat strategy during retrograde cerebral perfusion improves cerebral perfusion and tissue oxygenation. *Ann Thorac Surg* 2004 May;77(5):1664-70.
- (169) Kupriyanov VV, Dai G, Shaw RA et al. Noninvasive assessment of cardiac ischemic injury using (87)Rb and (23)Na MR imaging, (31)P MR, and optical spectroscopy. *Magn Reson Med* 2000 December;44(6):899-908.
- (170) Kupriyanov VV, Shaw RA, Xiang B, Mantsch H, Deslauriers R. Oxygen regulation of energy metabolism in isolated pig hearts: a near-IR spectroscopy study. *J Mol Cell Cardiol* 1997 September;29(9):2431-9.
- (171) Grubhofer G, Tonninger W, Keznickl P et al. A comparison of the monitors INVOS 3100 and NIRO 500 in detecting changes in cerebral oxygenation. *Acta Anaesthesiol Scand* 1999 April;43(4):470-5.
- (172) Dullenkopf A, Kolarova A, Schulz G, Frey B, Baenziger O, Weiss M. Reproducibility of cerebral oxygenation measurement in neonates and infants in the clinical setting using the NIRO 300 oximeter. *Pediatr Crit Care Med* 2005 May;6(3):344-7.
- (173) Bhindi R, Witting PK, McMahon AC, Khachigian LM, Lowe HC. Rat models of myocardial infarction. Pathogenetic insights and clinical relevance. *Thromb Haemost* 2006 November;96(5):602-10.
- (174) Goldman S, Raya TE. Rat infarct model of myocardial infarction and heart failure. *J Card Fail* 1995 March;1(2):169-77.
- (175) Langer GA. Interspecies variation in myocardial physiology: the anomalous rat. *Environ Health Perspect* 1978 October;26:175-9.
- (176) Varro A, Lathrop DA, Hester SB, Nanasi PP, Papp JG. Ionic currents and action potentials in rabbit, rat, and guinea pig ventricular myocytes. *Basic Res Cardiol* 1993 March;88(2):93-102.
- (177) Tanaka H, Namekata I, Nouchi H, Shigenobu K, Kawanishi T, Takahara A. New aspects for the treatment of cardiac diseases based on the diversity of functional controls on cardiac muscles: diversity in the excitation-contraction mechanisms of the heart. *J Pharmacol Sci* 2009 March;109(3):327-33.

- (178) Sham JS, Hatem SN, Morad M. Species differences in the activity of the Na(+)-Ca²⁺ exchanger in mammalian cardiac myocytes. *J Physiol* 1995 November 1;488 (Pt 3):623-31.
- (179) Morkin E. Regulation of myosin heavy chain genes in the heart. *Circulation* 1993 May;87(5):1451-60.
- (180) Geary GG, Smith GT, McNamara JJ. Defining the anatomic perfusion bed of an occluded coronary artery and the region at risk to infarction. A comparative study in the baboon, pig and dog. *Am J Cardiol* 1981 June;47(6):1240-7.
- (181) Haider HK, Ye L, Jiang S et al. Angiomyogenesis for cardiac repair using human myoblasts as carriers of human vascular endothelial growth factor. *J Mol Med* 2004 August;82(8):539-49.
- (182) Drake-Holland AJ, Belcher PR, Hynd J, Noble MI. Infarct size in rabbits: a modified method illustrated by the effects of propranolol and trimetazidine. *Basic Res Cardiol* 1993 May;88(3):250-8.
- (183) Baust J, Gage AA, Ma H, Zhang CM. Minimally invasive cryosurgery--technological advances. *Cryobiology* 1997 June;34(4):373-84.
- (184) Pegg DE. Principles of cryopreservation. *Methods Mol Biol* 2007;368:39-57.
- (185) Fowler A, Toner M. Cryo-injury and biopreservation. *Ann N Y Acad Sci* 2005 December;1066:119-35.
- (186) Gao D, Critser JK. Mechanisms of cryoinjury in living cells. *ILAR J* 2000;41(4):187-96.
- (187) Tsukui H, Hoshino S, Saito N, Nishiya Y, Usuda K. Successful surgical treatment of ventricular tachycardia that induced left ventricular aneurysm in 12-year-old boy. *Minerva Pediatr* 2002 February;54(1):53-6.
- (188) Watanabe H, Eguchi S, Miyamura H et al. Histologic findings of long-term cryolesions in a patient with ventricular tachycardia. *Cardiovasc Surg* 1996 June;4(3):409-11.
- (189) Cox JL. Cardiac surgery for arrhythmias. *J Cardiovasc Electrophysiol* 2004 February;15(2):250-62.
- (190) Miller JM, Marchlinski FE. Nonpharmacologic therapy of ventricular arrhythmias. *Cardiovasc Clin* 1992;22(1):117-46.
- (191) Jensen JA, Kosek JC, Hunt TK, Goodson WH, III, Miller DC. Cardiac cryolesions as an experimental model of myocardial wound healing. *Ann Surg* 1987 December;206(6):798-803.

- (192) Maroko PR, Libby P, Ginks WR et al. Coronary artery reperfusion. I. Early effects on local myocardial function and the extent of myocardial necrosis. *J Clin Invest* 1972 October;51(10):2710-6.
- (193) Kloner RA, Rezkalla SH. Cardiac protection during acute myocardial infarction: where do we stand in 2004? *J Am Coll Cardiol* 2004 July 21;44(2):276-86.
- (194) van de LA, Saubier B, Kalbhenn J, Koberne F, Zehender M. Primary percutaneous coronary intervention in acute myocardial infarction: direct transportation to catheterization laboratory by emergency teams reduces door-to-balloon time. *Clin Cardiol* 2006 March;29(3):112-6.
- (195) Ribatti D, Gualandris A, Belleri M et al. Alterations of blood vessel development by endothelial cells overexpressing fibroblast growth factor-2. *J Pathol* 1999 December;189(4):590-9.
- (196) Voisine P, Mathieu P, Doyle D et al. Influence of time elapsed between myocardial infarction and coronary artery bypass grafting surgery on operative mortality. *Eur J Cardiothorac Surg* 2006 March;29(3):319-23.
- (197) Pinto DS, Southard M, Ciaglo L, Gibson CM. Door-to-balloon delays with percutaneous coronary intervention in ST-elevation myocardial infarction. *Am Heart J* 2006 June;151(6 Suppl):S24-S29.
- (198) Schwarz ER, Speakman MT, Patterson M et al. Evaluation of the effects of intramyocardial injection of DNA expressing vascular endothelial growth factor (VEGF) in a myocardial infarction model in the rat--angiogenesis and angioma formation. *J Am Coll Cardiol* 2000 April;35(5):1323-30.
- (199) Freeman I, Cohen S. The influence of the sequential delivery of angiogenic factors from affinity-binding alginate scaffolds on vascularization. *Biomaterials* 2009 April;30(11):2122-31.
- (200) Hao X, Silva EA, Mansson-Broberg A et al. Angiogenic effects of sequential release of VEGF-A165 and PDGF-BB with alginate hydrogels after myocardial infarction. *Cardiovasc Res* 2007 July 1;75(1):178-85.
- (201) Chinen N, Tanihara M, Nakagawa M et al. Action of microparticles of heparin and alginate crosslinked gel when used as injectable artificial matrices to stabilize basic fibroblast growth factor and induce angiogenesis by controlling its release. *J Biomed Mater Res A* 2003 October 1;67(1):61-8.
- (202) Hariawala MD, Horowitz JR, Esakof D et al. VEGF improves myocardial blood flow but produces EDRF-mediated hypotension in porcine hearts. *J Surg Res* 1996 June;63(1):77-82.

- (203) Yla-Herttuala S, Rissanen TT, Vajanto I, Hartikainen J. Vascular endothelial growth factors: biology and current status of clinical applications in cardiovascular medicine. *J Am Coll Cardiol* 2007 March 13;49(10):1015-26.
- (204) Unger EF, Banai S, Shou M et al. A model to assess interventions to improve collateral blood flow: continuous administration of agents into the left coronary artery in dogs. *Cardiovasc Res* 1993 May;27(5):785-91.
- (205) Lazarous DF, Scheinowitz M, Shou M et al. Effects of chronic systemic administration of basic fibroblast growth factor on collateral development in the canine heart. *Circulation* 1995 January 1;91(1):145-53.
- (206) Sakakibara Y, Tambara K, Sakaguchi G et al. Toward surgical angiogenesis using slow-released basic fibroblast growth factor. *Eur J Cardiothorac Surg* 2003 July;24(1):105-11.
- (207) Lazarous DF, Shou M, Stiber JA et al. Pharmacodynamics of basic fibroblast growth factor: route of administration determines myocardial and systemic distribution. *Cardiovasc Res* 1997 October;36(1):78-85.
- (208) Sun XT, Ding YT, Yan XG et al. Angiogenic synergistic effect of basic fibroblast growth factor and vascular endothelial growth factor in an in vitro quantitative microcarrier-based three-dimensional fibrin angiogenesis system. *World J Gastroenterol* 2004 September 1;10(17):2524-8.
- (209) Hanley F, Messina LM, Baer RW, Uhlig PN, Hoffman JI. Direct measurement of left ventricular interstitial adenosine. *Am J Physiol* 1983 August;245(2):H327-H335.
- (210) Fujita M, Ikemoto M, Tanaka T et al. Marked elevation of vascular endothelial growth factor and basic fibroblast growth factor in pericardial fluid of patients with angina pectoris. *Angiogenesis* 1998;2(1):105-8.
- (211) Laham RJ, Simons M, Tofukuji M, Hung D, Sellke FW. Modulation of myocardial perfusion and vascular reactivity by pericardial basic fibroblast growth factor: insight into ischemia-induced reduction in endothelium-dependent vasodilatation. *J Thorac Cardiovasc Surg* 1998 December;116(6):1022-8.
- (212) Yoneda T, Fujita M, Kihara Y et al. Pericardial fluid from patients with ischemic heart disease accelerates the growth of human vascular smooth muscle cells. *Jpn Circ J* 2000 July;64(7):495-8.
- (213) Benjamin LE, Golijanin D, Itin A, Pode D, Keshet E. Selective ablation of immature blood vessels in established human tumors follows vascular endothelial growth factor withdrawal. *J Clin Invest* 1999 January;103(2):159-65.
- (214) Post MJ, Simons M. The rational phase of therapeutic angiogenesis. *Minerva Cardioangiol* 2003 October;51(5):421-32.

- (215) Richardson TP, Peters MC, Ennett AB, Mooney DJ. Polymeric system for dual growth factor delivery. *Nat Biotechnol* 2001 November;19(11):1029-34.
- (216) Tonnesen HH, Karlsen J. Alginate in drug delivery systems. *Drug Dev Ind Pharm* 2002 July;28(6):621-30.
- (217) Morch YA, Donati I, Strand BL, Skjak-Braek G. Effect of Ca²⁺, Ba²⁺, and Sr²⁺ on alginate microbeads. *Biomacromolecules* 2006 May;7(5):1471-80.
- (218) Davis TA, Llanes F, Volesky B, Mucci A. Metal selectivity of Sargassum spp. and their alginates in relation to their alpha-L-guluronic acid content and conformation. *Environ Sci Technol* 2003 January 15;37(2):261-7.
- (219) George M, Abraham TE. Polyionic hydrocolloids for the intestinal delivery of protein drugs: alginate and chitosan--a review. *J Control Release* 2006 August 10;114(1):1-14.
- (220) Orlic D, Kajstura J, Chimenti S, Bodine DM, Leri A, Anversa P. Bone marrow stem cells regenerate infarcted myocardium. *Pediatr Transplant* 2003;7 Suppl 3:86-8.
- (221) Ohta M, Suzuki Y, Chou H et al. Novel heparin/alginate gel combined with basic fibroblast growth factor promotes nerve regeneration in rat sciatic nerve. *J Biomed Mater Res A* 2004 December 15;71(4):661-8.
- (222) Peters MC, Isenberg BC, Rowley JA, Mooney DJ. Release from alginate enhances the biological activity of vascular endothelial growth factor. *J Biomater Sci Polym Ed* 1998;9(12):1267-78.
- (223) Zaragosi LE, Ailhaud G, Dani C. Autocrine fibroblast growth factor 2 signaling is critical for self-renewal of human multipotent adipose-derived stem cells. *Stem Cells* 2006 November;24(11):2412-9.
- (224) Suga H, Eto H, Shigeura T et al. IFATS collection: Fibroblast growth factor-2-induced hepatocyte growth factor secretion by adipose-derived stromal cells inhibits postinjury fibrogenesis through a c-Jun N-terminal kinase-dependent mechanism. *Stem Cells* 2009 January;27(1):238-49.
- (225) Nakagami H, Maeda K, Morishita R et al. Novel autologous cell therapy in ischemic limb disease through growth factor secretion by cultured adipose tissue-derived stromal cells. *Arterioscler Thromb Vasc Biol* 2005 December;25(12):2542-7.
- (226) Nighswander-Rempel SP, Kupriyanov VV, Shaw RA. Relative contributions of hemoglobin and myoglobin to near-infrared spectroscopic images of cardiac tissue. *Appl Spectrosc* 2005 February;59(2):190-3.

- (227) Shaw RA, Mansfield JR, Kupriyanov VV, Mantsch HH. In vivo optical/near-infrared spectroscopy and imaging of metalloproteins. *J Inorg Biochem* 2000 April;79(1-4):285-93.
- (228) Schuder S, Wittenberg JB, Haseltine B, Wittenberg BA. Spectrophotometric determination of myoglobin in cardiac and skeletal muscle: separation from hemoglobin by subunit-exchange chromatography. *Anal Biochem* 1979 January 15;92(2):473-81.
- (229) Pope RM, Fry ES. Absorption spectrum (380-700 nm) of pure water. II. Integrating cavity measurements. *Appl Opt* 1997 November 20;36(33):8710-23.
- (230) Khalil PN, Siebeck M, Huss R et al. Histochemical assessment of early myocardial infarction using 2,3,5-triphenyltetrazolium chloride in blood-perfused porcine hearts. *J Pharmacol Toxicol Methods* 2006 November;54(3):307-12.
- (231) Schwarz ER, Somoano Y, Hale SL, Kloner RA. What is the required reperfusion period for assessment of myocardial infarct size using triphenyltetrazolium chloride staining in the rat? *J Thromb Thrombolysis* 2000 October;10(2):181-7.
- (232) King DF, King LA. A brief historical note on staining by hematoxylin and eosin. *Am J Dermatopathol* 1986 April;8(2):168.
- (233) Fujiwara H, Onodera T, Tanaka M et al. Acceleration of cell necrosis following reperfusion after ischemia in the pig heart without collateral circulation. *Am J Cardiol* 1989 March 7;63(10):14E-8E.
- (234) Titford M. The long history of hematoxylin. *Biotech Histochem* 2005 March;80(2):73-8.
- (235) Yang Y, Gruwel ML, Sun J, Gervai P, Yang X, Kupriyanov VV. Manganese-enhanced MRI of acute cardiac ischemia and chronic infarction in pig hearts: kinetic analysis of enhancement development. *NMR Biomed* 2009 February;22(2):165-73.
- (236) Vohringer M, Mahrholdt H, Yilmaz A, Sechtem U. Significance of late gadolinium enhancement in cardiovascular magnetic resonance imaging (CMR). *Herz* 2007 March;32(2):129-37.
- (237) Misaki T, Allwork SP, Bentall HH. Longterm effects of cryosurgery in the sheep heart. *Cardiovasc Res* 1983 February;17(2):61-9.
- (238) Mikat EM, Hackel DB, Harrison L, Gallagher JJ, Wallace AG. Reaction of the myocardium and coronary arteries to cryosurgery. *Lab Invest* 1977 December;37(6):632-41.

- (239) Yang Y, Sun J, Gervai P et al. Characterization of cryoinjury-induced infarction with manganese-and gadolinium-enhanced MRI and optical spectroscopy in pig hearts. *Magn Reson Imaging* 2010 June;28(5):753-66.
- (240) Gruwel ML, Yang Y, de GP, Sun J, Kupriyanov VV. Magnetic resonance imaging tracking of alginate beads used for drug delivery of growth factors at sites of cardiac damage. *Magn Reson Imaging* 2009 September;27(7):970-5.
- (241) Wendland MF. Applications of manganese-enhanced magnetic resonance imaging (MEMRI) to imaging of the heart. *NMR Biomed* 2004 December;17(8):581-94.
- (242) Schaefer S, Lange RA, Gutekunst DP, Parkey RW, Willerson JT, Peshock RM. Contrast-enhanced magnetic resonance imaging of hypoperfused myocardium. *Invest Radiol* 1991 June;26(6):551-6.
- (243) Natanzon A, Aletras AH, Hsu LY, Arai AE. Determining canine myocardial area at risk with manganese-enhanced MR imaging. *Radiology* 2005 September;236(3):859-66.
- (244) Mendonca-Dias MH, Gaggelli E, Lauterbur PC. Paramagnetic contrast agents in nuclear magnetic resonance medical imaging. *Semin Nucl Med* 1983 October;13(4):364-76.
- (245) Patterson RE, Kirk ES. Analysis of coronary collateral structure, function, and ischemic border zones in pigs. *Am J Physiol* 1983 January;244(1):H23-H31.
- (246) Fujiwara H, Ashraf M, Sato S, Millard RW. Transmural cellular damage and blood flow distribution in early ischemia in pig hearts. *Circ Res* 1982 December;51(6):683-93.
- (247) Hu TC, Pautler RG, MacGowan GA, Koretsky AP. Manganese-enhanced MRI of mouse heart during changes in inotropy. *Magn Reson Med* 2001 November;46(5):884-90.
- (248) Liu QY, Rosenberg RL. Stimulation of cardiac L-type calcium channels by extracellular ATP. *Am J Physiol Cell Physiol* 2001 May;280(5):C1107-C1113.
- (249) Kaibara M, Kameyama M. Inhibition of the calcium channel by intracellular protons in single ventricular myocytes of the guinea-pig. *J Physiol* 1988 September;403:621-40.
- (250) Klein G, Schroder F, Vogler D et al. Increased open probability of single cardiac L-type calcium channels in patients with chronic atrial fibrillation. role of phosphatase 2A. *Cardiovasc Res* 2003 July 1;59(1):37-45.
- (251) Kamp TJ, Hell JW. Regulation of cardiac L-type calcium channels by protein kinase A and protein kinase C. *Circ Res* 2000 December 8;87(12):1095-102.

- (252) Koretsky AP, Silva AC. Manganese-enhanced magnetic resonance imaging (MEMRI). *NMR Biomed* 2004 December;17(8):527-31.
- (253) Nordhoy W, Anthonsen HW, Bruvold M, Jynge P, Krane J, Brurok H. Manganese ions as intracellular contrast agents: proton relaxation and calcium interactions in rat myocardium. *NMR Biomed* 2003 April;16(2):82-95.
- (254) Macchia DD, Polimeni PI. A program in BASIC for calculation of tissue extracellular space and ion distributions in vivo using morphometric and/or extracellular tracer methods. *Comput Biomed Res* 1982 December;15(6):592-7.
- (255) Polimeni PI, Cutilletta AF, Otten MD. Cation distributions in the hypertrophic myocardium (aortic constriction) of the rat. *Cardiovasc Res* 1983 March;17(3):170-6.
- (256) Polimeni PI, Buraczewski SI. Expansion of extracellular tracer spaces in the isolated heart perfused with crystalloid solutions: expansion of extracellular space, trans-sarcolemmal leakage, or both? *J Mol Cell Cardiol* 1988 January;20(1):15-22.
- (257) Lucaciu CM, Dragu C, Copaescu L, Morariu VV. Manganese transport through human erythrocyte membranes. An EPR study. *Biochim Biophys Acta* 1997 September 4;1328(2):90-8.
- (258) WEED RI, ROTHSTEIN A. The uptake of divalent manganese ion by mature normal human red blood cells. *J Gen Physiol* 1960 November;44:301-14.
- (259) Arai AE, Kasserra CE, Territo PR, Gandjbakhche AH, Balaban RS. Myocardial oxygenation in vivo: optical spectroscopy of cytoplasmic myoglobin and mitochondrial cytochromes. *Am J Physiol* 1999 August;277(2 Pt 2):H683-H697.
- (260) Niccoli G, Burzotta F, Galiuto L, Crea F. Myocardial no-reflow in humans. *J Am Coll Cardiol* 2009 July 21;54(4):281-92.
- (261) Miyazaki S, Fujiwara H, Onodera T et al. Quantitative analysis of contraction band and coagulation necrosis after ischemia and reperfusion in the porcine heart. *Circulation* 1987 May;75(5):1074-82.
- (262) Rezkalla SH, Kloner RA. Coronary no-reflow phenomenon: from the experimental laboratory to the cardiac catheterization laboratory. *Catheter Cardiovasc Interv* 2008 December 1;72(7):950-7.
- (263) Cleutjens JP, Kandala JC, Guarda E, Guntaka RV, Weber KT. Regulation of collagen degradation in the rat myocardium after infarction. *J Mol Cell Cardiol* 1995 June;27(6):1281-92.
- (264) Ertl G, Frantz S. Healing after myocardial infarction. *Cardiovasc Res* 2005 April 1;66(1):22-32.

- (265) Zheng W, Kim H, Zhao Q. Comparative toxicokinetics of manganese chloride and methylcyclopentadienyl manganese tricarbonyl (MMT) in Sprague-Dawley rats. *Toxicol Sci* 2000 April;54(2):295-301.
- (266) Haase H, Bartel S, Karczewski P, Morano I, Krause EG. In-vivo phosphorylation of the cardiac L-type calcium channel beta-subunit in response to catecholamines. *Mol Cell Biochem* 1996 October;163-164:99-106.
- (267) Zimmermann H, Shirley SG, Zimmermann U. Alginate-based encapsulation of cells: past, present, and future. *Curr Diab Rep* 2007 August;7(4):314-20.
- (268) Ahmad Z, Khuller GK. Alginate-based sustained release drug delivery systems for tuberculosis. *Expert Opin Drug Deliv* 2008 December;5(12):1323-34.
- (269) Matricardi P, Meo CD, Coviello T, Alhaique F. Recent advances and perspectives on coated alginate microspheres for modified drug delivery. *Expert Opin Drug Deliv* 2008 April;5(4):417-25.
- (270) Zhang Z, Nair SA, McMurry TJ. Gadolinium meets medicinal chemistry: MRI contrast agent development. *Curr Med Chem* 2005;12(7):751-78.
- (271) Ghimire KN, Inoue K, Ohto K, Hayashida T. Adsorption study of metal ions onto crosslinked seaweed *Laminaria japonica*. *Bioresour Technol* 2008 January;99(1):32-7.
- (272) Nokhodchi A, Tailor A. In situ cross-linking of sodium alginate with calcium and aluminum ions to sustain the release of theophylline from polymeric matrices. *Farmaco* 2004 December;59(12):999-1004.
- (273) Ersoy H, Rybicki FJ. Biochemical safety profiles of gadolinium-based extracellular contrast agents and nephrogenic systemic fibrosis. *J Magn Reson Imaging* 2007 November;26(5):1190-7.
- (274) Runge VM, Wells JW. Update: safety, new applications, new MR agents. *Top Magn Reson Imaging* 1995;7(3):181-95.
- (275) Rochitte CE, Lima JA, Bluemke DA et al. Magnitude and time course of microvascular obstruction and tissue injury after acute myocardial infarction. *Circulation* 1998 September 8;98(10):1006-14.
- (276) Wu KC, Kim RJ, Bluemke DA et al. Quantification and time course of microvascular obstruction by contrast-enhanced echocardiography and magnetic resonance imaging following acute myocardial infarction and reperfusion. *J Am Coll Cardiol* 1998 November 15;32(6):1756-64.
- (277) Kloner RA, Ganote CE, Jennings RB. The "no-reflow" phenomenon after temporary coronary occlusion in the dog. *J Clin Invest* 1974 December;54(6):1496-508.

- (278) Dickfeld T, Kato R, Zviman M et al. Characterization of radiofrequency ablation lesions with gadolinium-enhanced cardiovascular magnetic resonance imaging. *J Am Coll Cardiol* 2006 January 17;47(2):370-8.
- (279) Furlani AP, Kalil RA, Castro I et al. Effects of therapeutic angiogenesis with plasmid VEGF165 on ventricular function in a canine model of chronic myocardial infarction. *Rev Bras Cir Cardiovasc* 2009 June;24(2):143-9.
- (280) Nomi M, Miyake H, Sugita Y, Fujisawa M, Soker S. Role of growth factors and endothelial cells in therapeutic angiogenesis and tissue engineering. *Curr Stem Cell Res Ther* 2006 September;1(3):333-43.
- (281) van der Laan AM, Piek JJ, van RN. Targeting angiogenesis to restore the microcirculation after reperfused MI. *Nat Rev Cardiol* 2009 August;6(8):515-23.
- (282) Fam NP, Verma S, Kutryk M, Stewart DJ. Clinician guide to angiogenesis. *Circulation* 2003 November 25;108(21):2613-8.
- (283) Nakagawa K, Chen YX, Ishibashi H et al. Angiogenesis and its regulation: roles of vascular endothelial cell growth factor. *Semin Thromb Hemost* 2000;26(1):61-6.
- (284) Carmeliet P. VEGF as a key mediator of angiogenesis in cancer. *Oncology* 2005;69 Suppl 3:4-10.
- (285) Nillesen ST, Geutjes PJ, Wismans R, Schalkwijk J, Daamen WF, van Kuppevelt TH. Increased angiogenesis in acellular scaffolds by combined release of FGF2 and VEGF. *J Control Release* 2006 November 28;116(2):e88-e90.
- (286) Nillesen ST, Geutjes PJ, Wismans R, Schalkwijk J, Daamen WF, van Kuppevelt TH. Increased angiogenesis and blood vessel maturation in acellular collagen-heparin scaffolds containing both FGF2 and VEGF. *Biomaterials* 2007 February;28(6):1123-31.
- (287) Semenza GL. Vasculogenesis, angiogenesis, and arteriogenesis: mechanisms of blood vessel formation and remodeling. *J Cell Biochem* 2007 November 1;102(4):840-7.
- (288) Carmeliet P. Mechanisms of angiogenesis and arteriogenesis. *Nat Med* 2000 April;6(4):389-95.
- (289) Liu Y, Sun L, Huan Y, Zhao H, Deng J. Application of bFGF and BDNF to improve angiogenesis and cardiac function. *J Surg Res* 2006 November;136(1):85-91.
- (290) Lu H, Xu X, Zhang M et al. Combinatorial protein therapy of angiogenic and arteriogenic factors remarkably improves collateralogenesis and cardiac function in pigs. *Proc Natl Acad Sci U S A* 2007 July 17;104(29):12140-5.

- (291) Battler A, Scheinowitz M, Bor A et al. Intracoronary injection of basic fibroblast growth factor enhances angiogenesis in infarcted swine myocardium. *J Am Coll Cardiol* 1993 December;22(7):2001-6.
- (292) Sanz-Ruiz R, Fernandez-Santos E, Dominguez-Munoz M et al. Early translation of adipose-derived cell therapy for cardiovascular disease. *Cell Transplant* 2009;18(3):245-54.
- (293) Langlois G, Dusseault J, Bilodeau S, Tam SK, Magassouba D, Halle JP. Direct effect of alginate purification on the survival of islets immobilized in alginate-based microcapsules. *Acta Biomater* 2009 November;5(9):3433-40.
- (294) Abalovich AG, Bacque MC, Grana D, Milei J. Pig pancreatic islet transplantation into spontaneously diabetic dogs. *Transplant Proc* 2009 January;41(1):328-30.
- (295) Rider DA, Dombrowski C, Sawyer AA et al. Autocrine fibroblast growth factor 2 increases the multipotentiality of human adipose-derived mesenchymal stem cells. *Stem Cells* 2008 June;26(6):1598-608.
- (296) Bai X, Yan Y, Song YH et al. Both cultured and freshly isolated adipose tissue-derived stem cells enhance cardiac function after acute myocardial infarction. *Eur Heart J* 2009 December 25.
- (297) Okura H, Matsuyama A, Lee CM et al. Cardiomyoblast-like cells differentiated from human adipose tissue-derived mesenchymal stem cells improve left ventricular dysfunction and survival in a rat myocardial infarction model. *Tissue Eng Part C Methods* 2009 July 22.
- (298) Gwak SJ, Bhang SH, Yang HS et al. In vitro cardiomyogenic differentiation of adipose-derived stromal cells using transforming growth factor-beta1. *Cell Biochem Funct* 2009 April;27(3):148-54.

Abbreviations

$\Delta\Psi_m$	Electrochemical potential
ADP	Adenosine diphosphate
ADSCs	Adipose-derived stem cells
AMP	Adenosine monophosphate
ATP	Adenosine triphosphate
B_0	External magnetic field
bFGF	Basic fibroblast growth factor
BP	Blood pressure
BW	Body weight
deoxy-	Deoxygenated
ϵ	Molar absorptivity
ECF	Extracellular fluid
ECG	Electrocardiogram
FA	Fatty acid
FLASH	Fast low angle shot (MRI)
G	Guluronic acid
Gd-DTPA	Gd-Diethylenetriaminepentaacetate
Gd-MRI	Gd-DTPA-enhanced MRI
GRE	Gradient Recalled Echo
H&E	Hematoxylin & eosin
Hb	Hemoglobin
HR	Heart rate
I	Intensity of passed light
I_0	Intensity of incident light
ICG	Indocyanine green
IR676	IR-676 iodide; 1,1',3,3,3',3'-hexamethyl-4,5,4',5'-dibenzoindodicarbocyanine
KHB	Krebs-Henseleit buffer
LAD	Left anterior descending coronary artery

LV	Left ventricle
LVDP	Left ventricular developed pressure
M	Mannuronic
Mb	Myoglobin
MEMRI	Mn-enhanced MRI
Met-Hb	Methemoglobin
MI	Myocardial infarction
MnDPDP	Manganese dipyridoxyldiphosphate
Mn-TP	Manganese ethylenediaminetetraphosphonate
MR	Magnetic resonance
MRI	Magnetic resonance imaging
Mw	Molecular weight
NADH	Nicotinamide adenine dinucleotide
NIR	Near infrared
OSP	Oxygen saturation parameter
Oxy-	Oxygenated
PCr	Phosphocreatine
PET	Positron emission tomography
<i>pI</i>	Isoelectric point
PP	Perfusion pressure
r_1	Longitudinal relaxivity of a magnetic resonance contrast agent
r_2	Transverse relaxivity of a magnetic resonance contrast agent
RF	Radio frequency
ROS	Reactive oxygen species
SI	Signal intensity
SOD	Superoxide dismutase
SPECT	Single photon emission computed tomography
SR	Sarcoplasmic reticulum
SSFP	Steady-state free precession sequences
T_1	Spin-lattice relaxation time
T_2	Spin-spin relaxation time

TE	Echo times
TR	Repetition time
TTC	2,3,5-triphenyltetrazolium choloxide
VEGF	Vascular endothelial growth factor
γ	Gyromagnetic ratio
ω	Angular frequency of spin precession